University College London

Continuous Flow Synthesis of Gold Nanoparticles in Microfluidic Systems for SERS and Antimicrobial Applications

He Huang

A thesis submitted for the degree of

Doctor of Philosophy

From

University College London

Department of Chemical Engineering

Supervisors:

Prof. Asterios Gavriilidis

Prof. Ivan Parkin

February 2019

Declaration of Authorship and Originality

I, He Huang, confirm that the work presented in this thesis is my own. Where information has been derived from other sources, I confirm that this has been indicated in the thesis.

Signature: Date: February 2019

Abstract

In this thesis we focus on the synthesis of gold nanoparticles (Au NPs) which are mainly used for the Surface Enhanced Raman Scattering (SERS) and antimicrobial applications. As the properties of Au NPs are morphology-dependent, synthetic routes with good control are quite important to obtain the Au NPs with best performance during applications. The aim of this thesis was to investigate the adaptation of different synthetic routes of Au NPs from batch to continuous microfluidic systems to overcome some shortcomings in batch and achieve controllable fabrication.

Firstly, sub-3 nm citrate-capped gold nanoparticles were synthesized in continuous flow capillary reactors with enhanced nucleation for easier further functionalization compared to thiol-capped Au NPs in similar size range. It is speculated that the negatively charged tubing-water interface, offers heterogeneous nucleation sites for positively charged citrate-gold precursor species, stabilizing the nuclei and inhibiting their growth.

As a gaseous reducing agent, carbon monoxide (CO) has a big potential in nanoparticle synthesis as it is very easy to remove from the product. The second synthetic route was the synthesis of Au NPs by CO reduction in microfluidic system. With the aid of segmented microfluidic system, the polydispersity of Au NPs was reduced to < 5% compared to Au NPs with similar size synthesized in a batch system (11%). The CO-produced gold nanoparticles without any capping agent (26.6 nm) showed a good SERS performance with an average enhancement factor of 2.40 × 10^9 which were contributed by the narrower gap between particles and easier adsorption of analysing molecule onto naked surface of gold nanoparticles.

To improve hydrodynamics, CO-aqueous gold precursor flow system was changed by using a Teflon AF-2400 membrane contactor in a tube-in-tube set-up to pre-dissolve CO into organic phase at higher pressure. Since more concentrated CO enhanced the reduction rate, capping agent was important to obtain stable Au NPs with different sizes. After optimization, cysteine was chosen as the capping agent to develop a rapid (3 min compared to few hours ~ days in batch) and high-yield (yield>95%, throughput ~ 50 mg/h) synthesis of $Au_{25}(Cys)_{18}$ nanoclusters (NCs) via CO reduction in segmented microfluidic system. These Au NCs as a crystal violet (CV) photobactericidal enhancement agent was tested against *S. aureus,* which showed significantly enhanced bactericidal activity of crystal violet encapsulated in a silicon substrate under white light illumination of ~312 lux.

Impact Statement

Gold nanoparticles (Au NPs) have wide applications in the fields of labelling, imaging, sensing and catalysis due to their unique optical and physical properties, as well as biomedical applications due to the good biocompatibility. These applications highly depend on the size, shapes, and functionalization of the nanomaterials. Thus, the robust and reproducible synthetic process is of great importance.

Compared to conventional system, microreactors give good performance during the synthesis with precise control of operational parameters, controlled or fast mixing, enhanced mass/heat transfer and ease of scale-up. This PhD project was focus on adaptation the synthetic pathways of Au NPs from batch to microfluidic system for more efficient synthetic processes and better quality of the products.

Highlights:

(1) The negatively charged tubing-water interface was investigated for the enhancement of nucleation rates. Sub-3 nm gold nanoparticles, for which size previously demanded stronger capping agents, were synthesized in continuous flow capillary reactors in citrate-only system. Since this approach highlights the significant role of the interaction between tubing wall and reactants, it could instigate new research on nanoparticle synthesis in systems with high surface-to-volume ratio. The ultra-small size Au NPs capped by citrate could also be used for wider applications because of the ease of functionalization and non-toxicity.

(2) The translation of Au NPs synthesis via CO reduction from batch to microreactor was developed for enhanced safety (smaller volumetric usage of highly toxic CO gas) and cleaner products (no reducing agent left in colloidal solution). The combination between gaseous reductant and the microstructure device with special configuration design makes the particles more monodisperse (polydispersity < 5%), and the synthesis more flexible for various Au NPs with different sizes and capping agents, resulting in a big potential for different applications. Since this approach could produce highly controllable and reducing agent-free Au NPs in short time, it could be a very promising material preparation protocol for the study of gold nanoparticle applications. For example, the as-synthesized Au NPs can be used for Surface Enhanced Raman Scattering with similar enhancement factor of citrate-capped Au NPs but shorter production time (4 min vs. 30 min).

(3) The gas-liquid microfluidic system was further improved by using a Teflon AF-2400 membrane microreactor in a tube-in-tube set-up to pre-dissolve CO into organic phase to increase the amount of reducing agent at higher pressure. The main challenge was the Au NPs self-assembled on the water-organic interface which led to material loss and size changes. Different capping agents were investigated to solve this problem and the water-soluble thiol, cysteine, gave the best performance to prevent the yield loss without suppressing the reduction rate.

(4) A high-yield and rapid atomically precise synthetic pathway for $Au_{25}(Cys)_{18}$ nanoclusters (NCs) via CO in segmented microfluidic system was proposed. The reaction time was reduced to order of minutes compared to few hours ~ days in batch. The NCs was used as photobactericidal enhancement materials.

In antimicrobial testing against *S. aureus,* additional encapsulation of Au NCs into crystal impregnated silicone significantly enhanced photobactericidal activity (~1.7 log reduction in viable bacteria) upon 6 h illumination of about 312 lux in average.

Beyond the academic research, as-synthesized Au_{25} NCs are of great interest by hospitals which have higher requirement for antibacterial environment. Their robust and facile synthetic process gives the possibility for industrial manufacture.

Acknowledgements

First, I would like to express my deepest gratitude to my principal supervisor, Professor Asterios Gavriilidis, for his patient guidance, invaluable advice, encouragement and massive support all along these four years. Without him, I could not have done this work. His enthusiasm for scientific research and conscientious attitude towards science set me the best example of how to be a scholar. I'm very lucky to be his student and have him as my supervisor. I also would like to express my sincere appreciation to Professor Ivan Parkin for being my co-supervisor, whose solid and profound knowledge, especially in chemistry, filled the missing pieces of my research apart from engineering perspective. During the whole PhD period, I got a great deal of help from Professor Parkin’s group (Dr. Tom Macdonald, Dr. Sultan Ben-Jaber, Dr. William Peveler, Dr. Guanjie He, Dr. Sanjayan Sathasivam and Dr. Gi-Byoung Hwang) and had some very pleasant collaboration. A special mention also goes to Professor Peter Dobson and Professor Nguyen Thi Kim Thanh from MaFuMA Project for their invaluable and inspiring advice. It's a great honour to be involved in MaFuMA Project and have opportunity to know and work with the elites from different fields.

Secondly, I’d like to express my gratitude to Professor Gavriilidis’ lab group. Special thanks to Dr Razwan Baber, Dr. Hendrik du Toit and Dr Gaowei Wu, who had endless patience and unselfishly shared their experience and knowledge to help me gradually developing scientific research skills. I can always get useful suggestions and help from them timely. Thanks to Spyros and Luca who also worked on gold nanoparticle synthesis in our group. I did enjoy

discussing with my colleagues which inspired me a lot during the research. Thanks to Enhong, Katerina, Max, Anand, Baldo, Conor, Gleb and Valentina for their help in both research and life. It was them to keep me positive in working hours and enjoy the PhD life. My sincere thanks also go to the technicians in both Chemical Engineering and Chemistry Department, especially to Dr Simon Barrass, Dr. Steve Firth, Dr. Han Wu and Dr. Kersti Karu, who helped me a lot on the use of instruments and facilities in the lab.

I would like to thank my friends who I met in the UK, whom without I could not have got used to the life here such quickly. I'll always remember the time we spent together. Thanks to my friends and my family in China. Although time and distance separate us, I could always get the sweetest support whenever I need. Here I leave the sincerest gratitude to my parents, Ning and Jie, who give me the sweetest home in the world and endless courage to pursue my dream.

Finally, I would like to thank UCL-CSC Joint Scholarship for financial support.

Contents

List of Figures

List of tables

Nomenclature

A	specific interfacial area [m^2/m^3]
c	molar concentration [mol/m^3]
c_{bulk}	molar concentration of the powder, whose concentration is 1 [mol/m^3]
c_i	gas concentration in solvent [M]
$c_{i,mem}$	gas concentration in membrane [M]
$c_{i,0}$	concentration of gas phase [M]
Ca	Capillary number [-]
C_s	solubility [mol/L]
d	diameter [m]
D	dispersion coefficient or diffusivity [m^2/s]
D_i	diffusivity of gas in solvent [m^2/s]
D_c	coil diameter [m]
EF	enhancement factor
Fo	Fourier number [-]
g	gravitational constant [$g \cdot ms^{-2}$]
I	Intensity [a.u.]

H	thickness of AF-2400 tube
k	mass transfer coefficient [s^{-1}]
κ	Boltzmann's constant ($\kappa = 1.381\times10^{-23}$J/K)
K_H	Henry's law constant for gas with solvent
K_{mem}	mass transfer coefficient of gas in membrane [m/s]
l/g	liquid to gas flow ratio [-]
L	length [m]
N	number of molecules [-]
N_A	Avogadro constant= 6.02×10^{23} [mol^{-1}]
N_{bulk}	number of molecules probed in Raman sample [-]
N_{De}	Dean number [-]
N_{Re}	Reynolds number [-]
P	pressure [bar]
Q	Volumetric flow rate (ml/min)
r	radial position [mm]
R	particle radius [nm]
R_{inn}	inner radius [mm]
R_{outer}	outer radius of Teflon AF-2400 tube
S	area [m^2]

T	temperature [K]
t	time [s]
u	longitudinal superficial velocity [m/s]
$U_{streaming}$	Streaming potential [mV]
V	Volume [m^3]
V_b	Taylor bubble velocity [mL/mol]
z	axial position

Greek Symbols

$\mathscr{D}$	Diffusion coefficient [m^2/s]
μ	viscosity [Pa·s]
ρ	density [g/mL]
κ	Conductivity [µS/cm]
λ	curvature ratio [-]
ζ	zeta potential [mV]
δ_{film}	film thickness [m]
σ	surface tension [N/m]

Subscripts

Au	gold
c	capillary
CO	carbon monoxide
CO,slug	CO in the liquid slug
CO,flim	CO in the film surrounding gas bubbles
dos	dosing
film	film surrounding the bubble in droplet flow
g	gas phase
in	inlet of the reactor
inn	Inner radius of Teflon AF-2400 tube
input	input
L	liquid
L,cap	liquid phase in the hemispherical cap
L,film	liquid phase in the film surrounding the bubble
needed	needed
mem	membrane
out	Outlet of the reactor
outer	outer radius of the tube

RS	Raman spectra
scan	Raman scanning (here is the Raman spot size)
sub	substrate
SERS	Surface-enhanced Raman scattering
t	tubing
UC	unit cell

1. Introduction

1.1 Motivation and objectives

In the last decades, gold nanoparticles (Au NPs) have been a hot topic with an exponential increase in the number of publications because of their intriguing physicochemical, nontoxic, biological and catalytic properties, and ease of functionalization. The ultra-small size Au NPs (crystalline materials with quasicontinuous band structure) and clusters (molecular-like materials with discrete electronic structure)[1] with high catalytic activity are primarily synthesized to catalyse organic reactions.[2-5] The specific shapes of gold nanostructures like nanorods (NRs) could be used for *in vivo* applications,[6] selective targeting in photo-thermal therapeutics or selective biomarkers in biodiagnostics.[7] The various functionalized Au NPs have gained plenty of interest in cancer therapy,[8] analytical sciences,[6, 9-12] and nanomedicines.[13] As the sulfur ligands are abundant in DNA or other proteins,[14-15] Au NPs capped by amphipathic ligands, such as the hydrophobic alkanethiol interior and hydrophilic shell like thiolated polyethylene glycols (PEGs), have aroused great interest for bio-applications.[16-17] [14] In drug delivery, the multifunctional Au NPs-cored dendrimer could act as nanocarriers and produce proton-sponge effect to prevent lysosomal escape.[14] At the same time, the Au bimetallic NPs have also been a hot topic due to their specific optical,[18] electronic,[19-20] magnetic[21] and catalytic properties.[22] In order to to achieve the best performance for most of the applications, controllable and repeatable synthetic processes are very important as the performance of synthesized Au NPs are highly depended on the particle size, shape and functionalization.

Recently, most of the synthetic routes for Au NPs were developed and optimized in batch systems.[23] However, the reactants injection with limited mixing in conventional synthetic methods leads to high concentration spots and gradients which can cause variable reaction rates and multi-stages of reaction, resulting in broad size distribution of the final particles.[23-24] Moreover, heat/mass transfer provided by batch system limits the control of experimental conditions during the reactions with fast kinetics.[25] As the mass/heat transfer changes with reactor size, the batch processes are limited to provide rapid transfer and the quality of the NP products during scale-up is affected.[23]

Microreactors, which exhibit more controllable mixing due to the reduced diffusion paths and enhanced mass/heat transfer with larger surface-to-volume ratio and fast response time due to the small volume of the reactants, is an alternative way to solve the problems derived from batch system.[26] Additionally, the continuous flow system is easier to scale up with parallel operation if multiple microfluidic reactors used.[27] Thus, in this thesis, various microfluidic systems were tested to adapt different synthetic routes of Au NPs from batch to flow with precise control of experimental conditions.

1.2 Outline of thesis

In Chapter 1, the motivation of studying gold nanoparticle synthesis in microfluidic systems is introduced. The objectives are also given.

In Chapter 2, the commonly used synthetic routes of Au NPs based on different reducing and capping agents are introduced, followed by a review of Au NP synthesis in flow. The advantages of using microfluidic system for the synthesis are highlighted. Moreover, the existing problems of adapting synthetic processes from batch to flow revealed by previous investigations are also presented.

In Chapter 3, sub-3 nm citrate-capped Au NPs were synthesized in continuous flow capillary reactors by enhancing nucleation. It is speculated that the negatively charged tubing-water interface, offers heterogeneous nucleation sites for positively charged citrate-gold precursor species, stabilizing the nuclei and inhibiting their growth.

In Chapter 4, the second synthetic route of Au NPs via carbon monoxide (CO) reduction in gas-liquid microfluidic system was developed. As a gaseous reducing agent, CO has a big potential in nanoparticle synthesis as it is very easy to remove from the product by venting. A gas-liquid segmented flow was formed inside a 1 mm inner diameter (I.D.) coiled flow inverter (CFI) with aqueous gold precursor and gaseous reducing agent to produce monodisperse Au NPs.

In Chapter 5, the gas-liquid flow system was updated to improve hydrodynamics by using a Teflon AF-2400 membrane microreactor in a tube-in-tube set-up to pre-dissolve CO into organic phase at higher pressure before mixing with the gold precursor in CFI. Since the more concentrated CO enhanced the reduction rate, capping agent was important to obtain stable Au NPs. Different effects of operational parameters on Au NPs size, size distribution and stability were investigated to show pros and cons of using this microfluidic system in Au NPs synthesis via CO reduction.

In Chapter 6, a well-developed synthesis of cysteine-capped Au_{25} nanoclusters (NCs) via CO reduction using the same liquid-liquid microfluidic system in

Chapter 5 was presented. After optimization, high-yield (yield > 95%, throughput ~ 50 mg/h) $Au_{25}(Cys)_{18}$ NCs was formed within 3 min (compared to few hours ~ days in batch) at elevated temperature (80 °C). The antimicrobial activity of the nanoclusters with crystal violet (CV) was tested.

In Chapter 7, the conclusions of the thesis are summarized. Two microfluidic systems were developed: one makes use of the surface interaction between tubing wall and reactants in aqueous solution to enhance the nucleation rate; one is used to synthesize Au NPs with different sizes via CO reduction. The future work is also suggested either for further research based on recent findings, or the exploration of new systems and products derived from the experiences earned.

2. Literature Review

In general, there are two main processes in nanoparticle formation, nucleation and growth. Nucleation shown in **Figure 2-1a** is induced by the reaction between metal ions and reducing agent. The interaction between the precursor, reductant and coordinating ligands determines the formation of the nucleus. That is why nucleation is influenced heavily by the specific chemical properties of the relative substances.[28] In contrast to nucleation, the growth of nanoparticles shown in **Figure 2-1b** involves two separated electrochemical steps: positive metallic ions attach on the surface of the nucleus with negatively charged double layer, and ligands free from metal complex. The ligands with different functional groups have different donor ability on particle surface, which leads to the difference in stability and reactivity of the particles. In order to achieve colloidal stability, the ligands prevent synthesized particles aggregating via either steric (e.g. alkylthiols) or electrostatic (e.g. citrate) repulsion.[29] Based on the different reducing ability of the reducing agent and different binding strength and functional groups of capping agents, the mechanisms of Au NPs fabrication could be divided into three kinds of methods: seed-mediated growth and nucleation-growth-passivation during *in situ* synthesis (nucleation and growth are completed in the same process),[30] and seeded growth synthesis.

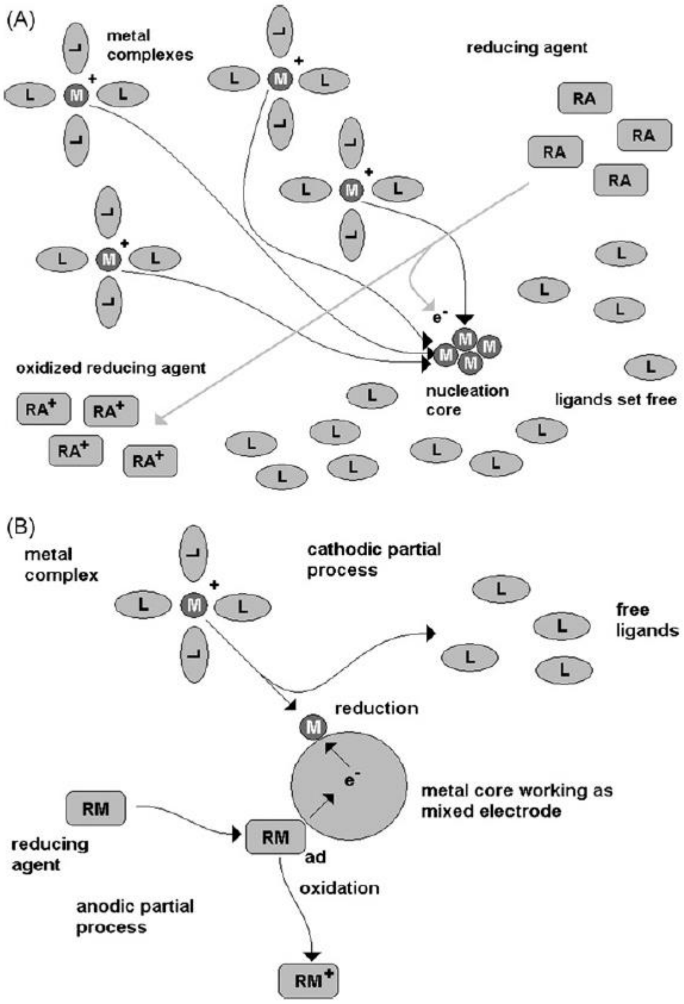

Figure 2-1 Nanoparticle formation (schematically): (A) nucleation and (B) electrochemical processes in particle growth (ad = adsorbed) (Adapted from ref.[28] with permission of The Royal Society of Chemistry).

The term "seed-mediated growth" method was proposed by Wuithschick *et al.*[31] to conclude a process which the nucleation occurred firstly with fast reaction, then a growth stage substitutes the nucleation as the gold ions are preferentially binding onto the existing solid gold surface with lower surface potential.[32] Thus, reduction only occurs on the seed particle surfaces. In other words, there will be no more new nucleus formed and only growth process exists as the autocatalysis on gold surface is in preference to the reduction in the bulk solution.[31] Thus, the separation of the nucleation and growth processes during reaction leads to monodisperse particle size. The advantages of the Au NPs synthesized from this method are narrow size distribution and easy functionalization of the Au NPs capped by exchangeable ligands for further application. Turkevich method, as a presentative of the seed-mediated growth method, have been regarded as the most popular method[33] to synthesize citrate-capped Au NPs since it was firstly proposed by Turkevich *et al.*[34] in 1951. Au NPs with around 20 nm were produced by adding tri-sodium citrate dehydrate quickly into a boiling tetrachloroauric acid ($HAuCl_4$) solution with vigorous stirring. On the basis of Turkevich method, numbers of papers were published to show the optimization of the this method,[35-39] new substitution of reducing agents[40] or capping agents[41-43] for various purposes such as smaller particle size, optimized operational conditions or wider applications.

However, the purpose of using mild reducing agents for thermodynamic controlled growth[31] in seed-mediated growth synthesis results in the limited reducing ability and relatively slow reaction rate, which is quite hard to obtain ultra-small size particles. Until recently the most widely used method to synthesize Au NP under 5 nm[44] is the Brust-Schiffrin method which is so-called nucleation-growth-passivation[45-46] synthesis involving both strong reducing agents (e.g. $NaBH_4$) and capping agent with a strong binding strength (e.g. thiols).[47] The strength of $NaBH_4$ is much higher than citrate[33] and the gold ions can be fully reduced to metallic atoms in the order-of-magnitude of milliseconds.[48] As $NaBH_4$ keeps reducing unconsumed precursor, nuclei are produced throughout the whole synthesis, which leads to a parallel process of nucleation and growth. In this case the capping agents (thiol) act a very decisive role to separate synthesized Au NPs spontaneously and thus, limit the growth of particles. This is why most of Au NPs with ultra-small size are stabilized by thiols.[33]

Even though one-pot synthesis is convenient and less time consuming, there are some limitations. When larger particle size or special shape of Au NPs is needed, roughly increasing the concentration of precursor could lead to parallel processes of nucleation and growth and make the reaction difficult to control, resulting in polydisperse particles and various shapes. Thus, seeded growth method was developed to grow Au NPs stepwise with manual control. There are two stages in this method. Firstly, the seed particles with small size are synthesized. Then the seed particles will mix with “growth solution” containing more gold precursor, reducing agents and capping agents for further growth. During second stage, in order to prevent new nucleation occurring, the reducing agents used are always with weak reducing ability,[33] so that the gold ions are preferentially reduced on the surface of seed particles by autocatalysis and no more nuclei are formed. The second stage could repeat several times to gradually enlarge the particle size with good control.

So far, most of the synthetic routes mentioned above for Au NPs fabrication were born and optimized in batch-based system.[33] However, the immediate feeding the reducing agent in conventional synthetic methods will lead to a partial high concentration (concentration gradients) which cause variable sizes and broad size distribution of final particles grew from the nuclei produced at different times. In addition, the macroscale volume of reactants inhibit the mass/heat transfer, which limits the precise control of the experimental conditions.[25] Based on this consideration, microreactors which could manipulate fluids with precise movement and mixing in sub-millimetre dimensions have come into prominence. Due to the large surface-to-volume ratio and decreased diffusion paths, microreactors exhibit much better mixing which plays an important role in monodisperse nanoparticle formation.[49] In addition, variable parameters (temperature, pressure, residence time, etc.)[50] could be controlled easily and safely due to the smaller dosage in microreactors, which leads to precise control of the reaction with shorter response time. Moreover, continuous microfluidic synthetic method can make scaling to large production possible with the parallel operation of multiple reactor units and reduce the labour and time consumption.[51]

2.1 Major synthetic routes used in flow synthesis of gold nanoparticles

In order to adapt the advantages of synthesis in flow, most of the literatures choose to improve and extend the synthetic routes on the basis of Turkevich or Brust-Schiffrin methods as they are still the major fabrication methods used for Au NPs synthesis and have been well-studied. Beyond that, the mechanism of thiolate-protected nanoclusters (NCs) formation is also introduced, which could produce atomically precise NCs (< 2 nm core diameter) with unique discrete electronic structure and molecular-like properties.

2.1.1 The mechanism of the Turkevich method

Figure 2-2 shows the basic chemistry behind the Turkevich method. The tri-sodium citrate ($Na_3C_6H_5O_7$) reduces tetrachloroauric acid ($HAuCl_4$) at elevated temperature and then stabilizes the synthesized gold nanoparticles. Biggs *et al.*firstly proposed the reason of the stable Au NP colloidal solution in the

Turkevich method.[32] Gold ions were reduced by citrate to Au^0 which could quickly adsorb other citrate and $[AuCl_4]^-$ species. The Au^0 clusters grew with adsorbed aurate and citrate ions. Due to preferential binding of aurate over citrate, the growing clusters had weak attractive forces between particles.[32] Therefore this kind of agglomeration was reversible and limited by a steric barrier produced by adsorbed ions. As the reaction proceeded, gold precursor was consumed and the released citrate capped the surface of synthesized particles, resulting in higher charges and repulsive potential on particles. The clusters then broke down to final size and a stable colloidal solution was obtained.

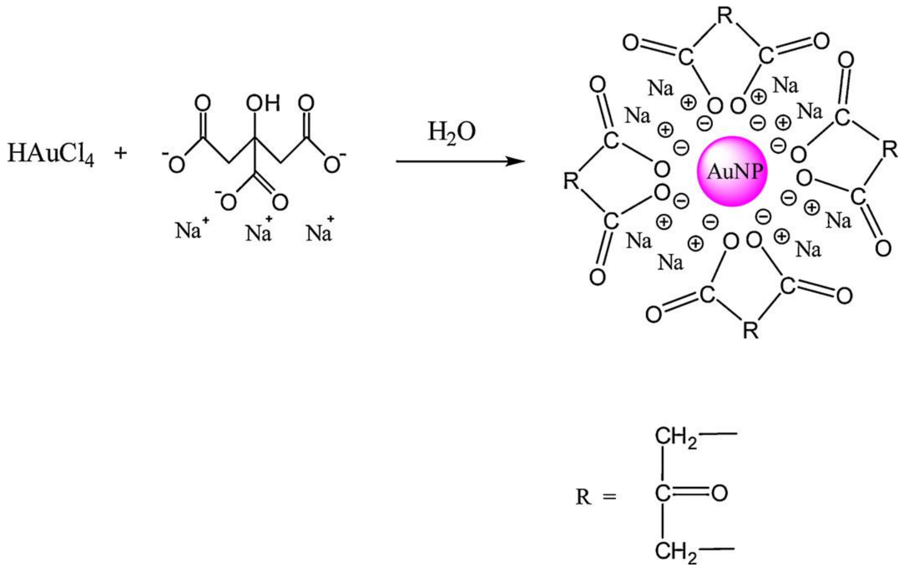

Figure 2-2 Chemistry of the Turkevich method (reprinted with permission from ref.[30] Copyright 2012, American Chemical Society).

However, the mechanism of the Turkevich method has not been figured out until recent years because the reactants used in this method have different species and reactivity at different pH. In this method citrate acts three roles: reducing agent, capping agent and pH mediator.[36] When the acidic $HAuCl_4$ mixes with alkaline citrate, species of both reactants change, reduction and side reaction occur at the same time, resulting in a very complex process. Polte's group used an experimental method to prove that the Au(III) species was the critical element to control particle size which determined fast nucleation rate and the separation between nucleation and growth processes.[31] **Figure 2-3** shows the nucleation and growth processes occurred in the typical Turkevich method when the initial pH of precursor was 3.3. Before mixing, $[AuCl_4]^-$ was the predominant species in the precursor. After the addition of citrate, precursor equilibrium went forward to less reactive gold complexes. A small fraction of reactive $[AuCl_4]^-$ was reduced quickly to Au(0) for seed particle formation which decided particle number and final particle size. When precursor complex equilibrium was reached, the mixture mainly or only contained $[AuCl_{3-x}OH_{1+x}]^-$, which had lower reactivity. Due to preferential binding of aurate over citrate,[32] the growing clusters with low surface potential preferentially attach on seed particles. The reduction only occurs on the seed particle surfaces. Namely, after complex equilibrium was reached, there would be no more new seed particles formed and only growth process existed. The separation of the nucleation and growth processes during the reaction was the key point to obtain monodisperse particle size.

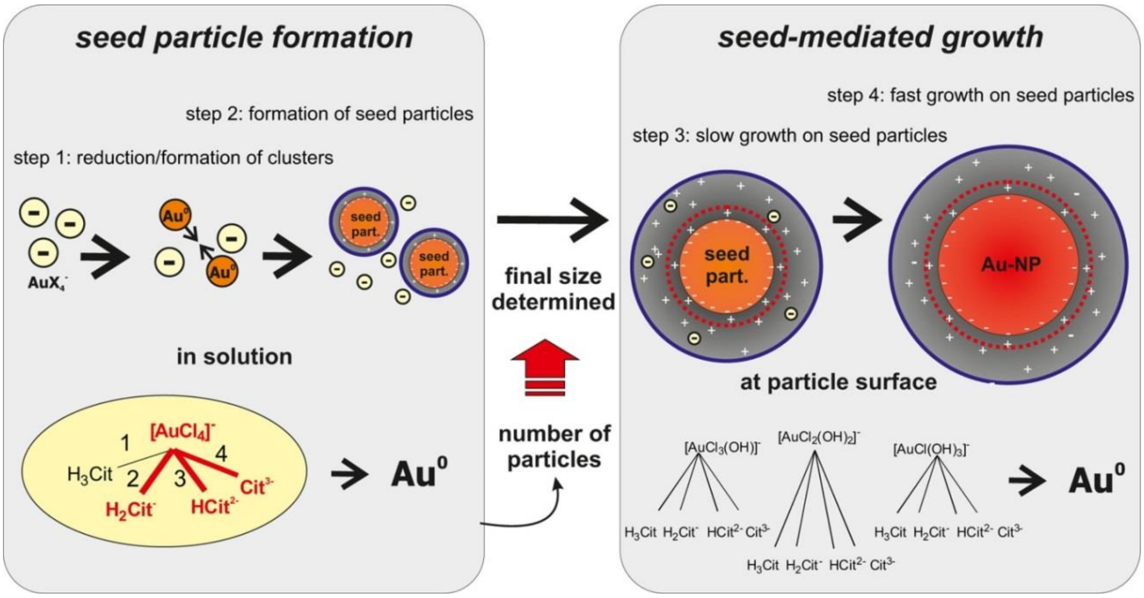

Figure 2-3 Schematic of the mechanism in the Turkevich method (reprinted with permission from ref.[52] Copyright 2012, American Chemical Society).

Lately, the same group studied the critical role of citrate protonation during the Turkevich method and figured out the key species of gold and citrate at different reaction stages. The study discovered the relationship between the citrate species and final size and polydispersity. It was found that the seed formation was mainly depended on the $[AuCl_4]^-$ reduced by $C_6H_6O_7^{2-}$. Then highly reproducible synthesis shown in **Figure 2-4** was obtained by tuning the solution pH between 5.4-6.8 which contained high amount of $C_6H_6O_7^{2-}$ for fast seed formation with $[AuCl_4]^-$. Then gold equilibrium shifted toward $[AuCl_{3-x}OH_{1+x}]^-$ to terminate the nucleation stage and initiated the seeded growth period for synthesizing monodisperse NPs. With this thought-provoking result, the mechanism of Turkevich method has been fully revealed which made the adapation of this method from batch to flow more attainable during the determination of operating conditions and reactor design.

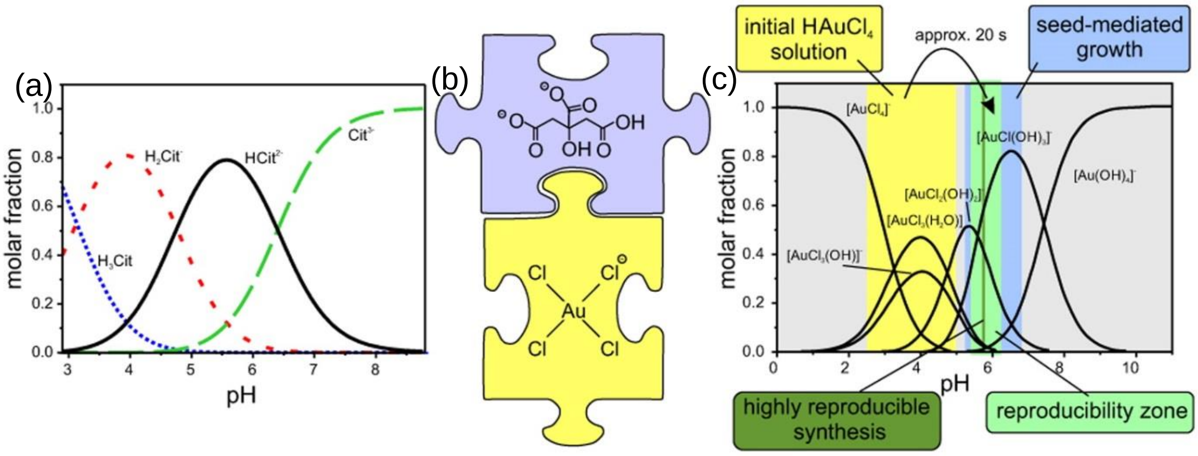

Figure 2-4 (a) Speciation of citrate at different pH values, derived from pKa values; (b) Two key species of gold and citrate for seed formation; (c) Speciation of $HAuCl_4$ solution (0.25 mM) in at different pH values (reprinted with permission from ref.[52] Copyright 2012, American Chemical Society).

2.1.2 The mechanism of the Brust-schiffrin method

Compare to the Turkevich method which is easily affected by experimental conditions (e.g. pH, temperature, the concentration of the reactants, etc.) and contains complex equilibriums and reactions between different species; the Brust-Schiffrin method is much more robust. This two-phase method became the most widely used synthetic route for small Au NPs synthesis since it was firstly published in 1994.[47] The gold precursor, $HAuCl_4$ in aqueous solution, was firstly mixed with a phase-transfer reagent of tetraoctylammonium bromide (TOAB) in toluene solution with stirring until the colourless aqueous phase is obtained, indicating all the gold precursor had been transferred into organic phase with a colour of wine-red. Then dodecanethiol ($C_{12}SH$) was added to the organic gold precursor solution for 1 h stirring until the solution back to clear and colourless. The aqueous reductant ($NaBH_4$) was slowly added and the colour of the organic phase changed from orange to deep brown within a few seconds. After 3 h stirring, 1-3 nm gold nanoparticles was obtained. Previously, it was widely accepted that the Au^{3+} was reduced to Au^{+} in a polymer-like structure of $[Au(I)SR]^{n-}$ by thiols.[53] However, by using the ^{1}H NMR to trace the metal salts, Lennox *et al.* showed that the actual complex of the metal precursor before adding $NaBH_4$ was the $[TOA][AuX_2]$ complex, rather than Au-S bonds.[54] On this basis, Li *et al.* used Raman spectroscopy to monitor the metal-S bonds and then demonstrated a general NP formation mechanism in Brust-Schiffrin method in **Figure 2-5**.[55] Before adding the reductant, the organic solution contained free thiol ligands and the $[TOA][M(I)X_2]$ complex in a form of micelles. The $NaBH_4$ firstly reduces the Au(I) complex to the uncapped, TOAB micelle-encapsulated Au NPs. Then the ligands (unreacted thiol and the thiolate from disulfide reduction) diffused through the micelle shell onto metal surface and formed ligand-protected metal NPs.

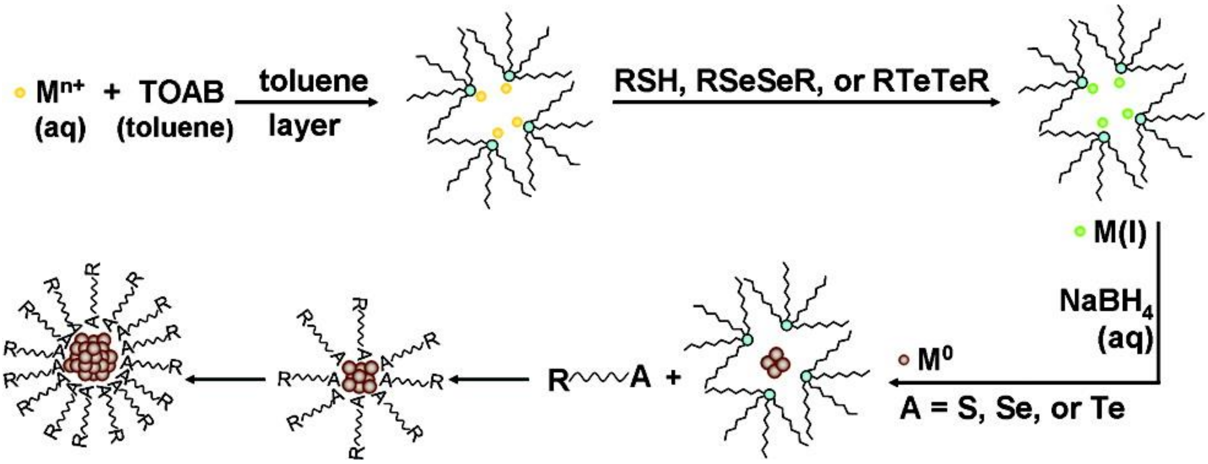

Figure 2-5 Mechanism extended to general synthesis of chalcogenate-protected metal nanoparticles based on the Brust−Schiffrin Method (reprinted with permission from ref.[55] Copyright 2012, American Chemical Society).

2.1.3 The mechanism of atomically precise Au_{25} nanoclusters formation

Jin gave the definition of ‘‘gold nanoclusters’’ (Au NCs) as ultra-small gold nanoparticles (< 2 nm) with discrete electronic structure to distinguish from the term “nanocrystals” which have quasicontinuous band structure and wide size range up to 100 nm.[1] The distinct structure makes the Au NCs hugely different to large size Au NPs with regard to atomic packing, structure, and electron transition properties. As cluster’s properties are highly sensitive to the cluster size, the synthetic control at atomic level is of importance. Even though the size of Au NPs from Brust-Schiffrin method could be smaller than 2 nm, the products are still crystalline without showing unique quantum size effects.[1] Thus, some researchers tried to modify the thiol-to-gold ratio from 0.2:1 in Brust-Schiffrin method to 2:1 to reduce the particle size to ~1.5 nm.[56-57] To narrow down the particle size distribution, Whetten *et al.* precipitated different sizes of particles by tuning ethanol amount.[58] Smaller cluster size of around 1.1 nm with ~38 atoms was produced by changing the thiolate chain length[59] and the molecular-like charge behaviour was observed.[60]

However, the true atomically precise synthesis was not attained with the above method. Actual cluster numbers were decided with the development of characterization methods, especially the utilization of electrospray ionization mass spectrometry (ESI-MS). The Au_{25} NCs produced via $NaBH_4$ reduction were firstly identified by Negishi *et al.* with ESI-MS analysis,[61] which proved later to be particularly stable compared to other cluster size.[62] Luo *et al.* studied the growth mechanism of Au_{25} NCs by monitoring the time evolution of gold precursor and NC intermediate species with ESI-MS.[63] As CO is a mild reducing agent compared to the common used reducing agent of $NaBH_4$ in most of papers synthesizing Au_{25} NCs,[61, 64-69] the synthesis time was increased to 72 h. This modification can leave enough time for mechanism study, as well as characterize all the intermediate NCs formed throughout the formation. A water-soluble thiol, 3-mercaptobenzoic acid (m-MBA), was mixed with $HAuCl_4$ solution under stirring for 2 h to reduce Au(III) to Au(I) complexes. CO was bubbled through aqueous solution (pH~11.6) for 2 min. Then, the flask was sealed for a reaction time of 72 h. A two-stage synthesis of atomically precise thiolated Au_{25} NCs was proposed based on the experimental results in **Figure 2-6**: a fast kinetically controlled reduction of soluble Au(I)–thiolate complexes to a mixture of thiolated Au NCs (the first ~40 min), followed by a slow thermodynamically controlled size-focusing to form final product of Au_{25} NCs (from 40 min to 72 h). The reaction enthalpy for $Au_{11}(SR)_9$ formation in Stage I was computed from density functional theory (DFT) to be about −155 kcal/mol, indicating a very favourable thermodynamic driving force. The Stage I ends when the reactive Au(I)–thiolate complex precursors are fully converted to NCs intermediate species. The Stage II (slow size-focusing) contains the conversion of smaller NCs to larger ones by excess thiols. The $[Au(SR)Cl]^-$ is abundant in the reaction solution, which could be added to $[Au_{23}(SR)_{16}]^-$ to form final product of $[Au_{25}(SR)_{18}]^-$. This process is slow due to only −11 kcal/mol of the enthalpy, whose driving force is much smaller than the reduction in Stage I.

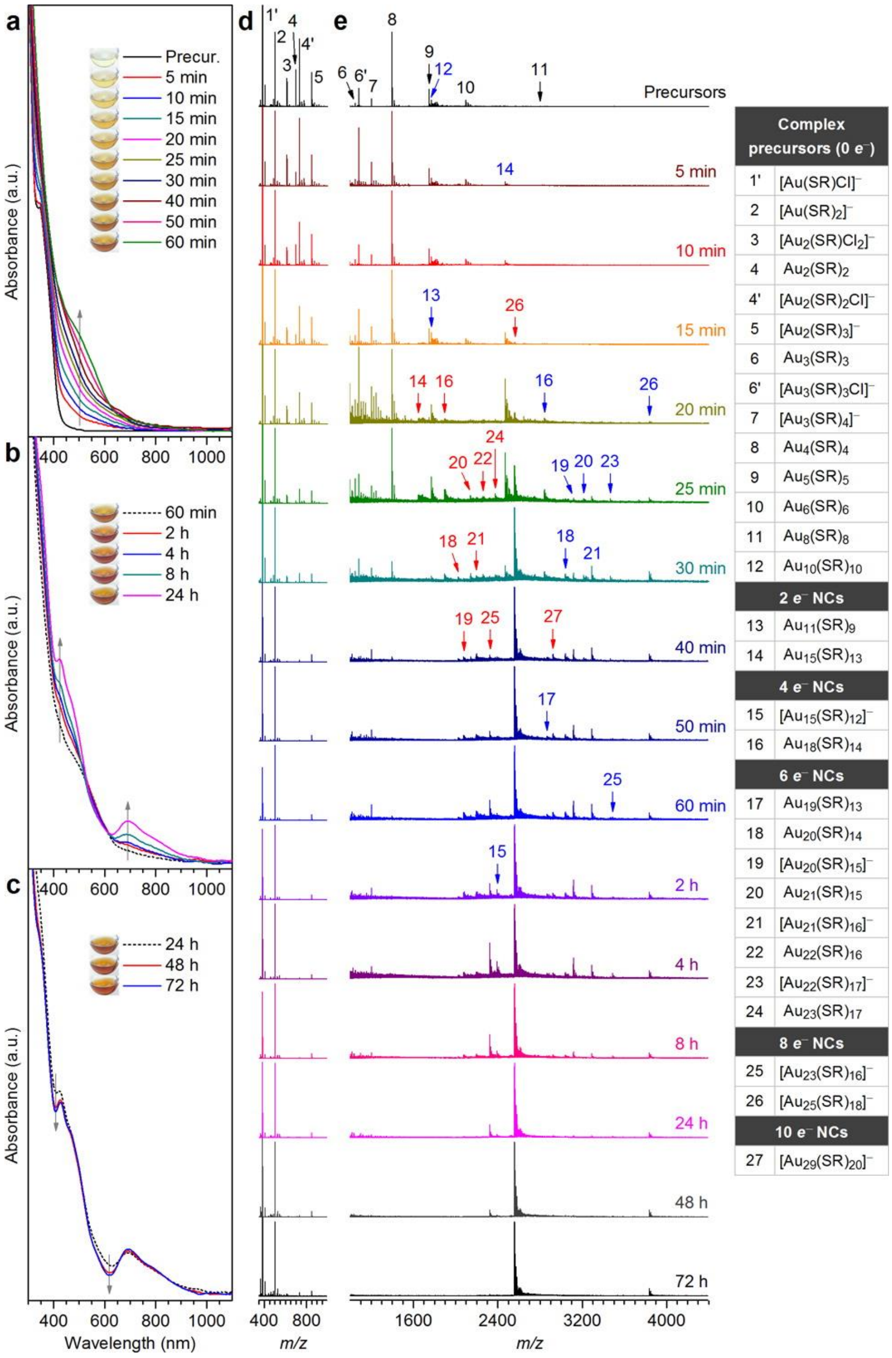

Figure 2-6 Time evolution of (a–c) UV–vis absorption and (d and e) ESI-MS spectra over the course of the $[Au_{25}(m\text{-}MBA)_{18}]^-$ synthesis. Insets in (a–c), colour of the reaction solution at different time. The black, blue, and red labels in (d and e) indicate that the ionic species are singly, doubly, and triply charged, respectively. The right panel in (e) is the molecular formulas and the classification of the labelled species according to the number of free valence

electrons (n*) (reprinted with permission from ref.[63] Copyright 2012, American Chemical Society).

Table 2-1 concludes the comparison of advantages and disadvantages for different Au NPs synthetic methods mentioned above.

Table 2-1 Comparison of different Au NPs synthetic methods.

Synthetic method	**Typical particle size range (nm)**	**Advantages**	**Disadvantages**
Seed-mediated growth (e.g. Turkevich)	7 - 20 nm	Monodisperse particle size due to the separation between nucleation and growth process	Hard to obtain particle size under 5 nm or large monodisperse particles (tens to hundreds nm)
		Ease of functionalization due to relatively weak capping agent used	

Nucleation-growth-passivation (e.g. Brust-Schiffrin)	< 5 nm	Gold nanoparticles below 5 nm or even gold nanoclusters with molecule-like structures could be formed.	Strong capping agents used which is hard to be removed if active sites on gold surface needed for further applications.
Seeded growth	Dependent on manual control	Particle sizes are tunable stepwise with manual control	Multiple addition processes needed and more time consuming
		Different shapes of NPs could be formed	

2.2 Stabilizers used in Au NPs synthesis

During the Au NPs synthesis, capping agents are used to control size and prevent aggregation.[29] The donor ability with particle surface of the ligands is related to different functional groups, which leads to the difference in stability and reactivity of the particles. In order to achieve colloidal stability, ligands prevent synthesized particle aggregation either by steric (e.g. alkylthiols) or electrostatic (e.g. citrate) repulsion.[29] The most widely used Au NP ligands are reported in **Table 2-2** and structures shown in **Figure 2-7**. The stability and solubility of Au NPs in different media mainly depend on the double layer of the particle surface. The surface charge of the particles was determined by measuring the zeta potential. Additionally, ligands can be removed from the NP surface by several methods like calcination,[70] oxygen treatment,[71] and ozone treatment.[72]

Table 2-2 Overview of Au NPs ligands, classified by the element of binding functionality.[29]

Atom of bind functionality	**Ligand**	**Size range of Au NPs/ nm**	**References**
O	Diglyme	1.9–8.9 [a]	73
	Citrate	15–150	74
N	Dodecylamine	2.5–7.0	75
	Lysine	6.5	75
P	TPP	1.4	76
	TPPMS	1.4	77
	BINAP	1.7	78
S	GSH	1.0	79-80
	PEG-SH	1.5-3.2	81
	Alkylthiols	1.5-3.2	47, 82
	DHLA	1.6	83
	GSH/cysteamine	2.7	84
	Tiopronin	2.8	85

[a] After capture of primary particles by thiols or amines.

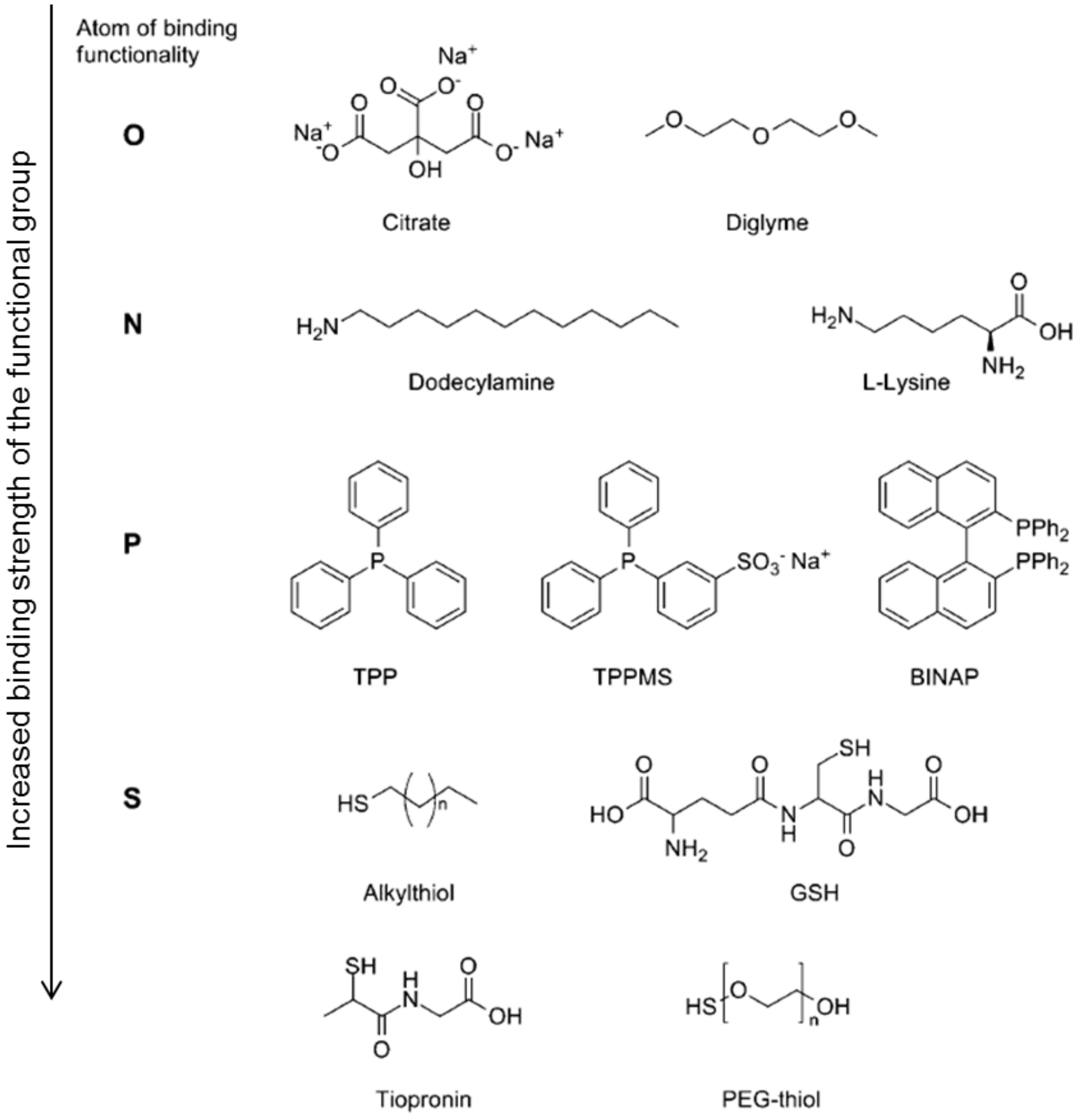

Figure 2-7 Structures of typical Au NP ligands, classified by the element of binding functionality (Adapted from ref.[29] with permission of The Royal Society of Chemistry).

The table above classifies the ligands based on the binding strength of different functional groups. Citrate is a typical example of carboxylate ligands which has a very weak binding ability among Au NP ligands and is easy to be removed by other stronger ligands. The salt concentration or pH can easily affect the stability of such particles and it’s impossible to re-disperse citrate-capped particles after drying. Compared to stronger ligands such as phosphines and thiols, the affinity of amine ligands is moderate. The binding energy of phosphines is lower than thiols. However, the sterical bulkiness and oxidation resistance phosphine, such as aryl phosphines like triphenyl phosphine (TPP) and its derivatives, is still capable to obtain highly stable Au NPs. Another type of phosphine ligands are diphosphines. Tamura *et al.* successfully produced 1.7 nm Au NPs stabilized by 2,2'-bis (diphenylphosphino)-1,1'-binaphthyl (BINAP).[78] Furthermore, Yanagimoto *et al.* stabilized Au_{11} clusters by using four BINAP molecules per particle.[86] The mechanism of ligand formation can be explored by electrospray ionization-mass spectrometry (ESI-MS).[87] Thiols are the most popular ligands for Au NPs due to its highest binding energy on particle surface. Love *et al.* measured the binding energy for thiols on flat gold surface.[88] However, because of the curvature of Au NPs, the binding energy between thiols and Au NP may be slightly different. Many papers have shown that some sulfur molecules e.g. disulfides, have a very weaker bonds to Au NPs.[89-95] By using time resolved fluorescence spectroscopy, Perumal *et al.* studied binding kinetics of thiols ligands with different valences on the Au NPs with different size.[96] They observed that dithiols showed the highest exchange rate to replace pyrene. They also found that the exchange rate increased with larger particle size. By using the spectrophotometric study on the degradation of cyanide in UV-Vis, Srisombat *et al.* proved the conclusion by Perumal's.[97]

2.3 Characterization techniques used in gold nanoparticle synthesis

This section contains a brief introduction about some most commonly used characterization techniques during gold nanoparticles synthesis. The proper choices of characterization method can deliver useful insights about the product and give guidance for further study and improvement. However, considering the limitation of specific characterization method, in usual a full picture of the product needs a combination of several different characterisation techniques.

2.3.1 Ultraviolet-visible spectroscopy

The UV-Vis spectroscopy has become the most used characterization technique due to its convenient use. Mie explained theoretically the extinction and scattering efficiencies of small metal particles in colloidal solution in 1908 by solving Maxwell's equation.[98] The absorption of UV light by gold nanoparticles can induce the oscillation of the conduction band electrons by interaction with an electromagnetic field. These resonances are known as surface plasmons.[99] **Table 2-3** concludes the information provided by UV-Vis spectroscopy.

Table 2-3 Information could be provided by UV-Vis spectroscopy.

Wavelength (nm)	Measured parameters	Trend	Ref.
200	Citrate protonation equilibrium upon addition of H^+	Absorption bands decrease and blue shift with lower pH and temperature	31
313	Hydroxylation of $[AuCl_4]^-$ to $[AuCl_{4-x}OH_x]^-$	Absorption bands decrease and blue shift with exchange of Cl^- by OH^- ions.	31

400	Au(0) concentration	Absorption band increases with Au(0) concentration	100
520-590	Au NPs size	Absorption bands red shift with larger particle size and increases with Au NP concentration	101
590-900	Aggregation and non-spherical shape		99

As the plasmonic properties can be affected by the electric double layer of the nanoparticles, UV-Vis spectroscopy can only give a qualitative analysis about the particle size and concentration if different ligand and solvent used or the particles are polydisperse.[102]

2.3.2 Transmission Electron Microscopy (TEM)

A TEM contains four parts: electron source, electromagnetic lens system, sample holder, and imaging system. The electron beam transmits through the specimen and replicates the patterns on the slide, forming an enlarged image on the screen. Thus, TEM can give the straightforward picture of synthesized NPs with size down to 1-2 nm. Additionally, for the image from High-Resolution

TEM, the lattice structures of metal particles can also be shown.[103] Besides the morphology of NPs, TEM equipped with energy dispersive X-ray spectroscopy (EDX) can identify the chemical elements.[104]

2.3.3 Differential Centrifugal Sedimentation (DCS)

DCS applies centrifugal force to sediment particles of different sizes. The theory of sedimentation is based on Stoke's Law in which the terminal setting velocity of particles is related to the particle diameter, fluid and particle density, gravitational acceleration and fluid viscosity.[105] Compared to UV-Vis, DCS can give more details for polydisperse NPs (e.g. bimodal distribution). Additionally, the total number of particles counted in was in the order of 10^{11}, which is more accurate than TEM (only hundreds of NPs counted in TEM) to give the size and size distribution. For Au NPs, DCS can measure the size down to 3 nm due to the large density of gold.[106] For the size smaller than 3 nm, NPs are in Brown motion and hard to be sedimented.

2.3.4 Electrospray Ionization Mass Spectroscopy (ESI-MS)

In electrospray ionisation (ESI), a spray of charged droplets is created by the application of a high voltage (typically 1-3 kV). The charged droplets evaporate and become unstable to form microdroplets when the Rayleigh limit (Coulomb repulsion = surface tension) is reached. This process repeats until individual solvated ions are formed.[107] Due to the mild fragmentation, ESI-MS is widely used to identify the actual cluster formula during the atomically precise synthesis of gold nanoclusters.

There are also some other characterization techniques used in this thesis which are all concluded in **Table 2-4**.

Table 2-4 Conclusion of characterization techniques used in the thesis.

Characterization technique	Use for
UV-Vis	Qualitative analysis of particle size and size distribution, Au(0) concentration and hydroxylation of reactant species.
TEM	Quantitative analysis of particle size (down to 1-2 nm) and shapes, lattice structure and chemical specificity to identify elements.
DCS	Quantitative analysis of particle size (down to 3 nm) and concentration.
ESI-MS	Identify the cluster formula of gold nanoclusters (up to 2-3 nm)
Scanning Electron Microscope (SEM)	Morphology of tubing surface and fouling observation.
X-ray Photoelectron Spectroscopy (XPS)	Oxidation status of gold and coordination between ligands and gold.
ATR-FTIR Spectroscopy	Coordination between ligands and gold.
Inductively Coupled Plasma Atomic Emission	Quantitative analysis of the yield of synthesized Au NPs.

Spectroscopy (ICP-AES)	
Raman Microscope	Molecules detection and Surface-enhanced Raman Scattering (SERS) performance test.
Dynamic Light Scattering (DLS)	Quantitative analysis of particle size and size distribution, and the zeta potential of NPs.
Small Angle X-ray Scattering (SAXS)	Qualitative analysis of gold nanocluster size.
Matrix-assisted Laser Desorption Ionization Mass Spectroscopy (MALDI-MS)	Identify the gold cluster size (gold core mass only due to stronger fragmentation than ESI-MS)
Electro-kinetic analyzer	Measure the zeta potential of the tubing wall.

2.4 Gold nanoparticle flow synthesis

2.4.1 Gold nanoparticle synthesis in single-phase flow systems

Microfluidic reactors

Most microfluidic reactors are made using microfabrication methods and have characteristic dimensions in the order of hundreds of microns. However, the use of capillary tubes is also gaining interest owing to their simplicity and low cost. A criterion for a capillary is defined by Bond number, *Bo*, in which there is no gas bubbles rising in vertical channel filled with liquid.[108] The *Bo* number is expressed as Eq. (1):[109]

$$Bo = {}^{g\Delta\rho L_c^2}/_{\sigma} < 3.386 \qquad \text{Eq. (1)}$$

where g is gravitational constant, ρ is the density, L_c is the characteristic length and σ is the surface tension.

Bo number can be used as approximation for the microreactor, even though viscosity or geometrical aspects of the channel is not taken into account.[108] However, for the sake of convenience, in latter review flow systems with characteristic size (such as diameter) smaller than 1 mm are referred to as microfluidic reactors, while those with larger size (up to some mm) are referred to as milli-fluidic reactors, as an important aspect for the application of continuous flow in the manufacturing of nanomaterials is its production capacity. For Au NPs synthesis, the most common microfabricated reactor materials are Si, glass and polydimethylsiloxane (PDMS). Glass and silicon not only involve special working conditions (clean room), but may also require careful sealing procedures, particularly for high temperature/pressure operation. Capillaries and tubes made of silica, polytetrafluoroethylene (PTFE) are common, while polyether ether ketone (PEEK), polyethylene (PE) and tygon have also been used.

In single-phase microfluidic systems, the flow pattern is usually laminar, characterised by low Reynolds number. [25] Thus, mixing only occurs at the interface between miscible streams by molecular diffusion. This characteristic is attractive for some synthetic processes which need precise control. Citrate-capped Au NPs are usually synthesized by the Turkevich method for around 30 min at elevated temperature. Singh *et al.* produced citrate-capped Au NPs with lower reaction time at room temperature by substituting citrate with the strong reducing agent $NaBH_4$ in the microreactor.[43] The laminar flow forming in the microreactor played an important role to slow down mixing and avoid the uncontrollable reaction owing to the high conversion rate of $NaBH_4$. On the other hand, for slower reducing agents efficient mixing is beneficial. Jun *et al.* studied the size control of Au NPs produced by ascorbic acid, by comparing different mixers. Similar size and size distribution were obtained with both microfluidic butterfly-shape and milli-fluidic compressed-tubing mixers (**Figure 2-8**), as long as the flow rate was sufficient to attain efficient mixing.[110] Sufficiently high flow rates could guarantee fast mixing, but too high flow rates did not allow enough time for the reaction to complete.

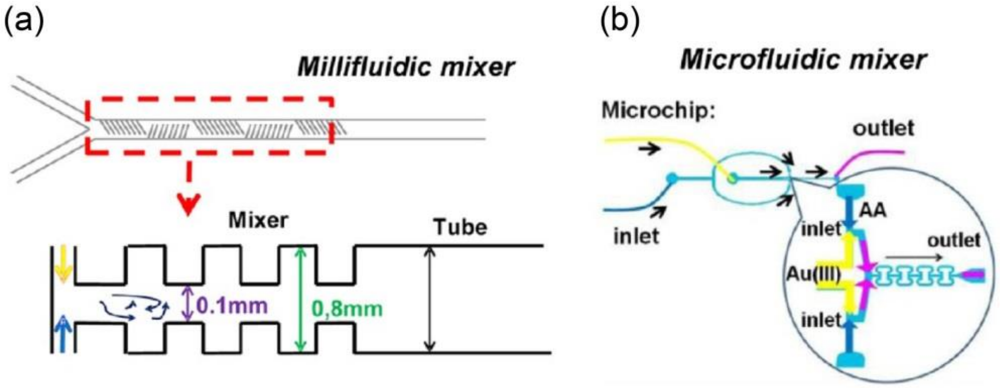

Figure 2-8 Schematic of different mixers used for Au NPs synthesis by ascorbic acid: (a) compressed Teflon milli-fluidic mixer and (b) butterfly microfluidic mixer. (reprinted with permission from ref.[110]. Copyright 2012, American Chemical Society).

Shalom *et al.* adapted the Brust-Schifrin method to a flow system by mixing a prepared thiolate polymer and aqueous $NaBH_4$ in a radial interdigitated mixer

(**Figure 2-9a**).[111] The reagents passed through a circular channel and were then split into eight streams flowing towards the centre of a mixing chamber, while the outlet was in the centre of the chamber. For the same gold-thiol ratio (e.g. 2), the size and standard deviation in the microfluidic reactor were smaller (2.9 ± 0.6 nm) than those in batch systems (4.9 ± 2.1 nm). Tsunoyama *et al.* used a similar mixing approach with a multi-laminated mixer (from IMM) to improve mixing (**Figure 2-9b**).[112] With $NaBH_4$ as reducing agent, they produced polyvinyl pyrrolidone (PVP)-stabilised sub-2nm Au NPs with high monodispersity, which showed higher catalytic activity in aerobic alcohol oxidation than Au NPs prepared in a batch reactor. Using the same micromixer, Luty-Błocho *et al.* studied the effect of flow rate on Au nanoparticle synthesis. Increasing the flow rate led to smaller polyvinyl alcohol (PVA)-capped Au NPs in the range of 1.5-3 nm when using ascorbic acid or $NaBH_4$ as reducing agent.[113] Interestingly, batch processing resulted in sediment formation after 1 h for the ascorbic acid system. For the $NaBH_4$ system, particles of similar sizes were obtained (~1.5 nm), but in the batch reactor much larger ones (~2 μm) were produced.

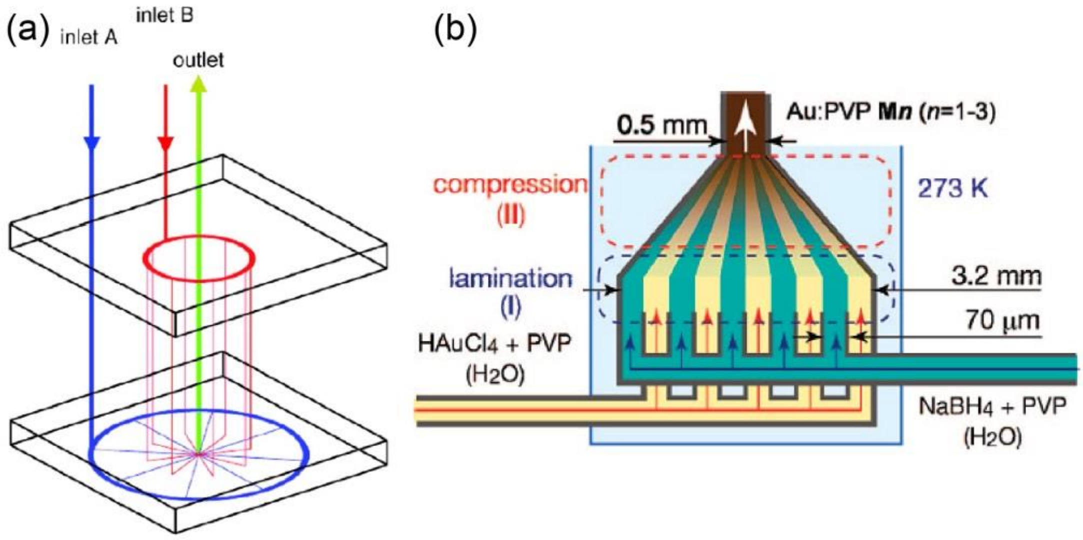

Figure 2-9 (a) Schematic of radial interdigitated mixer used for Au NPs synthesized by $NaBH_4$ (reprinted from Materials Letters, 61(4), Shalom *et al.*, Synthesis of thiol functionalized gold nanoparticles using a continuous flow microfluidic reactor, 1146-1150, Copyright 2018, with permission from Elsevier).[111] (b) Schematic of the multilaminated mixer used for Au NPs synthesis by $NaBH_4$ (reprinted with permission from ref. [112] Copyright 2008, American Chemical Society).

A glass-silicon microreactor with three mixing zones of split-and-recombine type allowing the consecutive addition of reducing agent solution containing ascorbic acid and Fe(II) and three modifier solutions (citric acid, sodium metasilicate and polyvinyl alcohol) was utilized to synthesize Au NPs.[114] Wagner and Köhler improved this glass/silicon reactor with eight split-recombine units (**Figure 2-10a**) which could provide improved residence time distribution and used it to synthesise PVP-capped Au NPs with sizes between 5 and 50 nm by ascorbic acid reduction.[115] Au NPs with coefficient of variation (CV) two times smaller than that in a conventional batch reactor was achieved and smaller Au NPs were obtained at high flow rates, high concentration of the reducing agent or stabiliser and high pH. In a subsequent design, residence loops were added to allow for multi-step addition of the reagents and reduction of the risk of fouling **(Figure 2-10b).**[116] They synthesized 4-7 nm Au NPs using $NaBH_4$ as the reducing agent. The Au NP size could be reduced by decreasing the reactant concentrations.

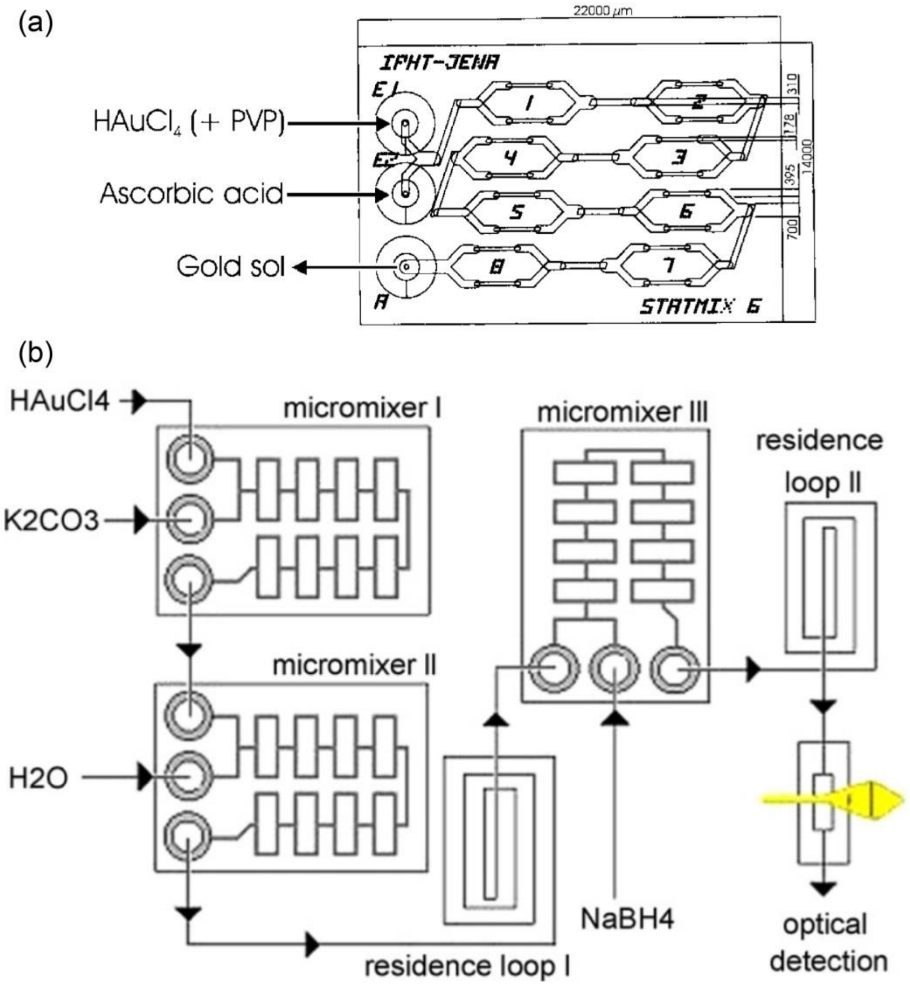

Figure 2-10 (a) Schematic of the reactor with split and recombine mixers used for synthesis of Au NPs by ascorbic acid (reprinted with permission from ref.[115] Copyright 2005, American Chemical Society). (b) Microreactor system with micromixers and residence loops used for synthesis of Au NPs by $NaBH_4$. (reprinted from Chemical Engineering Journal, 135, Wagner *et al*., Microfluidic

generation of metal nanoparticles by borohydride reduction, S104-S109, Copyright 2008, with permission from Elsevier).[116]

Sugano *et al.* developed a microreactor system comprising a Y-mixer and two piezoelectric valveless pumps to achieve pulsed mixing of chloroauric acid and trisodium citrate at room temperature (**Figure 2-11**).[117] The switching frequency controlled the thickness of the pulsed layers, the square of which has a proportional relationship with the diffusion time. The mixing time at 100 Hz was short enough as to reduce the CV of the PSD to ~10% for Au NPs of ~40 nm mean size.

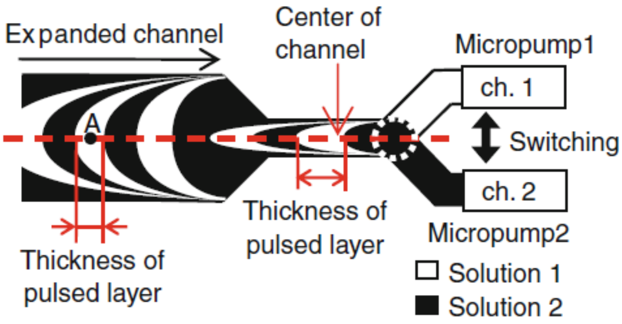

Figure 2-11 Y-shape pulsing mixer used for synthesis of Au NPs by trisodium citrate (reprinted by permission from Springer Customer Service Centre GmbH: Springer, Microfluidics and nanofluidics, ref.[117], Sugano *et al*., Copyright 2010).

Verma and Kumaran formed co-axial flow in a microchannel (H × W : 100µm × 1.5 mm) so that the gold precursor (chloroauric acid) was surrounded by the reducing agent (tannic acid). As the Reynolds number increased, the flow regime transitioned from laminar to turbulent. At high Reynolds number (up to ~350) the particle size distribution could be controlled better, while the mean particle size, between 4 and 7 nm (achieved at different molar ratios of tannic acid to chloroauric acid) was not significantly affected by mixing conditions.[118] Bandulasena *et al.* also used a co-axial flow set-up operating at laminar flow with an injection orifice diameter of the inner tube between 100 and 240 µm (**Figure 2-12**).[119] The particle size of PVP-capped Au NPs produced by ascorbic reduction decreased from ~135 nm to ~50 nm by decreasing the injection orifice diameter (which increased the mixing efficiency), increasing the flow rate of the ascorbic acid stream and increasing the pH (which enhanced the reducing power of ascorbic acid). However, polydispersity increased with increasing the flow rate and the pH of the ascorbic acid stream.

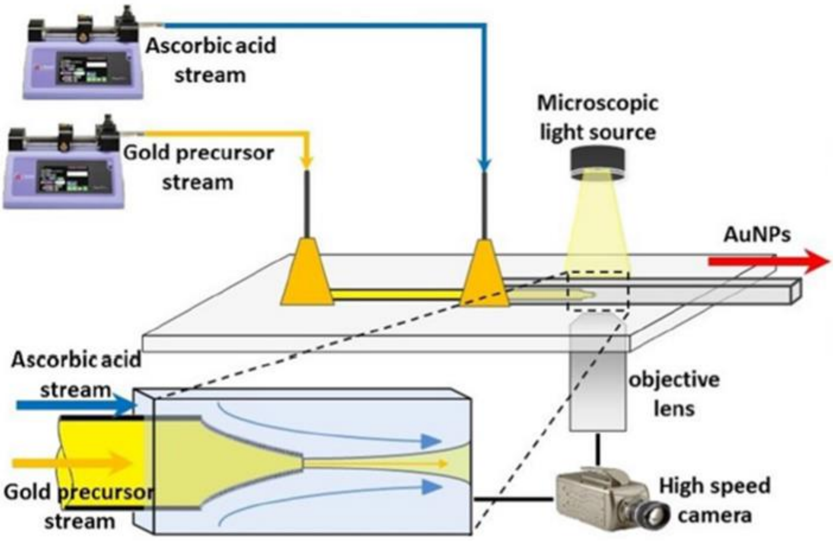

Figure 2-12 Schematic of the co-axial microfluidic set-up with round capillary orifice inside a square microchannel used for Au NPs synthesis by ascorbic acid (adapted from Bandulasena *et al.*, Copyright 2017 Elsevier, https://doi.org/10.1016/j.ces.2017.05.035, http://creativecommons.org/licenses/by/4.0).[119]

Baber *et al.* utilized a coaxial flow reactor comprised of an outer glass tube (2 mm I.D) and an inner glass tube (0.8 mm I.D.) to bring in contact chloroauric acid and trisodium citrate, while avoiding fouling. This was followed by an ethylene tetrafluoroethylene (ETFE) coiled flow inverter (CFI) with 0.75 mm I.D, which helped to improve the residence time distribution. Au NPs with minimum size of 17.9 ± 2.1 nm were synthesized at 80 °C (**Figure 2-13**).[120]

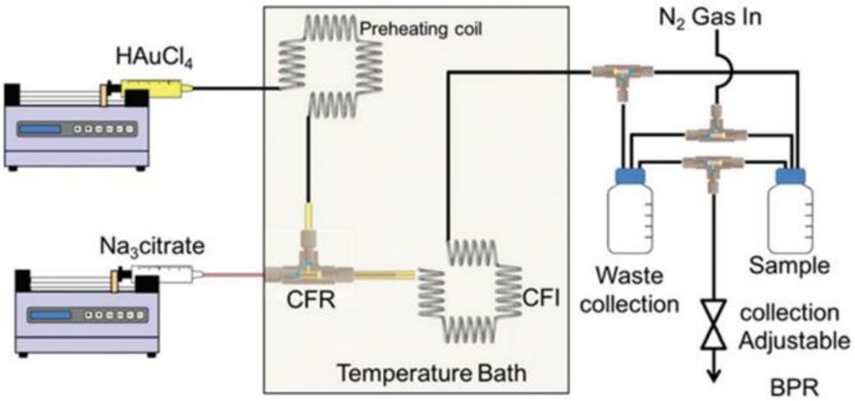

Figure 2-13 Schematic of the experimental set-up for Au NP synthesis by the Turkevich method comprising CFI for preheating, a coaxial flow reactor as a mixer, and another CFI as reactor. (adapted from Baber *et al.,* Copyright 2017 Royal Society of Chemistry, An engineering approach to synthesis of gold and silver nanoparticles by controlling hydrodynamics and mixing based on a coaxial flow reactor, https://doi.org/10.1039/C7NR04962E, https://creativecommons.org/licenses/by/3.0/legalcode).[120]

Yang *et al.* designed a vortex-type mixer in a three-layer microfluidic reaction chip (**Figure 2-14).**[121] Using the new chip, almost complete mixing was achieved within 1 s, and 19-58 nm Au NPs were obtained by tuning the volumes of citrate and gold precursor for the Turkevich method.

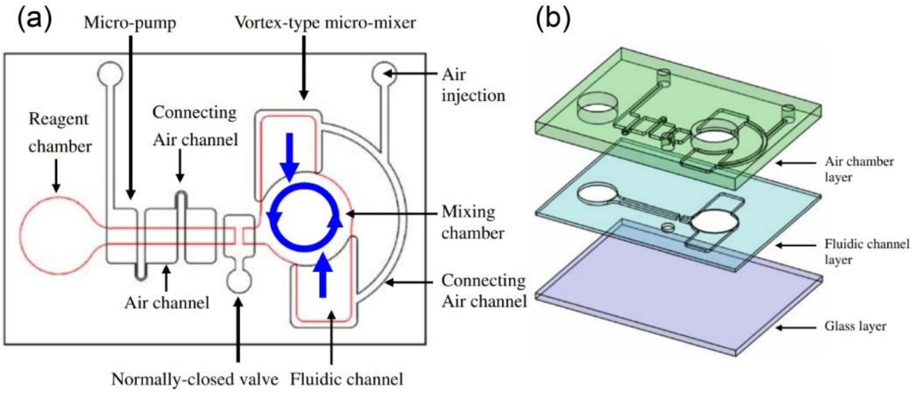

Figure 2-14 Components of 3-layer microfluidic reaction chip with vortex-type flow field used for Au NPs synthesis by trisodium citrate (a) top view and (b) exploded view (reprinted by permission from Springer Customer Service Centre GmbH: Springer, Microfluidics and Nanofluidics, ref.[121], Yang *et al.*, Copyright 2010).

Kitson *et al.* designed 3D printed serpentine reactors with 0.8 mm channels made of polypropylene (PP) to synthesize Au NPs.[122] Compared to the PDMS which is commonly used, PP is cheaper and the maximum material cost for one reactor was ca. \$0.31. Even though fouling was observed on the surface of the reactor, this design is attractive because of the low cost for each reactor, which is disposable after one use.

The batch Turkevich method does not produce Au NPs < 5 nm. However, Ftouni *et al.* produced ultra-small (i.e. < 2 nm) Au NPs at residence time < 50 s in a citrate-only system by taking advantage of efficient mixing and quick heating and quenching in a fused silica capillary (200 μm I.D).[123-124] As the residence time was quite short and the product was quenched rapidly to terminate the reaction, no further growth after the quenching led to NPs with ultra-small size. Gomez-de Pedro *et al.* fabricated a ceramic microfluidic device based on low-temperature co-fired ceramics technology.[125] The shape of the three-dimensional serpentine structure caused adventive patterns that enhanced the mixing. The reactor was used to synthesize 11-mercaptoundecanoic acid (MUA)-capped Au NPs. Pulsed dosing of $HAuCl_4$ solution to a continuous flow of $NaBH_4$, with a continuous downstream feed of an MUA solution, resulted in 2.7 nm Au NPs. Hydrophobic gold nanoparticles have attracted less attention. Sugie *et al.* used a Y-mixer/PTFE microreactor assembly maintained at 25–60°C to reduce $HAuCl_4$ in tetrahydrofuran (THF) solvent using organosilane as mild reducing agent and alkyl thiol (RSH) as capping agent.[126] Increasing residence time to over an hour led to the increase of the Au NP size from 4.3 to 8.7 nm.

Microfluidic systems have also been employed to form gold nanomaterials with different shapes. Kumar *et al.* used Br^- ions from cetyl-trimethyl-ammonium-bromide (CTAB) or HBr with citrate reduction to produce triangular gold nanoplates.[127] They implemented a Y-shape micromixer and a tubular PTFE tube with 0.9 mm internal diameter (I.D.) to tune the operational parameters (volumetric flow ratios, temperature and reagent concentrations) and improve the yield of triangular particles from ~25 to ~51%. Reducing the amount of citrate yielded a larger amount of polyhedral particles; this was attributed to the particle growth rate dominating the initial nucleation rates. Fu *et al.* developed a three-inlet micromixer and a subsequent PDMS microchannel (400 mm × 400 mm cross-section and 3 cm in length) for the synthesis of seed-mediated gold nanoplates.[128] The thickness of the nanoplates was tuned from 1 nm to a few nm by varying the flow rate. The nanoplates were rigid and flat when their thickness was > 2nm and had crumpled/rolled shapes when the thickness was ~1 nm. Sebastián *et al.* utilized a coiled PTFE tubing (0.76 mm I.D., **Figure 2-15**) to synthesize biocompatible gold nanorods (Au NRs) with a residence time of 10 min in continuous flow.[129] In order to circumvent toxicity issues of silver/CTABr that are typically used for Au nanorod synthesis, they employed lysine as capping agent with $NaBH_4$ as a reducing agent. The presence of two amino groups in the lysine is critical for the anisotropic growth of the Au particles. By tuning the lysine concentration, Au nanorods with strong absorption in the near infrared (700–900 nm) were prepared.

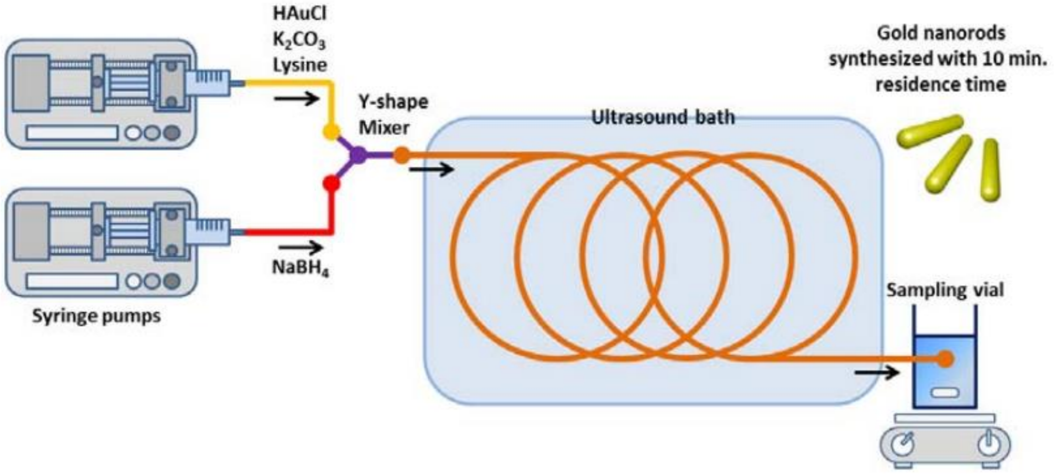

Figure 2-15 Schematic of continuous flow set-up Au NRs synthesis via $NaBH_4$ reduction with residence time of 10 min (Adapted from ref.[129] with permission of The Royal Society of Chemistry, https://doi.org/10.1039/C2CC32969G).

Ishizaka *et al.* made use of continuous flow to tune the pH of the gold precursor by adding the reagents stepwise (**Figure 2-16**).[130] Glucose was used as an environmentally benign reducing agent. Star-shape Au NPs were synthesized when the pH was 6.9, which was not observed in batch systems at similar experimental conditions; nevertheless, the particles gradually coalesced into single round shape particles.

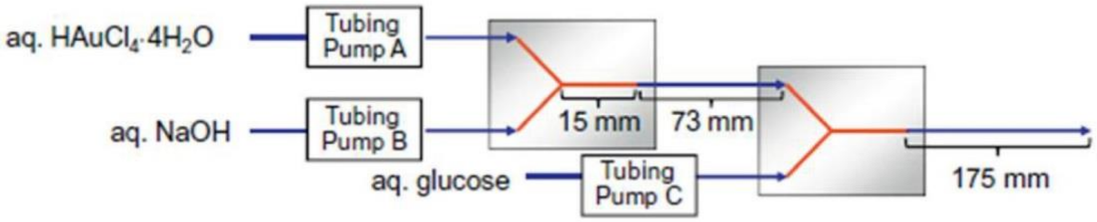

Figure 2-16 Schematic of multi-step addition in a microfluidic system for the synthesis of Au nanostars by glucose (reprinted from Journal of Colloid and Interface Science, 367(1), Ishizaka *et al.*, Dynamic control of gold nanoparticle morphology in a microchannel flow reactor by glucose reduction in aqueous sodium hydroxide solution, 135-138, Copyright 2018, with permission from Elsevier).[130]

An important issue during single-phase flow is the appearance of fouling on the microreactor wall. Wagner *et al.* observed gold precipitation on the wall of a glass microreactor, even though the synthesis was implemented carefully with small volume and short running time.[115, 131] They proposed various solutions to suppress fouling. Operation at high pH (~9.5) leads to negative charge on silicon surface because of the deprotonated Si-OH groups. As the citrate-capped gold nanoparticles are also negatively charged, the electrostatic repulsion between product and tubing wall prevented fouling. Another way is to reduce the wettability of the channel walls by turning the surface from hydrophilic to hydrophobic via silanization. Higher shear forces induced by increasing flow rate also seemed to help reduce fouling.

Milli-fluidic reactors

Because of potential fouling problems and their inherent small volume, it is difficult for microfluidic devices to provide gram-scale production.[23, 26, 132-134]

Milli-fluidic reactors, which have one order of magnitude larger dimensions compared to microreactors, mitigate the risk of fouling blockages and depend less on expensive fabrication technologies [135]. Compared to batch synthesis, milli-fluidic devices can still provide satisfactory mixing (although this depends on the synthesis) and are more amenable to scale-up.[110]

Lohse *et al.* proposed a milli-fluidic reactor system (**Figure 2-17**) comprised of simple components to improve the operation control compared to batch reactors, as well as to enable high-throughput synthesis at the gram scale of functionalized gold nanoparticles [136]. The reactants were mixed in a polyethylene (PE) Y-mixer (I.D. 1.79 mm), and the residence time was controlled by adjusting the length of the TYGON polyvinyl tubing reactor (I.D. 2.79 mm). The reactor could be integrated with online UV-vis absorbance spectroscopy analysis for product monitoring during synthesis, as well as flow NP purification techniques. Various functionalized (citrate, mercaptohexanoic acid and CTAB) spherical Au NPs with controlled sizes (4 nm, 2 nm and 2-40 nm, respectively) were produced by $NaBH_4$ reduction. Furthermore, CTAB-stabilized gold seeds (2.0 nm) were mixed with a growth solution containing chloroauric acid, CTAB, silver nitrate, and ascorbic acid leading to Au nanorods with various aspect ratios and lengths of 15-50 nm.

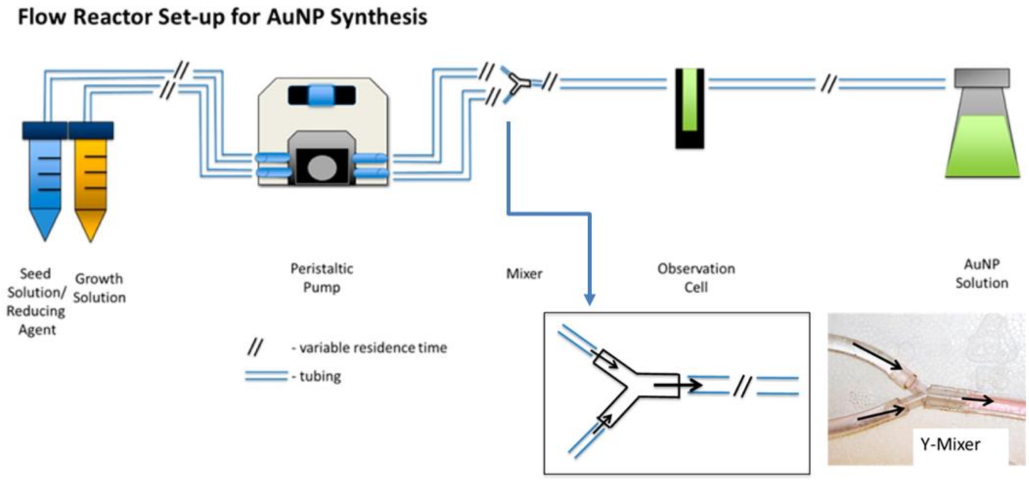

Figure 2-17 Schematic of a milli-fluidic reactor for Au nanomaterials synthesis by ascorbic acid (reprinted with permission from ref.[136] Copyright 2013, American Chemical Society).

Gomez *et al.* reported that the good quality of hollow Au NPs produced by galvanic replacement of cobalt nanoparticles synthesised by $NaBH_4$ reduction in batch reactors could only be achieved with a volume up to 480 mL, as insufficient mixing limited the scale-up.[137] They achieved higher productivity by scaling up a continuous flow reactor from a PTFE tube with I.D. of 0.8 mm and length of 913 cm to milli-fluidic scale with 10 times higher throughput (I.D. of 1.6 mm, length of 3088 cm) (**Figure 2-18**). Moreover, multiple reaction stages, by adding new streams into the coils with T-junctions, and downstream processes (functionalization and sterilization) could be incorporated. Uson *et al.* utilized a similar set-up based on PTFE tubing (I.D. = 1.016 mm) and PEEK Y-junctions to synthesize and functionalize Au nanorods in one continuous process.[138] The multi-addition of reactants allowed to separate and control – in a single stream – different stages of seed formation, nanorod growth and functionalization with poly(ethylene glycol)-methyl ether thiol (SH-PEG). Appropriate lengths of the tubing ensured the desired residence times (2-10 min) with a total residence time of 32 min. These short residence times eliminated detrimental effects associated with uncontrolled aging-related processes observed in batch synthesis. The continuous system allowed a 100-fold reduction in the consumption of SH-PEG compared to a conventional batch reactor.

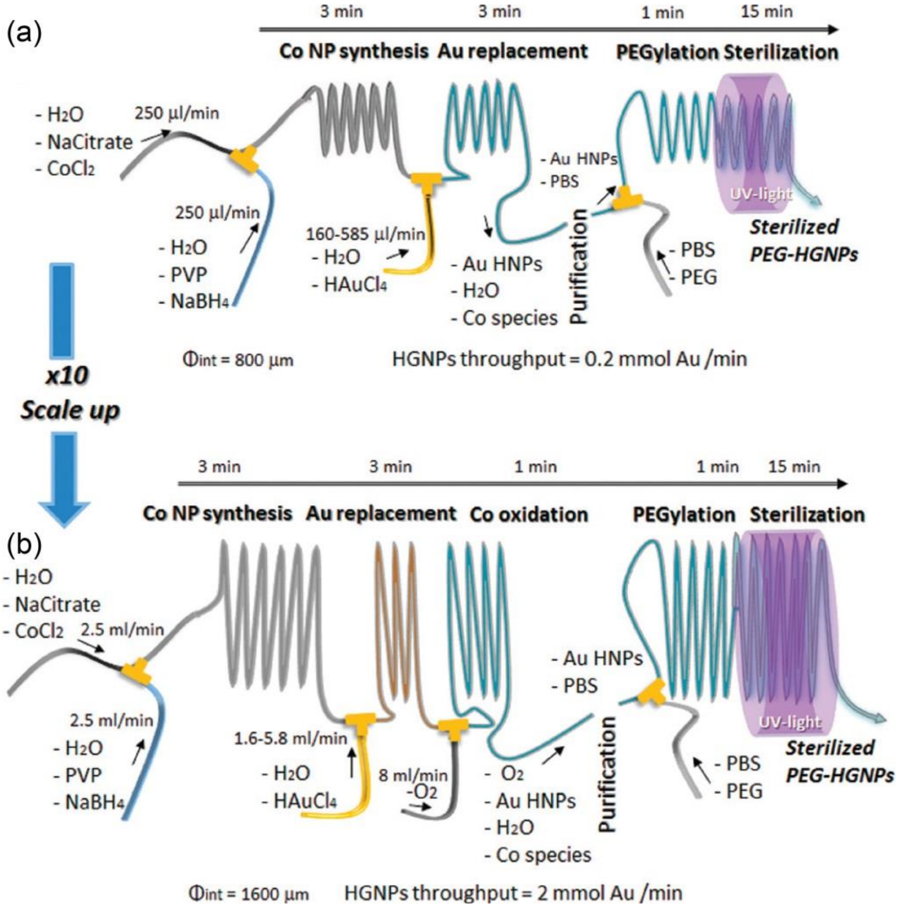

Figure 2-18 (a) Microfluidic set-up with coiled capillary (I.D. of 0.8 mm) for the synthesis of sterilized PEG-capped hollow Au NPs by $NaBH_4$ through a galvanic displacement process. (b) Milli-fluidic set-up with 10 times higher throughput (I.D. of 1.6 mm) than (a) (Adapted from ref.[137] with permission of The Royal Society of Chemistry).)

Bullen *et al.* used a rotating tube processor (RTP) with 6 cm I.D. and 30 cm in length with centrifugal force generating dynamic thin films 0.3 mm thick as the liquid moved along the rotating tube. The mixed reactant was delivered to a narrow channel processor (NCP) through jet feeds for longer residence time (**Figure 2-19**).[139] Using this flow system, Au seeds were prepared with $HAuCl_4$/CTAB/acetylacetone and $AgNO_3$/CTAB/carbonate solutions in the RTP and grown to Au nanorods in the NCP. Long term operation (19 days) was demonstrated with this system. Boleininger *et al.* grew Au NRs from Au seeds and $HAuCl_4$/CTAB/ascorbic acid in short polyvinyl chloride PVC tubing (1 mm I.D.).[140] The aspect ratio of the nanorods became smaller with a higher ratio of seed-to-growth solution or at higher growth temperature. Fouling was reduced by flushing polyethylene glycol before synthesis experiments. Different tubing materials were also tested. PVC, PTFE, polyether ether ketone (PEEK) and silicone tubes were filled with a growth solution containing gold precursor, ascorbic acid and CTAB for 3 h. There was no fouling observed in PVC and PEEK tubing, unlike PTFE and silicone.

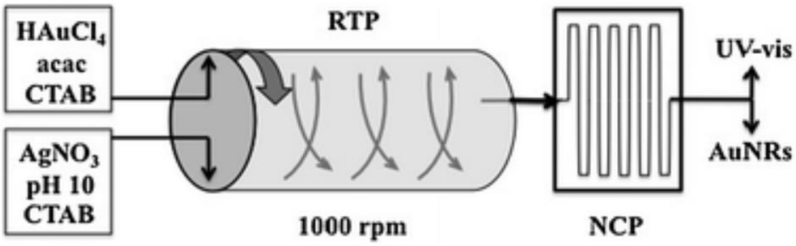

Figure 2-19 Schematic of the experimental set-up for synthesizing Au nanorods by acetylacetone with a rotating tube processor (RTP) and a sequential narrow channel processor (NCP) (Adapted from ref.[139] with permission of The Royal Society of Chemistry, https://doi.org/10.1039/C0CC05175F).

In addition to conventional heating for nanoparticle synthesis, there are other energy vectors that can be utilized. Sans *et al.* premixed the gold precursor and citrate at room temperature and then injected the solution into a coiled fluorinated ethylene propylene (FEP) tube (1.58 mm I.D.) placed inside a microwave cavity.[141] With this set-up, rapid feedback control during the experiments was obtained and hyper-branched gold nanostructures were discovered. Bayazit *et al.* used a microwave-assisted flow system to synthesize Au NPs.[142] The 3.2 mm O.D. PTFE tube reactor produced Au NPs with average particle width 4-15 nm and aspect ratio ~1.4 - 2.2 after only 90 s residence time.

2.4.2 Gold nanoparticle synthesis in two-phase flow systems

Microfluidic reactors

Segmented (also Taylor or slug) flow induced by an immiscible fluid stream can provide better mixing via transverse convection, enhanced mass transfer and reduced dispersion.[143-148] Furthermore, when the synthesis is conducted in the dispersed phase, the reactor wall is protected by a thin liquid film which helps to avoid fouling. However, some of the drawbacks are the necessity of downstream separation processes of the immiscible fluid streams, potential adsorption of NPs at the two-phase interface, keeping slugs uniform and avoiding their coalescence, and the difficulty of adding subsequent reactants in a uniform manner.

The slug length and slip velocity between the two phases are quite important parameters which determine the mass transfer between slugs.[149] In Cabeza *et al.*'s design (**Figure 2-20**),[150] the aqueous phase of gold precursor and $NaBH_4$ was segmented by air, toluene or silicone oil inside a silicon microchannel (H x

W: 0.4 mm × 0.4 mm). The air-water two-phase flow resulted in the smallest and most monodisperse Au NPs with size 2.8 ± 0.2 nm, even though the reaction was in the continuous phase; this was attributed mainly to improved internal recirculation in the slugs. This system also led to the smallest amount of particle loss by interfacial absorption.

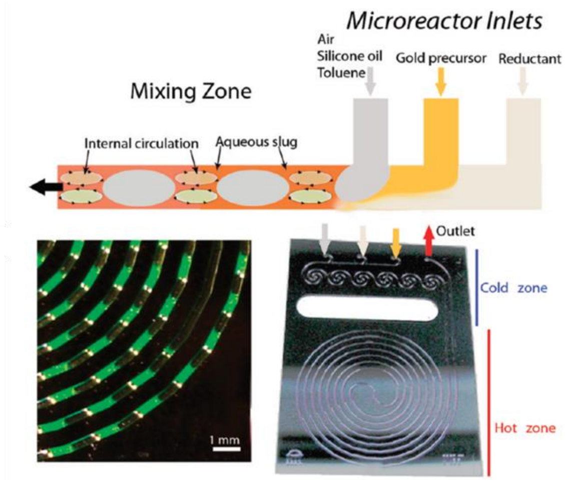

Figure 2-20 Segmented flow generation in a Si-glass microfluidic reactor used for Au NPs synthesis by $NaBH_4$ (reprinted with permission from ref.[150] . Copyright 2012, American Chemical Society).

The same silicon microreactor was used as a hydrophilic reactor by Kulkarni and Sebastian Cabeza, and compared with a hydrophobic PTFE reactor (2.5 mm I.D.) for biphasic synthesis of Au NPs at the interface between an aqueous gold precursor and organic reducing agents (triethylamine (TEA), butyl amine (BA), etc.) with cetyltrimethylammonium bromide (CTABr) as capping agent (**Figure 2-21**).[151] The authors made use of the internal convection in segmented flow to renew the reactant at the interface in order to synthesize and grow the gold nanostructures. Nanoparticle preferential self-assembly at the water-oil interface by Pickering stabilization may have played a role in this synthesis.[152] **Figure**

2-21 d) to g) indicates different locations of particle accumulation for different wettability of tubing wall, which ultimately determined the nanoparticle size and shape. In hydrophilic microchannels the particles remained in the continuous aqueous slug and were located at the lower pressure region at the end of the slug.[151] When the particles moved to the end of one slug, they could be transferred to the next one along the film in the continuous phase while the droplet of the reducing agent would provide successive growth for these particles. The particles grew to form hexagonal bypyramidal shapes with a size of 42 nm. On the other hand, in hydrophobic microchannels the particles were trapped in individual droplets. The nuclei preferentially formed at the front-end of the droplet and then moved to the low-pressure end as their size increased. This movement enhanced the internal-mixing which led to higher nucleation rates and smaller final Au NPs (12 nm), whilst retaining the spherical shape.

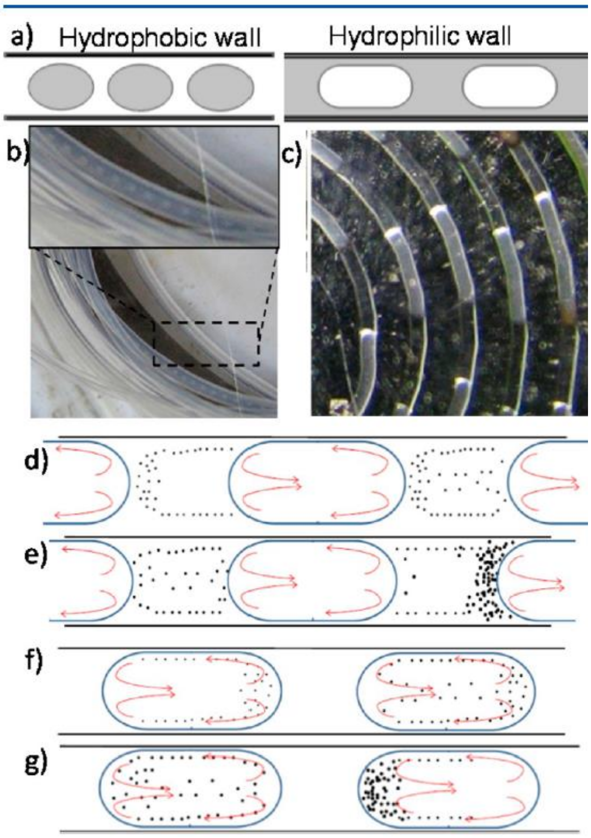

Figure 2-21 Schematic a) and photograph b) & c) of flow patterns inside hydrophobic PTFE (left) and hydrophilic silicon-glass (right) reactors during slug flow (aqueous phase in grey and organic phase in white); d) and e) nanomaterial formation in hydrophilic reactor; f) and g) nanomaterial formation in hydrophobic reactor (reprinted with permission from ref.[151] Copyright 2017, American Chemical Society).

Khan and Duraiswamy. utilized N_2-aqueous slug flow to synthesize Au NPs in a PDMS reactor with CTAB as a capping agent (W x D x L: 300 μm x 120 μm x 0.4 m) not only for better mixing, but also to stop the H_2 liberated from the $NaBH_4$ decomposition disrupting the flow (**Figure 2-22**).[153] The evolved H_2 transferred to the N_2 bubbles leading to controllable stable flow. The authors showed that ultra-small Au NPs (<5 nm) could be synthesized with satisfactory quality to be used as seeds for CTAB-capped Au nanorod formation by off-chip synthesis.

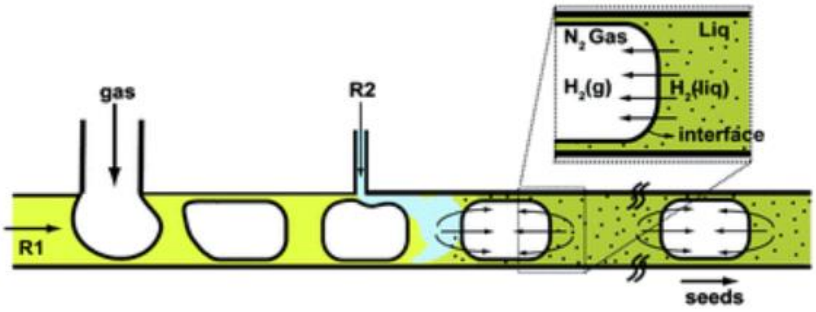

Figure 2-22 Schematic illustration of segmented N_2–liquid two-phase continuous flow for Au NPs synthesis by $NaBH_4$. The inset indicates the transport of H_2 from aqueous phase across to gas phase (Adapted from ref.[153] with permission of The Royal Society of Chemistry, https://doi.org/10.1039/C2LC21198J).

Although internal recirculation in the slugs helps improve mixing, the mixing time scale may not be sufficient for nanoparticle syntheses which exhibit fast kinetics. In this case, winding microchannels can help to break the symmetry of recirculation patterns and enhance mixing.[154-155] While this is easily implemented in a planar microsturcture device, it is rather more difficult if one uses standard tubing. Thus, Zhang and Xia employed periodically pinched PTFE tubes with I.D. of 0.5 mm during droplet flow to decrease the mixing time from 15 to less than 1 s (**Figure 2-23a**). which led to more monodisperse Au NPs (**Figure 2-23b**) compared to the product under the same experimental conditions except without a pinched mixing zone (**Figure 2-23c**).[156]

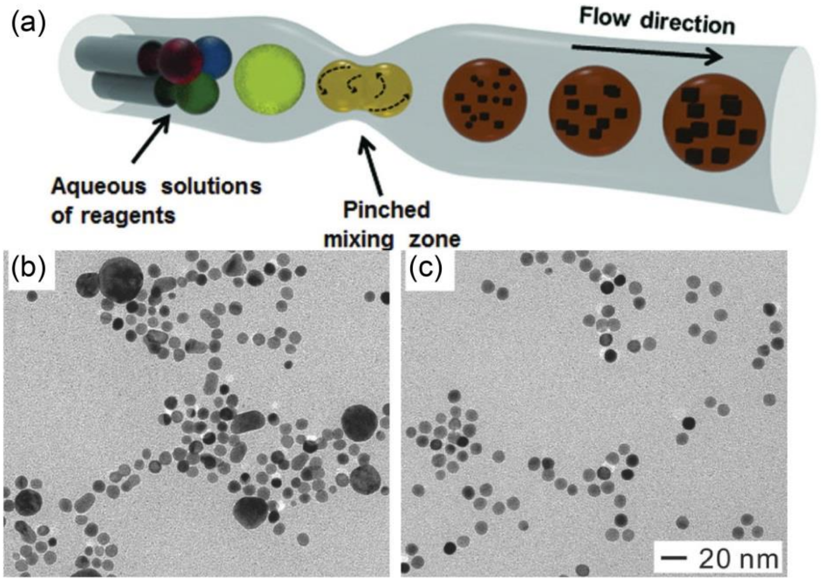

Figure 2-23 (a) Schematic of segmented flow inside 0.5 mm I.D. PTFE tube for Au NPs synthesis (b) with and (c) without pinched mixing zone. (reprinted from Zhang and Xia, Advanced Materials, Copyright 2014 with permission from John Wiley and Sons).[156]

The flow patterns in the droplet-based systems depend on fluid properties.[157] Sometimes, a high concentration of the surfactant in seeded growth methods is necessary to guide the orientated growth or maintain the colloidal stability. These surfactant-rich reagents could increase the viscosity of the aqueous phase and change interfacial tension to affect the droplet characteristics.[158] Duraiswamy and Khan employed a droplet-based microfluidic method during the surfactant-rich anisotropic Au nanorod synthesis (**Figure 2-24a**).[159] Three streams of gold seed solution, premixed gold precursor with capping agent (CTAB) and reducing agent (ascorbic acid) passed through one arm of the T-junction in a “flow-focusing” geometry and then mixed with silicone oil to form homogeneous droplets inside a PDMS microreactor. By manipulating reagent concentrations and flowrates, Au nanorods with aspect ratio of 2.3-2.7, as well as other shapes (e.g. cube, star, tetrapods), were obtained. Later, Duraiswamy and Khan combined the gold seed formation and the CTAB-capped nanorod growth together in a dual-stage continuous flow system (**Figure 2-24b** and **Figure 2-24c**). This time, the seed particles (< 5 nm) were formed inside the PDMS microchannel (W × L : 100 μm × 0.4 m) by $NaBH_4$ reduction and entered the subsequent growth section, which was a microchannel with W × L : 300 μm × 0.45 m. Au nanorods with mean length ~35 nm and width ~12 nm were obtained.[160] The set-up was further improved by adding a gas stream (N_2) to prevent the coalescence between droplets.[161] This microfluidic system was used to synthesize gold nanorods, but primarily gold-coated silicon-core particles by seeded growth.

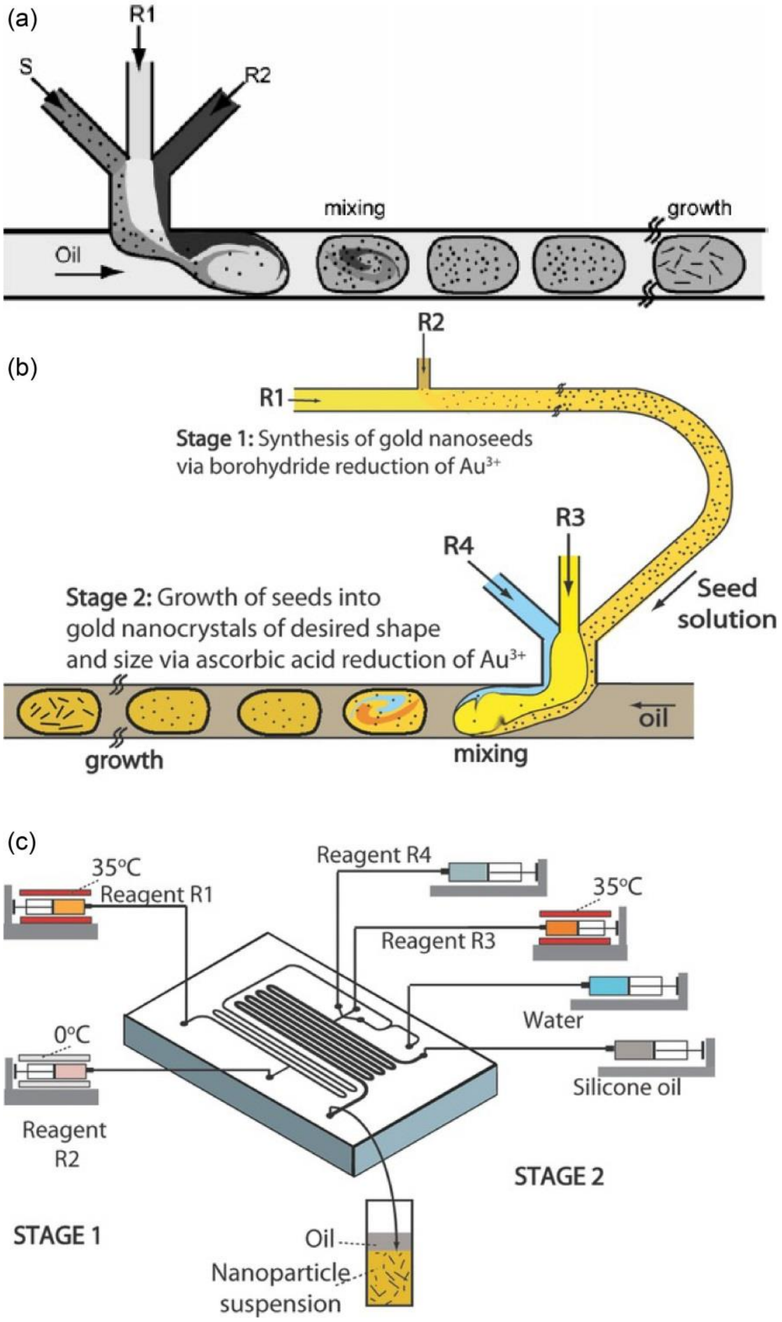

Figure 2-24 (a) Schematic of droplet-based microfluidic with three-arm mixer for aqueous droplet generation used for Au nanorod synthesis with ascorbic acid (reprinted from Duraiswamy and Khan, Small, Copyright 2009 with permission from John Wiley and Sons).[159] (b) Schematic of the two-stage microfluidic method included gold nanoparticle seeds formation in Stage 1 and the growth of gold nanocrystals in Stage 2 and (c) the experimental set-up (Reagent R1: aqueous mixture of gold salt and surfactant, Reagent R2:

aqueous $NaBH_4$ solution, Reagent R3: aqueous mixture of gold salt, surfactant, and $AgNO_3$ and Reagent R4: ascorbic acid) (reprinted from Duraiswamy and Khan, Particle & Particle Systems Characterization, Copyright 2014 with permission from John Wiley and Sons).[160]

Lazarus *et al.* employed a similar PDMS microreactor utilising ionic liquid as solvent to synthesize Au NPs,[162] Ionic liquids, such as the 1-butyl-3-methylimidazolium tetrafluoroborate ($BMIM\text{-}BF_4$) used, are salts in liquid form which have poorly coordinated ions. The high nucleation rate caused by the high concentration in pure salt, low interfacial tension and chemical stability makes ionic liquids attractive for nanoparticle synthesis. With the aid of the microfluidic device to form homogeneous and stable droplets of ionic liquid, spherical Au NPs were smaller and with lower polydispersity (4.38 ± 0.53 nm) compared to those obtained in single-phase flow (6.25 ± 1.29 nm). Later, Lazarus *et al.* altered the synthesis by substituting the capping agent $BMIM\text{-}BF_4$ with 1-butyl-3-methylimidazolium bis-(trifluoromethylsulfonyl)imide ($BMIM\text{-}Tf_2N$) for greater stability and substituting the reducing agent $NaBH_4$ with $BMIM\text{-}BH_4$ for better solubility and prevention of sodium-containing by-products using a similar droplet-based microfluidic system and obtained 4.28 ± 0.84 nm Au NPs.[163]

Taifur-Rahman *et al.* utilized carbon monoxide (CO) as a reducing agent in a membrane-based droplet microfluidic system to produce 10 nm Au NPs, as well as grow Au shells on gold nanoparticle seeds pre-attached on silica surfaces (**Figure 2-25**).[164] The CO flowed through a parallel gas channel (W x D x L: 100 µm x 124 µm x 21.8 cm) and could diffuse into the liquid channel (W x D x L: 300 µm × 124 µm x 91.5 cm) containing the water-fluorinated oil droplets flow via a PDMS membrane with thickness of 200 µm. Each droplet behaved as a reaction unit reacting with nearly equal amounts of CO with the same volume and good internal convection. The residence time could be controlled by the gas-liquid contact time. Calculations indicated that the CO mass transfer resistance in the liquid phase was the rate-limiting step. The mixing time (~0.1 s) was smaller by at least one order of magnitude than the residence time, enabling a controlled amount of the CO reducing agent to enter each droplet at shorter times.

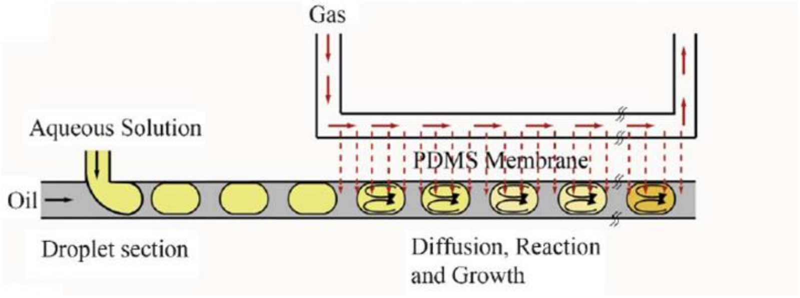

Figure 2-25 Schematic of the droplet microfluidic system with gas reducing agent (carbon monoxide) diffusing through a membrane (adapted from ref.[164] with permission of The Royal Society of Chemistry).

Abalde-Cela *et al.* mixed an aqueous solution with a continuous phase of HFE-7500 fluid containing 2.5% of Picosurf-1 surfactant for quick addition of ascorbic acid, which is critical for the synthesis of Au nanostars,[165] PDMS reactors with 100 µm × 75 µm or 80 µm × 75 µm T-junctions were utilised (**Figure 2-26**). The size of Au nanostars obtained was 170 ± 7.8 µm for a surfactant free synthesis and 90 ± 2.0 µm when PVP was utilised.

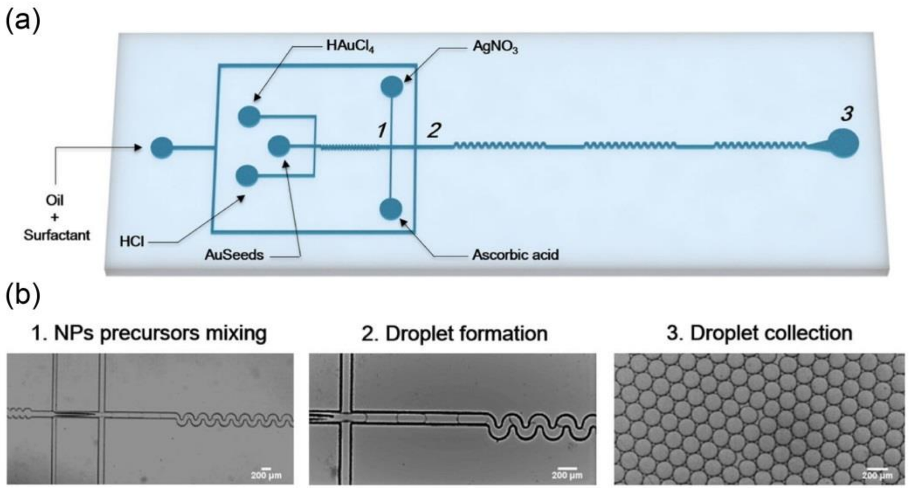

Figure 2-26 (a) Schematic and (b) optical images of a droplet microfluidic device to synthesize Au nanostars by ascorbic acid. (adapted from Abalde-Cela *et al.*, Copyright 2018 Scientific report, https://doi.org/10.1038/s41598-018-20754-x, http://creativecommons.org/licenses/by/4.0).[165]

UV irradiation has been utilised to initiate the nucleation of nanoparticles in segmented flow systems. Hafermann and Köhler used a solution of chloroauric acid, a photoinitiator and polyvinylpyrrolidone that was exposed to a UV ray for a short period of time (30-300 ms) to induce nucleation followed by a growth section in the same 0.5 mm I.D. PTFE tube. Perfluoromethyldecalin was used as the segmenting fluid. In this system nucleation and growth could be spatially separated. The particle size was tuned between 2.5 and 4 nm by varying the composition of reactant solutions or the flow rate.[166] Du Toit *et al.* synthesized citrate-capped Au NPs within heptane-water droplet flow using the Turkevich method.[106] UVC lamps were used to enhance the nucleation rate in a 0.8 mm I.D. glass capillary followed by FEP tube (1 mm I.D.) for controllable growth with conventional heating (**Figure 2-27**). By varying the UV intensity and growth temperature at an exposure time of 10 s, the nanoparticle size was tuned between 6.6 ± 0.8 nm and 36.1 ± 6.9 nm.

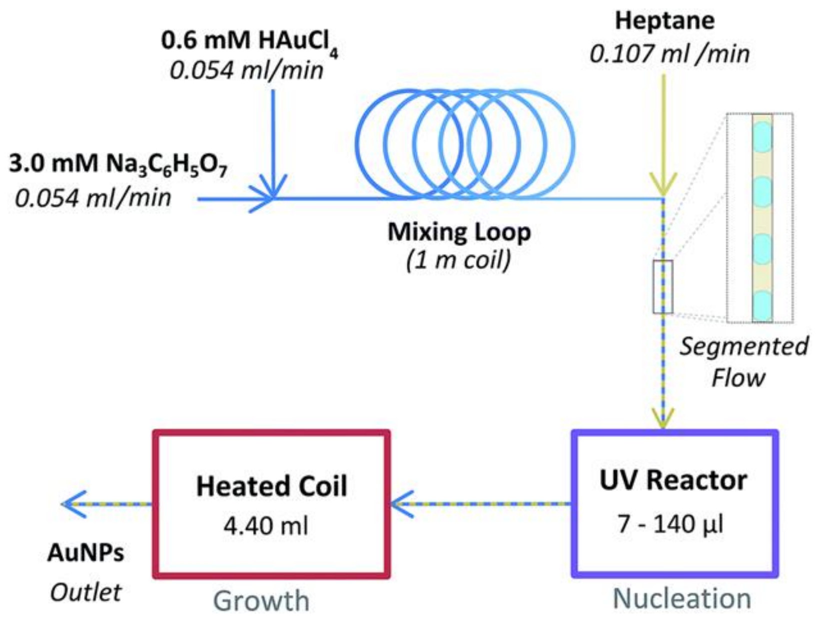

Figure 2-27 Schematic of continuous segmented flow for Au NPs synthesis with UV radiation by citrate (adapted from Du Toit *et al.*, Copyright 2017 Royal Society of Chemistry, Continuous flow synthesis of citrate capped gold nanoparticles using UV induced nucleation, https://doi.org/10.1039/C6RA27173A, https://creativecommons.org/licenses/by/3.0/legalcode).[106]

All the above systems operated under Taylor flow (i.e. the equivalent droplet diameter was larger than the microchannel diameter). Lee *et al.* employed a flow focusing microfluidic device (orifice W × H: 50 µm × 110 µm) to generate microdroplets forming an emulsion (**Figure 2-28**). They used a silicone emulsifier (Abil-Em90) to prevent the coalescence of the microdroplets. The microdroplets contained N-isopropylacrylamide (NIPAM) matrix, and when the NIPAM was polymerized it created a permeable membrane to isolate the inner compounds from the carrier solution. Thus, each droplet could function as an individual artificial cellular bioreactor to synthesize NPs by precursor solutions diffusing into the droplet. Au NPs with size 5-40 nm were obtained when different precursor concentrations (5-50 mM) were used.[167]

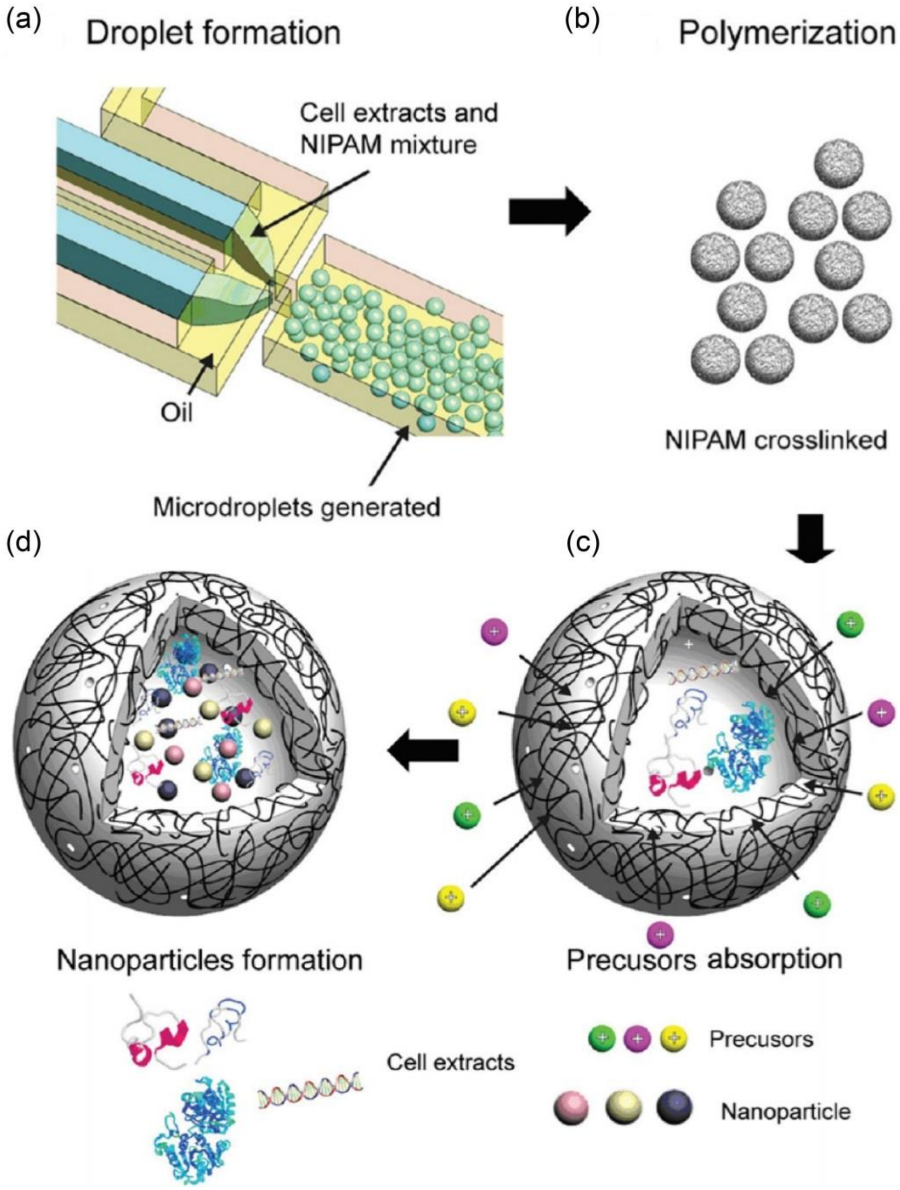

Figure 2-28 Schematic of microdroplet generation with the mixture of cell extracts and NIPAM monomer in a microfluidic device for nanoparticle synthesis (reprinted with permission from ref.[167] Copyright 2012, American Chemical Society).

Gu *et al.* proposed a novel method to dose the reducing agent ascorbic acid in the form of a mini emulsion (continuous phase) into microfluidic droplets of gold precursor (dispersed phase). Transport of ascorbic acid from the mini emulsion nanodroplets into the microdroplets was achieved via electro-coalescence, induced by an applied alternating electrical field (**Figure 2-29**).[168] The electrical field was applied between two parallel electrodes placed outside the fluoroethylene polymer (FEP) tube reactor (0.76 mm I.D) without any physical contact with the reactants and controlled the rate of addition of the reducing agent nanodroplets to the gold precursor microdroplets. PVP-capped Au NPs were produced with size tailored from 44.6 ± 12.6 nm to 81.2 ± 25.5 nm by the strength of the electrical field from 11400 V/cm to 4300 V/cm.

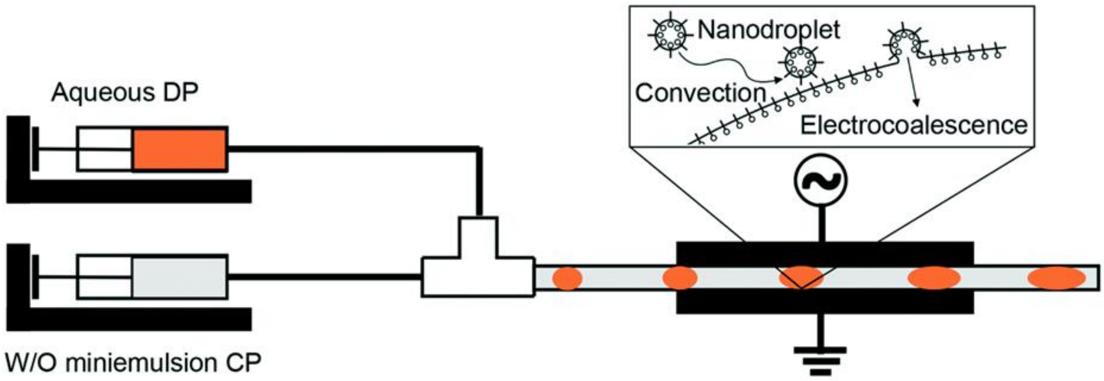

Figure 2-29 Experimental set-up for dosing ascorbic acid from nanodroplets by electrocoalescence at high strength electrical field to synthesize Au NPs. (Adapted from ref.[168] with permission of The Royal Society of Chemistry, https://doi.org/10.1039/C8LC00114F).

Milli-fluidic reactors

Milli-fluidic slug flow reactors are less common due to difficulties in attaining stable slug flow in larger channels. Furthermore, as the size of the tube, and hence of the droplet, increases, mixing by internal recirculation within the droplet becomes less efficient. For this reason synthesis of NPs in milli-fluidic reactors has received less attention. Zhang *et al.* demonstrated a milli-droplet reactor which could produce droplets with a volume of 0.25 mL inside a PTFE tube of I.D. 5.8 mm (**Figure 2-30a**).[169] Co-axial flow with reversed flow direction of two streams was used to obtain better mixing in mixer T1 (**Figure 2-30b**). The well-mixed reagents were subsequently merged with silicon oil and formed a coaxial jet instead of droplets in the channel in mixer T2 and the exiting PTFE tube (I.D. = 1.58 mm). The jet was stabilized due to the high flow rate of the silicone oil stream, but when it entered the PTFE tube (I.D. = 5.8 mm) the flow rate for the silicone oil suddenly dropped, resulting in mL-sized droplets together with small, satellite droplets (**Figure 2-30e**). The satellite droplets merged quickly with the adjacent large droplets before they entered the reaction zone. With this set-up, 10-30 nm spherical cetyltrimethylammonium chloride (CTAC)-capped Au NPs were produced by seeded growth with ascorbic acid, as well as Au cubes 50 nm in edge length. The productivity of this system was in the 1-10 g/h range. The PTFE tube size of 5.8 mm appeared to be the largest size that could be used when silicone oil was employed as the carrier phase. When tubes with larger diameter were used, it became difficult to generate stable droplets.[147]

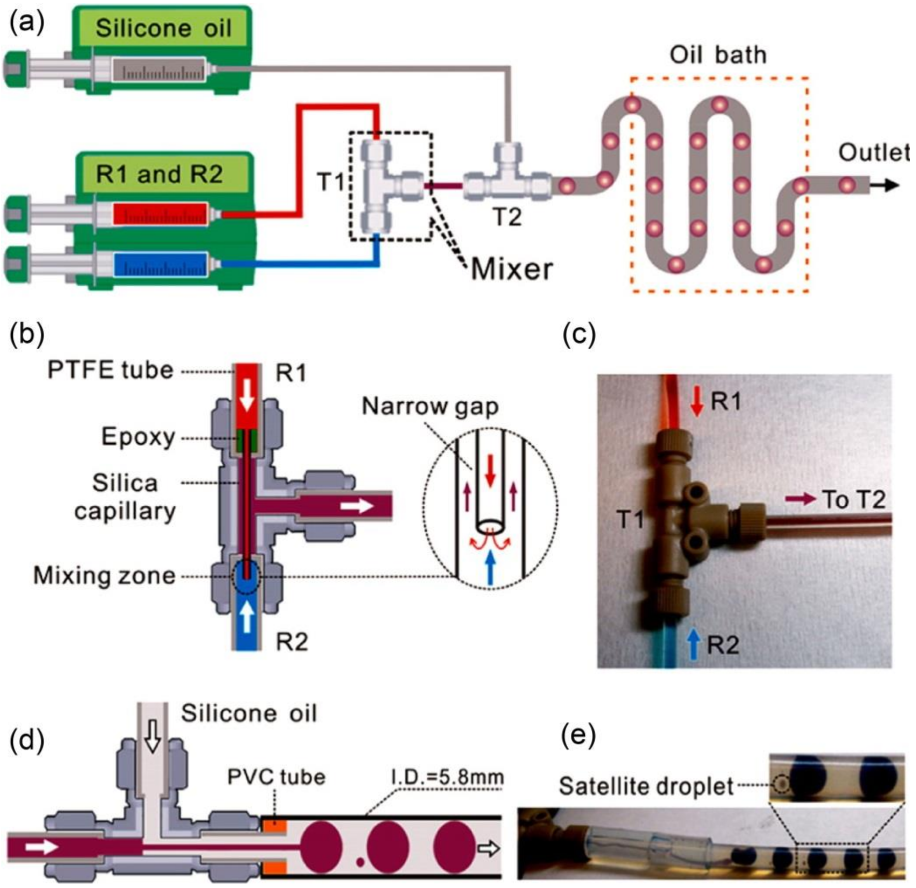

Figure 2-30 (a) Schematic illustration of the milliliter-sized droplet reactor used for the synthesis of Au NPs by ascorbic acid. (b) Schematic illustration of the flow mixer (T1) with three PTFE tubes connected to the T-junction and one silica tube fixed in the centre of the top PTFE tube. (c) Photograph of mixing demo based on the design of (b) with red and blue dye. (d) Schematic illustration of the design for droplet generating (T2). (e) Photograph of 0.25 mL droplets and 0.5 µl satellite droplets in the PTFE tube with an I.D. of 5.8 mm (reprinted with permission from ref.[169] Copyright 2014, American Chemical Society).

Table 2-5 concludes the comparison of advantages and disadvantages for micro and milli-fluidic reactors mentioned above.

Table 2-5 Comparison of advantages and disadvantages for micro and milli-fluidic reactors.

Reactor Type		Advantages		Disadvantages	
Micro-fluidic reactors	**One-phase**	Enhanced heat and mass transfer compared to batch system. Precise control of the operational parameters and improved safety profiles with less volume of reactants.	The mixing of laminar flow only occurs at the interface between miscible streams by molecular diffusion, which can limit uncontrollable reaction when strong capping agents used. Ease of further reagents addition.	Difficult to provide gram-scale production	Mixing needs to be improved to obtain monodisperse particle size. Fouling or even blockages might occur.
	Multi-phase		Mixing improved via transverse convection, enhanced mass transfer and reduced dispersion. Fouling can be prevented by isolating the reactant from tubing wall		The necessity of downstream separation processes of the immiscible fluid streams. Potential adsorption of NPs at the two-phase interface.

					Difficulty of adding subsequent reactants in a uniform manner.
Milli-fluidic reactors	**One-phase**	Enhanced heat and mass transfer compared to batch system. Depend less on expensive fabrication technologies. More amenable to scale-up compared to micro-fluidic reactors	Mitigate the risk of fouling blockages with larger characteristic size compared to micro-fluidic reactors.	Heat and mass transfer might not as good as micro-fluidic reactors.	Fouling issue still existed
	Multi-phase		Mixing improved via transverse convection, enhanced mass transfer and reduced dispersion. Fouling could be prevented by isolating the reactant from tubing wall		Harder to keep slugs uniform and avoid their coalescence compared to micro-fluidic reactors. Internal recirculation within the droplet becomes less efficient.

In conclusion, micro- and milli-fluidic reactors have big potential to synthesize nanoparticles with precise control and safer procedures. The hydrodynamics could be improved via reactor design like tuning characteristic size, compressed tubing, split and recombine, radial interdigitation, pulsed reactants injection, co-axial flow, coiled flow, vortex flow or using multi-phase flow. The selection of the reactor type in later experimental work depended on different synthetic mechanisms. The reactor in Chapter 3 was circular capillary with small inner diameter (~0.3 mm) in which the laminar flow at low flow rate could provide the enough contact and reaction time and surface-to-volume ratio between tubing wall and aqueous reactants for nucleation enhancement. In Chapter 4, carbon monoxide was used as gaseous reducing agent. Due to the stronger reducing ability of CO compared to citrated used in Chapter 3, coiled flow inverter with 1 mm inner diameter was chosen to improve mixing for more monodisperse particle size and less coalescence of liquid slugs. In Chapter 5 and 6, coiled flow inverter continues to be used to stabilize the droplets. At the same time, CO was compressed into an organic phase for higher pressure operation and preventing fouling.

3. Continuous Flow Synthesis of Ultrasmall Gold Nanoparticles in a Microreactor using Trisodium Citrate and their SERS Performance[*]

3.1 Introduction

The production of gold nanoparticles with a size of approximately 15 nm from the reduction of tetrachloroauric acid by trisodium citrate at high temperatures was proposed by Turkevich in 1951.[170] In this method citrate plays three roles during synthesis: a reducing agent, a capping agent and a pH mediator.[36] However, because of the complex equilibrium of reactant species and parallel side reactions, the predominant parameter to control particle size is still disputed, and most mechanistic studies have been conducted in poorly characterised batch systems. A study by Kumar et al. concluded that the dicarboxy acetone (DCA) formed from citrate reduction plays a predominant role which aids nucleation and its side product, acetone, could continue reducing the gold nanoparticles precursor and speed up growth.[171] Even though the model agreed with several literature results, it does not yield satisfactory predictions in other cases, because it does not take account of the acid-base properties of the reactants.[172] Wuithschick *et al.* demonstrated experimentally that the Au(III) species are the critical element to control particle size.[31] In their study, the formation of monodispersed gold nanoparticles in the Turkevich method was investigated. When the initial pH of the gold precursor is in the range of 2.7 to 4,

---

[*] This chapter has been published as:
Huang, H., Du Toit, H., Besenhard, M. O., Ben-Jaber, S., Dobson, P., Parkin, I., & Gavriilidis, A, *Chemical Engineering Science,* 2018,**189**, 422-430.
Copyright © 2018, Elsevier.

a shift of equilibrium to the gold species with less reactivity occurs when changing the pH by adding citrate. When $AuCl_4^-$ ions are totally converted into hydroxylated species, nucleation stops, and the rest of gold ions are consumed for growth. Based on this hypothesis, Wuithschick et al. reversed the addition order of the reactants to add gold precursor to boiled citrate instead of adding citrate to boiled gold precursor proposed in the Turkevich method. As the gold precursor has a higher concentration, which is associated with lower pH and the presence of more $[AuCl_4]^-$ at the early stages, the final particle size obtained by the inverse Turkevich method could be as low as 7.6 nm without any additional strong reducing agents or ligands.

It has been established that fast nucleation is the key in order to achieve monodispersed and small gold nanoparticles.[31] However, since citrate is a moderately weak reducing agent, the nucleation rate using citrate reduction is not as fast as with some strong reducing agents such as $NaBH_4$. That is why the typical minimum nanoparticle diameter is in the range of 7 nm.[31] However, the low toxicity[173] and the ease with which such citrate-capped gold nanoparticles can be functionalised, keeps researchers motivated to improve this method. This is also the reason why the current study has focused on a citrate-only system. In order to decrease the overall size and particle size distribution of the citrate-capped gold nanoparticles, several approaches have been implemented and the reasons were concluded in **Table 3-1**, such as using a stronger reducing agent,[40-43] tuning citrate concentration,[37] reaction temperature,[31] solution pH,[36] reactant pre-mixing at room temperature, adding Ag^+ ions,[174] employing UV irradiation[106] and ultrasound.[175] In batch systems, it seems that only with a stronger reducing agent can the size of citrate-capped gold nanoparticles be made smaller than 5 nm.

Table 3-1 Conclusion of the parameters tuned by previous literatures for particle size control and the reasons.

Parameter	Reasons
Stronger reducing agent	Faster nucleation rate compared to mild reducing agent, citrate.
Tuning citrate concentration	Faster reduction rate with higher amount of reducing agent
Reaction temperature	Increase the reaction rate and accelerate the thermodynamic control stage in growth process.
pH	Tuning the reaction rate based on different reactivities of reactant species at different pH.
Reactant pre-mixing at room temperature	To eliminate the concentration gradient for narrower size distribution.
Adding Ag^+ ions	Accelerate the growth process via Ag^+-directed growth.
UV irradiation	Faster nucleation rate induced by UV light.
Ultrasound	Faster nucleation rate via ultrasound and reduced fouling.

Microreactors have many advantages over batch reactors, such as better mixing, enhanced mass and heat transfer,[176] high surface-to-volume ratios, easier and safer control of different process parameters of the process and they are potentially easier to scale up.[177] Thus, many researchers have adapted the use of microreactors for the production of citrate-capped gold nanoparticles. In most cases researchers take advantage of better mixing in different types of microreactors[117, 178-180] in order to reduce the polydispersity of synthesized gold nanoparticles and tune the particle size by parameter optimization.[136] Nonetheless, without strong reducing agents, faster mixing itself cannot fundamentally increase nucleation rate. Thus, the final size of the particles could only be reduced to around 7 nm.[31] It is noteworthy that Ftouni *et al.* produced ultrasmall size gold nanoparticles of mean diameter 1.8 nm at a residence time of 47 s in a citrate-only system by taking advantage of the short mixing, heating and quenching times in a continuous flow capillary reactor.[181] As the residence time was quite short and the product could be quenched to terminate the reaction, no further growth after the formation of seed particles leads to this result, which is also the smallest particle size obtained by a citrate-only reduction so far. However, it is likely that not all the gold precursor was used, since it has been shown that only 1-2% of the gold precursor is consumed in the process of seed particle formation.[31] If that was the case, most of the gold precursor would not have been utilised, while unconsumed $HAuCl_4$ in the product could lead to instability of particle size.

One of the most widely used methods to synthesize gold nanoparticles under 5 nm is the Brust-Schiffrin method which involves both a strong reducing agent ($NaBH_4$) and a capping agent with a strong binding strength (namely thiols).[47] As $NaBH_4$ keeps reducing unconsumed Au(III) precursor, nuclei are produced throughout the whole synthesis which leads to overlapping of nucleation and growth processes. In this case the thiol plays a decisive role to separate synthesized gold nanoparticle efficiently and thus limit the growth of particles. This is why most of gold nanoparticles with ultrasmall size are stabilized by thiols. However, thiols are not vital to stabilize ultrasmall gold nanoparticles. As a stabilizing agent, citrate has been shown to be capable of stabilizing gold nanoparticles of ca. 2 nm reduced by $NaBH_4$.[182] Thus, in order to synthesize sub-5 nm gold nanoparticles reduced by citrate, the key point is the enhancement of the nucleation rate, as the final particle size can be determined by the amount of nuclei formed. At high nucleation rates, more nuclei are produced, and thus less gold precursor is available for growth.

In this chapter, we tested the feasibility of a new approach to enhance nucleation rate by using the surface interaction between reactants and the negatively-charged tubing wall of different capillary microreactors. A low flow rate ensures enough time for surface interactions to consume the entire gold precursor. The size of the synthesized citrate-capped gold nanoparticles could thus be reduced below 3 nm. The particles obtained show a better SERS performance compared to phosphate-capped gold nanoparticles with similar size.

3.2 Experimental

3.2.1 Experimental set-up

The experimental set-up shown in **Figure 3-1** was based on circular capillary microreactors (length 2.5 m) with different internal diameter (I.D.) and of different materials: polytetrafluoroethylene (PTFE, 0.3-1.0 mm I.D.), fluorinated ethylene propylene (FEP, 0.25 mm I.D.), polyetheretherketone (PEEK, 0.25 mm I.D.) (SUPELCO) and fused silica (0.32 mm I.D., Polymicro Technologies). It also employed a micromixer chip (Dolomite, Part No. 3000144), a stirred glycerol (99.5 %,VWR) bath on a hot plate (Stuart, UC152D with SCT temperature controller) to keep the microreactor temperature at 70-100 ˚C, a double syringe pump (Harvard PhD Ultra), a sample and waste collection unit (including two 4 ml cuvettes and a 700 ml steel vessel) with back pressure regulator (Swagelok, SPL Back Pressure Regulator, max pressure 1000 kPa) adjusted to 275 kPa to supress boiling.

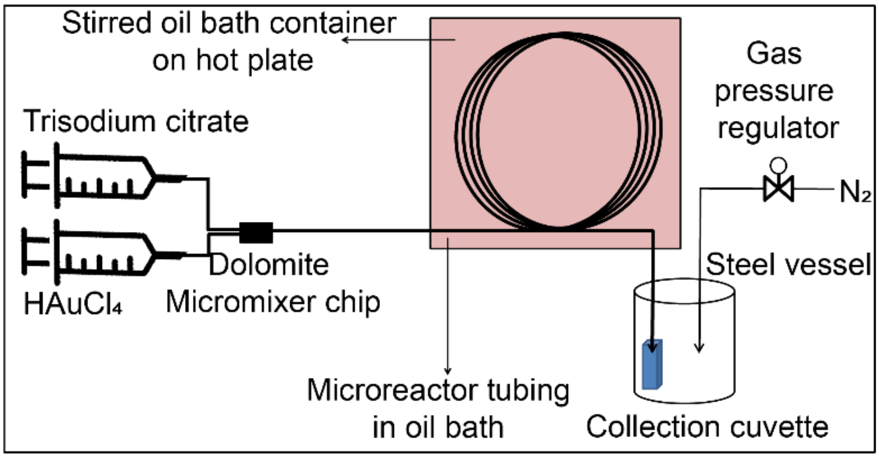

Figure 3-1 Experimental set-up of continuous flow synthesis of ultrasmall gold nanoparticles in capillary tubing using chloroauric acid and trisodium citrate as reactants.

3.2.2 General synthetic procedure

In a typical synthesis procedure Gold (III) chloride trihydrate (Sigma-Aldrich, 99.9+%) and trisodium citrate (Sigma-Aldrich, 99+%) were dissolved in deionized water (15 MΩ cm). All the reagents were filtered (GVS Filter Technology, Polyethylene, 0.2 µm) before pumping into tubing made of different materials and I.D.s. 0.54 mM $HAuCl_4$ and 1.7 mM trisodium citrate solutions were injected through two glass syringes using a double syringe pump at a constant volumetric flow ratio of 1. Freshly prepared aqua regia and then deionized water were used to clean the system after every experiment. For slug flow experiments a stream of pure octane (Sigma-Aldrich, 99.9+%) and the aqueous reactant mixture (1/1 citrate/gold volumetric flowrate ratio) were merged in a T-mixer (IDEX Health & Science LLC, 0.5 mm through hole), at 1/1 organic/aqueous volumetric flowrate ratio. Slug flow was used to prevent the interaction between reagents and PTFE tubing wall by forming a thin lubricating layer between the droplets and tubing wall. All the parameters used for the slug-flow experiment were kept constant (0.3 mm I.D. PTFE tubing, average residence time of 30 min, temperature of 100 ˚C, 275 kPa back pressure and citrate/gold molar ratio of 3.15).

3.2.3 Analysis

UV-Vis absorption spectra of gold nanoparticle solutions were recorded using an Ocean Optics UV-Vis-ES spectrometer (USB 2000+ Spectrometer and DT-Mini-2-GS light source). The spectra were recorded immediately after the experiments and the samples for transmission electron microscopy (TEM) analysis were prepared concurrently. TEM images and selected area electron diffraction (SAED) analysis were taken on a JEOL 2100 EXii microscope with a 120 kV acceleration voltage. TEM samples were prepared by dipping a drop of the colloidal solution onto lacey carbon film on a 400 mesh copper grid (E M Resist Ltd) and allowed to dry in air. The polydispersity of the synthesized particles is defined as the standard deviation of the particle size distribution. Scanning electron microscope (SEM) images of the inner surface of the capillary tubing were taken on a JEOL JSM-6701F microscope. X-ray photoelectron spectroscopy (XPS) was performed using a Thermo Scientific K-alpha photoelectron spectrometer using monochromatic Alkα radiation. Higher resolution scans were recorded for the principal peaks of Au(4f) and C(1s) at a pass energy of 50 eV. The peaks were modelled using CasaXPS software with binding energies adjusted to adventitious carbon (284.8 eV) for charge correction. ATR-FTIR spectroscopy was performed using a Perkin-Elmer 1605 FT-IR spectrometer with a resolution of 0.5 cm^{-1} and wavenumber range 500-4000 cm^{-1}. Inductively coupled plasma atomic emission spectroscopy (Varian 720 ICP-AES, axial configuration) was used to measure the gold amount of synthesized ultrasmall gold nanoparticles. 1 ml product solution was centrifuged at speed of 100,000 rpm for 1 h by ultracentrifuge (Beckman Coulter, Optima MAX) to precipitate the particles. Subsequently, both the precipitate and supernatant were digested by aqua regia and diluted to 5 ml. The yield was calculated by the amount of gold in the precipitate detected by ICP-AES over the original amount of gold precursor.

Raman signals were measured with a Renishaw Raman inVia microscope with a 633 nm He-Ne excitation laser (1.9 eV, 0.7 mW, pore size ~ 4.4 μm^2). A comparison of Surface-Enhanced Raman Scattering (SERS) performance between our synthesized citrate-capped gold nanoparticles from fused silica tubing and gold colloid stabilized in phosphate buffered saline (PBS) buffer solution with similar particle size (2 nm, EM.GC2, BBI Solutions) was carried out. 10^{-5} M of the aqueous analyte Rhodamine-6G was mixed with the same volume of gold nanoparticle solution and then stirred for 20 min to leave enough time for the molecules to bind onto the gold surface. The solutions were then drop-cast onto glass substrate to dry and create SERS hotspots.

The zeta potential of the four different tubing materials was determined using the SurPASS 3 (Anton Paar) electro-kinetic analyser for macroscopic solids based on a streaming potential measurement. Tubing samples were measured using the SurPASS 3 measuring cell for flexible tubing. 1 mM KCL solutions were used for all measurements. Further details on the performed zeta potential analysis can be found in the Supporting Information.

3.3 Results and discussion

3.3.1 Influence of flow rate

The flow rate in our study was low as we aimed to provide more opportunity for surface interaction between the reagents and the tubing wall and consume all of the Au(III) within the microreactor leading to a more stable product. The dispersion number was calculated in **Table 3-2** for the slowest flow rate in the smallest tubing size in our study. For the reagents, as well as the synthesized gold nanoparticles, the dispersion number was always < 0.01, which indicates plug flow behaviour.[183] Thus, the low flow rate is not expected to increase the size heterogeneity.

Table 3-2 Reactor dispersion number for various components.

Item	**Diffusion coefficient $\mathscr{D}$ (m^2s^{-1})**	**Dispersion Coefficient *D* (m^2s^{-1})**	**Dispersion number**
Equation	$\mathscr{D}=\kappa T/(6\pi\mu R)$ [a]	$D=u^2d_t^2/(192\mathscr{D})$[184]	D/uL [184]
0.3 mm I.D. (gold atom-0.166 nm)	3.7×10^{-9} [a]	2.5×10^{-7}	7.1×10^{-5}
0.3 mm I.D. (gold nanoparticles-2 nm)	3.1×10^{-10} [a]	3.1×10^{-6}	8.6×10^{-4}
0.3 mm I.D. (citrate)	6.3×10^{-10}[185]	1.5×10^{-6}	4.2×10^{-4}

a: The equation is applied for the calculation of gold atom and 2 nm gold nanoparticles [186].

UV-Vis was used to monitor the microreactor effluent instantly. The initial concentration of $HAuCl_4$ after mixing was kept relatively high at 0.54 mM to facilitate UV-Vis measurements. The I.D. of the PTFE tube used for these experiments was 0.5 mm. Under these conditions, products with different colours were synthesized as shown in **Figure 3-2 (a)**. By changing the inlet flow rate (14 – 260 µl/min), the product exited the microreactor after a residence time of 1.5-30 min. The colour of the product obtained depended on the residence time. The microreactor product colour changes shown in **Figure 3-2 (a) inset** show the same trend as observed in a batch system as a function of synthesis time; from blue to purple to red as reaction progresses.[170] The different colours represent different stages of the nucleation and growth processes. The above indicate that the microreactor system did not change the general reaction pathway of the Turkevich method. With the first three flow rates used (14, 26, and 42 µl/min), the peak absorption of the obtained solutions nearly overlapped, which indicates that the flow rate did not have a big effect on gold nanoparticle synthesis, provided enough time was allowed in the reactor to complete particle growth. **Figure 3-2 (b)** shows that the peak absorbance, which is related to the final concentration of the product,[187] was influenced by flow rate. There was overall a decreasing trend of absorbance as flow rate increased. For flow rates > 50 µl/min, the residence time was too short for the reduction, and unconsumed gold precursor in solution led to the low absorbance in UV-Vis. **Figure 3-2 (c)** indicates the effect of flow rate on wavelength of maximum absorption (λ_{max}), which is related to gold nanoparticle particle size.[187] As it is very hard to identify a peak for the sample at the highest flow rate (260 µl/min), there is no data presented for this condition. For flow rates < 50 µl/min, the solutions had the same λ_{max}, which indicates that the nanoparticles that did not change in size. No further growth was observed with increasing residence time between the flow rate of 42 µl/min and 14 µl/min. For this reason, all subsequent experiments were performed with low flow rates. The increasing λ_{max} at higher flow rates (78 - 260 µl/min), which is associated with colour change from purple to red, has been investigated by several literatures[36, 188-191] and attributed to aggregate formation at the early stages of the synthesis. However, recent research suggests that it could probably be caused by the attachment of gold ions on the surface of nuclei.[102]

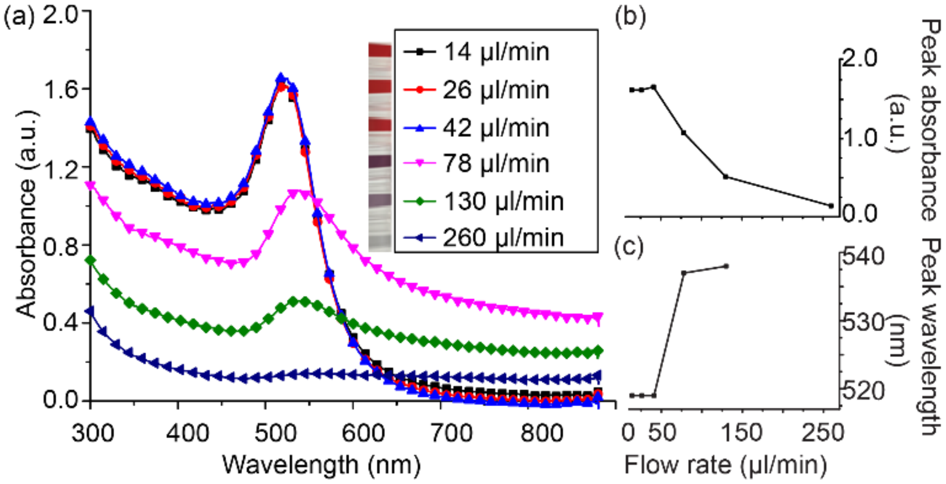

Figure 3-2 (a): UV-vis spectra of gold nanoparticles synthesized in PTFE tubing with an I.D. of 0.5 mm, at temperature of 80 ^{o}C and total flow rates as indicated, corresponding to average residence times 1.5 - 30 min. Inset: colour of the products at different flow rates. (b): Maximum peak absorbance of gold nanoparticle solutions at various flow rates from UV-Vis spectroscopy. (c): Wavelength of maximum absorption (λ_{max}) at various flow rates. Solutions of 1.08 mM $HAuCl_4$ and 5.4 mM citrate were mixed at 1/1 volumetric flowrate ratio.

3.3.2 Synthesis of ultrasmall size gold nanoparticles

The bottleneck of synthesizing sub-5 nm gold nanoparticles in the Turkevich method is the slow nucleation rate obtained by the moderately weak reducing strength of the citrate. If the nucleation rate could be enhanced, gold nanoparticles of smaller size would be expected. Turkevich and co-workers suggested that in citrate reduction, the dicarboxyacetone (DCA) formed from trisodium citrate by thermal decomposition or reduction reaction acts as an organizer to assemble gold ions in a form of multi-molecular complex.[170, 192] The increasing local concentration of precursor facilitates the reduction of Au(III).[192] The nucleation rate is reportedly enhanced if another stronger organizer (which plays a similar role to DCA) is used.

It has been demonstrated that in the layer-by-layer process (a thin film fabrication technique), oppositely charged reactants and polymers form multiple layers of inorganic–polymer by electrostatic attraction.[193] By making use of this feature[194] improved the catalytic performance of gold nanoparticles with the aid of polydopamine (PDA) nanoparticles (~200 nm) compared with the same amount of gold nanoparticle suspension. In their study, PDA carriers with negative charge increased the concentration of positively charged reactant for the loaded catalysts (gold nanoparticles) on the carriers due to the electrostatic attraction.

Inspired by this concept, we used the tubing wall of the microreactor as an organizer to increase the local concentration of Au(III) and thus enhance the nucleation rate. Because of the large surface-to-volume ratio, the interaction between reactants and tubing wall was enhanced compared to a batch reactor system. **Figure 3-3** proposes a possible process which enhances the nucleation rate in this study. The $HAuCl_4$ and trisodium citrate are premixed at room temperature before being pumped into the microreactor system. Initially positively charged citrate-gold ion complexes are formed.[195] The tubing wall with negative surface potential increases the local concentration of opposite charged citrate-gold ion complexes by electrostatic attraction.[194] As the increasing concentration of gold precursor accelerates the nucleation rate,[196] more seed gold nanoparticles are formed which is expected to lead to smaller final nanoparticle size.[31] Once gold nanoparticles are synthesized and capped with citrate, they become negatively charged.[197] With the resulting electrostatic repulsion gold nanoparticles could be repelled from the wall and transfer back into the bulk solution without further attachment on the tubing wall. As it will be shown later, this is only partly successful, and a portion of nanoparticles irreversibly attach on the wall giving rise to fouling. After the entire gold precursor is consumed, no electrostatic attraction exists. This is consistent with the fact that no fouling was observed on the latter section of tubing, because of repulsion between stabilized gold nanoparticles and tubing wall with the same charge.

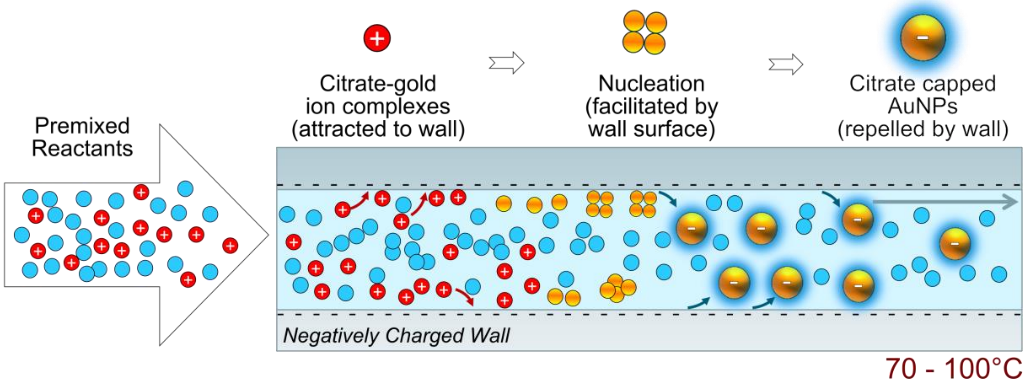

Figure 3-3 Schematic illustration of the enhancement of nucleation during gold nanoparticle synthesis by surface interaction between the reactants and the microreactor wall.

In order to adsorb positively charged citrate-gold complexes, the tubing wall must carry negative charge; the latter depends on the pH of solution.[198] However, the Turkevich method is a pH-dependent reaction.[36] In the experiments in this section, the initial concentration of precursor before mixing was 0.54 mM (with initial pH of 3.3), which is in the optimal pH range of 2.7-4 proposed for the synthesis of monodispersed gold nanoparticles by citrate reduction.[31] At a citrate to gold precursor ratio of 3.15, the final pH of the solution is around 6. PTFE has a negative surface potential at this pH.[199] The inner tubing diameter was small, at 0.3 mm, in order to provide more opportunity for surface interaction between the solution and tubing wall. To consume all the gold precursor, synthesis was conducted using low total flow rate (6 µl/min).

A colourless product which did not exhibit a Localized Surface Plasmon Resonance (LSPR) band was obtained, indicating gold nanoparticles with diameter below 2 nm.[200] The TEM image shown in **Figure 3-4 (a)** verified that the colourless solution contained gold nanoparticles with ultrasmall size of 1.9 ± 0.2 nm (12.8%). The high magnification HR-TEM image in **Figure 3-4 (b)** shows a gold nanoparticle with lattice spacing consistent with Au [201]. The selected area electron diffraction (SAED) pattern in **Figure 3-4 (c)** was diffuse due to the small diameter of gold nanoparticles.[181]

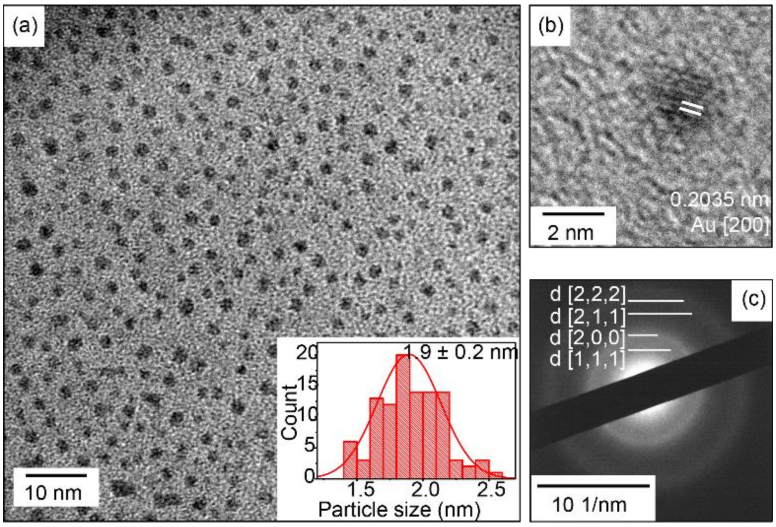

Figure 3-4 TEM images of gold nanoparticles synthesized with total flow rate of 0.006 ml/min (residence time 30 min), at 100 ˚C using PTFE capillary tubing (0.3 mm I.D.). (a) Colourless product of gold nanoparticles with a size of 1.9 ± 0.2 nm (polydispersity 12.7%) (b) HR-TEM image showing the inter-planar spacing in the [200] direction. (c) SAED pattern of the gold nanoparticles synthesized. Solutions of 0.54 mM $HAuCl_4$ and 1.7 mM citrate were mixed at 1/1 volumetric flowrate ratio.

With time, a section of “dark fouling” followed by “pink fouling” was observed near the inlet of the PTFE tube (**Figure A-1**). This seems to be congruent with the blue colour appearing during citrate reduction. Moreover, this so-called “dark fouling” was not firmly attached like the “pink fouling” (the “dark fouling” was quite easily removed by increasing the flow rate, while the “pink fouling” could only be removed by aqua regia). Polte and co-workes showed that the blue colour during the early stages of gold nanoparticle synthesis by citrate reduction was not due to particle aggregation, as no significant scattering signal was detected by ultrasmall angle X-ray scattering (USAXS).[31] In their study, they proposed that this blue colour was due to the attachment of gold ions in an electric double layer, resulting in a change of plasmonic properties.[102] The dark fouling solution was frozen by liquid nitrogen and then dried by freeze dryer. The dried dark material was analysed by XPS* and IR* and showed the existence of citrate-gold complexes and a mixture of gold atoms and gold ions. **Figure 3-5a** shows a peak shift compared to COO(H) group because of the coordination between COO^- and Na^+ or gold.[197] **Figure 3-5b** shows that the gold in the dark material existed as a mixture of Au(0) and Au(III). This co-existence indicated that at the stage of the dark tube section (**Figure A-1b**, section i), part of the gold precursor was reduced to gold atoms in the presence of gold ions. However, it is hard to separate the contribution of $COO\text{-}Na^+$ and the coordination between COO^- and gold based on the peak shift through XPS, as the binding energy of peak #1 from dark fouling and pure trisodium citrate are nearly identical (~288.3 eV) (**Figure 3-5c**). Thus, the IR spectra were used to investigate the coordination between citrate and gold. In **Figure 3-5d** a vibration could be observed in the range between 1700 and 1800 cm^{-1} for the dark fouling. Compared to the purified citrate-capped gold nanoparticles in literature,[197] the intensity of this peak in the dark solution is higher because of the higher amount of the coordination between citrate and gold from the citrate-gold complexes. The characterization of the “dark fouling” showed the co-existence of Au(0) and unconsumed gold ions, as well as a high amount of citrate-gold complex. As this material was observed at the tubing surface, the “dark fouling” is supportive evidence for nucleation sites and adsorption of gold ions around the tubing wall, caused possibly by electrostatic attraction. With decreasing concentration of gold ions along the reactor, the colour of the fouling changed to pink indicating

---

[*] *The XPS analysis was carried out by Dr. Sanjayan Sathasivam, University College London*
[*] *The IR analysis was carried out by Jijia Xie, University College London*

gold nanoparticles irreversibly attached on the tubing wall, most probably by van der Waals forces.

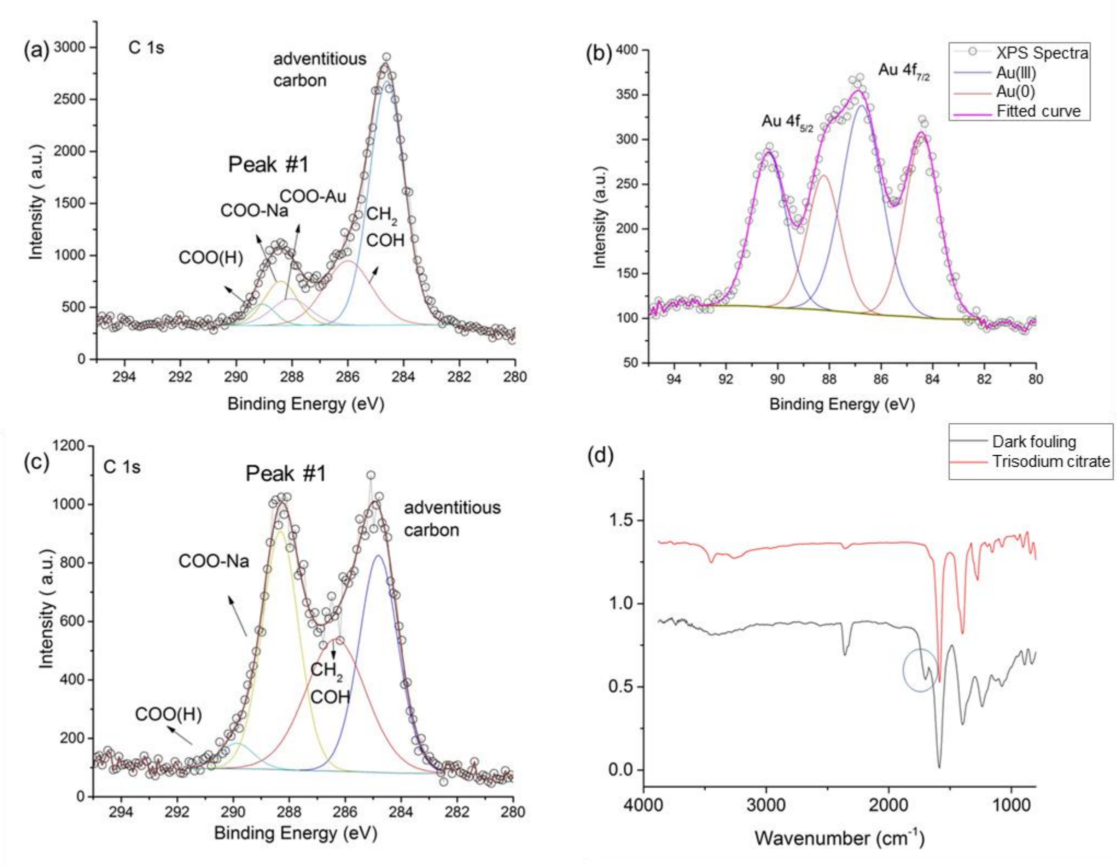

Figure 3-5 Characterization of dark fouling observed towards the tube inlet. (a) XPS spectrum of C 1s binding energy of dark fouling, (b) XPS spectrum of Au 4f binding energy of dark fouling, (c) XPS spectrum of C 1s binding energy of pure trisodium citrate, (d) IR Spectra of dark fouling, showing a small peak between 1700 - 1800 cm^{-1}, and pure trisodium citrate.*

3.3.3 Influence of tube surface-to-volume ratio

To demonstrate that the PTFE tubing wall plays a crucial role in obtaining ultrasmall particles, experiments with the same length (2.5 m) but different inner tube diameters and hence surface-to-volume ratios were carried out. **Figure 3-6** shows TEM images of the synthesized gold nanoparticles (**Figure 3-6a-d**) and

---

* *The XPS analysis was carried out by Dr. Sanjayan Sathasivam, University College London*

the trend of nanoparticle size obtained as a function of the reactor surface-to-volume ratio (**Figure 3-6e**). The diameter of the synthesized gold nanoparticle obtained from slug flow when the surface-to-volume ratio is zero was 17.4 ± 1.4 nm (8.2%). This is in the typical size range for gold nanoparticles synthesized in batch by the Turkevich method (e.g. 17.4 nm with polydispersity of 10% in.[31] The result indicates that without interaction between reagents and the tubing wall, there was no enhancement of nucleation, even though a small tube (0.3 mm I.D.) was used. The segmented flow microfluidic system has sufficient mixing and narrow residence time distribution to achieve low polydispersity of particle size. When the solution of reactants was in contact with the tubing wall, the wall nucleation rate was enhanced. With increasing the I.D. (0.5 mm, 0.8 mm and 1 mm) the surface-to-volume ratio decreased, and the bulk nucleation was dominant at large tube sizes rather than enhanced nucleation by the tubing wall. For the gold nanoparticles synthesized with the 1 mm tube (**Figure 3-6b)**, a mean particle size of 17.3 ± 4.5 nm (polydispersity 25.8%) was obtained and for the 0.8 mm tube (**Figure 3-6c)**, it was 17.5 ± 3.8 nm (polydispersity 21.7%). In both cases the particle size distribution was broader compared to slug flow synthesis (**Figure 3-6a**, 17.4 ± 1.4 nm, 8.2%); this is in accordance with the broader particle size distribution that He *et al.*[202] observed when bulk solution interacted with the tubing wall. We propose that this broad size distribution is due to the fact that even though surface interaction still existed in these two cases, the amount of gold ions adsorbed by the tubing wall was proportionally small. The rest of the gold ions were reduced in the bulk fluid. Two nucleation processes with different rates occurred at the same time which affected the separation of nucleation and growth. For the 0.8 and 1 mm capillaries, the gold nanoparticles obtained were more polydisperse than the classical citrate reduction. In contrast, the wall surface of the 0.5 mm capillary started to affect nucleation and there were two different types of gold nanoparticles formed: polydisperse gold nanoparticles from uncontrollable growth and small gold nanoparticles with sizes of around 4.1 ± 0.5 nm (11.3%) (**Figure 3-6d**). In this case, more citrate-gold complexes had the opportunity to interact with the tube surface and thus less precursor was left for bulk nucleation/growth. Hence, even though two nucleation processes took place, more Au(III) was consumed by enhanced nucleation at the wall because of the larger surface-to-volume ratio. Compared with gold nanoparticles synthesized in the 0.3 mm I.D. tubing, the particle size of small gold nanoparticles synthesized with the 0.5 mm I.D. tubing in **Figure 3-6d (inset)** was larger, possibly because the amount of unconsumed gold precursor in the 0.5 mm tubing was higher than the 0.3 mm tubing. After the enhanced nucleation stage, the seed particles were repelled by the tubing wall and entered the flow for further growth. The larger amount of unconsumed gold precursor left in solution led to the larger particle size obtained after full growth. The large size particles disappeared when the surface-to-volume ratio was >13 (tubing with 0.3 mm I.D.) and monodisperse gold nanoparticles with ultrasmall size of 1.9 ± 0.2 nm were obtained (**Figure 3-4**). It is worth noting that He et al.[202] obtained monodisperse silver nanoparticles using PTFE tubing with a very small I.D., and they also proposed the presence of enhanced nucleation at the tube surface.

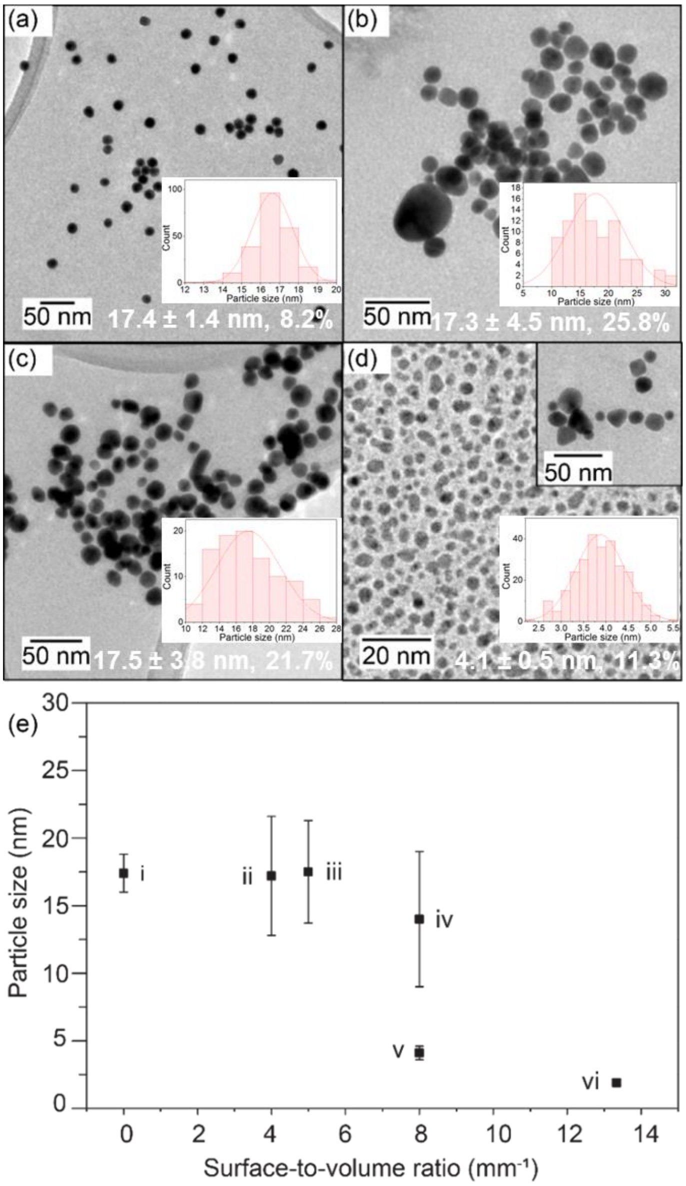

Figure 3-6 TEM images of gold nanoparticles synthesized at the same average residence time (30 min), with PTFE tubing of varying I.D. at 100 °C. (a) Aqueous phase segmented by octane in capillary with an I.D. of 0.3 mm, and single-phase flow in capillary with I.D. of (b) 1 mm, (c) 0.8 mm, (d) 0.5 mm. The inset shows the larger size gold nanoparticles found on another area of the same TEM grid of (d). (e) Nanoparticle size obtained as a function of the reactor surface-to-volume ratio from i) slug flow, ii) 1 mm I.D. tube, iii) 0.8 mm I.D. tube, iv) and v) 0.5 I.D. mm tube and vi) 0.3 mm I.D. tube. Error bars represent the standard deviation of nanoparticle size distribution. Solutions of 0.54 mM $HAuCl_4$ and 1.7 mM citrate were mixed at 1/1 volumetric flowrate ratio.

3.3.4 Influence of temperature

The effect of temperature has on the gold nanoparticle size is dependent on a combination of different processes in the citrate reduction method. Firstly, the rate of gold ion reduction and formation of seed particles increases with increasing temperature, which leads to the formation of more nuclei. Secondly, increasing temperature promotes a shift of the gold precursor equilibrium to more hydroxylated species of $HAuCl_4$ which have lower reactivity, and thus lead to the formation of fewer nuclei.[31] These two opposite effects result in a non-monotonic trend of final particle size versus temperature depending on specific conditions. In the present study, gold nanoparticles were synthesized at temperatures of 70-100 °C in order to investigate the effect of temperature on this new synthesis approach. As shown in **Figure 3-7**, the size and size distribution decreased with increasing temperature. The largest particle size obtained was 3.0 ± 0.5 nm at 70 °C, which was still small compared with the typical particle size in the Turkevich method. This suggested that the enhanced nucleation rate by the tubing wall played a predominant role on particle size and the effect of the decreasing reactivity of hydroxylated gold precursor species was not affecting this synthesis. Furthermore, a higher temperature speeded up the reduction rate which also enhanced the nucleation rate. Thus, the larger amount of gold atoms available during the nucleation stage produced more seed particles and the total precursor was distributed to more particles, resulting in smaller and gold nanoparticles at higher temperature.

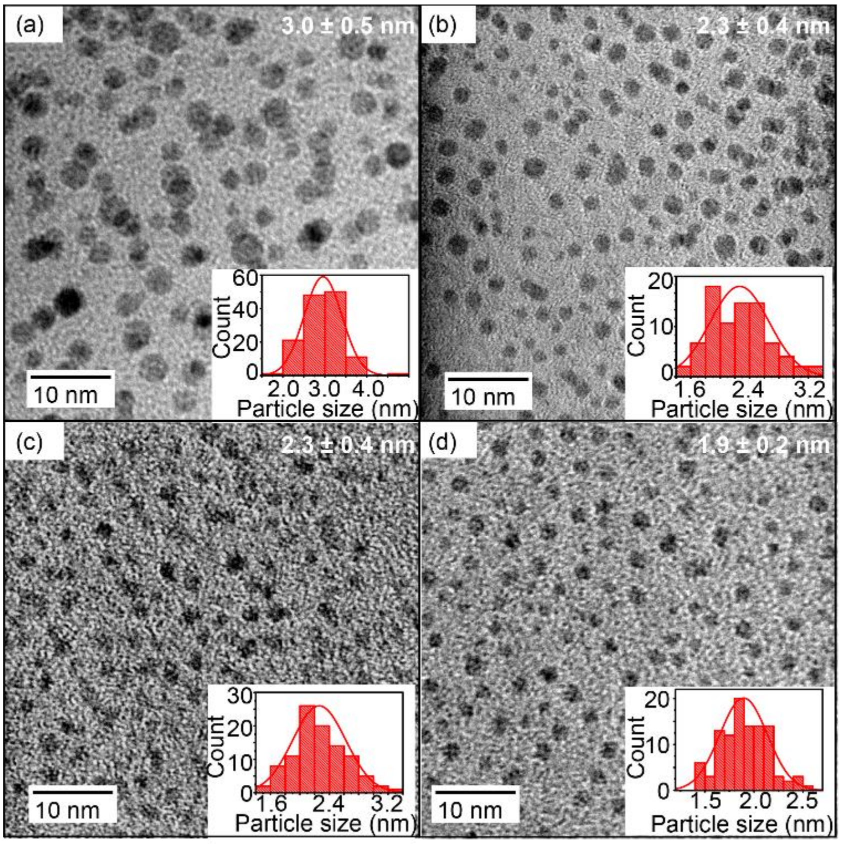

Figure 3-7 TEM images of the gold nanoparticles synthesized at different temperature. (a) 70 °C, with size of 3.0 ± 0.5 nm, (b) 80 °C, with size of 2.3 ± 0.4 nm, (c) 90 °C, with size of 2.3 ± 0.4 nm, (d) 100 °C, with size of 1.9 ± 0.2 nm. PTFE tubing with 0.3 mm I.D. was used with total flow rate of 0.006 ml/min (average residence time 30 min). Solutions of 0.54 mM $HAuCl_4$ and 1.7 mM citrate were mixed at 1/1 volumetric flowrate ratio.

3.3.5 Influence of tube material

Based on the hypothesis above, the synthesized negatively-charged particles should be repelled from the wall; however, fouling issues were still present. We hypothesised that fouling was influenced by tubing roughness. Since rough surfaces have increased surface area on which particle nucleation can occur, there might be an excessively high level of nucleation occurring simultaneously. Liu et al. suggested that coarser polymeric tubes could provide more sites for nucleation due to larger superficial area. They observed that silver nanoparticles were more prone to depositing on the surface of a coarser tube and the nanoparticles also had larger average size and wider size distribution.[203] The high concentration of nuclei can lead to the formation of larger particles by nuclei aggregation, which can foul prior to citrate stabilisation. The rough tube surface may also locally disrupt the near-wall flow potentially trapping particles, and increasing the probability of fouling on the wall. With longer operation time, fresh gold precursor passed over these particles causing them to grow and form a fouling layer. Changing the tubing material could also change the zeta potential and surface charge of the tubing wall, resulting in different nucleation rates. Three other tubing materials, FEP (0.25 mm I.D.), PEEK (0.25 mm I.D.), and fused silica (0.32 mm I.D.), were tested at the same experimental conditions as PTFE (residence time of 30 min, 100 ^{o}C at citrate/gold molar ratios of 3.15). The relative roughness of these four materials as determined by SEM[*] in **Figure A-2**) was found qualitatively to be PTFE>PEEK>FEP>fused silica, which is in accordance with the literature.[204]

Table 3-3 lists the zeta potential values[*] at pH~6.5 of the tested materials at room temperature, which are in good agreement with literature values. The pH dependent zeta potentials were shown in **Figure A-4**. All tested materials exhibited a negative zeta potential at process relevant pH values, and the most negative zeta potential was obtained for fused silica. Hydrophobic surfaces without functional groups, such as polymers, have negative surface potentials (at pH > 4, i.e. the typical isoelectric point for these surfaces) due to increased concentration of hydroxide ions rendering the surface charge negative. The zeta

---

[*] *The SEM image was taken by Yaomin Li, University College London*

[*] *The zeta potential measurement was carried out by Dr. Maximilian Besenhard, University College London, Thomas Luxbacher and Renate Kohl, Anton Paar, Austria*

potential of the fused silica tubing is comparatively lower, because of ionisation of surface silanol groups. Thus, the different characteristics of the tubing material result to different electrostatic attraction and therefore different nucleation rates. It is noteworthy that the zeta potential is expected to be more negative at higher temperatures.[205]

Table 3-3 Zeta potential values of tubing materials and comparison with literature values. Further details on the pH dependence are shown in **Figure A-4**.

Material	**Zeta potential at pH~6.5 from streaming potential**	**Zeta potential at pH~6.5 from literature**
PTFE	-25 mV	-24 mV[206]
PEEK	-20 mV	-22.5 mV[207]
FEP	-28 mV	-
Fused silica	-88 mV	-100 mV[208]

Figure 3-8 shows the average gold nanoparticle size obtained at different operation times with different tube materials (size obtained from TEM images (**Figure A-5**). As all the capillaries were negatively charged and nucleation rates were enhanced, they all produced ultrasmall gold nanoparticles of ~2-3 nm. The particle sizes did not change much with increasing operation time, which was in accordance with the conclusion obtained from **Figure 3-2**, i.e. that the fouling did not affect the particle size to a great extent, as was also observed by previous literature.[115] However, for the FEP tubing, there were some larger size particles (**FEP_2** in **Figure 3-8**) together with small size particles (**FEP_1** in

Figure 3-8). Compared to the PTFE tubing, the FEP tubing had a smoother surface, so it was postulated that when the particles on the tube wall grew to a large size, it was harder to be held on the surface of FEP tubing than PTFE tubing; hence some large particles came out with the flow. The yield of the gold nanoparticles (**Figure A-6**) obtained with all tubing materials decreased with longer operation time, as more Au(III) was consumed and fouling on the wall increased (the loss originated from fouling, as there was no gold detected by ICP in the supernatant after centrifugation). The highest yield of 29.1% obtained (FEP tubing with operation time of 6.5 h) could be attributed to the presence of large particles (**FEP_2** in **Figure 3-8**). This is the reason why yield sharply decreased as the size of large particles at different operation time decreased. The fused silica produced the smallest particle size with high yield (23.1%) although the inner tube diameter was not the smallest, possibly because its zeta potential was the most negative. Even though the surface of fused silica was also very smooth, the highly negative zeta potential guaranteed a fast nucleation and that less precursor was left for growth or fouling. During the first 23 h of operation time, there was no sharp decrease of the yield, indicating that the rate of fouling was slower than other tubing materials.

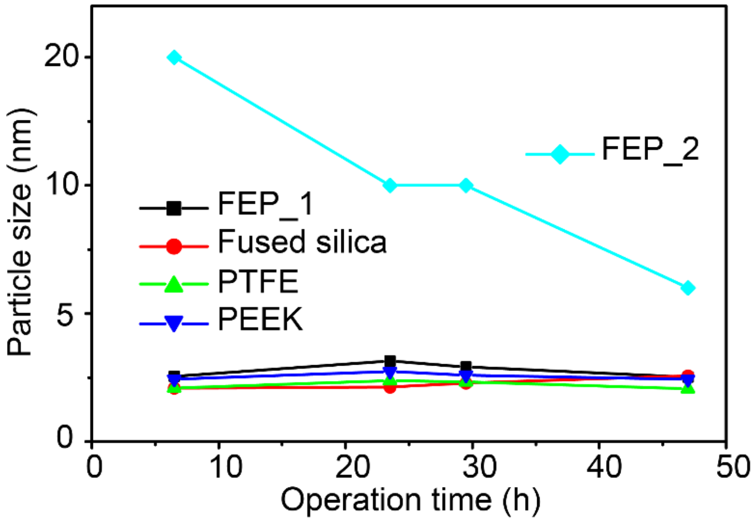

Figure 3-8 Size of gold nanoparticles synthesized at average residence time of 30 min and 100 °C using different tube materials (fluorinated ethylene propylene, FEP (0.25 mm I.D.), polytetrafluoroethylene, PTFE (0.3 mm I.D), polyether ether ketone, PEEK (0.25 mm I.D.) and fused silica (0.32 mm I.D.)). Samples were collected at different operation times. FEP_1 and FEP_2 correspond to different types of particles observed on the same TEM grid obtained from FEP tubing. Solutions of 0.54 mM $HAuCl_4$ and 1.7 mM citrate were mixed at 1/1 volumetric flow rate ratio.

3.3.6 SERS experiments with ultrasmall gold nanoparticles

Surface-enhanced Raman Scattering (SERS) is widely used in Analytical Chemistry for the detection of molecules with strong enhancement of Raman signals by absorbing the molecules onto metal surfaces (e.g. gold nanoparticles).[209-212] The enhancement of the signals is mainly caused by two effects: electromagnetic (EM) enhancement and a chemical contribution.[213] Compared with EM enhancement, the charge transfer-based chemical contribution provides a much smaller enhancement and the actual mechanism is still in dispute.[214-216] The electromagnetic enhancement utilizes the LSPR of nanostructures to form incident electric field which could drive the conduction electrons. Thus, the EM enhancement is strongly affected by the morphology of the noble-metal structures.[217] Additionally, the EM enhancement decays exponentially with the distance between the metal surface and analyte molecules.[210] As mentioned above, the citrate on electrostatically stabilized citrate-capped gold nanoparticles can be easily removed for further functionalization, resulting in closer and easier interaction between the metal surface and analyte molecules. Even though the gold nanoparticles used for SERS are usually in the size range of 20-100 nm,[218] the aggregation caused by mixing the analyte with 2 nm gold nanoparticles could increase the hotspot population on the substrate that give rise to SERS enhancement. A comparison of SERS performance[*] between our synthesized citrate-capped gold nanoparticles from fused silica tubing (corresponding to **Figure 3-8**) and commercial phosphate-capped gold nanoparticles with similar particle size (~2 nm) was carried out. The original Raman spectra of 5×10^{-6} M Rh6G solution without gold nanoparticles were shown as the red curve in **Figure 3-9**. For the concentration of 5×10^{-6} M, the “signature” bands of Rh6G are hard to see. **Figure 3-9** indicates that both 2 nm gold nanoparticle samples could enhance Raman bands of Rh6G, as most of the molecule bands were successfully observed. The average enhancement factors (AEF) based on three intensities at different vibrational shifts (611 cm^{-1}, 1359 cm^{-1} and 1509 cm^{-1}) for both gold nanoparticle samples were shown in **Table A-1**. The AEF of 2 nm gold nanoparticles capped by citrate from our work (AEF = 1.54×10^{8}) was nearly double when compared to the phosphate-capped commercial gold nanoparticles (AEF = 7.34×10^{7}). This was attributed to the fact that the adsorption of analyte molecules onto citrate-capped gold surface is easier due

---

[*] *The SERS experiments were performed by Dr. Sultan Ben-Jaber, University College London*

to the weaker binding strength of the carboxylate ligand. Additionally, during the drying process, gold nanoparticles capped with the weaker capping agent could form hotspots with narrower gaps between neighbouring particles, which gives rise to improved enhancement.[219]

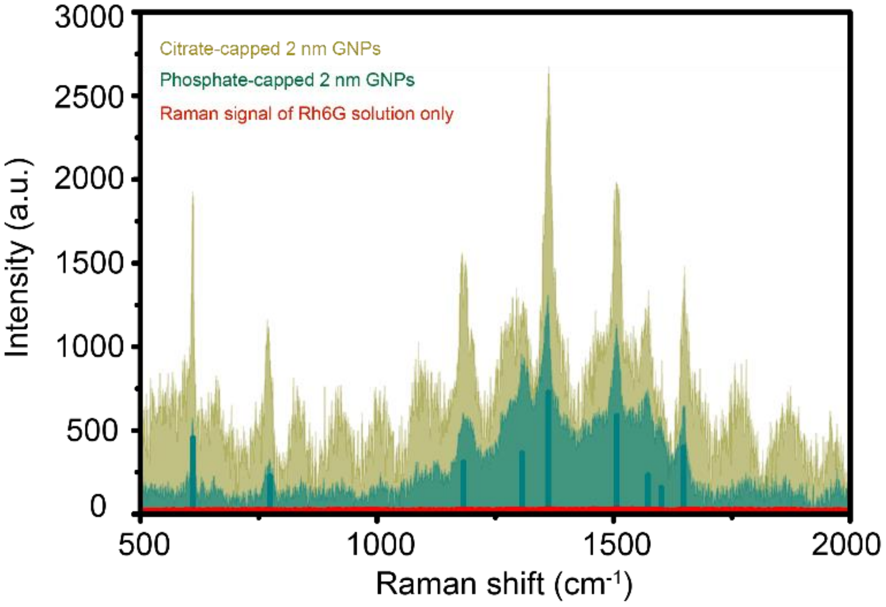

Figure 3-9 Raman signal of Rh6G solution (red colour) and SERS spectra of Rh6G-tagged gold nanoparticles from citrate-capped gold colloid (yellow colour) and phosphate-capped gold colloid (green colour) with similar size of 2 nm.

3.4 Conclusions

Sub-3 nm citrate-capped gold nanoparticles were synthesized in continuous flow capillary reactors by enhancing nucleation through interaction between reactants and the tubing wall. It is speculated that the negatively charged tubing-water interface, offers heterogeneous nucleation sites for positively charged citrate-gold precursor species, stabilizing the nuclei and inhibiting their growth. The change of the surface charge (from positive to negative) as gold ions form gold nanoparticles provides electrostatic repulsion to remove the synthesized gold nanoparticles from the tubing wall. With our continuous flow experimental conditions, the effect of temperature becomes less important in defining the final particle size, as compared to the classical batch Turkevich method. One of the disadvantages of our method is that fouling was observed and could not be avoided. Among four different tubing materials we tried, fused silica tubing showed the highest productivity because of its low zeta potential and smooth inner surface, which decreased fouling. The SERS performance of these citrate-capped gold nanoparticles was evaluated. A higher enhancement factor was observed compared to commercial phosphate-capped gold nanoparticles, because of more “hot spots” forming from weaker capping agent (citrate)-capped gold nanoparticles. This study provides a new point of view about using the feature of high surface-to-volume ratio in microfluidic systems in the synthesis of gold nanoparticles.

4. Synthesis of Monodisperse Gold Nanoparticles with Carbon Monoxide in Gas-Liquid Microfluidic Segmented Flow system

4.1 Introduction

Even though ultra-small Au NPs were successful produced in the last chapter via nucleation enhancement by tubing wall, the yield is not satisfactory due to inevitable fouling. Thus, stronger capping agent than citrate was taken to consideration. As the properties of gold nanoparticles are mainly decided by their size and morphology, and it is quite challenging to reproduce the same quality of the particles between different batches due to the uncontrollable operational parameters such as the location of addition and efficiency of mixing of the reactants in batch reactors. The situation becomes even more complex when the conventional batch systems are scaled up, because of the relatively low rates of heat and mass transfer achieved.

In typical batch processes, gold ions (Au^{3+} or Au^{+}) in solution are reduced by either a strong reducing agent (e.g. $NaBH_4$)[220] to form gold nanoparticles under 5 nm in diameter, or mild reducing agent (e.g. tri-sodium citrate)[170] to form larger gold nanoparticles with sizes ranging between 10 and 40 nm in diameter[221] following a seeded growth synthesis. In order to produce even larger gold nanoparticles (with diameters of between tens and hundreds of nanometres), seeded growth methods are widely employed. In these instances small gold nanoparticles (or seeds) were synthesised using citrate or $NaBH_4$ reduction which were then subsequently grown to much larger sizes by the gradual addition of growth solution (containing additional gold precursor, reducing agent, capping agent and sometimes some additives like silver nitrate).[136, 222-224] Once formed, gold nanoparticles generally require stabilisation to prevent the aggregation of particles. This is achieved in many different ways generally using surfactants which bind temporally of permanently to the gold nanoparticles' surfaces and provide steric or electrostatic repulsion.[29] In general, the formation of gold nanoparticles is divided into two stages: nucleation and growth.[28] A key element which has been identified in order to obtain monodisperse particles is the separation between nucleation and growth processes. This separation can be obtained by the transition between gold species with different reactivity to terminate nucleation and allow preferential autocatalysis on the existing gold surface for further growth.[31]

In this context, microfluidic reactor systems are of interest since the reaction time could be precisely controlled by the residence time inside the microfluidic channel. Thus, it is much easier to terminate the reaction at different stages of nucleation and growth. Since Wagner *et al.* first proposed the use of microfluidic reactors to fabricate gold nanoparticles,[225] their use has been widely investigated due to the possibility for the precise control of operational parameters, enhanced mass/heat transfer,[176] large surface-to-volume ratio,[50] high efficiency of mixing,[226] potential ease for scale up or scale out[177] and compatibility with in-situ characterization techniques.[227] Additionally, the high efficiency of mixing helps to eliminate uneven reduction rate caused by concentration gradients, and thus leads to monodisperse particles and reproducible synthesis.

A detailed study into gold nanoparticle synthesis by reduction with gaseous carbon monoxide (CO) in a batch system has been presented by Young *et al.*.[228] The CO was introduced via a gas diffuser with 60 µm pore size from the bottom of an amber bottle (200 ml) into the aqueous $HAuCl_4$ solution at different flow rates with solubility of ~ 1 mM in water at atmospheric pressure and room temperature.[229] Compared with typical gold nanoparticle synthesis routes, which rely on non-gas reducing agents, reduction by CO has various advantages such as no reducing agent is left in the product following synthesis, easier control of experimental conditions (at room temperature) and shorter residence times (3-5 min) compared to typical Turkevich method (around 30 min)[230]. Guo synthesized Au NPs with size of 1.7-12.8 nm via carbonylation with CO and H_2O in 1-Butyl-3-methylimidazolium tetrafluoroborate ($BFImBF_4$) ionic liquid.[231] Their work showed that CO could play the role of ligand during gold complex formation, as well as reducing agent for Au NPs synthesis. Even though H_2 is a similar gaseous reducing agent like CO (redox potential of CO = -0.101 V,[228] redox potential of H_2 = 0 V at pH=0, at 25 °C and pressure of 1 atm),[232] no Au NPs formed with H_2 as it is non-coordinating agent. Kang *et al.* made use of CO to produce oleylamine-capped gold nanowires (Au NWs) at 60 °C which decreased the synthetic time from hours or even days to less than 10 min.[233] Pretzer *et al.* bubbled CO at an average flow rate of 3.3 ml/s for 30 s to grow controllably 2.8 nm Au seed to 12 nm.[234] The authors proposed that the reaction proceeded through electron transfer from the oxidation of CO catalysed by gold nanoparticles to the gold ionic species (the reduction equation could be written as: $2[AuCl_{4-x}(OH)_x]^- + 3CO + 3H_2O \rightarrow 2Au^0 + 3CO_2 + 6H^+ + 2xOH^- + 2(4-x)Cl^-$). The mixing between CO and aqueous $HAuCl_4$ solution employed in their batch system, where small bubbles of gaseous reducing agent were formed and dispersed throughout the water, could lead to coalescence of the CO bubbles. The changing bubble size resulting from coalescence led to decreasing surface-to-volume ratio, which can influence reduction rates at different locations in the batch reactor. Taifur-Rahman *et al.* utilized CO in a membrane-based droplet microfluidic system to produce 10 nm Au NPs, as well as grow Au shells on silica nanoparticles with pre-attached gold nanoparticle seeds.[164] The residence time was controlled by the gas-liquid contact time and was much larger than the calculated mixing time, enabling controlled dosing of CO into each droplet.

In this chapter, we present a facile method to produce gold nanoparticles in a microreactor at room temperature via CO reduction. As this reaction employs two phases, using multiple phases in a microfluidic reactor with a larger surface-to-volume ratio is expected to provide repeatable flow regimes and enhanced mass transfer between gas and liquid.[155] Additionally, the combination of plug-like flow and CFI should improve mixing and narrow the residence time distribution.[235]

4.2 Experimental

4.2.1Experimental set-up and general synthetic procedure

All the chemicals used in this chapter were purchased from Sigma-Aldrich and used without any further treatment or purification. The experimental set-up with a schematic of coiled flow inverter (CFI) reactor is shown in **Figure 4-1**. A CFI made of fluorinated ethylene propylene (FEP) tubing, 1 mm internal diameter, 2 mm outside diameter, 3.6 m length (VICI Jour) was utilized. There were 100 coils in total formed on a PTFE support plate and the coil diameter was 1 cm. A

90^o bend was utilized for every 5 coils to induce multiple flow inversion for narrower the residence time distribution.[236] An aqueous $HAuCl_4$ solution was mixed with CO gas (99.5%, BOC gases) through a Tefzel T junction (0.5 mm I.D., P632, IDEX), which then formed segmented flow inside the CFI at atmospheric pressure. The liquid flow rate was fixed at 0.5 ml/min using a syringe pump (Legato 270P, KD Scientific; 25 ml glass syringe, Mod 1025 Syr 25ML Tll Terminus, Biochrom Ltd.) and different liquid to gas flow ratios (2 to 20) were achieved by tuning the gas flow rate in the range of 0.025 to 0.25 ml/min with a mass flow controller (EL Flow, Bronkhorst). The residence time was adjusted to 3-5 min by altering only the gas flow rate. It was measured based on the time for one slug to pass through the whole CFI. Other operation parameters are shown in **Table 4-1** and **Table 4-2.**

The molar flow ratio was obtained below by Eq. (2):

$$\frac{CO}{Au}\ molar\ ratio = C_{co}Q_G/C_{Au}Q_L \qquad \text{Eq. (2)}$$

where C_{co} is the concentration of CO in gas phase (40.7 mM) at atmospheric pressure, C_{Au} is the initial concentration of gold precursor (0.27 mM), Q_G is gas volumetric flow rate and Q_L is liquid volumetric flow rate.

The ratio of CO amount input to the system CO to amount needed to complete the reduction was obtained below by Eq. (3):

$$\frac{CO_{input}}{CO_{needed}} = 2C_{co}Q_G/3C_{Au}Q_L \qquad \text{Eq. (3)}$$

Where CO_{input} is the CO amount input to the system per minute, CO_{needed} is the CO amount needed to complete the reduction per minute, the stoichiometry of CO/Au during CO reduction is 2/3.

Table 4-1 Operation parameters at different gas/liquid volumetric flow ratios. Liquid volumetric flow rate Q_L (0.5 ml/min) and superficial velocity (0.011 m/s) was constant, reactor length is 3.6 m.

L/G volumetric flow ratio	Gas volumetric flow rate Q_G (ml/min) $*10^2$	Gas superficial velocity (m/s)$*10^3$	Residence time (min)
20	2.5	0.5	5.0
10	5.0	1.1	4.3
5	10.0	2.1	4.2
2	25.0	5.3	3.4

Table 4-2 Operation parameters at different gas/liquid volumetric flow ratios. The liquid molar flow rates are 1.5×10^{-5} mM/min (0.030 mM), 13.5×10^{-5} mM/min (0.27 mM) and 2.7×10^{-4} mM/min (0.54 mM).

		Initial concentration of gold precursor (mM)											
		0.030				**0.27**				**0.54**			
L/G volumetric flow ratio	**Gas molar flow rate (mM/min) $*10^3$**	**CO/Au^{3+} molar ratio**	$\frac{CO_{input}}{CO_{needed}}$	CO_{needed} **(mM/min) $*10^6$**	**Particle size (nm)**	**CO/Au^{3+} molar ratio**	$\frac{CO_{input}}{CO_{needed}}$	CO_{needed} **(mM/min) $*10^3$**	**Particle size (nm)**	**CO/Au^{3+} molar ratio**	$\frac{CO_{input}}{CO_{needed}}$	CO_{needed} **(mM/min) $*10^3$**	**Particle size (nm)**
20	1.0	67.8	45.2	22.1	8.2 ± 1.6 (19.5%)	7.5	5.0	0.2	7.9 ± 0.4 (4.5%)	3.8	2.5	0.4	14.8 ± 4.6 (31.1%)

10	2.0	135.7	90.4	22.1	5.6 ± 0.7 (12.5%)	15.1	10.0	0.2	7.7 ± 0.3 (4.1%)	7.5	0.7	2.9	8.9 ± 1.1 (12.4%)
5	4.1	271.3	180.9	22.7	5.6 ± 0.9 (16.1%)	30.1	5.0	0.8	7.5 ± 0.7 (9.9%)	15.1	0.4	10.3	15.1 ± 3.7 (24.5%)
2	10.2	678.3	452.2	22.6	3.1 ± 0.6 (19.3%)	75.4	2.0	5.1	9.3 ± 1.0 (10.4%)	37.7	0.1	102.0	26.6 ± 13.4 (50.4%)

4.2.2 Analysis

The solution pH was measured by pH meter (SevenCompact^{TM} pH/Ion S220). UV-vis absorption spectra of gold nanoparticles were recorded immediately after collection from the reactor using an Ocean Optics UV-Vis spectrometer (USB 2000+ Spectrometer and DT-Mini-2-GS light source). The resulting gold nanoparticle size was measured by Differential Centrifugal Sedimentation (DCS) (CPS 24000 Disc Centrifuge, CPS Instruments; the total number of particles counted was in the order of 10^{11}. Transmission electron microscopy (TEM) (Jeol 2010) at 200 kV was used to give both qualitative and quantitative analysis of particle size and polydispersity (defined as standard deviation over the average particle size). Zeta potential measurement was performed with a data acquisition time of 10 s with a Dynamic Light Scattering apparatus (DLS) (DelsaMax-Pro, Beckman Coulter) using the supplied flow cell system in batch mode at 22°C. For the synthesis at different initial pH, the precursor was mixed with K_2CO_3 one day in advance to ensure the gold species achieved equilibrium. The sample was monitored by UV-Vis and found to be stable without any capping agents for 1 week at room temperature and 1 month when kept at 4 ^{o}C in fridge. ATR-FTIR spectroscopy was performed using a Perkin-Elmer 1605 FT-IR spectrometer with a resolution of 0.5 cm^{-1} and wavenumber range 0-5000 cm^{-1}. Raman spectra were obtained with a Renishaw Raman inVia microscope with a 633 nm He–Ne excitation laser (1.9 eV, 0.7 mW, pore size ~ 4.4 μm^2). A Rhodamine 6G (Rh6G) solution with concentration 4×10^{-6} M was obtained by mixing with gold nanoparticle solutions at a volume ratio of 2:3 and then stirred for 20 min to allow enough time for the Rh6G molecules to bind onto the gold surface. The mixed solutions were dropped onto glass substrates and dried at ambient conditions to create SERS hotspots. The commercial citrate-capped gold nanoparticles were from BBI.

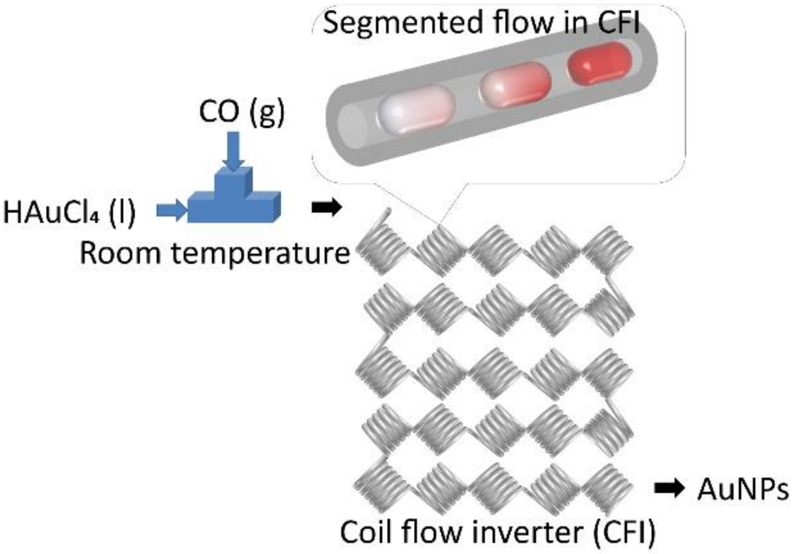

Figure 4-1 Schematic illustration of microfluidic segmented flow system.

In our system, as these CO-produced gold nanoparticles are positively charged, adding tri-sodium citrate after reaction leads to immediate aggregation. Thus, the citrate solution (0.54 mM) was premixed with $HAuCl_4$ solution (0.54 mM) via a micromixer chip (Dolomite, Part No. 3000144) before mixing with CO via T junction (P-632, IDEX Health & Science LLC) at room temperature. The residence time was 3.4 min with the volumetric flow rate of CO, citrate and gold precursor 0.25 ml/min, 0.25 ml/min and 0.25 ml/min respectively. 0.27 mM polysorbate 80 (TWEEN 80) was mixed with gold precursor (0.54 mM) with the same flow rate of 0.25 ml/min via micromixer chip before forming segmented flow with CO (0.1 ml/min) in CFI. For oleylamine-capped Au NPs, the final concentration of 0.27 mM tetrachloroauric acid was obtained by dissolving solid gold(III) chloride trihydrate into a pure octane solution containing 0.54 mM oleylamine. This gold solution was reduced by CO (0.1 ml/min) in the microfluidic segmented system at 100 °C, placed in a stirred glycerol (99.5 %, VWR) bath on a hot plate (Stuart, UC152D with SCT temperature controller) with residence time of 4.2 min and gas to liquid flow ratio of 5. The synthesized gold nanoparticles were precipitated by acetone and then centrifuged at 6000 rpm (Heraeus Multifuge X1R, ThermoFisher) for 30 min. The precipitated Au NPs was re-dispersed in toluene for TEM sample preparation. For the synthesis of gold nanoparticle capped by Thiol-PEG-COOH, firstly 0.3% w/w poly(sodium 4-styrenesulfonate) (PSS) was premixed with 0.27 mM gold precursor to stabilize Au NPs temporarily via micromixer chip with the same flow rate of 0.125 ml/min and then reacted with CO (0.1 ml/min) in CFI with residence time of 7.5 min. Then 5 ml Thiol-PEG-COOH solution (100 µg/ml) was added to 5 ml product with stirring overnight at room temperature to substrate the PSS.

4.3 Results and discussion

4.3.1 Influence of gas/liquid volumetric flow ratio

An aqueous $HAuCl_4$ solution was merged with pure CO gas through a T junction, which then formed segmented flow (CO solubility of ~ 1 mM in water)[229] inside the CFI at atmospheric pressure. Under this condition, the concentration of CO in the gas phase was estimated to be 40.7 mM, which was at least 2.5 times higher than the CO needed to reduce the gold precursor in this paper (calculated based on 0.54 mM initial concentration of gold precursor at the highest liquid to gas flow ratio of 20, the lowest CO/Au^{3+} molar flow ratio = 3.8 in **Table 4-2**). Thus, the gaseous CO acted as a reservoir to continuously dose the liquid slugs throughout the whole reduction process. **Figure 4-2** shows the characterization results of the product from a 0.27 mM $HAuCl_4$ solution at different gas to liquid flow ratios at room temperature (maintained between 20-22 ^{o}C). The residence time was between 3.4 to 5 min based on the time measured for one slug to pass through the whole CFI. UV-Vis spectra do not give much information as synthesized Au NPs have similar particle size. With the assistance of CO, nonspherical particles were observed from TEM images in **Figure 4-2** which is consistent with previous literature,[228, 237] rather than spherical shape from citrate reduction. The particle sizes and size distribution obtained from TEM and DCS were concluded in **Table 4-3**. The particle size from TEM and DCS shows good agreement. The polydispersity (defined as the standard deviation over the average particle size) from TEM were higher than DCS result. This is because for TEM analysis, we only counted 100-300 particles, whereas we injected 0.1 ml solution (total particle number of 10^{11} order-of-magnitude) into DCS. Thus, further discussion about polydispersity is based on the result from DCS.

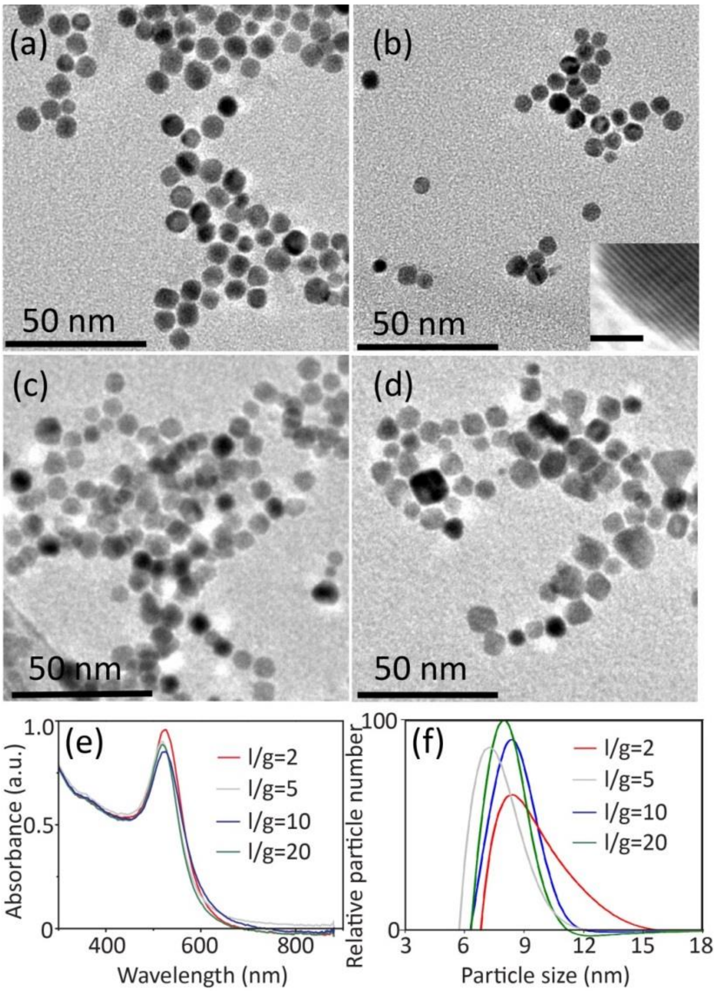

Figure 4-2 TEM images of synthesized gold nanoparticles at liquid to gas volumetric flow ratios of a) 20 (residence time 5 min), b) 10 (residence time 4.4 min), c) 5 (residence time 4.2 min) and d) 2 (residence time 3.4 min) with 0.27 mM initial concentration of $HAuCl_4$ at room temperature in microfluidic segmented flow system. Insert in b) is the lattice plane spacing of gold nanoparticle which indicates Au [111] surface with scale bar of 1 nm. UV-Vis spectra of synthesized Au NPs and the particle size and size distribution obtained from DCS (normalised by area under each curve) are shown in e) and f) respectively.

Table 4-3 Particle size and size distribution obtained from TEM (around 100 particles counted) and DCS (particle number of 10^{11} order-of-magnitude).

L/G ratio	Size from TEM (nm)	Size from DCS (nm)
20	7.9 ± 0.6 (7.9%)	7.9 ± 0.4 (4.5%)
10	7.9 ± 0.7 (8.9%)	7.7 ± 0.3 (4.1%)
5	7.5 ± 0.9 (11.6%)	7.5 ± 0.7 (9.9%)
2	9.4 ± 1.3 (14.2%)	9.3 ± 1.0 (10.4%)

As shown in DCS, the polydispersity is reduced below 5% which is smaller than the CO-produced Au NPs in batch by Young *et al.* with similar initial concentration of gold precursor (0.3 mM, standard deviation of 11%), most likely due to the good mixing provided by the use of segmentation[155] and CFI.[235] With decreasing liquid/gas flow ratio from 20 to 5, the final particle size didn't change much. It is speculated that enough CO amount (at least 5 times higher amount of input CO compared to the CO amount needed for reduction) made the reaction was not sensitive to the changes of CO amount. However, at the lowest liquid/gas flow ratio of 2 ($CO_{input}/CO_{needed} = 2$), the mean particle size and standard deviation increased. This could be because there are two growth mechanisms during the CO reduction as proposed by Young *et al.* and shown in **Figure 4-3**.[228] The first mechanism is the formation of nuclei followed by further growth from autocatalysis on the surface. If there is a sufficiently high concentration of nuclei, the rest of the $HAuCl_4$ will be preferentially reduced on the surface of the nuclei resulting in growth, and thus nucleation stops. This leads to a separation between nucleation and growth processes and thus this mechanism would result in monodisperse gold nanoparticles. The second growth mechanism occurs when the nuclei concentration is high and the nuclei start to coalesce, resulting in polydisperse Au NPs with larger size.

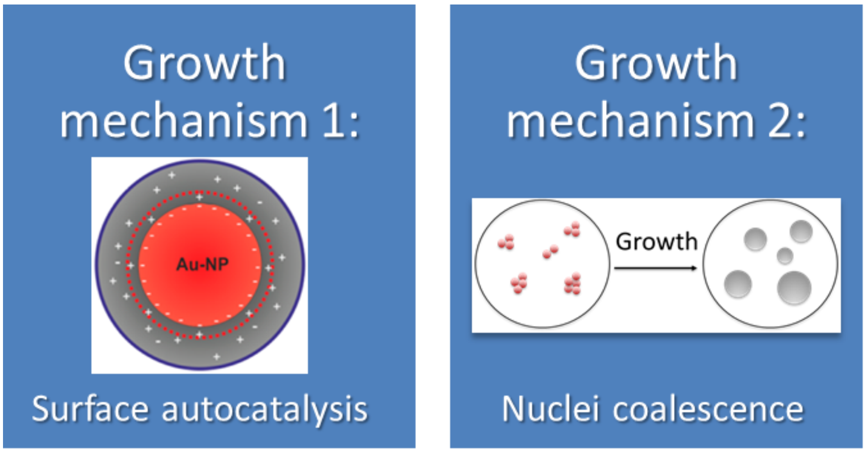

Figure 4-3 Two growth mechanisms during the CO reduction as proposed by Young *et al.*:[228] Growth mechanism 1 is the formation of nuclei followed by further growth from autocatalysis on the surface; Growth mechanism 2 is the nuclei coalescence to grow to polydisperse Au NPs with larger size.(scheme in Growth mechanism 1 reprinted with permission from ref.[52] Copyright 2012, American Chemical Society).

For the liquid to gas volumetric flowrate ratios in the range of 20 to 2, the flow pattern remained as segmented flow, but with different liquid slug lengths (**Figure 4-4**). From these, average lengths of gas bubbles and liquid slugs were estimated in **Table 4-4**. In slug flow, the gas is in the form of elongated bubbles with nearly identical diameter as the tube, also known as Taylor bubbles.[238] Gas-liquid mass transfer coefficients were calculated using properties of CO and water and the set flow rates (0.5 ml/min of liquid and different liquid to gas flow ratios of 2 to 20).

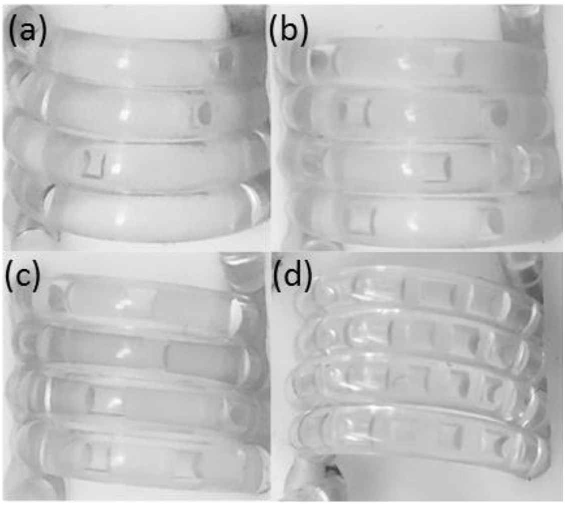

Figure 4-4 Flow pattern in the coiled flow inverter (CFI) at the liquid to gas flow ratios of (a) 20, (b) 10, (c) 5 and (d) 2 with 0.27 mM initial concentration of $HAuCl_4$ at room temperature in microfluidic segmented flow system.

Table 4-4 Length of gas bubble and liquid slug at different liquid to gas flow ratios.

Liquid to gas flow ratio	Liquid slug length (mm)	Gas bubble length (mm)
20	5.46	0.61
10	4.91	0.98
5	2.31	1.16
2	0.94	1.17

The mass transfer occurred through two parts: from the hemispherical cap to the surrounding liquid and from the film surrounding the bubble.[239] The cap mass transfer coefficient was calculated via Eq. (4) below:

$$k_{L,cap} = 2\sqrt{2\frac{D_{CO}V_b}{\pi^2 d_c}} \qquad \text{Eq. (4)}$$

Where D_{CO} = 2×10^{-9} m^2/s[229] is the liquid phase diffusivity of CO, V_b is the Taylor bubble velocity (calculated based on residence time and the length of the CFI) and d_c is the capillary diameter.

The volumetric mass transfer coeffieicent, $k_{L,cap}a_{cap}$ was obtained by multiplying Eq. (4) with the specific interfacial area for the two hemispherical caps:

$$a_{cap} = \frac{4}{L_{UC}} \qquad \text{Eq. (5)}$$

Where the L_{UC} is the unit cell length (one gas bubble length+liquid slug length).

For calculating the film mass transfer coefficient, the equation depends on the Fourier number (*Fo*):[240]

$$Fo = \frac{D_{CO}t}{\delta_{film}^2} \qquad \text{Eq. (6)}$$

Where *t* is the contact time between liquid and bubble (defined as liquid film length/liquid velocity)[240] and δ_{film} could be calculated by Eq. (7)[241] when $7\times10^{-6} \leqslant \mathrm{Ca} \leqslant 2\times10^{-4}$:

$$\frac{\delta_{film}}{d_c} = (0.89 - \frac{0.05}{u_g^{1/2}})Ca^{1/2}\text{ ; } Ca = \frac{\mu_L V_b}{\sigma} \qquad \text{Eq. (7)}$$

Where u_g is the superficial gas velocity, *Ca* is Capillary number, μ_L is liquid viscosity, σ is the surface tension. The results for *Fo* are shown in **Table 4-5**.

Table 4-5 Fourier number at different liquid to gas flow ratios.

Liquid to gas flow ratio	**Capillary number $\times 10^4$**	**Film thickness $\times 10^6$ (m)**	**Contact time (s)**	**Fourier number**
20	1.48	8.20	0.06	1.70
10	1.71	9.64	0.09	1.99
5	1.77	10.4	0.11	2.02
2	2.20	12.2	0.11	1.49

Since all the *Fo*>1, the volumetric mass transfer coefficient for the film $k_{L,film}a_{film}$ could be obtained by Eq. (8)[239]:

$$k_{L,film} = 3.41\frac{D_{CO}}{\delta_{film}}; \; a_{film} = 4\frac{L_{film}}{d_c}\frac{1}{L_{UC}} \qquad \text{Eq. (8)}$$

Where L_{film} is the liquid film length (here estimated as bubble length). Based on Eq. (1), (2), (5), the volumetric mass transfer for both cap and film and the total volumetric mass transfer (defined as the summation of cap and film volumetric mass transfer)[239] were calculated and are summarized in **Table 4-6**:

Table 4-6 Calculated volumetric mass transfer coefficients.

Liquid to gas flow ratio	**$k_{L,cap}$ x 10^4 (m/s)**	**a_{cap} (m^2/m^3)**	**$k_{L,cap}a_{cap}$ (s^{-1})**	**$k_{L,film}$ x 10^4 (m/s)**	**a_{film} (m^2/m^3)**	**$k_{L,film}a_{film}$ (s^{-1})**	**Total K_La (s^{-1})**
20	1.40	659	0.092	8.32	400	0.33	0.42
10	1.50	678	0.10	7.08	666	0.47	0.57
5	1.52	1153	0.18	6.57	1333	0.88	1.05
2	1.70	1892	0.32	5.59	2217	1.24	1.56

We next consider a simplified mass transfer model, where mass transfer takes place between the gas-liquid interface (which is at equilibrium with the gas) and the liquid phase (where we assume instantaneous mixing and reaction of CO). Rate of amount of CO transferred into the liquid phase (N_{CO}/t) could be obtained by Eq. (9):

$$N_{CO}/t = kaV_L(C_s\text{-}0) \qquad \text{Eq. (9)}$$

Where V_L is the liquid volume. The upper limit of the CO concentration is dependent on solubility of CO in water. Then the dosing time (t_{dos}) of CO into each liquid slug (where the majority of liquid exists) or film surrounding the bubble to obtain the required amount of CO for reducing the gold precursor could then be calculated via Eq. (10)[229] and shown in **Table 4-7**:

$$t_{dos,slug} = \frac{N_{co,slug}}{k_L a C_s V_{slug}}\,;\; t_{dos,film} = \frac{N_{co,film}}{k_L a C_s V_{film}} \qquad \text{Eq. (10)}$$

Where N_{co} is the number of moles of CO needed for 0.27 mM gold precursor reduction in different liquid volumes at different flow patterns, C_s ~ 1 mM is the solubility of CO in water,[229] V_{slug} and V_{film} is the volume of liquid slug and liquid film shell surrounding the gas bubble, respectively.

Table 4-7 Dosing time (t_{dos}) of CO into each slug or film surrounding the bubble to obtain the moles needed for reducing 0.27 mM gold precursor in different volumes of slugs.

Liquid to gas flow ratio	**Residence time (min)**	**V_{slug} (mm^3)**	**$N_{co,slug}$ $\times 10^9$ (mole)**	**$t_{dos,slug}$ (s)**	**V_{film} (mm^3)**	**$N_{co,film}$ $\times 10^{11}$ (mole)**	**$t_{dos,film}$ (s)**
20	5.0	4.28	1.74	4.72	0.015	0.63	1.30
10	4.3	3.86	1.56	4.27	0.029	1.19	0.92
5	4.2	1.82	0.74	2.47	0.037	1.51	0.50
2	3.4	0.74	0.30	1.35	0.044	1.79	0.35

The above calculations are estimations based on straight tube; the secondary flow profile (Dean vortices) induced by centrifugal force and inversions with 90° bends[236] in CFI were not taken into account. The Dean number (N_{De}) for the liquid phase could be calculated by Eq (11) below:

$$N_{De} = N_{\mathrm{Re}} / \sqrt{\lambda}\ ;\ N_{\mathrm{Re}} = d_c u \rho / \mu\ ;\ \lambda = D_{coil} / d_c \qquad \text{Eq. (11)}$$

Where N_{Re} is Reynolds number, u is the superficial liquid velocity, ρ is the liquid density, μ is the liquid viscosity, λ is the curvature ratio and D_{coil} is coil diameter.

Based on the calculation, the Dean number of the liquid phase was 3.76, which is large enough to reduce axial dispersion by inducing chaotic mixing at the bends.[242] Thus, we expect the mass transfer in our reactor to be better than the mass transfer estimation due to the radial convective transfer intensification by the CFI.[243] In conclusion, the estimation demonstrated the enhanced mass transfer with decreasing liquid to gas flow ratio at constant liquid flowrate.

As shown above, increasing the gas flow rate with constant liquid flow rate led to more frequent and shorter liquid slugs with larger interfacial area-to-volume ratio, which enhanced the mass transfer between gas and liquid phase. The volumetric mass transfer (k_La) increased, as the liquid to gas flowrate ratio decreased from 20 to 2, leading to faster dosing of CO into liquid phase. Even though the dosing times were much shorter than residence times (3-5 min), the faster mass transfer in early stage still affected the nucleation rates, resulting in different final particle sizes (**Figure 4-5**). When the amount of formed nuclei was under the aggregation level (e.g., in the range of liquid to gas flow ratio 5-20 at 0.27 mM initial concentration of gold precursor) the particle size decreased with lower liquid to gas flow ratio (from 7.9 nm to 7.5 nm), likely because more nuclei were formed with faster mass transfer of CO. Less unconsumed gold ions were left and were distributed to the nuclei for growth, leading to decreasing NP size. As no capping agents were used in our system, the stability of nuclei in solution is expected to be limited. When the CO transferred faster into the liquid phase at the liquid to gas flow ratio of 2, the amount of nuclei increased (and this amount was larger for larger initial gold concentration) and overcame the aggregation barrier, leading to random, uncontrollable aggregation which resulted not only to larger particles, but also broader final size distribution.

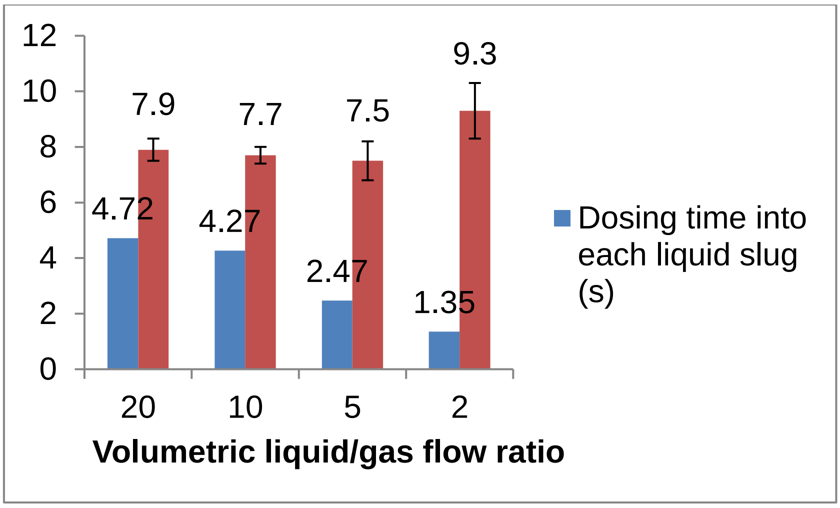

Figure 4-5 The relationship between particle sizes obtained from DCS and dosing time of CO into each liquid slug to obtain the moles needed for reducing 0.27 mM initial concentration of gold precursor in different volumes of slugs at varied liquid/gas flow ratio.

4.3.2 Influence of initial concentration of gold precursor

The effect of initial concentration of $HAuCl_4$ on particle size and size distribution was studied next. The results are shown in

Figure 4-6. As DCS uses higher sample volume (total particle number of 10^{11} order-of-magnitude counted by the DCS instrument compared to hundreds of particles observed in TEM), most of the particle size and size distribution measurements were based on DCS for higher accuracy. However, since DCS is limited to gold nanoparticles above 3 nm,[106] the particle size at 0.030 mM concentration of gold precursor was provided based on TEM (see **Figure B-1**). When the initial concentration of $HAuCl_4$ was extremely low (0.030 mM), even for the highest presumed nucleation rate at a liquid to gas ratio of 2, the nuclei could still be stable in the solution. It is possible that only the first growth mechanism exists during synthesis which is beneficial for the formation of monodisperse particles. The particle size decreased with a decreasing liquid to gas flow ratio. For the $HAuCl_4$ solution of 0.27 mM, there was a minimum in particle size with respect to gas-liquid ratio suggesting a transition from the first mechanism (autocatalysis on surface) to the second mechanism (coalescence of nuclei) when the liquid to gas flow ratio decreased to 2. The second mechanism was more dominant at high initial $HAuCl_4$ concentration.[228] That is why there was an increasing particle size and polydispersity for 0.27 mM $HAuCl_4$ at the lowest liquid to gas flow ratio of 2, whereas for 0.54 mM, the particle size started to increase at the ratio of 5. The experiment showing the smallest particle size at liquid to gas flow ratio of 10 with (8.9 ± 1.1 nm, 12.4%) was repeated (8.6 ± 1.4 nm, 16.5%) to check reproducibility. When the second mechanism was dominant, the particle size was uncontrollable and polydispersity of particle size started to increase (e.g. 26.6 ± 14.4 nm, 50.6% at 0.54 mM $HAuCl_4$ and gas to liquid flow ratio of 2).

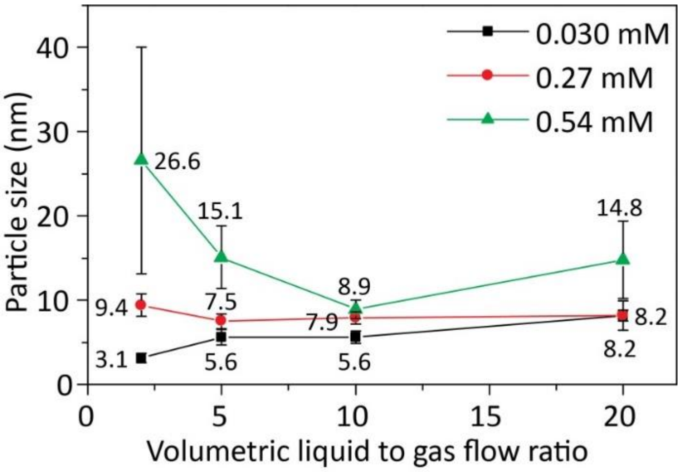

Figure 4-6 Particle size and size distribution concluded from TEM and DCS (Figure B-1 and Figure B-2) at different concentration of $HAuCl_4$ and liquid to gas flow ratios as indicated at room temperature in the residence time range between 3 to 5 min (details see Table 4-2).

4.3.3 Influence of initial pH of the gold precursor

In order to obtain more monodisperse particles, the nucleation stage should be controlled carefully. If the concentration of nuclei increases sharply over short period, the final particle will be highly polydisperse because of nuclei aggregation. However, if the reduction rate is low, the seed-mediated growth mechanism is less dominant and there is no separation between nucleation and growth in a similar fashion as synthesis at high pH of gold precursor in the Turkevich method.[31] The formation of nuclei and growth occurs in parallel, which also leads to polydisperse nanoparticles. It is known that the reactivity of $HAuCl_4$ species decreases with the equilibrium of species shifting to $[AuCl_x(OH)_{4-x}]^-$ with increasing pH.[36] It has also been shown that during CO reduction, the more hydroxyls the Au (III) complex contains, the less reactive it is.[228] Thus, the reduction rate could be controlled by tuning the initial pH of $HAuCl_4$. As the zeta potential of the gold nanoparticles obtained before pH tuning without stabilising surfactants was +12 mV, the pH range was limited up to 7 to avoid destroying the charge stability in the solution (the colour of the solution with higher pH changed from red to purple, indicating agglomerates). **Figure 4-7** shows the characterization of gold nanoparticles synthesized at different initial pH of $HAuCl_4$ tuned by the addition of K_2CO_3. The particle size analysis based on TEM and DCS is shown in **Table 4-8,** which shows reasonable similarities. As mentioned above, the discussion about the particle size and size distribution were on the basis of DCS results. The average particle size at pH = 4 (9.8 nm) was slightly larger than the Au NPs obtained from pH = 3 (9.3 nm) (the difference was statistically significant with P value <0.0001 by unpaired t-test, due to the high total particle number of 10^{11} order-of-magnitude counted from DCS result), as the nucleation rate at pH = 3 was faster due to the higher amount of highly reactive gold species $[AuCl_4]^-$ compared to the dominant species of $[AuCl_3(OH)]^-$ at pH = 4.[244] When the initial pH > 4.0, the nucleation rate decreased and provided enough nuclei surface for autocatalysis, resulting in parallel processes of nucleation and growth and thus in increased polydispersity (14.6% at pH = 5.1 and 20.7% at pH=6.7).

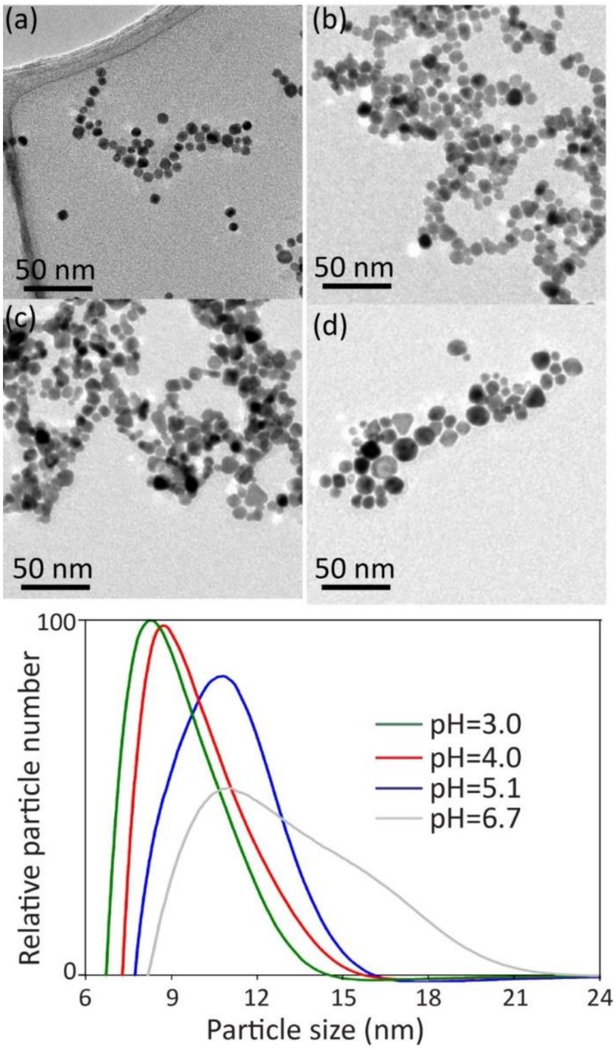

Figure 4-7 Characterization of synthesized gold nanoparticles at different initial pH (a) 3.2, (b) 4.0, (c) 5.1 and (d) 6.7 and inlet contained 0.27 mM $HAuCl_4$ at liquid to gas flow ratio of 2 and room temperature; e) is the particle size and size distribution of synthesized Au NPs from DCS.

Table 4-8 Particle size and size distribution obtained from TEM (around 100 particles counted) and DCS (particle number of 10^{11} order-of-magnitude).

Initial pH of gold precursor	**Size from TEM (nm)**	**Size from DCS (nm)**
3.0	9.4 ± 0.8 (8.1%)	9.3 ± 1.0 (10.4%)
4.0	9.7 ± 1.5 (15.5%)	9.8 ± 0.8 (8.4%)
5.1	10.6 ± 1.7 (15.8%)	10.9 ± 1.6 (14.6%)
6.7	15.1 ± 3.0 (19.9%)	13.0 ± 2.7 (20.7%)

4.3.4 SERS performance test with synthesized CO-produced Au NPs

Compared with conventional methods for producing gold nanoparticles, our method produces uncapped nanoparticles; no CO was found on the surface of gold nanoparticles (as measured by IR,[*] see **Figure B-3**). Furthermore, the NPs are produced rapidly, at room temperature and show good monodispersity (polydispersity reduced to 5%).

In order to verify the applicability of these Au NPs, they were tested for Surface-Enhanced Raman Scattering (SERS). It is widely accepted that the Raman signal amplification with the aid of metal particles (typically Ag or Au) is due to the localized surface plasmon resonance (LSPR) on the surface of metal particles.[245] To achieve better enhancement, it is crucial to deposit gold nanoparticles on a substrate to create "hotspots" with narrow gaps between neighbouring particles.[219] It has been shown from TEM images in **Figure 4-2**, in the absence of any capping agent, the gold nanoparticles formed from CO reduction would aggregate during drying. Additionally, the Raman signal decays

---

[*] *The IR analysis was carried out by Dr. Tom Macdonald, University College London*

exponentially with the distance between the metal surface and analyte molecules.[210] The gold nanoparticles without capping surfactants provide free sites to absorb the molecules, which also gives higher enhancement. The SERS performance[*] of CO-produced and citrate-capped Au NPs with different particle sizes is shown in **Figure 4-8**. The average enhancement factor (AEF) was calculated from three intensities with different Raman shifts (611 cm^{-1}, 1359 cm^{-1} and 1509 cm^{-1}) in **Table B-1,** ESI. The CO-produced gold nanoparticles with an average size of 26.6 nm (obtained from 0.54 mM initial concentration of gold precursor at liquid/gas flow ratio of 2 in

Figure 4-6) gave the highest enhancement with an AEF of 2.40×10^9, as it is in the optimal size range (20-100 nm) for SERS application.[218] Compared to commercial 30 nm citrate-capped Au NPs with AEF of 2.19×10^9, the enhancement of 26.6 nm CO-produced Au NPs was similar (see Table S5). However, considering the synthesis time of 30 min in a typical protocol of citrate-capped Au NPs via the Turkevich method,[230] the CO- produced Au NPs is still attractive due to the shorter synthesis time (<4 min) and room temperature operation, with similar performance for SERS application. When the particle size was outside the optimal size range (20-100 nm), the CO- produced gold nanoparticles showed better SERS performance compared to the citrate-stabilised Au NPs. Compared to 10 nm citrate-capped gold nanoparticles (AEF = 3.70×10^8), the 7.6 nm CO-produced gold nanoparticles gave nearly three times higher enhancement (AEF = 1.31×10^9), which is attributed to the

---

[*] *The SERS performance was tested by Dr. Sultan Ben-Jaber, University College London*

narrower gap between particles and easier adsorption of analyte molecule onto the naked surface of gold nanoparticles.

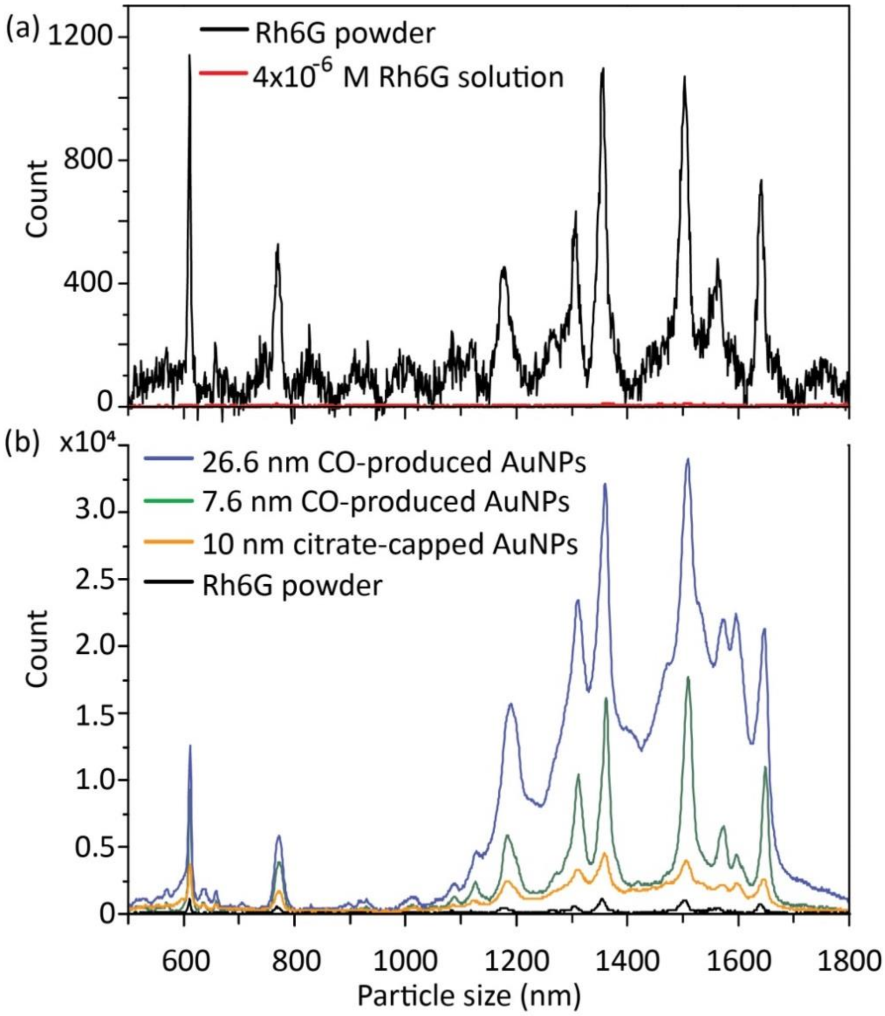

Figure 4-8 (a) Typical Raman signal of pure solid Rh6G powder (in black) and 4×10^{-6} M Rh6G solution (in red); (b) SERS spectra of 4×10^{-6} M Rh6G solution enhanced by 26.6 nm CO-produced gold nanoparticles (in blue), 7.6 nm CO-produced nanoparticles (in green) and 10 nm citrate-capped gold nanoparticles (in yellow), compared to the pure solid Rh6G powder (in black) without enhancement.

4.3.5 Au NPs synthesized with different capping agents

The synthesized gold nanoparticles were monitored by UV-Vis and proven to be stable for at least one month when stored at 4 °C. Longer shelf lives (from 1 week to at least 1 month at room temperature) could be obtained by adding different capping agents, either during or immediately after the synthesis. **Figure 4-9** shows the gold nanoparticles obtained from different capping agents based on our set-up, namely trisodium citrate, polysorbate 80 (TWEEN 80), oleylamine and Poly(ethyleneglycol)-2-mercaptoethyl ether acetic acid (Thiol-PEG-COOH).

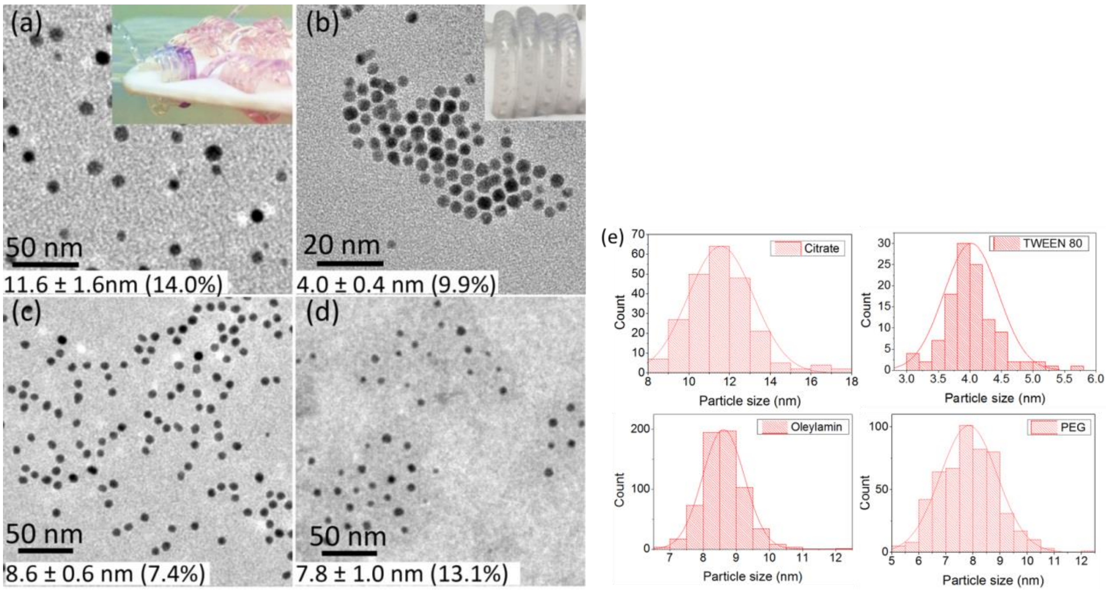

Figure 4-9 TEM images of gold nanoparticles capped by (a) trisodium citrate premixed with $HAuCl_4$ (inset is the flow regime inside CFI), (b) TWEEN 80 (inset is the flow regime inside CFI), (c) oleylamine in octane and (d) Thiol-PEG-COOH (MW 3163 Da) (inset is the post-synthetic functionalization in batch) with 0.27 mM $HAuCl_4$ reduced by CO in microfluidic segmented flow system at room temperature. (e) shows the particle size distribution based on TEM.

Because of the low toxicity[173] and the ease of further functionalisation, researchers maintain a high motivation to optimise the synthesis of citrate-capped gold nanoparticles. The size of citrate-capped particle (11.6 ± 1.6 nm, 14.0%) shown in **Figure 4-9a** was higher compared to the $HAuCl_4$ only system (9.3 ± 1.00, 10.4%) for the same operational conditions. This is because adding the alkaline citrate increases the pH of the solution, which leads to a shift of equilibrium to the gold species with less reactivity[31] and decrease of the nucleation rate.[228] With fewer nuclei forming and higher amount of gold precursor available for growth, larger particle size was obtained. Compared with typical citrate-capped gold nanoparticles synthesis processes (such as the Turkevich method), the CO reduction in our microfluidic segmented flow system is more facile with shorter reaction times (5 min) at a lower reaction temperature.

TWEEN 80 has been shown to be a weaker reducing agent with reaction time of 6 h at room temperature compared to CO, as well as a non-ionic surfactant for Au NPs synthesis.[246] Additionally, it changes the surface tension of the solvent, leading to smaller bubble size (**inset** in **Figure 4-9b**) compared to that when no capping agents were used (**Figure 4-4**). The enhanced mass transfer between gas and liquid due to the increased surface-to-volume ratio and the good protecting ability of TWEEN 80 produced gold seeds with size of 2.7 ± 0.4 nm (14.6%) at residence time 3.4 min. The seed particles subsequently grew to 4.0 ± 0.4 nm (9.9%) inside the container reduced by excess TWEEN 80 within 8 days, with a stability of more than 1-month for a TWEEN 80 to gold ratio of 0.5. TWEEN 80 could act as a capping agent[247] and also suppress the reduction rate.[248] Thus, the reaction continued in the collection container as monitored by UV-Vis. The particle size increased from 2.7 ± 0.4 nm (14.6%) in **Figure 4-10b** to 4.0± 0.4 nm (9.9%) in **Figure 4-9b** over a period of 8 days. The polydispersity decreased after 8 days as the TWEEN 80 could also act as a weaker reducing agent for seed-mediated growth.[246] This suggests that the CO reduction inside the CFI formed a high amount of seed particles without consuming the entire gold precursor. The remaining TWEEN 80 subsequently reduced the precursor with a size-focusing effect[223] to form monodisperse particles.

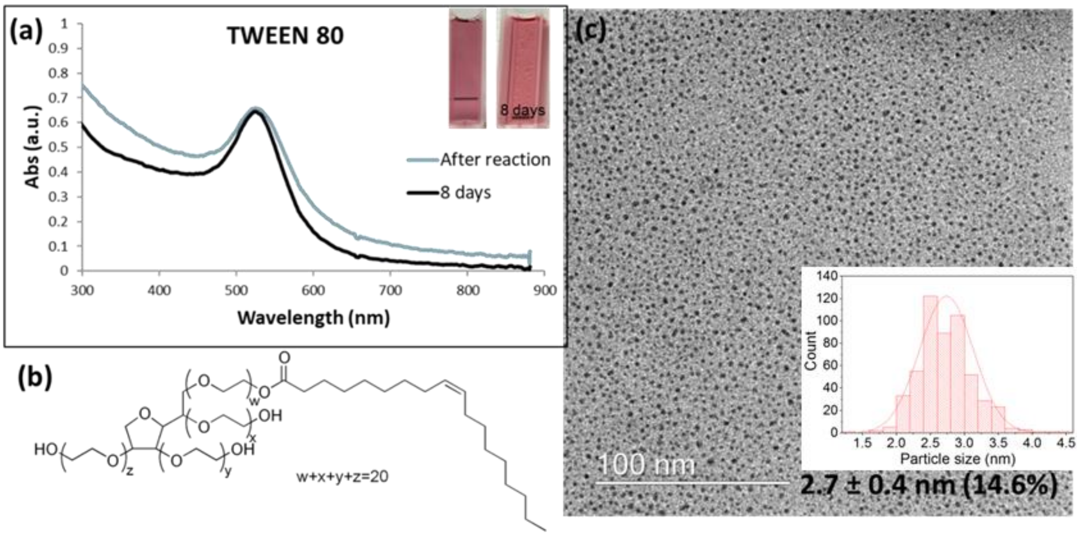

Figure 4-10 (a) UV-Vis spectra of the Au NPs capped by TWEEN 80 produced via CO reduction intermediate after reaction and after 8 days (inset is the colour of the samples); (b) the structure of TWEEN 80; (c) TEM image of fresh Au NPs capped by TWEEN 80 (insert: particle size distribution) from mixed streams of 0.27 mM TWEEN 80 and 0.54 mM gold precursor at the same flow rate of 0.25 ml/min via micromixer chip and then mixed with 0.1 ml/min gaseous CO in CFI with residence time of 4.2 min.

Using the same set-up, hydrophobic gold nanoparticles could also be synthesized by using oleylamine as a capping agent at 100 °C. The higher operation temperature led to spherical shape Au NPs rather than gold nanowires (Au NWs) formed via CO at 60 °C in previous batch synthesis.[233] A TEM image of the synthesised gold nanoparticles with size of 8.6 ± 0.6 nm (7.4%) is shown in **Figure 4-9c**. A comparative experiment using N_2 instead of CO was conducted at the same experimental conditions to prove that the CO is the dominant reducing agent rather than oleylamine (**Figure B-4**). Nanowires were formed without CO like previous literature[249] observed in oleylamine reduction.

Thiol-PEG-COOH gold nanoparticles are widely used in drug and gene delivery[250-251] as relatively non-toxic carriers and could be obtained with our system by post-synthetic modification methods. To synthesize PEG-capped Au NPs, poly(sodium 4-styrenesulfonate) (PSS) was used during the CO reduction stage to stabilize the Au NPs temporarily. Subsequently, thiol-PEG-COOH was added into the gold nanoparticle solution obtained and stirred overnight. Because of the stronger binding strength of thiols, the Thiol-PEG-COOH was quickly adsorbed onto the gold nanoparticles without size alteration (compared to PSS-capped Au NPs with size of 7.8 ± 1.2 nm, 15.4% in **Figure 4-11**), and no further aggregation was observed (**Figure 4-9d**).

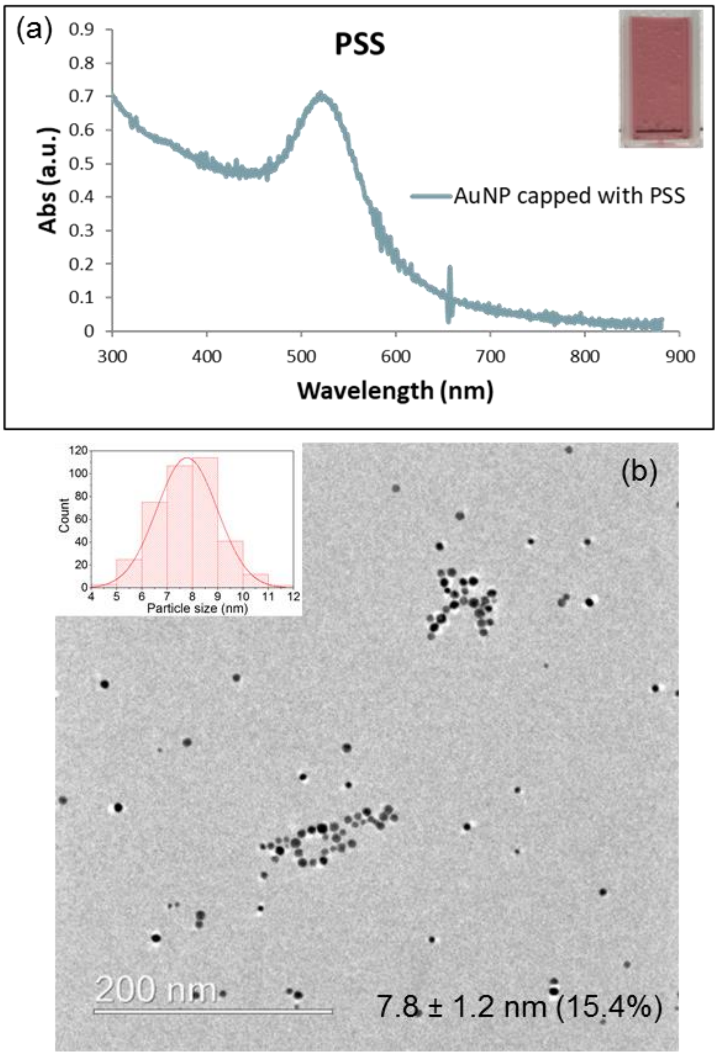

Figure 4-11 (a) UV-Vis spectra of the Au NPs capped by PSS via CO reduction (inset is the colour of the sample); (b) TEM image (insert: size distribution) of Au NPs capped by PSS from the mixed streams of 0.27 mM gold precursor and 0.3% w/w PSS via micromixer chip with the same flow rate of 0.125 ml/min and then mixed with 0.1 ml/min CO in CFI with residence time of 7.5 min.

4.4 Conclusion

In this chapter, we demonstrated a facile synthesis of monodisperse gold nanoparticles with carbon monoxide in a microfluidic segmented flow system. The reducing strength of CO is between that of $NaBH_4$ and citrate,[252] which aids the synthesis of sub-10 nm gold nanoparticles with better control. The use of microfluidic segmented flow in a coiled flow inverter leads to monodisperse particles and the synthesis can continuously produce gold nanoparticles, whose size can be tuned by different operational parameters and capping agents (concluded in **Table 4-9**). Since this approach could produce highly controllable and reducing agent-free gold nanoparticles in short time, it could be a very promising material preparation protocol for the study of gold nanoparticle applications. However, fouling of the reactor was observed to some extent for all the capping agents after around 10 min operation, and this must be resolved for long term operation, or employ intermediate cleaning of the reactor.

Table 4-9 Conclusion and comments of all the capping agents used in this chapter.

Capping agent	Residence time (nm)	Particle size (nm)	Advantages	Drawbacks
Citrate	3.4	11.6 ± 1.6 (14.0%)	Stability > 1 month	Polydispersity increased
TWEEN 80	4.2	4.0 ± 0.4 (9.9%)	Stability > 1 month & smaller size particles (< 5 nm) obtained	Needs two-stage growth, unfinished reaction inside CFI
Oleylamine	4.2[a]	8.6 ± 0.6 (7.4%)	Stability > 1 month & monodisperse	Needs high temperature and subsequent washing process
PEG	7.5	7.8 ± 1.0 (13.1%)	Stability > 2 month	Additional process of ligand exchange needed

[a] All the experiments were conducted at room temperature except oleylamine which was at 100 °C.

5. Synthesis of Gold Nanoparticles in Microfluidic system with Carbon Monoxide-Saturated Organic Solution in Tube-in-Tube Set-up

5.1 Introduction

In the last chapter, CO showed big potential as a reducing agent to synthesize Au NPs with a gas-liquid segmented microfluidic system. However, as mentioned above, fouling was observed during the experiment which led to the loss of yield. In addition, the amount of CO at atmospheric pressure had limited reducing ability if higher nucleation rate or strong capping agent was needed. Based on Henry's law, the amount of dissolved gas is proportional to partial pressure of the gas phase.[184] Therefore the concentration of CO could be tuned by pressurizing the system. However, it is hard to retain the stable and homogeneous flow patterns in gas-liquid flow at higher pressure. One of the solutions is to pre-dissolve the CO into the organic phase and then form liquid-liquid flow inside the reactor which could maintain stable slug flow pattern with good mixing, as well as isolate the reactant from the wall to prevent fouling. To dissolve gas into solution, different gas-permeable membranes were utilized in either a tube-in-tube set-up with concentric capillaries (fluoropolymer, Teflon AF-2400)[253] or parallel flow with poly(dimethylsiloxane) (PDMS) membrane separating two microchannels.[164] This kind of materials are gas-permeable and could retain the liquid inside the original tube.[254] The small volume of the microreactor significantly reduces the hazards of toxic and high-pressure gas to enhance safety.[255] Hansen *et al.* demonstrated the capability of the tube-in-tube reactor to supply CO from oxalyl chloride as an alternative way of pressurized toxic gas cylinder for flow chemistry reactions.[256] In addition to this, the high surface-to-volume ratio provided by the microreactor with small inner diameters improves the mass/heat transfer compared to the batch system, resulting in faster and more homogeneous solution of gas.[253] Yang and Jensen established models for predicting gas concentration profiles within tube-in-tube reactor.[257] Koos *et al.* made use of tube-in-tube set-up to develop a controllable continuous flow process for palladium transition-catalysed carbonyl insertion reaction with an in-line FTIR to monitor the CO concentration in the solution due to the distinctive IR absorption of CO.[255] The set-up provided a convenient way for the real-time measurement of the gas concentration which may find use during gas-liquid flow chemistry. Brzozowski *et al.* developed a computer-aided imaging technique with a tube-in-tube reactor for *in situ* analysis of gas dissolving in various gas-liquid reactions for C-C, C-O and C-N bond formation and hydrogeneration.[253] Taifur-Rahman *et al.* utilized PDMS membrane-based droplet microfluidic method to precisely dose CO from parallel flows into droplets of growth solution with homogeneous size containing gold precursor and seed particles to grow gold coat on silica nanoparticles.[164] Each droplet was an individual reactor unit where the reaction could be efficiently terminated by tuning the contact length between CO and liquid.

In this chapter, Teflon AF-2400 was used to make a tube-in-tube set-up as a CO saturator to pre-dissolve CO into an organic phase (pure octane or heptane) at high pressure before contacting with gold precursor to initiate the Au NPs formation. Different effects of operation parameters on Au NPs size, size distribution and stability were investigated to study the translation of Au NPs synthesis from batch to this microfluidic system. Since more concentrated CO enhanced the reduction rate, various capping agents were tested to produce stable Au NPs.

5.2 Experimental

5.2.1 Experimental set-up

Figure 5-1 shows the microfluidic segmented flow system consisting of a tube-in-tube section at room temperature and a microreactor (either straight tubing or a coiled flow inverter,CFI) for the synthesis of Au NPs. The tube-in-tube section used Teflon AF-2400 tubing (0.8 mm inner diameter I.D., 1.0 mm outer diameter O.D., Biogeneral USA) as the contacting interface inside a Polytetrafluoroethylene (PTFE) tubing (2.6 mm I.D., VICI Jour) to saturate the organic solution with pure CO (BOC gases) at 500 kPa maintained by back pressure regulator (BPR-10, Zaiput). The operation parameters were decided based on tube-in-tube model developed by Yang.[257] The shell part was the membrane of the AF-2400 tubing contained up to 203 mM CO at 500 kPa. The inner tubing contained organic flow. Heptane and octane were chosen as the carrier flow for CO due to the immiscibility with water and more than 50 times higher solubility of CO compared to water. The organic solvent was also used to prevent fouling by forming organic-water two-phase flow in latter coiled flow inverter. As both heptane and octane are flammable liquids, the organic solution should be kept away from heat, hot surfaces, sparks, open flames or other ignition sources. The gloves were necessary to avoid prolonged or repeated exposure, as well as aspiration irritation. For the tubing length of 2 m used in this study, it was long enough to saturate CO in heptane (58.4 mM) or octane (53.6 mM) at the outlet of the tube-in-tube set-up (see **Section 5.3.1**). Straight fluorinated ethylene propylene (FEP) tubing (0.5 mm and 1 mm I.D., 25 cm in length, VICI Jour) was used when citrate was the capping agent. When the capping agents were different kinds of thiol, CFI made of fluorinated ethylene propylene (FEP) tubing (1 mm I.D., VICI Jour) and perfluoroalkoxy alkanes (PFA) tubing (0.5 mm, 1 mm and i.55 mm I.D., VICI Jour) were used consisting different number of coils with coil diameter of 1 cm. A 90° bend was utilized for every 5 coils and the total length of the CFI was 9.0 m, 3.6 m and 2.5 m, respectively. As CO is highly toxic, the whole system was fully sealed and one line of nitrogen (N_2) by mass flow controller (Brooks 5850 TR) was installed to flush the remaining CO dissolved in liquid phase.

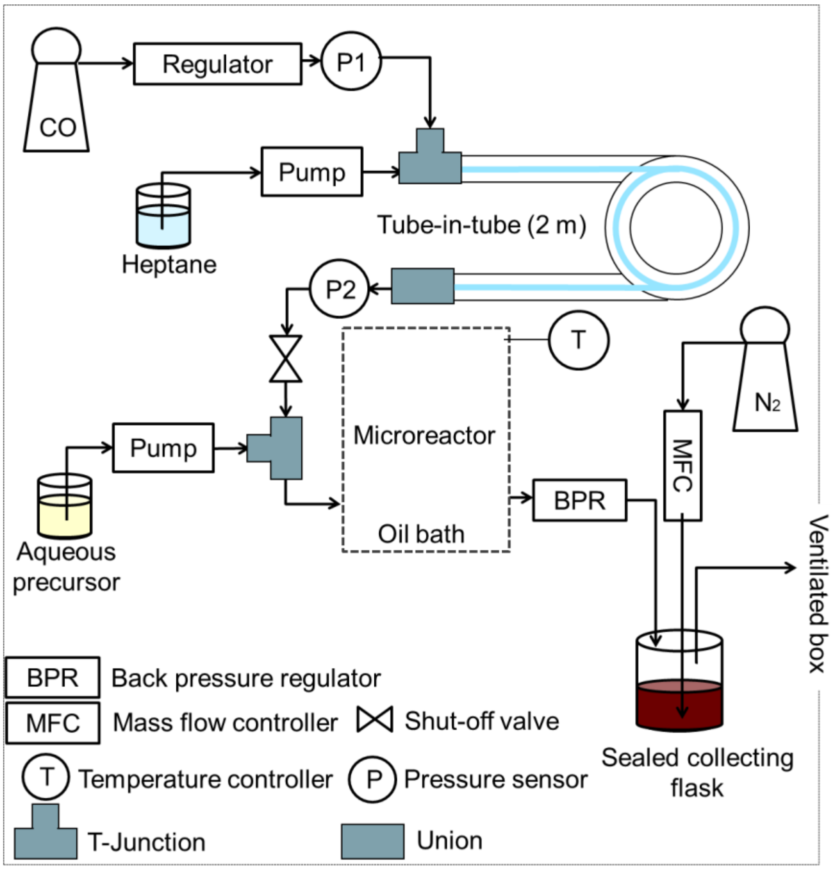

Figure 5-1 Schematic of microfluidic segmented flow system with tube-in-tube membrane saturator for synthesis of Au NPs.

5.2.2 General synthetic procedure

All the chemicals used in this chapter were purchased from Sigma-Aldrich without any further treatment or purification and made into solution with specific concentrations by 15.0 MΩ reverse osmosis water. When citrate was the capping agent, a cross junction (P-722, 0.5 mm thru-hole, IDEX Health & Science LLC) was used to mix citrate and gold precursor solution into one aqueous stream (citrate to gold concentration ratio of 10 with final concentration of gold precursor of 0.27 mM). The full mixing was expected due to the inner convection in droplet flow. The flow pattern is shown in **Figure C-1**. Two aqueous streams of citrate and gold precursor were substitute by blue and pink dye aqueous solution to obtain clearer flow patterns at volumetric flow rate of

CO-saturated organic /citrate/gold solution of 0.2 ml/min, 0.1ml/min and 0.1 ml/min. The pH was tuned by citric acid ($C_6H_8O_7$) and NaOH which were added in advance into the citrate stream. For thiol capping agents, typically the colour of thiol and $HAuCl_4$ mixture turned to colourless in 10 min. However the aqueous reaction solution was left for 2 hours to make sure the full conversion from Au(III) to Au(I) complexes. Then the aqueous stream was mixed with CO-saturated heptane at flow rate ratio of heptane/aqueous solution of 2 by T-mixer (P-632, IDEX Health & Science LLC) and then formed microfluidic segmented flow inside the CFI.

5.2.3 Analysis

The solution pH was measured by pH meter (SevenCompact^{TM} pH/Ion S220). UV-vis absorption spectra of gold nanoparticles were recorded immediately after sample collection or washing using an Ocean Optics UV-Vis-ES spectrometer (USB 2000+ Spectrometer and DT-Mini-2-GS light source). The resulting gold nanoparticles were measured via Differential Centrifugal Sedimentation (DCS) (CPS 24000 Disc Centrifuge, CPS Instruments), and transmission electron microscopy (TEM) (Jeol 2010 – 200 kV) to give both qualitative and quantitative analysis of particle size and polydispersity. Inductively coupled plasma atomic emission spectroscopy (Varian 720 ICP-AES, axial configuration) was used to measure the gold amount of synthesized Au NPs. The product solution was precipitated by acetone and then centrifuged at speed of 7500 rpm (Heraeus Multifuge X1R, ThermoFisher SCIENTIFIC, rotor model: F15-8x50cy) for 30 min. Subsequently aqua regia was added to the precipitate and supernatant. The yield was calculated by the amount of gold in the precipitate detected by ICP-AES over the original amount of gold precursor. This judgement was proved by selectively comparing ICP results of the supernatant and precipitate from three samples in **Table 5-1.** The amount of gold detected in supernatant and precipitate is reasonable compare to the total amount of gold input.

Table 5-1 ICP measurement error test.

Sample	**Initial gold concentration (mM)**	**Gold concentration in supernatant (mM)**	**Gold concentration in precipitate (mM)**	**Yield from supernatant (%)**	**Yield from precipitate (%)**
1	1	0.15	0.79	14.89	78.93
2	1	0.00020	1.14	0.020	114.39
3	1	0.0016	1.01	1.55	101.52

5.3 Results and discussion

5.3.1 Tube-in-tube model

The tube-in-tube model was used to confirm the organic phase was saturated by CO at the outlet of the tube-in-tube contactor.[*] The model framework is based on the previous work by Yang[257] and the simulation was ran by COMSOL Multiphysics software (version 5.2a). **Figure 5-2** shows how two-dimensional model works in COMSOL (heptane was picked as example in simulation).

---

[*] *The tube-in-tube model was built by Dr. Gaowei Wu, University College London.*

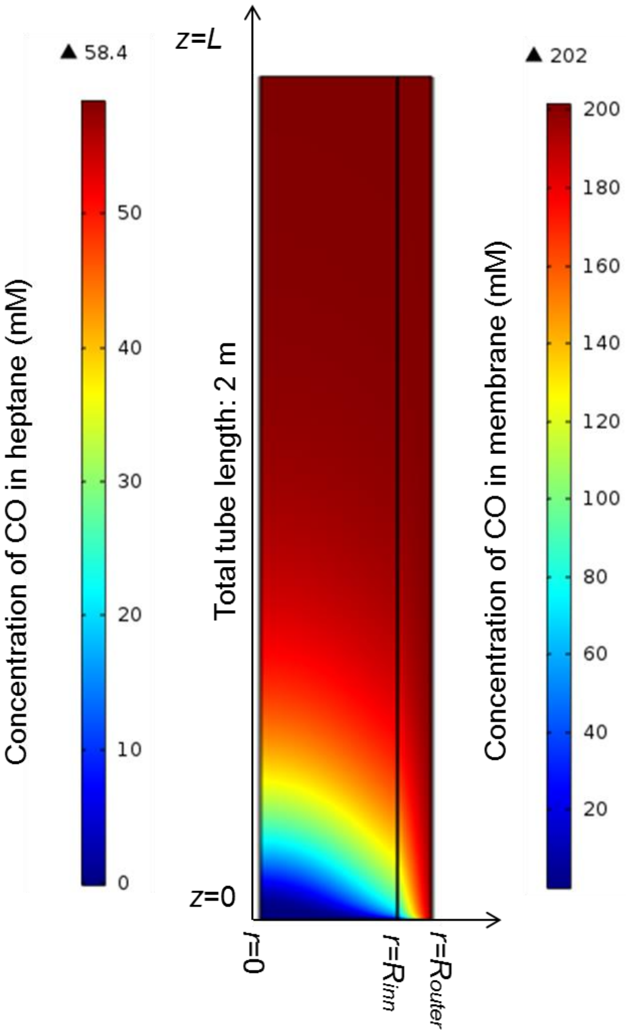

Figure 5-2 Two-dimensional model of tube-in-tube contactor with simulated concentration profile of CO in both membrane of A-2400 (shell side) and heptane (inner tube) at 298K, 500 kPa and average liquid superficial velocity of 0.03 m/s.

The assumptions in the model are listed below:[257]

1. steady-state mass transfer in an axial symmetric geometry at isothermal conditions
2. laminar flow (a parabolic velocity profile with invariant axial position) in the inner tube

3. Henry's law applied to the membrane-liquid interface in which the whole area is available for mass transfer
4. ideal gas in gas phase
5. negligible liquid pervaporation through the membrane to the gas phase.

In the inner tube domain, the mole balance for gas considering axial convection, axial diffusion and radial diffusion can be obtained by:[257]

$$2u_L\left[1-\left({r}/{R_{inn}}\right)^2\right]{\partial c_i}/{\partial z} - D_i({\partial^2 c_i}/{\partial z^2}) = D_i\,{1}/{r}\,{\partial}/{\partial r}\left(r\,{\partial c_i}/{\partial r}\right) \qquad \text{Eq.(12)}$$

where u_L is the average velocity of liquid flow. r is the radial position, R_{inn} the radius of the inner tube, c_i is gas concentration in solvent, z is the axial position, D_i is the gas (here is CO) molecular diffusion coefficient in solvent.

Boundary conditions:

$$at\ r = 0,\ {\partial c_i}/{\partial r} = 0 \qquad \text{Eq.(13)}$$

$$at\ r = R_{inn},\ c_i = {c_{i,mem}}/{K_H} \qquad \text{Eq.(14)}$$

$$at\ z = 0,\ c_i = c_{i,out} \qquad \text{Eq.(15)}$$

$$at\ z = L,\ {\partial c_i}/{\partial r} = 0 \qquad \text{Eq.(16)}$$

where K_H is Henry's law constant of gas in solvent at 298 K, $c_{i,mem}$ is the gas concentration in the membrane, $c_{i,out}$ is the gas concentration at the outlet point of the reactor, L is tubing length.

In the membrane domain, the steady-state mole balance of gas only counts diffusion (axial+radial):

$$D_{i,mem}\left[\frac{\partial^2 c_{i,mem}}{\partial z^2}+\frac{1}{r}\frac{\partial}{\partial r}\left(r\frac{\partial c_{i,mem}}{\partial r}\right)\right]=0 \qquad \text{Eq.(17)}$$

Boundary conditions:

$$at\ r=R_{inn},\ c_{i,mem}=K_H c_i \qquad \text{Eq.(18)}$$

$$at\ r=R_{outer},\ c_{i,mem}=c_{i,g} \qquad \text{Eq.(19)}$$

$$at\ z=0,\ {\partial c_{i,mem}}/{\partial z}=0 \qquad \text{Eq.(20)}$$

$$at\ z=L,\ {\partial c_{i,mem}}/{\partial z}=0 \qquad \text{Eq.(21)}$$

where R_{outer} is the out radius of Teflon AF-2400 tube, $D_{i,m}$ is the diffusion coefficient of gas in the membrane, $c_{i,g}$ is gas concentration in the gas phase.

Table 5-2 and **Table 5-3** list all the variables and values needed. As the model is to check if the tubing length is enough to saturate organic solvent, the highest liquid flow rate (0.64 ml/min) in experiments was used.

Table 5-2 Experimental parameters used in the model.

Parameter		**Value**
Teflon AF-2400 tubing	Inner radius (R_{inn}, mm)	0.4
	Wall thickness (H, mm)	0.1
	Length (L, m)	2
Flow rate (Q, ml/min)		0.64

As the membrane permeability of CO is not available, the model used nitrogen (N_2) for estimation due to the similar kinetic sizes (N_2: 3.64 Å, CO: 3.76 Å) and critical temperatures (N_2: -147 °C, CO: -132.9 °C), which are directly related to the diffusivity of gas inside the membrane.[258] The diffusion coefficient of N_2 in the AF-2400 membrane ($D_{i,mem}$) based on the N_2 concentration in the gas phase is calculated by Eq (22):[257]

$$D_{i,mem} = T/(273\text{K})\times(1.01\text{ bar}) \times \kappa = 0.63\times10^{-9}\ (\text{m s}^{-1}) \qquad \text{Eq.(22)}$$

Where T is the 298 K, κ is the membrane permeability of N_2 (780 barrer).[259]

Table 5-3 List of variables and values used in the model

Parameters	**Value**
Average velocity of flow (u_{ave})	$0.03\ \text{m}\cdot\text{s}^{-1}$
Pressure (P)	500 kPa
Temperature (T)	298 K
Tube length (L)	2 m
Concentration of gas phase at 5 bar (C_{io})	$203\ \text{mol}\cdot\text{dm}^{-3}$
Diffusivity of CO in solvent (D_i)	$8.12 \times 10^{-9}\ \text{m}^2\cdot\text{s}^{-1}$ [b] [260]
Diffusivity of N_2 in membrane ($D_{i,mem}$)	$0.63 \times 10^{-9}\ \text{m}^2\cdot\text{s}^{-1}$ [a]
Henry's law constant for gas with solvent (K_H)	5.84×10^4 kPa [b] [261] 6.36×10^4 kPa [c] [261]

[a] The diffusivity of CO in membrane is not available, which used N_2 for estimation.[259]

[b] heptane

[c] octane

Figure 5-3 shows the concentration profile of CO in the solvents used in this thesis by numerical simulation. The simulation proved that 2 m tube was enough to saturate organic phases by CO with final concentration of 58.4 mM (heptane) and 53.6 mM (octane).

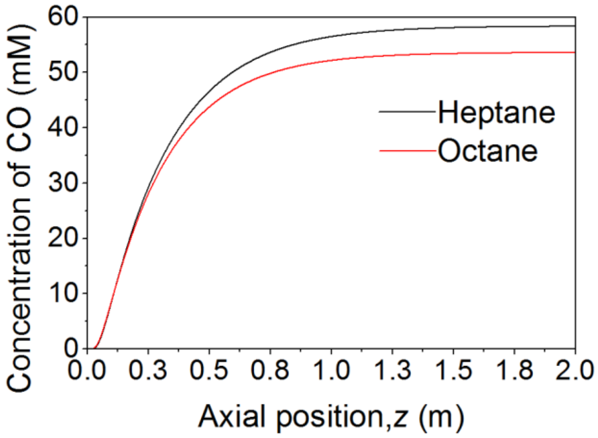

Figure 5-3 Simulation results of CO concentration in heptane (black line) and octane (red line) at the centre of inner tube with increasing tubing length at 298K, 500 kPa and average liquid velocity of 0.03 m/s.

5.3.2 Influence of initial pH of the gold precursor

As shown in Chapter 4, the polydispersity of CO-produced Au NPs without capping agent increased with lower liquid/gas flow rate ratio due to the fast nucleation and coalescence of nuclei at early stage. Since the tube-in-tube set-up increased pressure in the system, higher solubility of CO in solution (from~1 mM to ~5 mM) could facilitate the reduction. Thus, capping agent is necessary to achieve controllable reduction and narrow particle size distribution. Firstly, citrate was used as capping agent to test the performance of the liquid-liquid microfluidic system during CO reduction. The influence of initial pH of the gold precursor was investigated based on gold speciation changing. The citrate to gold concentration ratio was fixed at 10. Citric acid and NaOH was used to tune the pH. Considering the faster reduction rate at high pressure in the tube-in-tube set-up, the residence time was less than 1 min by tuning the liquid flow rates based on the time measured for one slug to pass through the 1 mm I.D. FEP tubing (length of 25 cm). **Table 5-4** shows the dominant species at the set pH values of initial mixture of the reactant and the final pH in product solution at different residence times measured by pH meter. pH decreased after reaction, due to CO_2 produced in CO reduction.[262]

Table 5-4 Speciation of 0.27 mM $HAuCl_4$ solution at different pH values and the final pH in product solution at different residence times (RT).

Initial pH of the reactant mixture	Dominant species at the mixture pH[52]	RT = 9.8 s Final pH	RT = 20 s Final pH	RT = 40 s Final pH	RT = 56 s Final pH
2.08	$[AuCl_4]^-$	2.20	2.11	-	2.19
4.06	$[AuCl_3(H_2O)]^-$	4.00	3.97	4.01	4.01
5.09	$[AuCl_2(OH)_2]^-$	4.86	4.86	4.88	4.86
5.62	$[AuCl_2(OH)_2]^-$ & $[AuCl(OH)_3]^-$	5.26	5.28	5.24	5.27
6.81	$[AuCl(OH)_3]^-$	6.28	6.33	6.39	6.36
10.47	$[Au(OH)_4]^-$	7.15	7.26	7.16	7.26

Figure 5-4 shows the UV-Vis spectra and the colour of the product after CO reduction. The UV-Vis peak absorbance and wavelength range of plasmon peaks were concluded in **Table 5-5**. The When pH = 2.08, there were only $[AuCl_4]^-$ complex in the precursor solution which maintained the fast reaction rate over the course of whole reduction process. The nuclei were formed

continuously and there was no separation between nucleation and growth, resulting in highly polydisperse Au NPs (purple color). Black precipitation was observed at the front-end of the droplet when the residence time increased. It has been known that the nanoparticles preferentially self-assemble at the water-oil interface by Pickering stabilization.[152] When the solution pH was low, large amount of nuclei were formed in short time with weak capping agent (citrate). When the synthesized particles accumulated on the water-organic interface, irreversible aggregation occurred, resulting in black precipitation as observed (**Figure C-2**), as well as in literature.[151]

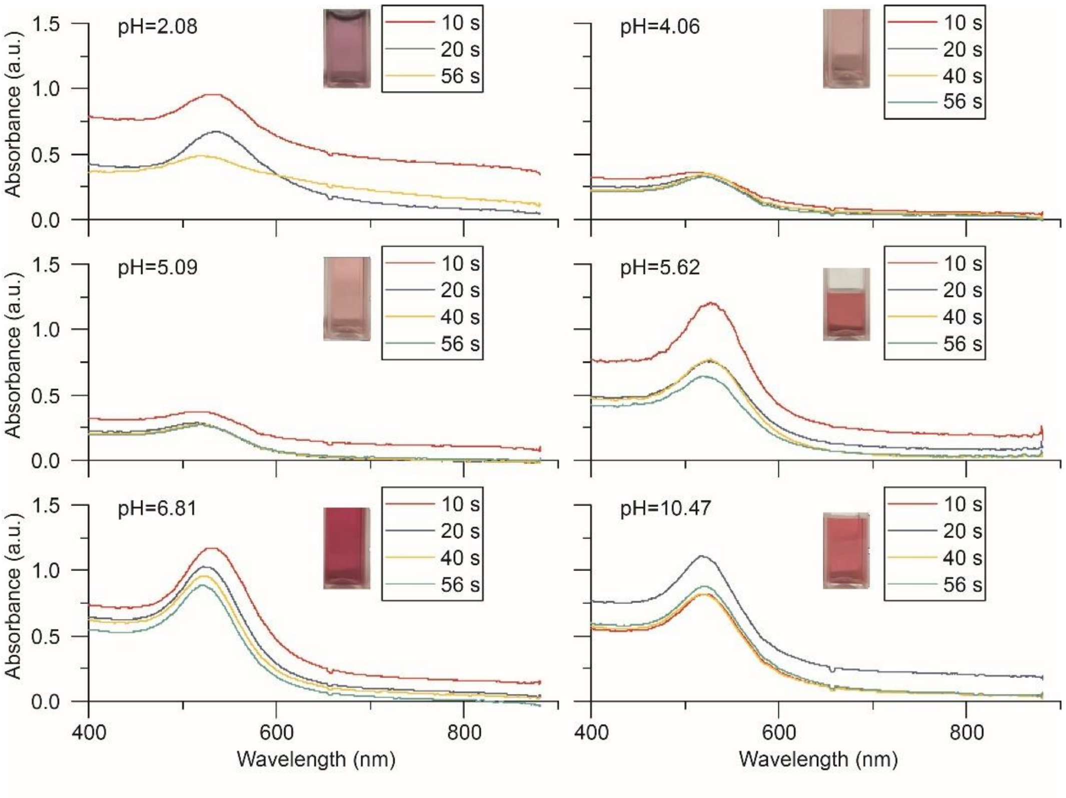

Figure 5-4 UV-vis spectra of CO-produced Au NPs from 0.27 mM $HAuCl_4$ and CO-saturated octane in straight FEP tubing with 1 mm I.D. and 25 cm length at room temperature with initial pH of reactant mixture and residence times as indicated. Inset: colour of the products at residence time of 9.8 s at different pH values.

Table 5-5 Conclusion of UV-Vis peak absorbance and wavelength range of plasmon peak in Figure 5-4.

Initial pH of the reactant mixture	**RT = 9.8 s Peak absorbance**	**RT = 20 s Peak absorbance**	**RT = 40 s Peak absorbance**	**RT = 56 s Peak absorbance**	**Wavelength range of plasmon peak (9.8 s to 56 s) (nm)**
2.08	0.967	0.669	-	0.484	534.5 to 521.6
4.06	0.361	0.332	0.346	0.329	513.3 to 522.7
5.09	0.375	0.289	0.278	0.270	519.0 to 519.6
5.62	1.212	0.758	0.769	0.240	527.0 to 526.4
6.81	1.158	1.026	0.953	0.875	531.8 to 521.6
10.47	0.822	1.099	0.818	0.877	520.6 to 520.3

The products formed at pH = 4.06 and 5.09 were similar due to a sufficient amount of $[AuCl_4]^-$ during the nucleation stage. After adding citrate, the gold species moved towards less reactive ones but still contained high reactivity. Thus, the nucleation occurred throughout the whole synthesis. The particles size in **Figure 5-5a** showed that 9.8 s was too short to finish the reaction and the particle did not get enough time for fully growth. This particle size was in accordance with the TEM image in **Figure 5-5b**, in which the particle size was around 5.7 nm. However, smaller particles (**Figure 5-5b inset**) were also observed in TEM which were not shown from DCS results due to the limitation of this technology.[106] Compared to the product obtained from 9.8 s residence time, the particle size increased either with longer residence time, or longer aging time after reaction inside the container (**Figure 5-5c**). The similar particle size and size distribution with storage time of 20 days (**Figure 5-5d**) compared to 6 days indicated that the particles were fully mature after 6 days and could be stable for at least two weeks. It is worthy to note that the mean particle size of the product at residence time of 40 s was similar with the product of 9.8 s residence time and 6-day aging inside container (6.9 nm vs. 6.8 nm), whereas the polydispersity had nearly doubled (21.6% vs. 9.7%) in **Figure 5-5**. This was because the nucleation and growth process at residence time of 40 s was overlapping. However, two-stage growth occurred for the 9.8 s sample after collection which was the key point to form monodisperse particles by separating the nucleation and growth stages. The small-size Au NPs were formed after 9.8 s via CO reduction, and then the fast reduction was quenched as the product flowed out of the reactor and stopped contacting with CO. The synthesized small-size Au NPs acted like seed particles and the unconsumed precursor was reduced slowly by excess citrate inside the container. As the citrate reduction is slow at room temperature, more controllable growth occurred without producing more nuclei due to the autocatalysis on the existing gold surface.[31] NPs preferentially grow in a size focusing regime, in which the smaller particles grow faster than larger ones,[222] resulting narrower size distribution after growth.

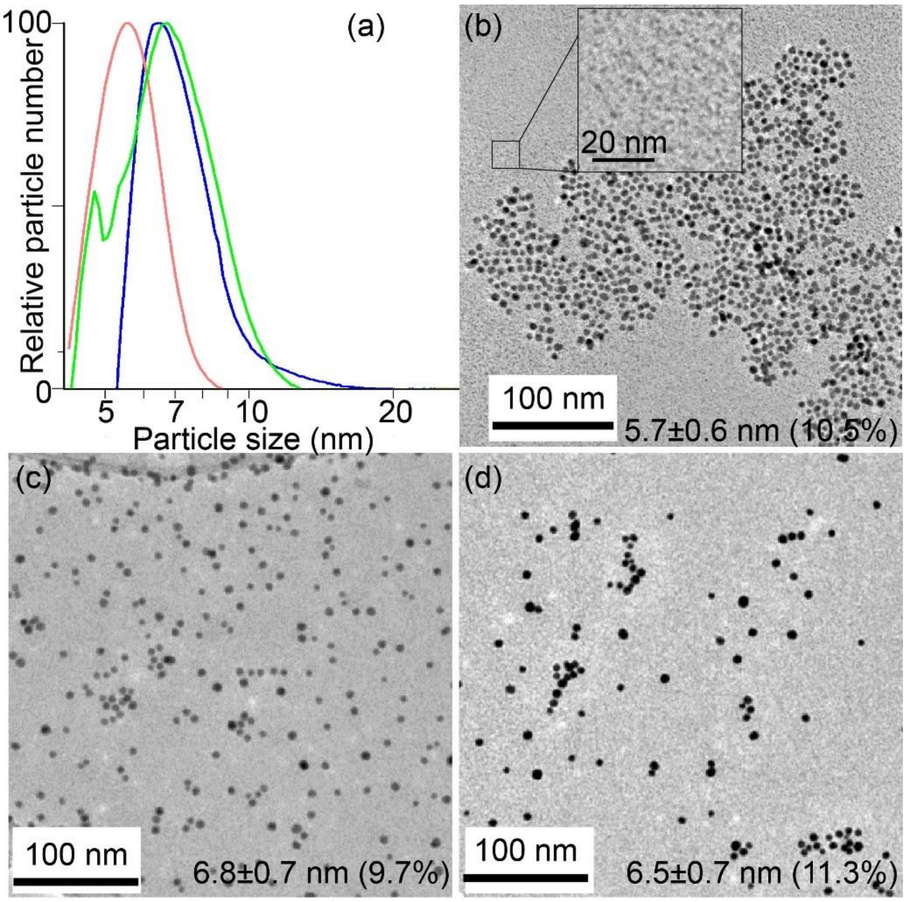

Figure 5-5 (a) Particle size and size distribution of CO-produced Au NPs at pH = 4.06 in Figure 5-4 from 0.27 mM $HAuCl_4$ and CO-saturated octane in straight FEP tubing with 1 mm I.D. and 25 cm length at room temperature at residence time of 9.8 s (orange line): 5.6 ± 0.8 nm (13.9%), 20 s (blue line): 7.3 ± 1.5 nm (20.0%) and 40 s (green line): 6.9 ± 1.5 nm (21.6%), respectively based on DCS measurement (analyzed immediately after reaction). TEM image of CO-produced Au NPs at pH = 4.06 and residence time of 10 s (b) the product after reaction, inset: zoomed-in area of smaller size particles (c) the product after 6 days and (d) the product after 20 days at room temperature.

Kettemann *et al.* proposed that pH = 5.6 was the optimal final pH value of reactant mixture for reproducible synthesis in Turkevich method due to the maximum concertation of $C_6H_6O_7^{2-}$ for seed formation and equilibrium shift from $[AuCl_4]^-$ to $[AuCl_{4-x}(OH)_x]^-$ for seed growth.[52] Further increasing pH could suppress the reducing ability of citrate. However, this pH range was not applicable for CO reduction as the reactivity of CO steadily increases with pH. CO_3^{2-} produced from CO reduction in alkaline conditions could facilitate the reaction as it makes CO more soluble in aqueous solutions.[252] However, increasing pH has opposing effects as the reactivity of gold speciation decreased after hydroxylation, resulting in suppressed nucleation. **Figure 5-6** shows the average particle size range (8~20 nm) was larger than the Au NPs at pH = 4.06 (5-7 nm) due to slow nucleation rate and fewer nuclei formed during the seed formation stage. The polydispersity also increased (>25%) as the nucleation and growth processes were overlapping, resulting in broad size distribution. When pH = 6.81, the particle size decreased with longer residence time. The residence time was tuned by total flow rate. For shorter residence time, faster velocity increased internal convection inside aqueous droplets. We speculated that if higher concentration of nanoparticles occurred at interface by self-assembling (**Figure C-2**), faster mixing could renew the reactant at the interface to grow the accumulated gold nanostructures. Kulkarni *et al.* successfully synthesized and grew gold nanoparticles by making use of the nanoparticle self-assembly at the water-oil interface.[151] When the flow rate decrease at longer residence time, the growth slowed down, resulting in smaller particles. At pH = 10.67, the average particle size did not change much and showed high polydispersity compared to pH = 5.62. This is because the gold species had less reactivity at high pH, thus both nucleation and growth proceeded slowly. 1 min residence time would be still insufficient compared to the total reaction time needed.

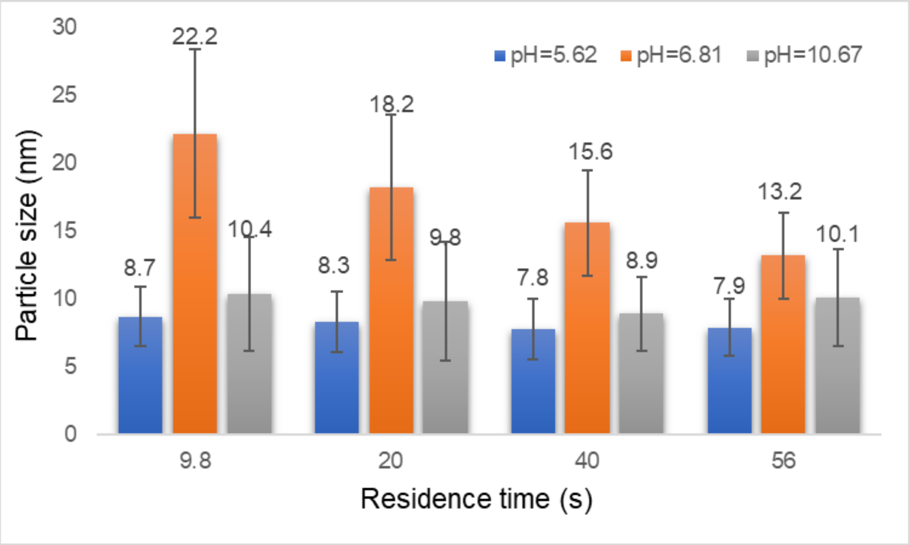

Figure 5-6 Particle size and size distribution of CO-produced Au NPs in Figure 5-4 from 0.27 mM $HAuCl_4$ and CO-saturated octane in straight FEP tubing with 1 mm I.D. and 25 cm length at room temperature at different residence times and initial pH of 5.62, 6.81 and 10.67 based on DCS measurement. Error bars represent the standard deviation of nanoparticle size distribution.

However, increasing the pH led to higher yield. For instance higher absorbance at 400 nm wavelength in UV-Vis was observed at pH = 5.62 (0.75) compared to pH = 4.06 (0.3) in **Figure 5-4**, which is proportional to the Au(0) concentration.[100] A rough estimation about the yield of Au NPs based on DCS result also prove that at residence time of 9.8 s, the yield (18.79%) at pH = 4.06 was lower than the yield (58.16%) at pH = 5.62 (estimated from particle mass measured in DCS with the same 0.1 ml volume of the samples, see **Table C-3**). We speculated that the electrostatic repulsion between nanoparticles at high pH is stronger for citrate-capped Au NPs, which to some extent suppressed interfacial absorption of Au NPs precipitating at water-oil interface. Thus, before further optimization for this liquid-liquid microfluidic set-up, a better control of interfacial absorption effect was required.

5.3.2 Influence of interfacial absorption

The interfacial absorption of nanoparticles in colloidal solution has shown their ability to prevent the decomposition of emulsions.[263] This binding behaviour is affected by particle size, contact angle and oil-water interfacial energy.[264] It was found that a particle with size of a few microns can reform the interface due to its own weight or buoyancy.[264] Two particles at the interface will attract with each other to reduce this deformation, which is known as “Cheerios effect”.[265] This is why particles can self-assemble at the water-oil interface. The contact angle is related to the particle wettability. Since citric acid is nearly insoluble in octane,[266] our citrate-capped Au NPs won’t be wetted by the oil phase. Reynaert *et al.* observed that adding salt or ionic surfactant to the aqueous phase containing charged particles led to aggregation.[267] Thus, the effect of higher amount of citrate on interfacial absorption in our system was investigated by tuning citrate to gold concentration ratio (citrate/Au ratio) with 0.54 mM initial concentration of gold precursor. The pH was maintained ~5.6 at different citrate/Au ratios by adding citric acid. Higher amount of capping agent can increase the stability of the synthesized nanoparticles. However, as citrate is an ionic capping agent, adding too much citrate could increase the ion strength in the solution, which suppresses the electronic double layer of the particles, resulting in aggregation or larger size particles.[268] This phenomenon could be even worse in liquid-liquid flow system as the surface absorption of Au NPs at water-oil interface decrease the distance between particles, which facilitated irreversible aggregation. Three different ratios of citrate to gold (citrate/Au) were tested and the UV-Vis spectra were shown in **Figure 5-7** and **Table 5-6**. The particle size and polydispersity of the as-synthesized Au NPs are shown in **Table 5-7**. Hendel *et al.* found that the absorbance at 400 nm wavelength in UV-Vis has a linear relationship with the Au(0) concentration, which could be used as an estimation for the concentration of the reduced gold.[100] Based on the absorption at 400 nm wavelength, **Figure 5-7** indicated a decreased yield of Au NPs with increasing citrate/Au ratio. In fact, the citrate amount used in our case is not enough to induce the aggregation in single-phase synthesis as Ji *et al.* used similar initial concentration of gold precursor (0.25 mM) like ours (0.27 mM) to produce stable gold nanoparticle colloidal solution at citrate/Au ratio up to 17.5.[269] Thus, we speculated that water-oil interfacial absorption in two-phase flow made the stability of the NPs less tolerant to the ion strength change. Au NPs at high citrate/Au ratio were easier to aggregate and then precipitated on the water-organic interface. This hypothesis could be further proved by studying the absorbance trend at different residence times. When citrate/Au ratio = 6, the absorbance and the particle size increased with longer residence time, which followed the typical particle growth process. However, for citrate/Au ratio = 10 and 12, the absorbance and particle size decreased with longer residence time inside the tubing (e.g. the average particle size at ratio=12 decreased from 6.6 nm to 5.5 nm). We speculated that with the continuous self-assembly for longer operation time, more particles precipitated, resulting in lower yield. Additionally, larger size particles were easier to aggregate, thus only smaller size particle contained in the solution which were detected by further characterization. In conclusion, the longer residence time and higher citrate/Au ratio, the smaller particle size and lower yield obtained. For the products with polydispersity under 15%, stability was tested after three weeks. All the particle size increased, indicating the unfinished reaction in the reactor.

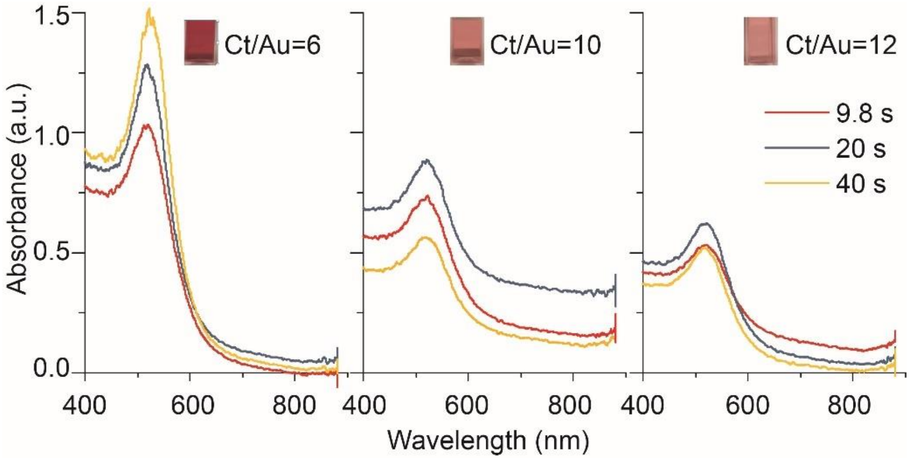

Figure 5-7 UV-vis spectra of CO-produced Au NPs from 0.27 mM $HAuCl_4$ and CO-saturated octane at initial pH ~5.6 (maintained by adding citric acid) in straight FEP tubing with 1 mm I.D. and 25 cm length at room temperature at different residence times and citrate to gold concentration ratios. Inset: colour of the products at residence time of 9.8 s at different citrate to gold ratios.

Table 5-6 Conclusion of UV-Vis peak absorbance and wavelength range of plasmon peak in Figure 5-7.

Initial Ct/Au	**RT = 9.8 s Peak absorbance**	**RT = 20 s Peak absorbance**	**RT = 40 s Peak absorbance**	**Wavelength range of plasmon peak (9.8 s to 56 s) (nm)**
6	1.018	0.730	0.530	518.0 to 521.6
10	1.274	0.880	0.530	~ 518.0
12	1.517	0.564	0.617	~ 518.1

Table 5-7 Particle size and polydispersity of CO-produced Au NPs in Figure 5-7 based on DCS measurements. The products with polydispersity under 15% were tested for stability after 3 weeks.

Citrate/Au ratio	Mixture pH	RT = 9.8 s	RT = 20 s	RT = 40 s
6	5.58	5.5 ± 1.5 nm (27.1%)	5.9 ± 1.1 nm (19.0%)	7.2 ± 2.1 nm (29.4%)
10	5.69	6.3 ± 0.7 (11.7%) 7.5±0.9 nm (11.9%) _after 3 weeks	6.6 ± 1.4 nm (21.9%)	6.2 ± 1.7 nm (26.8%)
12	5.61	6.6 ± 0.8 nm (12.1%) 7.0 ± 1.2 nm (16.9%) _after 3 weeks	6.0 ± 1.7 nm (12.9%) 6.9 ± 0.9 nm (12.6%) _after 3 weeks	5.5 ± 1.5 nm (27.1%)

Based on above experiments, we speculated that the unpredictable particle size trend was due to the particle loss from interfacial absorption. The existence of surface absorption could be further proved by changing the inner diameter of the tubing. If the loss of the yield was caused by interfacial absorption, the smaller inner diameter with higher surface-to-volume ratio (8.72 at 0.5 mm I.D. vs. 4.95 at 1 mm I.D., see **Table C-1**) would aggravate the loss. The colour of the products (**Figure 5-8a)** from larger tube was darker than 0.5 mm I.D. tube, which was in accordance with the yield indicated in **Figure 5-8b** (estimated based on DCS results, details see **Table C-4**). For both initial concentration of gold precursor, the yield of Au NPs from 0.5 mm I.D. tubing was lower than 1 mm I.D. tubing (22.71% vs. 58.16% at 0.27 mM, 6.60 % vs. 26.70% at 1.08 mM). The decrease of the yield with higher surface-to-volume ratio proved the big influence of interfacial absorption. In addition to the material loss, the occurrence of interfacial absorption can also affect the size and size distribution of the particles that remain. The influence became more obvious at higher initial concentration of gold precursor. The yield decreased from 58.16% (0.27 mM) to 26.70% (1.08 mM) with the same 1 mm I.D. tube due to the easier precipitation from interfacial absorption at high reactant concentration.

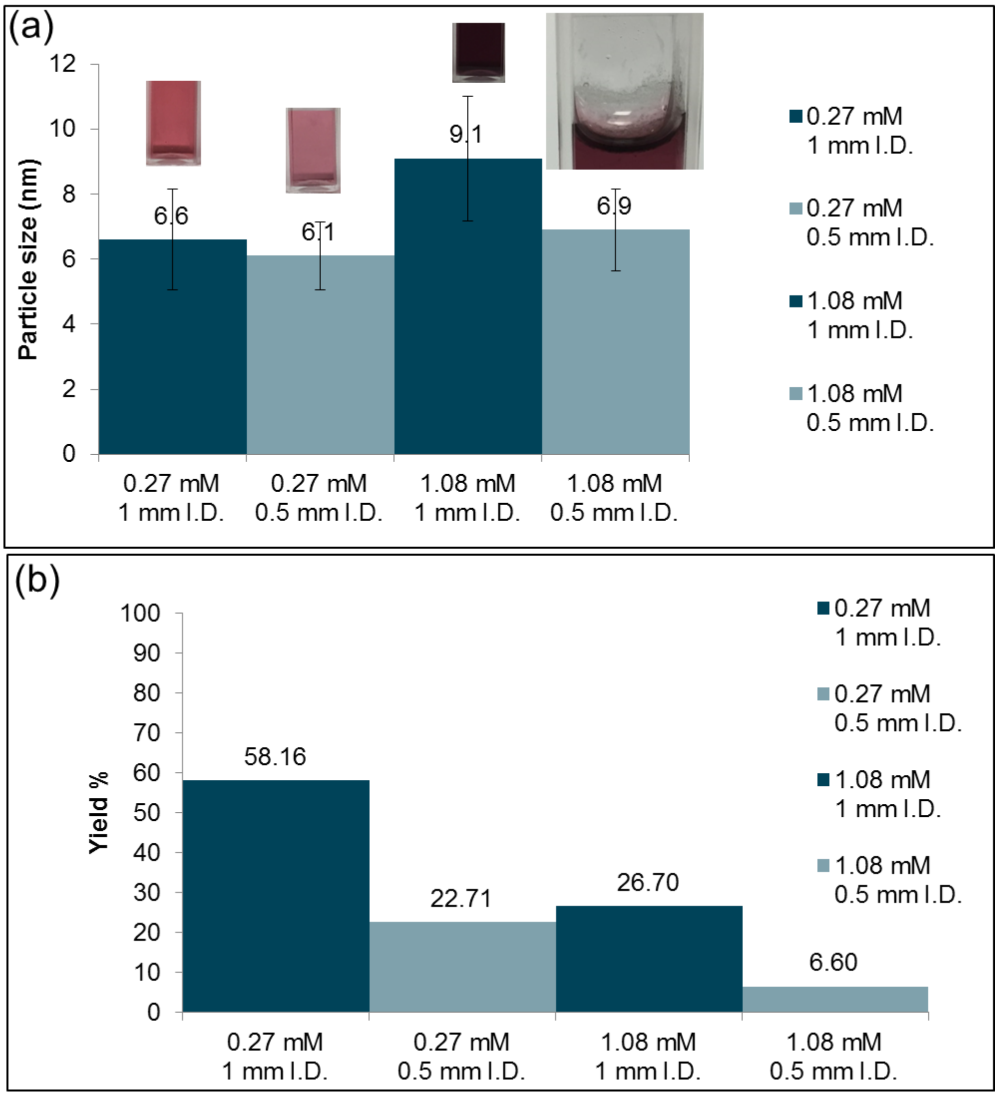

Figure 5-8 (a) Particle size of CO-produced Au NPs from aqueous $HAuCl_4$ and CO-saturated octane in straight FEP tubing with different inner diameters (0.5 mm and 1 mm I.D.) and 25 cm length at room temperature, residence time of 9.8 s and citrate/Au concentration ratio=12, Inset: colour of the products at different experimental conditions, as well as the most severe black precipitation obtained at 1.08 mM and 0.5 mm I.D. tubing. Error bars represent the standard deviation of nanoparticle size distribution. (b) The comparison of the yield estimated from particle mass from 0.1 ml sample measured in DCS.

We speculated that the main reason why interfacial absorption was so serious was the charged stabilizer we used. The capping ability of citrate relies on the electrostatic repulsion. The binding strength of COO^- onto gold surface is also weak. Thus, the aggregation of citrate-capped Au NPs is irreversible. Once the particles assembled and aggregated, there was no chance to re-disperse. Based on the above investigation, stronger capping agent was necessary to mitigate the effects of interfacial absorption. For example, Au NPs conjugated with thiol-based molecules could be re-dispersed after drying. This means that even though particles might still self-assemble onto the interface, no irreversible aggregation or precipitation would occur. The product could retain in the solution without material loss. Thus, different kinds of thiol were employed for later liquid-liquid flow synthesis.

5.3.3 Au NPs synthesis with hydrophobic thiol

As the typical capping agent in Brust-Schiffrin method, thiols were widely used for Au NPs synthesis due to strong capping ability. Firstly, 1-Dodecanethiol (DDT) was tried for Au NPs synthesis in CO reduction, which can provide steric repulsion to stabilize Au NPs. As DDT was soluble in organic phase, single phase was used to conduct the reduction in the solvent with higher solubility of CO. The 2 mM $HAuCl_4$ was phase transferred into toluene from an aqueous phase using 8.8 mM TOAB as phase transfer catalyst. The use of TOAB is necessary to make sure hydrophobic thiol could react with Au (III) species.[270] Then toluene stream with gold precursor was mixed with CO-saturated heptane containing different concentrations of 1-Dodecanethiol (DDT) via dolomite microchip mixer at the same flow rate of 0.045 ml/min. The residence time in 1 mm I.D. CFI (355 cm in length, 2.8 ml in volume) was 30 min. The products were characterized by TEM and shown in **Figure 5-9**. For thiol/Au ratio = 1, the amount of thiol was not enough to fully convert the Au(III) to Au(I) as colour of the solution was still pale yellow. After 30 min of reaction with CO, the colour of the product was like the original gold precursor. For thiol/Au ratio = 8, the solution became colourless once mixed with capping agent, indicating Au(I) was formed. However, there was also no change of the colour after 30 min reduction. The particles observed via TEM shows decreased size at higher thiol/Au ratio. The productivity was unsatisfactory as typical DDT-capped Au NPs from Brust-Shiffrin method should have dark brown colour. However, there is still some useful information that could be extracted from the preliminary trial. Firstly, CO has the ability to reduce thiol-Au(I) complexes (particles observed from TEM image), even though the reduction rate was slower than $NaBH_4$. Secondly, the thiol with long chain length (higher linear C-H numbers) stabilized the synthesized Au NPs by steric repulsion, which hampered the Au(III) species from reducing agent and further suppressed the reduction. Lastly, unlike the reduction mechanism observed when citrate was the capping agent, the thiol-capped Au NPs reduced by CO maintained relatively small size as the growth was passivated by strong capping agent of thiol without the risk of nuclei aggregation. Thus, the particle size could continuously decrease with more thiol.

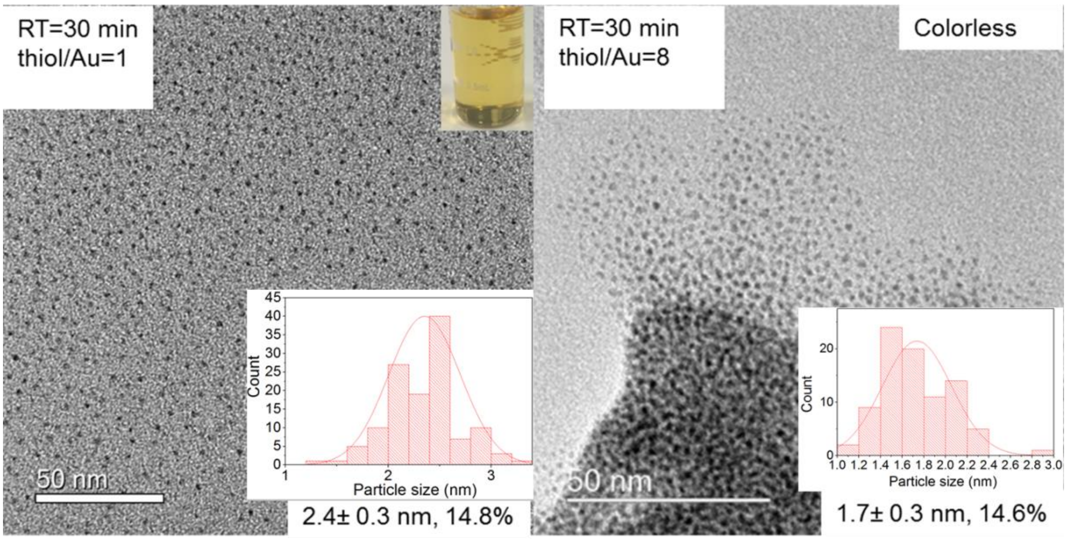

Figure 5-9 TEM images of DDT-capped Au NPs from single-phase mixture of 1 mM $HAuCl_4$ & 4.4 mM TOAB in toluene and CO-saturated heptane inside 1 mm I.D. FEP CFI with 355 cm length at room temperature, residence time of 30 min and different thiol to gold ratio. Inset: colour of the product at thiol/Au ratio = 1.

5.3.4 Au NPs synthesis with water-soluble thiol

Shimmin *et al.* proposed that polar thiol could enhance the nucleation by coordinating the functional groups with gold atoms.[81] Furthermore, Shon *et al.* demonstrated that gold atoms did not irreversibly fix to a single thiol molecule throughout the reaction, which also had opportunity to coordinate to PEG.[271] Thus, Shimmin *et al.* gave a new hypothesis that PEG and possibly other polar polymers could enhance the nucleation by directing gold atoms to unstably small gold clusters to form nuclei with higher stability at early stages of reduction. Thus, growth terminated and smaller particle size was obtained because of depleted gold supply with fast nucleation rate. Even though this was only a speculation, the water-soluble thiols were still worthy to try in the purpose of decreasing overall reaction time.

The products were usually called monolayer protected clusters (MPCs), which exhibited molecular or bulk metallic properties depending upon their size.[272] The synthetic route was divided into two steps:[46] Au(I)-thiolate complexes formation by thiol ligands and MPCs synthesis by strong reducing agent. The later work emphasized the importance of Au(I)-thiolate complexes as the X-ray crystal structure of MPCs consisted of a metallic core surrounded by Au(I)-S bonds “staple structures”.[273] Thus, tiopronin was firstly used to adapt the synthesis of water-soluble MPCs into microfluidic system via two-step reaction. The solid tiopronin was dissolved in 1 mM aqueous $HAuCl_4$ solution and left for one night to form Au(I)-thiolate complexes. The pH was tuned to 11.5 with NaOH to increase the solubility of Au(I)-thiolate complexes. Then the second step of MPCs formation was conducted by mixing Au(I)-thiolate complexes with CO-saturated heptane via T mixer at volumetric flow ratio of 1/2 in FEP CFI with 1 mm I.D. and 2.8 ml in volume. The TEM images and UV-Vis spectra of tiopronin-capped MPCs are shown in **Figure 5-10.** The residence time of 14 h was achieved by creating the droplet flow inside the CFI and storing the droplets in CFI for 14 h. The average particle size based on TEM did not change much with longer residence time, whereas the yield increased as the absorbance of UV-Vis spectra increased. This proved that the synthetic pathway of thiol-capped gold in CO reduction followed similar nucleation-passivated growth processes in the Brust-Schiffrin method, in which longer residence time could only affect the productivity, whereas the particle size do not change much.[30]

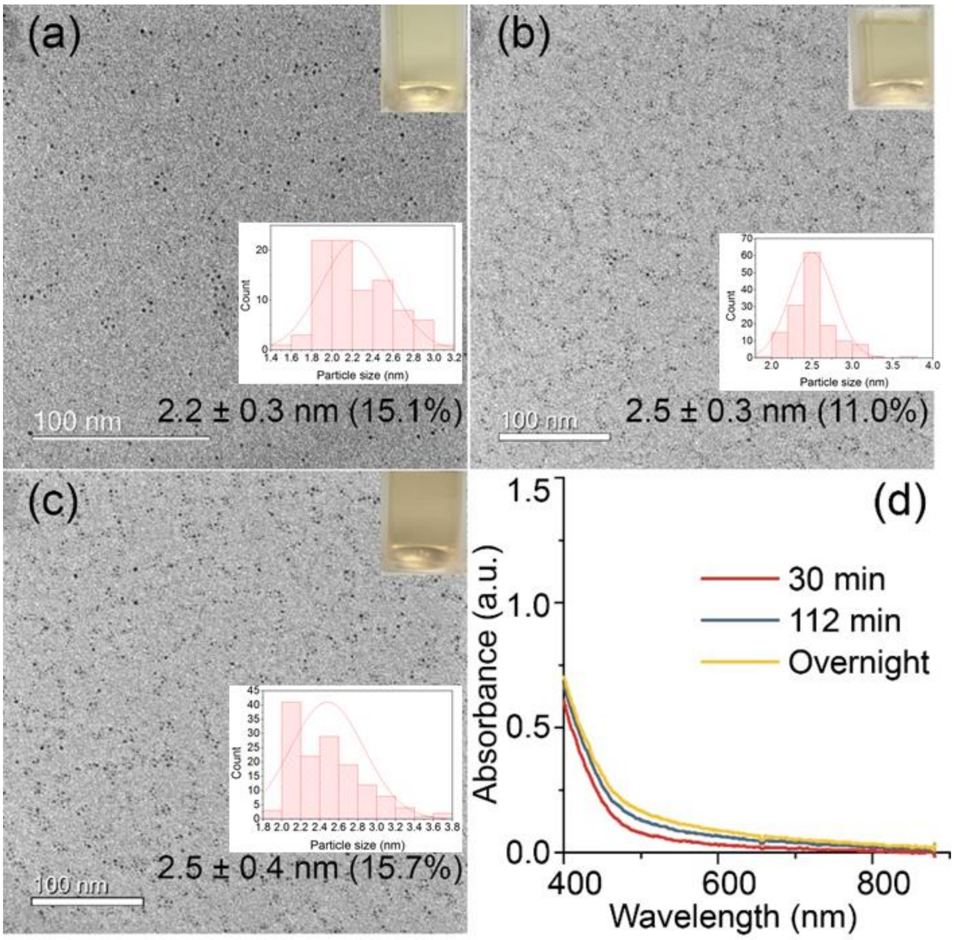

Figure 5-10 TEM images of tiopronin-capped monolayer protected clusters (MPCs) from segmented flow of 1 mM aqueous thiolate-Au(I) (tiopronin/Au=1) and CO-saturated heptane in 1 mm I.D. FEP CFI with 355 length at room temperature and different residence times of (a) 30 min, (b) 112 min and (c) 14 h. Insets: colour of the products. (d) UV-Vis spectra of as-synthesized MPCs.

Even though the preliminary study demonstrated the feasibility of the Au MPCs synthesis in flow, the reaction time is still unfavourably long for continuous flow synthesis at high volumes. In the original protocol, the gold precursor first forms thiolate-Au(I) complexes at alkaline conditions with tiopronin. The reduction rate of CO with Au(I)-thiolate complexes was slower than immediate reacting with Au(III) ions. To promote the reduction rate, the aqueous solution at pH ~11.7

was prepared as two separate streams: one is acidic gold precursor with 1 mM $[AuCl_4]^-$ ions, another stream is the alkaline 1 mM tiopronin solution tuned by NaOH. The thiol was added with base as the tiopronin forms precipitate with $HAuCl_4$ at acidic condition which could result in clogging inside the mixer. These two streams were mixed through a micromixer chip (Dolomite, Part No. 3000144) several seconds in advance before mixing with CO-saturated heptane stream at volumetric flow ratio of 1/1/4 (total flow rates were 0.9 ml/min at residence time of 3 min, 0.4 ml/min at residence time of 7 min, 0.2 ml/min at residence time of 14 min). **Figure 5-11** shows the TEM and UV-Vis spectra of synthesized Au MPCs after modifying the tiopronin incubation time (from 2 h to few seconds) before reacting with CO. The absorbance at wavelength of 400 nm (~1.25) in UV-Vis was higher than that in **Figure 5-10** (~0.7), indicating more gold were reduced to Au(0).[100] Two different sizes of nanoparticles were observed via TEM. There were some small particles around 1-2 nm dispersed on TEM grid. The larger particles with similar size of 3.6 nm assembled in line with multiple orientations to form a twinned cluster of nanoparticles (**a**), which could be also observed during the samples with longer residence time (**b and c**). The absorbance peak at wavelength of around 500 nm in UV-Vis was mainly contributed by these larger size particles. The reason for the formation of nanoparticles with two different average sizes was the occurrence of two reduction rates during the synthesis. The mixture of gold precursor and tiopronin quickly contacted with CO and the residence time was too short for thiol to bind and reduce Au(III). Thus, part of the gold ions were reduced by CO as Au(I)-thiolate complexes like typical two-step reaction to form 1-2 nm particles, whereas others were reduced by CO as form of Au(III) as thiol haven't got enough time to bind onto the gold surface. This short time difference between gold reduction and thiol binding gave an opportunity to grow to the size of around 3.6 nm. As the tiopronin-gold molecule could form straight chain or ring structure **Figure 5-11e**),[274] the synthesized gold nanoparticles linked by tiopronin assembled in line or twisted in different orientations to form the clusters assembled by individual nanoparticles shown in **Figure 5-11a**. The result suggested that using the Au(III) species before protecting by thiol could enhance the reduction rate. However, there were several parallel reactions occurring inside the CFI: the thiol reduction to form thiolate-Au (I) complexes and the CO reduction on gold (III) ions or thiolate-Au (I) complexes:

$AuCl_4^-+HS\text{-}R \rightarrow (\text{-}Au^+SR\text{-})_n$

$2AuCl_4^-+3CO+6\ H_2O \rightarrow 2Au^0+3HCO_3^-+9H^++8Cl^-$

$CO+2HS\text{-}Au^++2H_2O \rightarrow 2Au^0+HCO_3^-+3H^+$

The fast reduction with different rates could form different particle sizes. Thus, preparing fully-converted thiolate-Au (I) complexes solution is necessary for the synthesis of monodisperse MPCs.

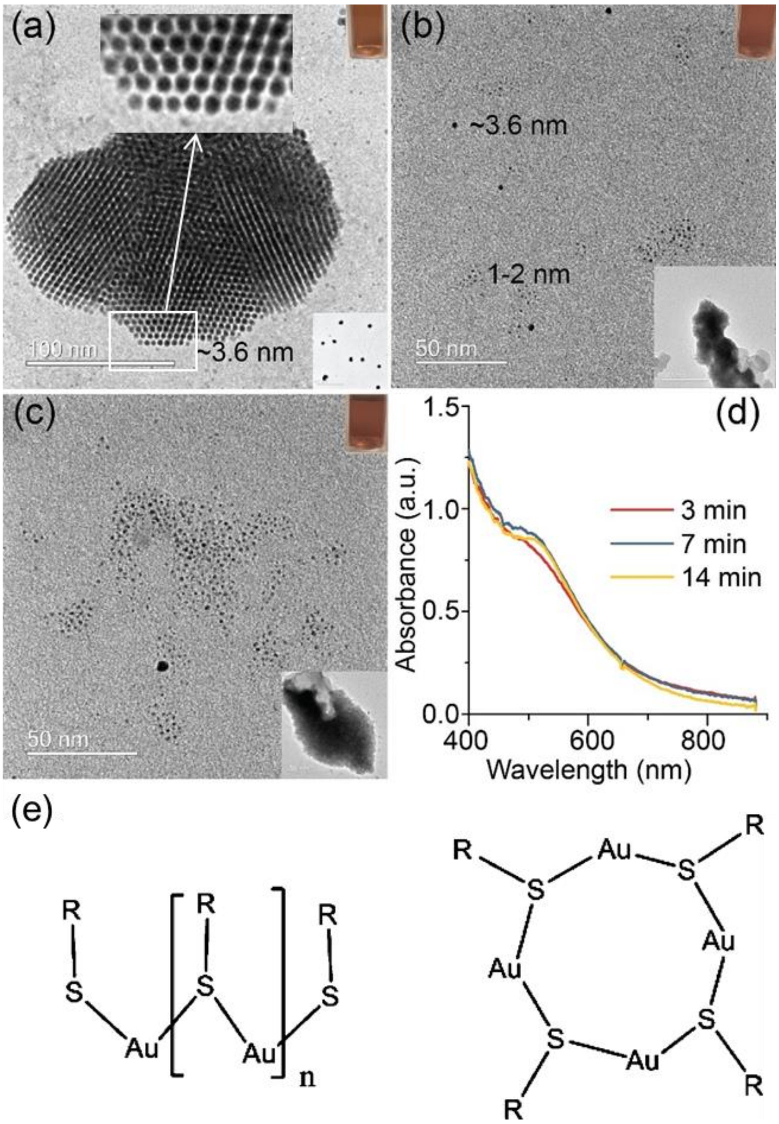

Figure 5-11 TEM images of tiopronin-capped MPCs from segmented flow of 1 mM aqueous thiolate-Au(I) (tiopronin/Au=1) and CO-saturated heptane in 1 mm I.D. FEP CFI with 355 length at room temperature and different residence times of (a) 3 min, (b) 7 min and (c) 14 min. Insets: right top:colour of the products, right bottom: overview of the TEM grid full of assembled structure with scale bar of (a)2 um, (b) and (c): 200 nm. (d) UV-Vis spectra of as-synthesized gold nanoparticles. (e) Proposed structures for precursor molecule (reprinted with permission from ref.[274] Copyright 2012, American Chemical Society).

To decrease the reaction time, elevated temperature was investigated as it could increase the reduction rate of thiolate-Au(I) complexes.[64] The synthesized products at a residence time of 15 min (CO-saturated heptane flow rate of 0.12 ml/min and aqueous thiolated-Au(I) flow rate of 0.12 ml/min) inside 1 mm I.D. FEP CFI with length of 355 cm at tiopronin/Au concentration ratio=1 and different temperatures were shown in **Figure 5-12**. The absorbance of the peak at 400 nm in UV-Vis increased with higher temperature, suggesting more gold was reduced. The products at 60 °C and 80 °C had similar size compared to the products at room temperature (**Figure 5-10**). It is worthy to note that it only took 15 min to achieve the absorbance of 0.9 at 400 nm at 80 °C, whereas at room temperature the absorbance was 0.7 with much longer reaction time of 14 h. For similar product, the reaction time largely decreased by using higher temperature up to 80 °C. However, for higher temperature (100 °C and 120 °C), the particle size increased to around 3 nm with broader size distribution (polydispersity > 20%). This might either be due to uncontrollable reduction or insufficient capping agent to prevent particle growth. During higher temperature, the reduction was quite fast, the formation of protecting layer was limited due to the insufficient thiol in the system. Therefore, the synthesized particles grew large before being stabilized by thiols.

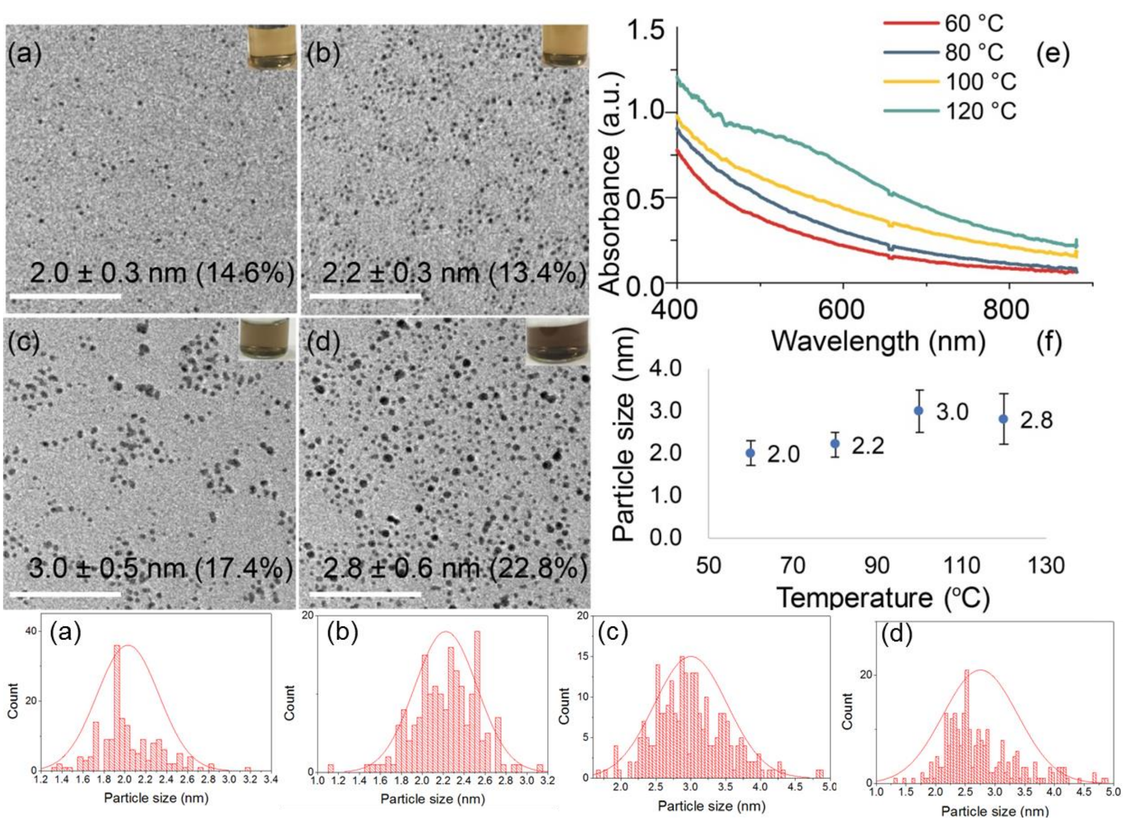

Figure 5-12 TEM images (bottom: size distribution) of tiopronin-capped MPCs at a residence time of 15 min (CO-saturated heptane flow rate of 0.12 ml/min and 1 mM aqueous thiolated-Au(I) flow rate of 0.06 ml/min) inside 1 mm I.D. FEP CFI with length of 355 cm at tiopronin/Au concentration ratio=1 and different temperatures of (a) 60 °C, (b) 80 °C, (c) 100 °C and (d) 120 °C. Insets: colour of the products. The scale bar was 50 nm. (e) UV-Vis spectra and (f) conclusion of particle size of as-synthesized MPCs based on TEM images, error bars represent the standard deviation of nanoparticle size distribution.

To give better protection of synthesized Au MPCs, higher concentration ratio of tiopronin to gold precursor (tiopronin/Au ratio) was investigated. The synthesized products with a residence time of 18 min are shown in **Figure 5-13**. Except the product at tiopronin/Au ratio = 1, all others were colourless solution. Thus, UV-Vis was not used and the particle size was determined by TEM There were some numerically rare large-particle outliers (>3 nm) observed in the TEM shown in **Figure 5-13b** to **Figure 5-13d**. With larger tiopronin/Au ratio, the amount and the size of large-particles decreased. Thus, increasing the tiopronin/Au ratio was an efficient way to give better control of the reaction, resulting in monodisperse particles with smaller size at high temperature of 120 °C (from 3.3 nm, polydispersity of 22.8% at ratio of 1 in **Figure 5-12d** to 1.5 nm and polydispersity <15% at ratio of 8 in **Figure 5-13d**). However, at tiopronin/Au ratio=10, multi-sized particles were formed (**Figure 5-13e)** and the mean particle size increased again. The small particles did form but they were the minority product and most of the gold precursor was consumed for large particles. A similar U-shape size trend (**Figure 5-13f**) with increasing thiol to gold ratio was observed by Chen *et al.* who speculated that the excess thiol broke down the Au (I)-thiolate complexes to short length which could only stabilize large Au cores and large NPs.[275] Thus, the thiol to gold ratio could not be limitlessly increased.

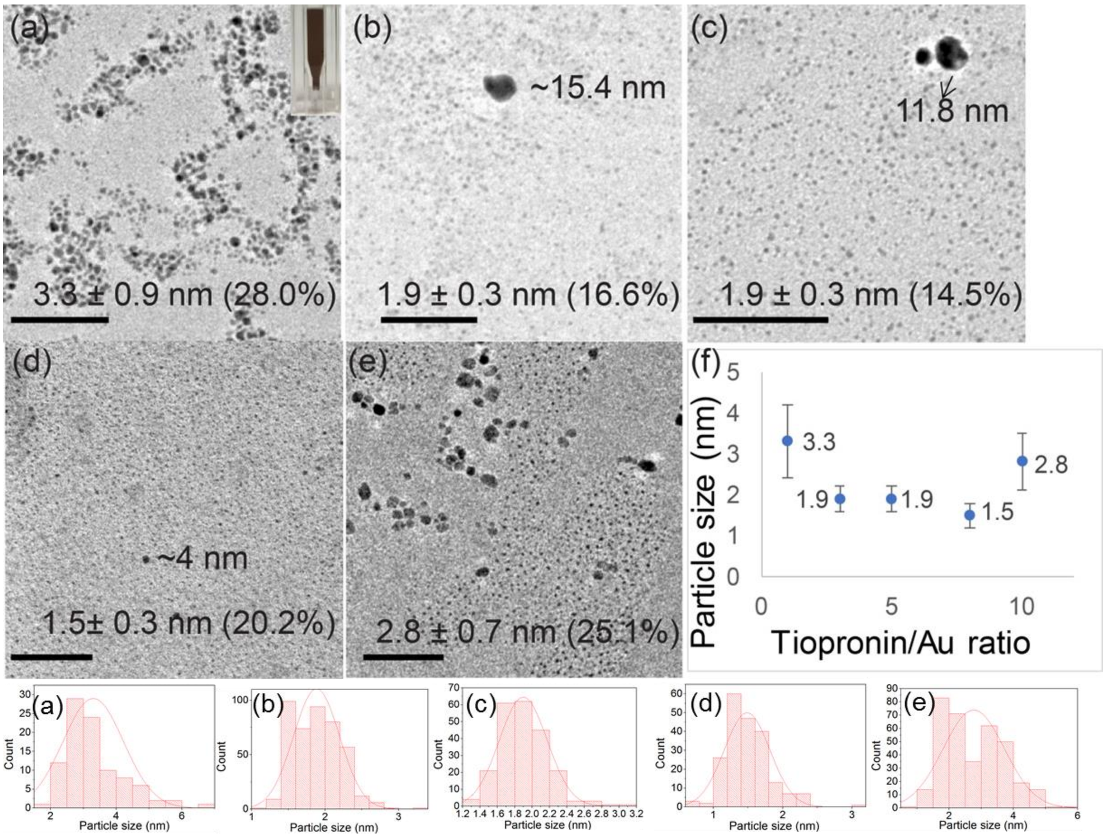

Figure 5-13 TEM images (bottom: size distribution) of tiopronin-capped MPCs at a residence time of 18 min (CO-saturated heptane flow rate of 0.216 ml/min and 1 mM aqueous thiolated-Au(I) flow rate of 0.108 ml/min) inside 1.55 mm I.D. PFA CFI with length of 254 cm at temperature of 120 °C and different tiopronin/Au concentration ratio of (a) 1 (insets: colour of the product), (b) 3, (c) 5, (d) 8 and (e) 10. The scale bar was 50 nm (f) conclusion of particle size of MPCs based on TEM images, error bars represent the standard deviation of nanoparticle size distribution.

Another water-soluble thiol with amine group, cysteine, was tested to substitute tiopronin for MPCs synthesis at the same experimental conditions. The TEM images of synthesized products were shown in **Figure 5-14**. The products turned to colourless with higher cysteine/Au ratio like the tiopronin-capped MPCs and similar U-shape size trend was observed. The syntheses showed a decrease in nanoparticle size with increasing Cys/Au ratio up to 5.

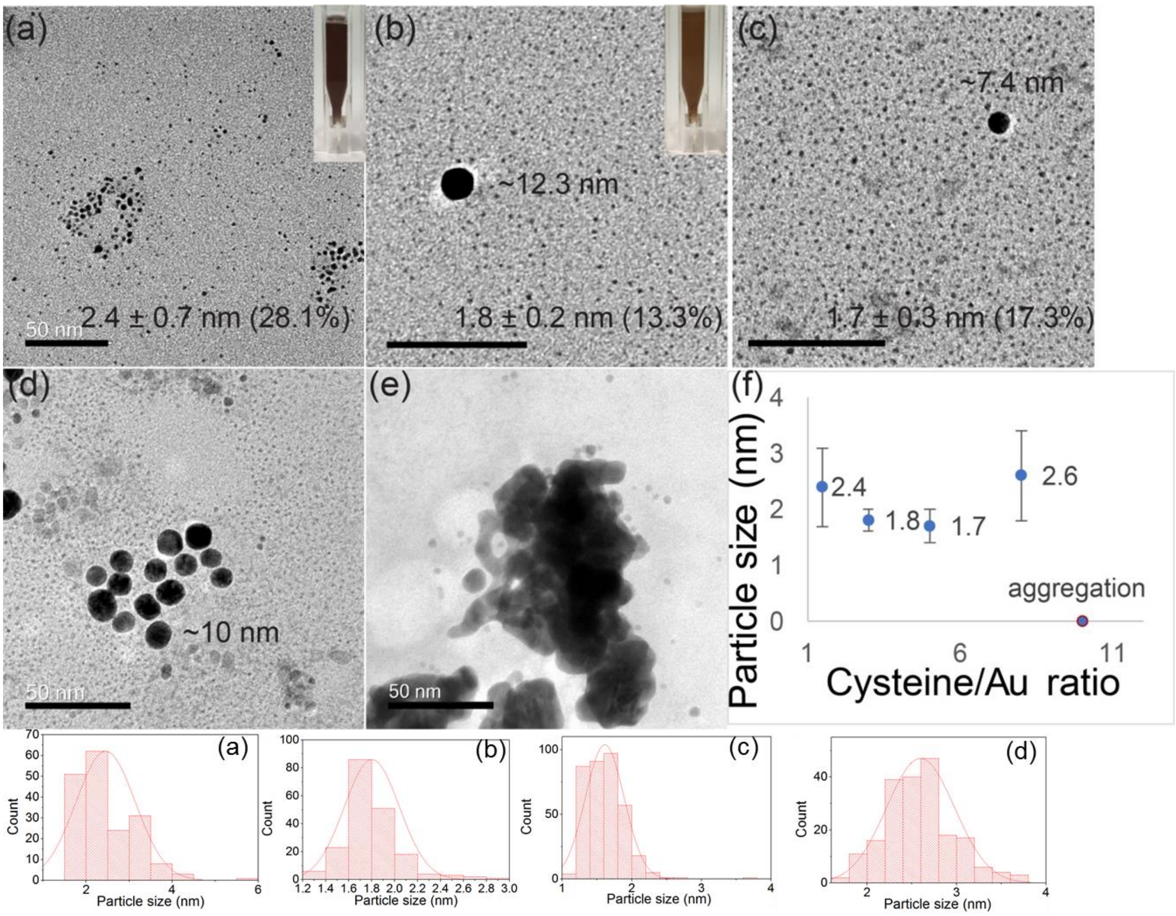

Figure 5-14 TEM images of cysteine-capped MPCs at a residence time of 18 min (CO-saturated heptane flow rate of 0.216 ml/min and 1 mM aqueous thiolated-Au(I) flow rate of 0.108 ml/min) inside 1.55 mm I.D. PFA CFI with length of 254 cm at temperature of 120 °C and different cysteine/Au concentration ratio of (a) 1.5 (insets: colour of the product), (b) 3, (c) 5, (d) 8 and (e) 10. The scale bar was 50 nm (f) conclusion of particle size of MPCs based on TEM images; error bars represent the standard deviation of nanoparticle size distribution.

The thiol/Au ratio was chosen to produce the smallest particle size based on above results and the particle sizes at different inner diameters of the tube are shown in **Figure 5-15**. Compared to citrate-capping reduction, stronger capping agent of thiol solved the issue of the precipitation caused by interfacial absorption in water-organic phase as no black precipitation observed at the water-heptane interface. Thus, the inner diameter of the reactor could only affect the CO mass transfer due to different surface-to-volume ratio (from 3.67 to 9.90 with decreasing inner diameter, see **Table C-2**). As the CO supply in the proposed set-up was sufficient (CO in heptane/CO needed for the reduction of 1 mM thiolated-Au (I) = 233.6, the molar ratio of CO/1 mM thiolated-Au(I) = 116.8 at heptane/water flow ratio of 2), the, difference of particle size was not obvious with decreasing tube diameter.

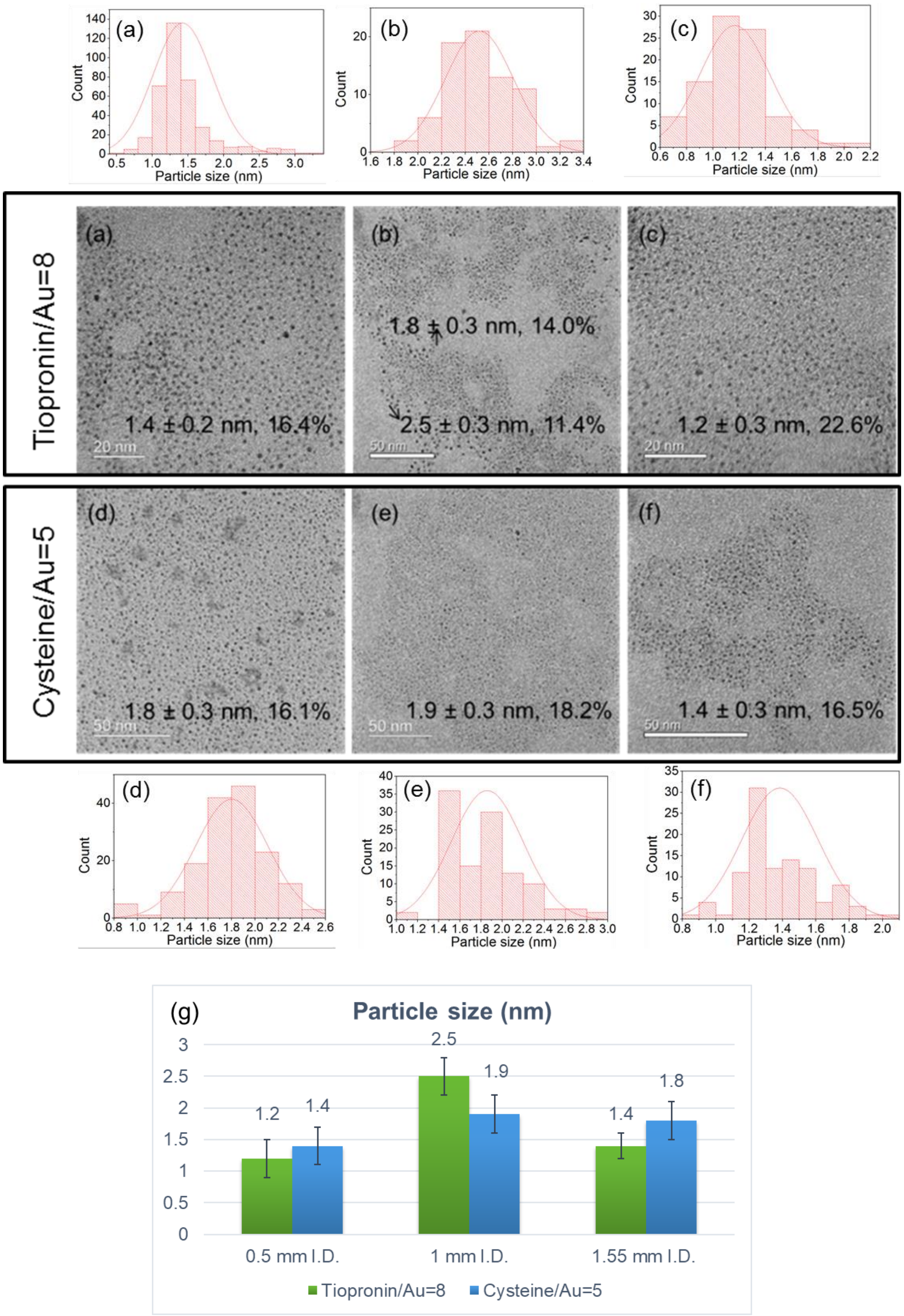

Figure 5-15 TEM images and particle size distributions of water-soluble thiolated MPCs (CO-saturated heptane and 1 mM aqueous thiolated-Au(I) at flow ratio of 2 at temperature of 120 °C, residence time of 32.4 min and cysteine/Au concentration ratio of 5 and tiopronin/Au concentration ratio of 8 in (a) and (d) 1.55 mm I.D. PFA CFI with length of 254 cm, (b) and (e) 1 mm I.D. PFA CFI with length of 355 cm and (c) and (f) 0.5 mm I.D. PFA CFI with length

of 900 cm; (g) conclusion of particle size of MPCs based on TEM images; error bars represent the standard deviation of nanoparticle size distribution.

The yield of synthesized MPCs measured by ICP[*] based on the gold amount from digested precipitate is shown in **Figure 5-16**. Similar productivity for the samples with the same capping agent but different CFIs proved that interfacial absorption did not occur when a stronger capping agent was used. Overall, the yield of tiopronin-capped MPCs was lower than cysteine-capped MPCs, Thus, cysteine seems to be the best as a capping agent during MPCs synthesis in microfluidic system with CO-saturated organic solution by tube-in-tube set-up.

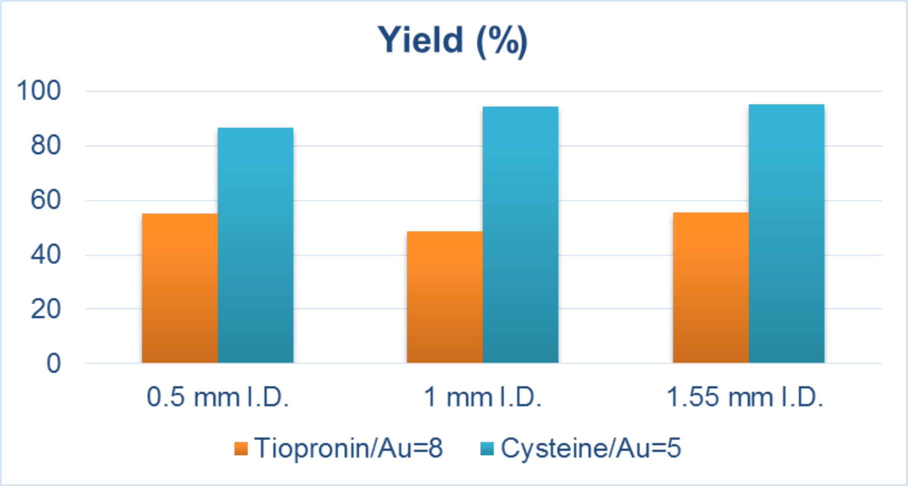

Figure 5-16 Yield based on ICP analysis of water-soluble thiolated MPCs (CO-saturated heptane and 1 mM aqueous thiolated-Au(I) at flow ratio of 2 at temperature of 120 °C, residence time of 32.4 min and cysteine/Au concentration ratio of 5 and tiopronin/Au concentration ratio of 8 in PFA CFI with different inner diameter and length (1.55 mm I.D. PFA CFI with length of 254 cm, 1 mm I.D. PFA CFI with length of 355 cm and 0.5 mm I.D. PFA CFI with length of 900 cm).

---

[*] *The ICP measurement was carried out by Ms Becki Belgrave, University College London.*

5.4 Conclusion

In this chapter, a new set-up consisting of a Teflon AF-2400 tube-in-tube saturator and different kinds of microreactors were tested to synthesize gold nanoparticles via CO reduction. The gaseous CO was pre-dissolved in an organic phase and then reacted with gold precursor in water-organic two-phase flow. Interfacial absorption was problematic when using weak capping agent in water-organic two-phase flow in microreactors. The experiments showed unpredictable particle size trend and broad size distribution due to either aggregation facilitated by NPs self-assembly, or different growth rate between interface and bulk solution. The high concentration of NPs at the interface created by interfacial absorption consumed reactants faster than dispersed NPs in solution for further growth. In addition, yield of the citrate-capped Au NPs decreased at higher reactant concentrations or using smaller inner diameter tubing (higher surface-to-volume ratio). This is because interfacial absorption led to aggregation of NPs due to closer distances during self-assembly. Citrate-capped Au NPs will continuously grow and aggregate to larger size until precipitate are formed, resulting in material loss. Thus, the capping agent should be strong enough to prevent irreversible aggregation from self-assembling of synthesized gold nanoparticles at water-oil interface.

Various thiols (both hydrophobic and polar) were employed, which showed good performance in preventing the black precipitation at interface and material loss. The experiment showed that in order to obtain monodisperse NPs, it might be best to leave enough time for thiol to reduce the Au(III) species to thiolated-Au(I) complexes before introducing CO for NPs formation. The reaction rate was suppressed at room temperature, especially for the reduction of hydrophobic thiolate-Au (I) complexes. The reduction rate was increased by employing polar thiols (tiopronin and cysteine) and heating. Similar yield of the thiol-capped Au NPs synthesized from CFIs with different inner diameter tubing in water-heptane two-phase flow confirmed that the polar thiol effectively weakened the negative influence of interfacial absorption. By tuning the temperature and thiol/gold ratio, the particle size could be tailored to around 1.5 nm (polydispersity < 15%) at cysteine/Au concentration ratio of 8 (1 mM initial concentration of gold precursor), temperature of 120 °C and residence time of 30 min (yield > 95%) in water-heptane (CO-saturated) segmented microfluidic system.

6. Rapid and High-yield Synthesis of $Au_{25}(Cys)_{18}$ Nanoclusters via Carbon Monoxide in Liquid-Liquid Microfluidic Segmented Flow system and their antimicrobial performance

6.1 Introduction

In the last chapter, ultra-small size water-soluble monolayer protected clusters (MPC) (~1.5 nm based on transmission electron microscopy, TEM) were successfully produced in the water-heptane (CO-saturated) microfluidic segmented flow system. Even though we called them clusters, it was not confirmed the actual cluster number at atomic level due to the limitation of TEM. To further explore this system, the synthesis of atomically precise nanoclusters was tried by employing electrospray ionization mass spectrometry (ESI-MS) for cluster size determination. Atomically precise gold nanoclusters (Au NCs) contain discrete numbers of gold atoms with a defined ligand shell.[276] Due to their small size they exhibit quantum size effects and have drawn significant attention in recent years due to their unusual molecular-like properties, such as discrete electronic transitions for enhanced optical properties,[79] photoluminescence for bio-labels,[277] quantized charging for self-assembly control[278] and atomically precise size for catalysis.[279] Among Au NCs, thiolated Au NCs, especially $Au_{25}(SR)_{18}$ nanoclusters, are extensively investigated owing to their high thermodynamic stability in the presence of excess thiol ligands.[280]

Typically, the Au NCs protected by thiol ligands are produced with the use of a strong reducing agent (such as sodium borohydride, $NaBH_4$) to reduce thiolate-

Au(I) complexes,[66] which typically first lead to mixture of different cluster sizes due to the fast and uncontrolled reduction kinetics akin to the rapid formation of small gold nanoparticles (Au NPs) by similar methods.[47] It has been well established that during this stage, using lower temperatures (e.g. ice-cold solutions) to suppress the reducing ability of $NaBH_4$ is helpful to control the size distribution of the Au NPs.[47, 281] A similar strategy was also utilized during the synthesis of Au NCs by adding $NaBH_4$ to a thiolate-Au(I) solution at 0°C.[282] In this case a high purity of $[Au_{25}(SR)_{18}]$, which has the highest thermodynamic stability,[62] could be obtained with long aging times under the gentle environment created due to the etching effect by excess thiol ligands.[280] The free thiol can remove the gold atoms from the synthesized $Au_n(SR)_m$ clusters to participate growth of more stable clusters. As this stage is thermodynamically controlled, the general synthetic time could be a few hours to days [65-67] in order to leave enough time for cluster size evolution and focusing. During this “size-focusing” stage, heating, which is the most efficient method of energy input, is favourable to facilitate the transformation process of mix-sized Au NCs into more thermodynamic stable Au NCs of atomic precision and can decrease the total reaction time required.[64] Considering the conflicted favourable conditions at different synthetic stages, Qian and Jin used a two-step method to synthesize high purity $Au_{144}(SCH_2CH_2Ph)_{60}$ nanoclusters, comprising a modified Brust-Schiffrin method for first-stage reduction and an addition of excess thiol at 80 °C for 24 h to finish the size-focusing stage.[283] Katla *et al.* sacrificed product purity to develop a one-pot synthesis at an elevated temperature (60 °C) to speed up the aging process and the whole reaction time could be reduced to 2 h.[69] Besides the adjustment of temperature, Yuan *et al.*[68] made use of adding NaOH to tame the reducing ability of $NaBH_4$, as well as increasing the etching ability of thiols to synthesize $Au_{25}(SR)_{18}$ clusters. Based on this work, Chen *et al.*[64] further studied the temperature effect on the atomically precise nanoclusters formation and concluded that 40 °C is the optimal temperature for $NaBH_4$ reduction to speed up the reaction rate without further irreversible transformation into mix-sized Au NCs in aqueous solutions.

Instead of using $NaBH_4$, Xie's group proposed a new reduction system utilising gaseous carbon monoxide as a substitute for strong reducing agents to direct a slow and size-controlled synthesis of $[Au_{25}(SR)_{18}]$, which leads to a highly pure product at room temperature.[252] The mechanism of $[Au_{25}(SR)_{18}]$ formation was investigated extensively by the same group under CO reduction to show the cluster evolution from Au(I) precursor to final Au_{25} clusters by UV-Vis spectroscopy and electrospray ionization mass spectrometry (ESI-MS).[63] As CO is a mild reducing agent compared to $NaBH_4$, the synthesis time was increased to 72 h, which left enough time for mechanistic study on this two-stage synthesis, as well as characterization of all the intermediate NCs formed throughout the formation. The first stage governed by kinetic control was finished in the first 40 min, which reduced most of Au(I) complexes into NCs with cluster numbers ranging from 4 to 10. Then the remaining time up to 72 h was the slow "size-focusing" growth governed by thermodynamic control to converge all the intermediate NCs to $[Au_{25}(SR)_{18}]$ with high purity. This study also revealed that the reduction rate during the synthesis of $Au_{25}(SR)_{18}$ NCs would not affect the final cluster size, as the same product of Au_{25} NCs was obtained from both $NaBH_4$ and CO reduction. This was also our initial motivation to use a microfluidic system to optimize the synthetic routes, which could provide enhanced mass transfer without affecting the quality of the product. Additionally, the use of this alternate mild reducing agent revealed a potential to develop “One-pot synthetic process” for Au NCs, as there is no need to suppress the reducing agent ability like what previous work did, by adding $NaBH_4$ to a thiolate-Au(I) solution at 0°C for first-stage reduction.[282] Thus, the two-stage synthesis by $NaBH_4$ could be replaced by one-pot synthesis with CO as a mild reducing agent. In Xie’s group work,[252] alkaline condition was employed due to the fact stabilising ability of cysteine is highly dependent on the pH. This resulted in less aggregated thiolate-Au(I) complexes and an increased reduction rate at high pH.[252] Moreover, CO_3^{2-} produced from CO reduction in alkaline conditions could facilitate the reaction as it makes CO more soluble in aqueous solutions.[252].

In this chapter, we present an improved method to fabricate high purity $Au_{25}(Cys)_{18}$ NCs based on the CO-directed synthesis proposed by Yu *et al.*[252] with the aid of a microfluidic segmented flow system at elevated temperatures. Instead of bubbling CO through the solution, we saturated the gaseous reducing agent into heptane in a concentric membrane set-up, which had an enhanced safety profile with fully sealed CO gas (highly toxic) inside the outer tube. The transfer of the CO to the aqueous phase was facilitated by directly contacting the CO saturated heptane with the aqueous stream by forming segmented flow with high interfacial surface areas in a capillary with inner diameter of 1 mm. Thus, the controlled addition of CO could be achieved to the aqueous phase from a high excess CO reservoir. We demonstrate better control of the reaction and the enhanced mass transfer provided by segmented flow and a coiled flow inverter (CFI), to produce more concentrated $Au_{25}(Cys)_{18}$ Au NCs with peak absorbance at 670 nm of up to 3.63 (almost 10 times higher than previously reported) in as little as 3 min which was successful to enhance the antimicrobial activity of crystal violet.

6.2 Experimental

6.2.1 Tube-in-tube set-up and segmented flow system

Figure 6-1 shows the microfluidic segmented flow system which consisted of a tube-in-tube section at room temperature and a coiled flow inverter (CFI) sub-merged inside a stirred glycerol (99.5 %, VWR) bath on a hot plate (Stuart, UC152D with SCT temperature controller) for the synthesis of Au NCs at elevated temperature. The tube-in-tube set-up used Teflon AF-2400 tubing (0.8 mm inner diameter, 1.0 mm outer diameter, Biogeneral USA) as the contacting interface inside a polytetrafluoroethylene (PTFE) tubing (2.4 mm inner diameter,3.2 mm outer diameter, VICI Jour) assembled together by two T-pieces (Upchurch, hole size: 1.0 mm to saturate the heptane fed by HPLC pump (KNAUER, Germany) with up to 203 mM pure CO (BOC gases) in the annulus between the inner and outer tube at 500 kPa maintained by a gas pressure regulator (Swagelok, K series) and monitored by a pressure sensor (40PC150G, Honeywell) placed at the inlet of the annulus. A microfluidic CFI was used as a reactor once the organic phase mixed with aqueous gold precursor to form segmented flow. Combining with the plug-like flow inside the CFI, better mixing and narrow residence time distribution could be achieved,[235] resulting in more controllable operation conditions. The CFI was made of fluorinated ethylene propylene (FEP) tubing (1 mm ID, VICI Jour) and consisted of 100 coils in total with coil diameter of 1 cm. A 90° bend was utilized for every 5 coils and the total length of the CFI was 3.6 m (volume of 2.83 ml). As the CO is highly toxic, the whole system was fully sealed and one line of N_2 with volumetric flow rate of 1 ml/min by mass flow controller (Brooks 5850 TR) was installed to flush the residue of CO in product collected in glass vial.

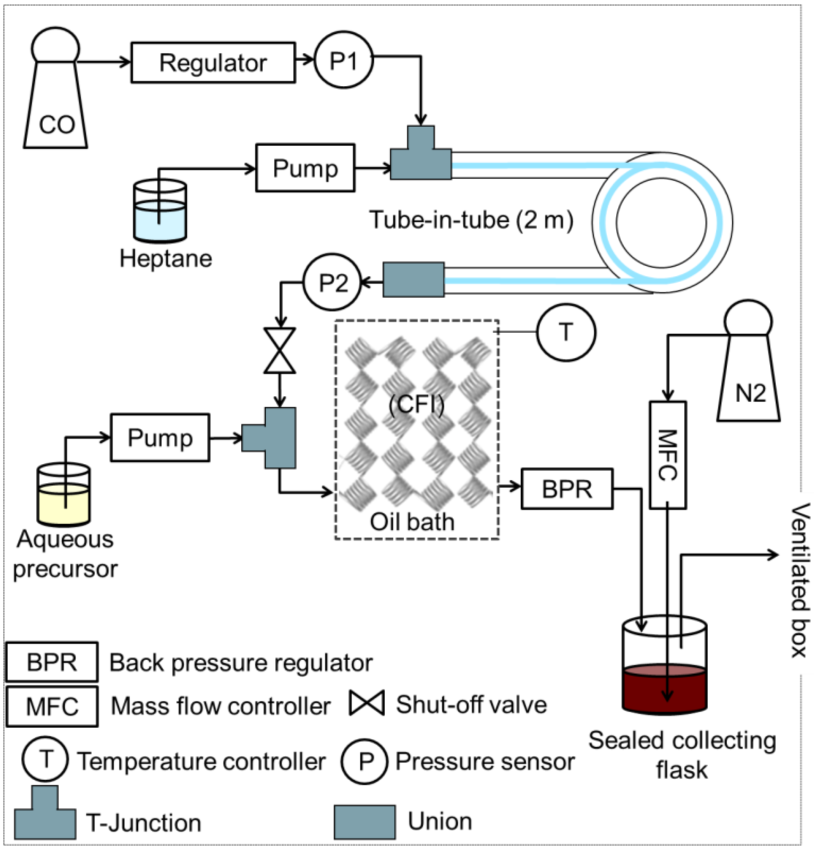

Figure 6-1 Schematic of microfluidic segmented flow system for synthesis of $Au_{25}(Cys)_{18}$ NCs.

6.2.2 General synthetic procedure for $Au_{25}(Cys)_{18}$ nanoclusters synthesis

The chemistry of the synthetic route was based on the reported condition proposed by Yu *et al.*[252] with some modifications for adaptation into flow. An aqueous solution containing 1 mM $HAuCl_4$ and 1.5 mM cysteine was prepared using 15.0 MΩ reverse osmosis water with pH tuning to 11.6 by NaOH. All reagents were of analytical grade and purchased from Sigma-Aldrich. The aqueous reaction solution was left for at least 2 h to fully convert Au(III) to Au(I) complexes to avoid forming irreversible larger size particles in later synthesis (see **Appendix D1**). Then the aqueous stream pumped into the CFI by a piston pump (milliGAT LF) and merged with CO-saturated heptane at flow ratio of organic to aqueous solution of 2 by T-mixer (0.5 mm inner diameter, P-632, IDEX Health & Science LLC) forming microfluidic segmented flow. The outlet of the CFI was connected to a back-pressure regulator (BPR-10, Zaiput) and the liquid phase pressure was maintained at 500 kPa by a nitrogen pressure regulator (Swagelok, K series). The CO concentration in heptane was estimated based on tube-in-tube model developed by Yang.[257] The simulation in **Section 5.3.1** has showed that 2 m tube was enough to saturate the heptane with around 58.4 mM final concentration of CO at the outlet of the tube-in-tube set-up, which was at least 11.6 times higher than the CO needed to reduce the gold precursor in this paper (calculated based on 20 mM initial concentration of gold precursor at the organic flow rate of 0.64 ml/min and 0.32 ml/min aqueous flow rate. The lowest CO/Au^+ molar flow ratio=5.8). The product was washed and precipitated right after reaction with acetone and PVDF syringe filter (0.2 µm hole size, Alpha Laboratories Limited) to avoid further reaction inside container and for long-time storage. The stability as form of solid was more than 2 months. However, the sample was unstable if they were stored as colloidal solution in water (see **Appendix D2**).

6.2.3 Analysis

The solution pH was measured by pH meter (SevenCompact^{TM} pH/Ion S220). UV-Vis absorption spectra of $Au_{25}(Cys)_{18}$ NCs solution were recorded using an Ocean Optics UV-Vis-ES spectrometer (USB 2000+ Spectrometer and DT-Mini-2-GS light source). As some of the absorbance values of synthesised $Au_{25}(Cys)_{18}$ NCs suspension exceed the detection limit of this UV-Vis spectrometer, diluted nanocluster suspensions were used during measurement and then the data of absorbance peaks were multiplied by the dilution factor to obtain the final UV-Vis spectra. TEM image was taken on a JEOL 2100 EXii microscope with a 120 kV acceleration voltage. TEM samples were prepared by dipping a drop of the colloidal solution onto TEM grid (EM Resist Ltd) and allowed to dry in air. Inductively coupled plasma atomic emission spectroscopy (Varian 720 ICP-AES, axial configuration) was used to measure the gold amount of the synthesized Au NCs. The Au NCs were precipitated by acetone and then centrifuged at speed of 7500 rpm (Heraeus Multifuge X1R, ThermoFisher SCIENTIFIC, rotor model: F15-8x50cy) for 30 min to extract all the gold for the digestion by aqua regia. The yield was calculated by the amount of gold detected by ICP over the original amount of gold precursor. The particle size in solution was analysed using a small/wide angle x-ray scattering (SAXS/WASX, Ganesha 300XL, Xenocs/SAXSLAB) at the Centre for Nature Inspired Engineering, University College London. Microfocus x-ray generated from a copper source with a motorised collimation system and the whole-vacuum design allows quick measurement of liquid samples in 1.0mm borosilicate glass capillaries. The System was equipped with a movable solid-state photon-counting detector (PILATUS 300K, Dectris, Switzerland) and calibrated using LaB6 and Agbeh.

The calibration was validated again before each measurement. The capillary and solvent signals were subtracted from each measurement before data analysis. The particle size was calculated by using software 'SAXSGUI' applying Guinier fit, and full fit using a dilute monodispersed sphere model. The sample for electrospray ionization mass spectrometry (ESI-MS, Micromass LCT Premier) came from the dried precipitate of nanoclusters and was diluted in 0.01 µM cesium acetate in water (operation procedure in **Appendix D4**). Data acquisition was performed in profile mode with the mass range from *m/z* 10 to 10000. The dried nanoclusters were also analysed by ATR-FTIR spectroscopy using a Perkin-Elmer 1605 FT-IR spectrometer with a resolution of 0.5 cm^{-1} and wavenumber range 0-5000 cm^{-1}. The sample for matrix-assisted laser desorption ionization mass spectrum (MALDI-MS, Micromass MALDI-TOF) was prepared by mixing 2 µL of the raw product with 2 µL of matrix solution (saturated α-cyano-4-hydroxycinnamic acid (CHCA) solution in methonal) and allowed for recrystallization in air prior to the analysis. The data were collected in linear mode.

6.3 Results and discussion

6.3.1 Adaptation of the synthetic process from batch to flow

To the best of our knowledge, the single-step synthesis of atomically precise Au NCs in continuous flow systems has seldom been investigated. This might be because the prolonged "size-focusing" time of up to several days is hard to adapt to a flow system. The current challenge is in achieving good control of the fast reduction stage as well as to facilitate the slow size evolution into atomically precise Au NCs in a one-pot (or indeed one tube or microfluidic chip) synthesis.

Based on this consideration the relatively mild reducing agent, CO, was chosen in order to better control the first 'fast reduction' stage instead of cooling reactants as favoured by other researchers. A tube-in-tube set-up was employed to create an organic carrier with excess CO. Based on Henry's law, the amount of dissolved gas is proportional to its partial pressure in the gas phase.[184] Therefore the concentration of CO could be tuned by pressurising the microfluidic system. Additionally the heptane, which boasts a higher CO solubility (nearly 10 times) than water,[261] could act as a CO reservoir to continuously provide reducing agent to the aqueous segments. The reaction could be precisely controlled as each segment could be regarded as an individual reactor with equal volume and nearly identical reaction conditions (flow pattern with average aqueous droplet length ~ 2.5 mm and heptane slug length ~ 4.5 mm, see **Figure 6-2**).

Figure 6-2 The flow pattern inside the CFI during the synthesis of 10 mM initial concentration of gold precursor at residence time of 2.9 min at 80 °C, constant organic to aqueous flow ratio of 2 and cysteine to gold concentration ratio of 1.5.

A preliminary study of the adaptation from batch to flow was conducted at room temperature to investigate the enhancement furnished purely by the use of this innovative ‘liquidised CO reservoir’ liquid-liquid segmented flow system without the application of any heat. The UV-Vis spectra of the products at different residence times (obtained by varying the flow rates with constant organic to aqueous flow ratio of 2) are shown in **Figure 6-3**. Unlike the single absorption peak observed with larger Au NPs (caused by surface plasmon resonance), the nanoclusters, which more closely resemble molecules,[284] have quantized energy levels from electronic transitions, and thus, exhibit multiple absorption bands in UV–vis spectroscopy.[59] The typical spectrum of thiolated Au_{25} NCs exhibits four peaks at the wavelengths of 400, 450, 670 and 770 nm, respectively.[252] The pronounced lift of the peak at 670 nm is typically used to determine whether the reaction has reached completion.[64] Based on Xie's work, the thiolate-Au(I) complexes could be fully reduced into Au NCs with mixed sizes during the first 0.5 h of reaction,[285] which is the required time for the first 'fast reduction' phase of reaction. The peak at 670 nm gradually appears only after the second stage of slow "size-focusing" growth due to the increasing concentration of Au_{25} NCs. However, in **Figure 6-3**, the absorbance peak at 670 nm was observed after just 0.25 h in our microfluidic set-up (compared with 3 h reported in previous work for the CO reduction in batch).[252] The absorption increased at residence time 0.5 h, indicating the increasing yield of Au_{25} NCs. At residence time for 2 h, a substantial absorption peak with absorbance of 0.33 at 670 nm wavelength was observed. The 48 h reaction was achieved by sealing the droplet flow inside the CFI with no flow to obtain a comparable residence time to that in the previously reported batch study. Compared to the peak absorbance of 0.36 at 48 h, the absorbance at 2 h was only 0.03 lower, which indicated that most of the Au_{25} clusters had been formed during the first 2 h. Due to the high concentration of CO in heptane furnished by the tube-in-tube set-up, and the enhanced mass transfer and good mixing provided by segmented flow in the CFI, the time scale of the reaction was effectively decreased from a day (24 h) to mere hours. Additionally, the design of the tube-in-tube set-up for CO saturation made it easier to flexibly tune the concentration of the CO. This preliminary trial of the adaptation for the synthesis of $Au_{25}(Cys)_{18}$ from batch to flow proved to be successful even without applying heat.

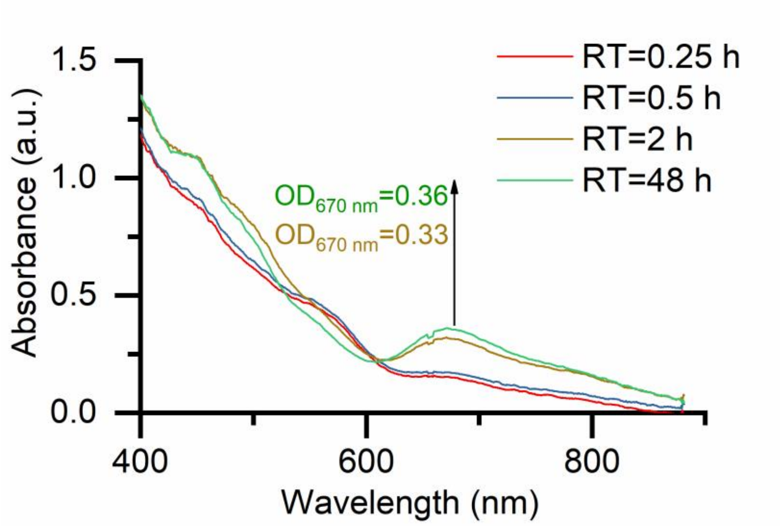

Figure 6-3 UV-Vis spectra of the reactor effluent with 1 mM initial concentration of $HAuCl_4$ observed at room temperature and different residence times (RT) by tuning the flow rate with constant organic to aqueous flow ratio of 2 and cysteine to gold concentration ratio of 1.5.

6.3.2 Influence of temperature

Even though the preliminary study demonstrated the feasibility of the Au NC synthesis in flow, a reaction time of more than 2 h is still unfavourably long for continuous flow synthesis at high volumes. The effect of temperature on the one-pot synthesis of $Au_{25}(SR)_{18}$ clusters reduced by $NaBH_4$ in batch has been well investigated by Chen *et al.*.[64] Their work proved that heating could increase the reduction rate of thiolate-Au(I) complexes, as well as decrease the size-focusing time to form the most thermodynamically stable $Au_{25}(SR)_{18}$ clusters. However, overheating the system leads to further formation of mix-sized NCs from $[Au_{25}(SR)_{18}]$ and this process is irreversible. They found that 40 °C was the optimal temperature which could speed up the reduction rate without degrading the synthesized $[Au_{25}(SR)_{18}]$ to other cluster sizes. However, using $NaBH_4$ as a reducing agent has one inevitable problem: the $NaBH_4$ decomposes quickly under heating. Thus, the CO used as a reductant has potential to give better performance as it does not decompose with time evolution. In addition to this, the microfluidic system with enhanced heat transfer could provide more precise control of the temperature and shorter heating time.

The synthesized products at a residence time of 15 min at different temperatures are shown in **Figure 6-4**. The absorbance at 670 nm was nearly identical at 60 and 80 °C, suggesting that the synthesis had finished in 15 min at 60°C. The product at 80°C should be the fully reacted Au_{25} NCs as the final peak absorbance in the UV-Vis is comparable to the final product obtained after 48 h at room temperature as shown in **Figure 6-3** with a better defined plateau of the characteristic peak at wavelength of 450 nm. The size distribution from TEM images in **Figure 6-4a** and **Figure 6-4b** also verified that the size-focusing process progressed further at 80°C as evidenced by a lower coefficient of variation of 11.6%. Additionally, the peak at 670 nm kept its shape after the absorption stopped increasing, indicating that the synthesized $Au_{25}(Cys)_{18}$ clusters did not transform to other cluster sizes at 80°C. When the temperature was increased to 100 and 120 °C, multiple cluster sizes formed as observed in previous literature,[64] suggesting these temperatures were excessively high for the synthesis. According to this temperature-dependent study, the optimal temperature for our system was 80°C, which could decrease the total reaction time to less than 15 min, whilst at the same time maintaining the high purity of $Au_{25}(Cys)_{18}$ NCs.

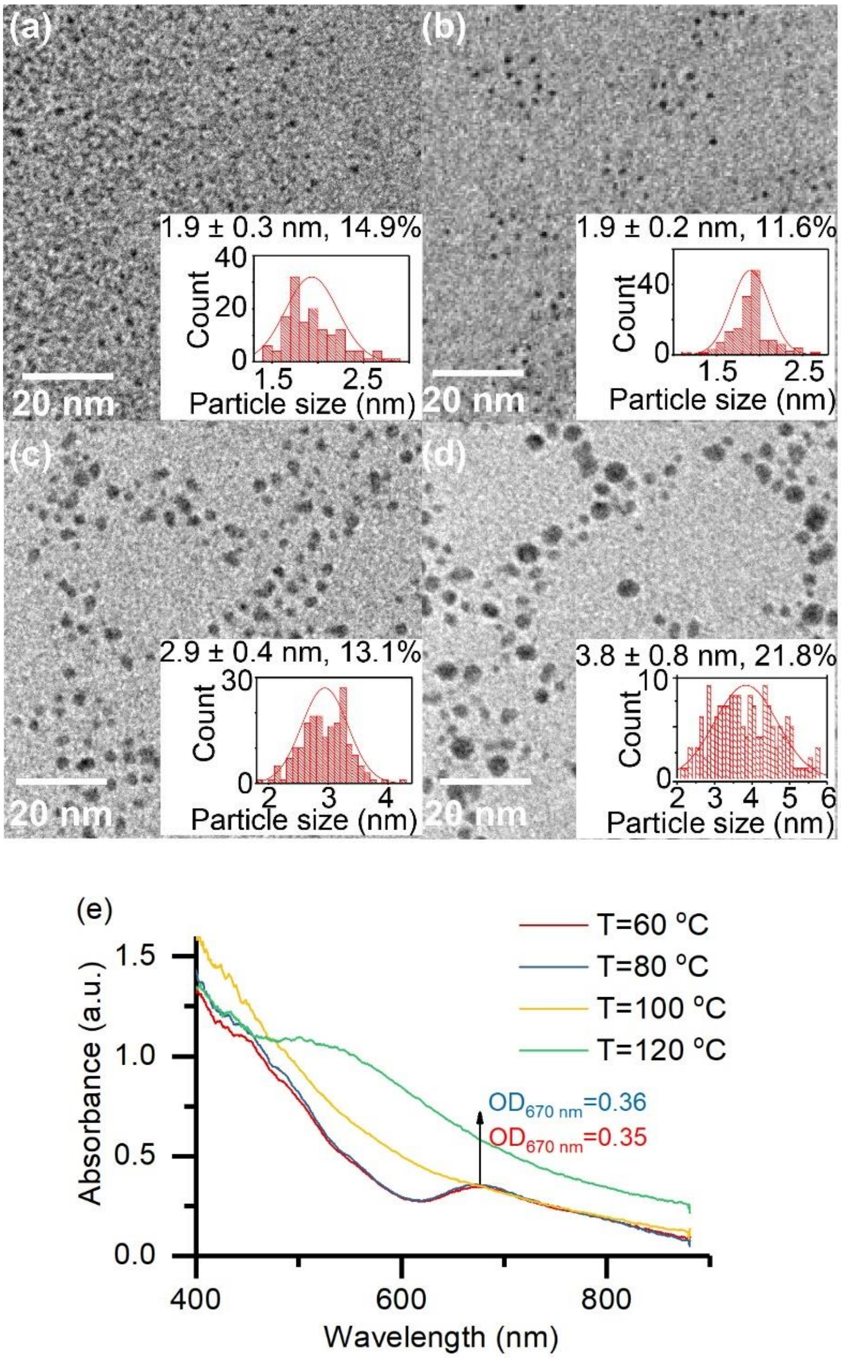

Figure 6-4 TEM images of Au NCs produced from 1 mM $HAuCl_4$ at temperature of (a) 60 °C: 1.9 ± 0.3 nm, coefficient of variation,14.9%, (b) 80 °C: 1.9 ± 0.2 nm, 11.6%, (c) 100 °C: 2.9 ± 0.4 nm, 13.1%, and (d) 120 °C: 3.8 ± 0.8 nm, 21.6%, and (e) corresponding UV-Vis spectra. Residence time was 15 min with aqueous flow rate of 0.064 ml/min at organic to aqueous flow ratio of 2 and cysteine to gold concentration ratio of 1.5.

6.3.3 Throughput optimization

Based on the study above, the reaction seemed have reached completion at a residence time of 15 min at 80°C. Thus, even shorter times were tested to try and increase the throughput of the proposed microfluidic system by increasing the flow rates. However, the output solutions became turbid and could not be analysed by UV-Vis due to the high levels of signal noise (**Figure 6-5a**). The turbidity of this solution was due to the significant mixing capability of segmented flow regimes inside CFIs (proved by comparable trial using circular tube instead of CFI, see **Appendix D3**) resulting in the heptane forming homogeneous microdroplets inside the aqueous phase. The insert in **Figure 6-5a** shows a typical turbid solution obtained from the droplet flow of DI-water and heptane at same flow rates used for a residence time of 2.9 min. Whilst maintaining the segmented flow pattern, the heptane microdroplets in turbid solutions increased the interface area between the aqueous and organic phases, resulting in even faster mass transfer compared to pure segmented flow in this microfluidic system. These samples were thus, washed and precipitated by acetone and filter paper to remove the heptane, and then re-dissolved in water for analysis with UV-Vis spectroscopy. The absorbance of the peaks at 670 nm wavelength in **Figure 6-5b** were not as high as the sample at residence time of 15 min (**Figure 6-4e**) due to part of synthesized Au NCs stayed inside the filter paper during sample washing procedure. The results show that the peak absorption at 670 nm wavelength is nearly identical for the four different residence times considered, which proved that the enhanced mass transfer only influenced the required reaction time without changing the cluster size. The residence time of 2.9 min was finally chosen as the optimal residence time as it gave better defined absorption peaks with highest peak ratio of $I_{670\ nm}/I_{610\ nm}$ which indicated further completion of the product.[63]

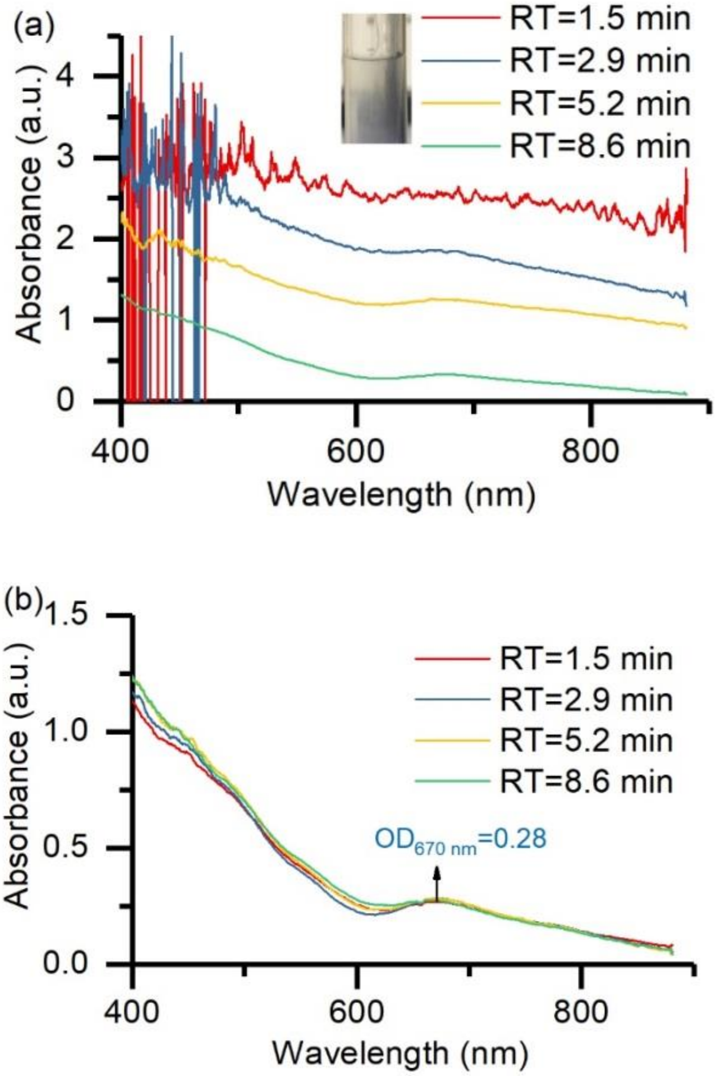

Figure 6-5 UV-Vis spectra of the synthesized products from 1 mM $HAuCl_4$ recorded (a) immediately after collection and (b) after washing and re-dissolving experiments were at different residence times (RT), 80 °C, organic to aqueous flow ratio of 2 and cysteine to gold concentration ratio of 1.5. The insert in (a) is the cloudy solution formed from DI-water and heptane droplet flow at a residence time of 2.9 min.

Since this protocol was quite robust in terms of variation of residence time, higher initial concentrations of thiolated-Au(I) complexes were tested by increasing the concentration of cysteine and $HAuCl_4$ at constant concentration ratio of cysteine to $HAuCl_4$ of 1.5 to study the limitation of this system. The samples were precipitated and washed immediately after reaction by acetone and syringe filter to avoid further synthesis after collection. Then the solids obtained re-dissolved in DI-water for UV-Vis measurement. As the absorbance value of synthesised $Au_{25}(Cys)_{18}$ NCs suspension exceeded the linear detection range of UV-Vis spectrometer, a diluted solution was used in this measurement and the data were multiplied by dilution factore to produce **Figure 6-6a**. The sharp absorption peak at 670 nm indicated the high concentration of $Au_{25}(SR)_{18}$ NCs[64] with increasing initial concentration of gold precursor. There was a red shift of the peak observed (**Figure 6-6b**) when the initial concentration of $HAuCl_4$ was over 10 mM, which might contribute to the formation of larger cluster sizes.[282] The result of UV-Vis suggested that the proposed system could produce $Au_{25}(Cys)_{18}$ NCs with the initial concentration of up to 10 mM. Exceeding 10 mM, larger cluster size was formed. The yield for synthesized $Au_{25}(Cys)_{18}$ NCs was > 95% on gold concentration basis, determined by ICP-AES[*] (**Figure 6-6c)**. Thus, the total throughput of the $Au_{25}(Cys)_{18}$ NCs in our method was increased to more than 50 mg/h at aqueous flow rate of 0.32 ml/min.

---

[*] *The ICP measurement was carried out by Dr. June Callison, Rutherford Appleton Laboratory.*

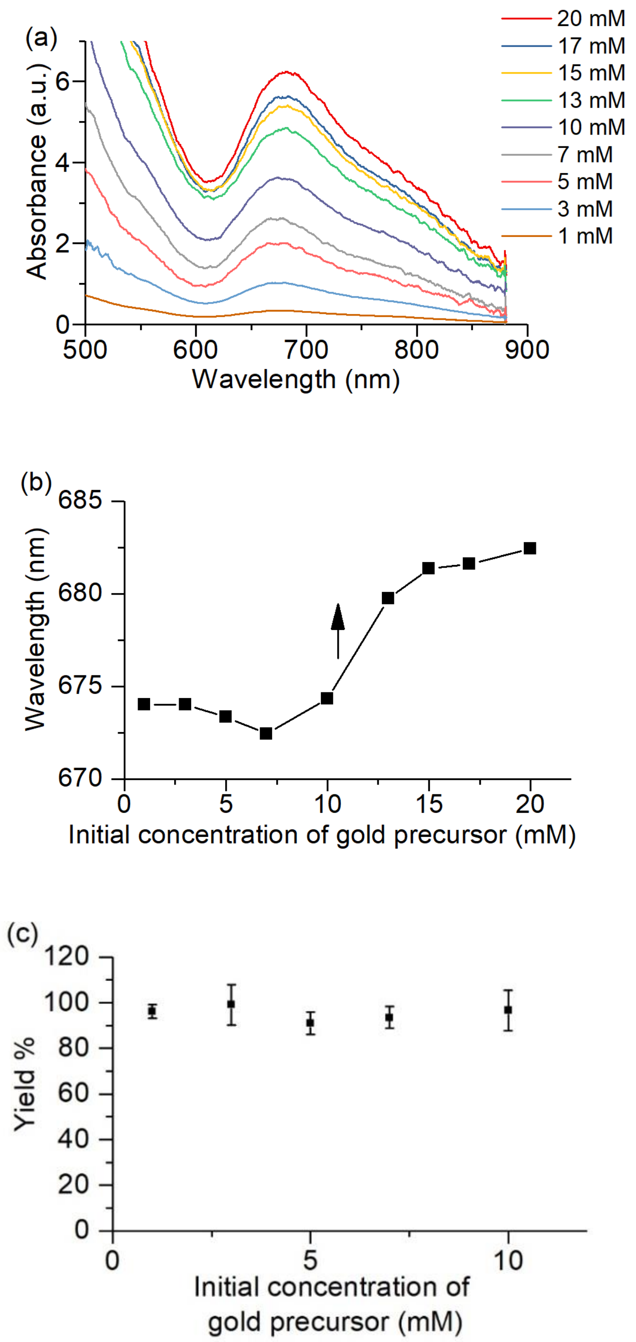

Figure 6-6 (a) UV-Vis spectra and (b) peak wavelength based on half-width of the peak around 670 nm and (c) yield calculation based on ICP-AES of the synthesized Au NCs with different initial concentration of gold precursor at residence time of 2.9 min at 80 °C, constant organic to aqueous flow ratio of 2 and cysteine to gold concentration ratio of 1.5. Error bars represent the standard deviation of the yield with three measurements.

6.3.4 Characterization of synthesized Au NCs

Using the optimized conditions, it only took 3 min to fabricate Au_{25} NCs with ten times (10 mM) the original concentration (1 mM) of the reactants compared to previously reported work[252] at 80 °C, which still maintained high yield and pronounced absorbance peak at a wavelength of 670 nm in UV-Vis (implying a high concentration of $Au_{25}(Cys)_{18}$ NCs) in the microfluidic system. The IR spectra[*] confirmed the Au-S interaction in the solid Au_{25} NCs (**Figure 6-7**) compared to pure cysteine solid. A weak band in black spectra near 2550 cm^{-1} indicates the presence of S-H group in the cysteine molecule. Whereas no band was observed at the same wavenumber in the spectra of $Au_{25}(Cys)_{18}$, confirming the Au-S interaction.[286]

---

[*] *IR measurement was carried out by Dr. Christopher Windle, University College London.*

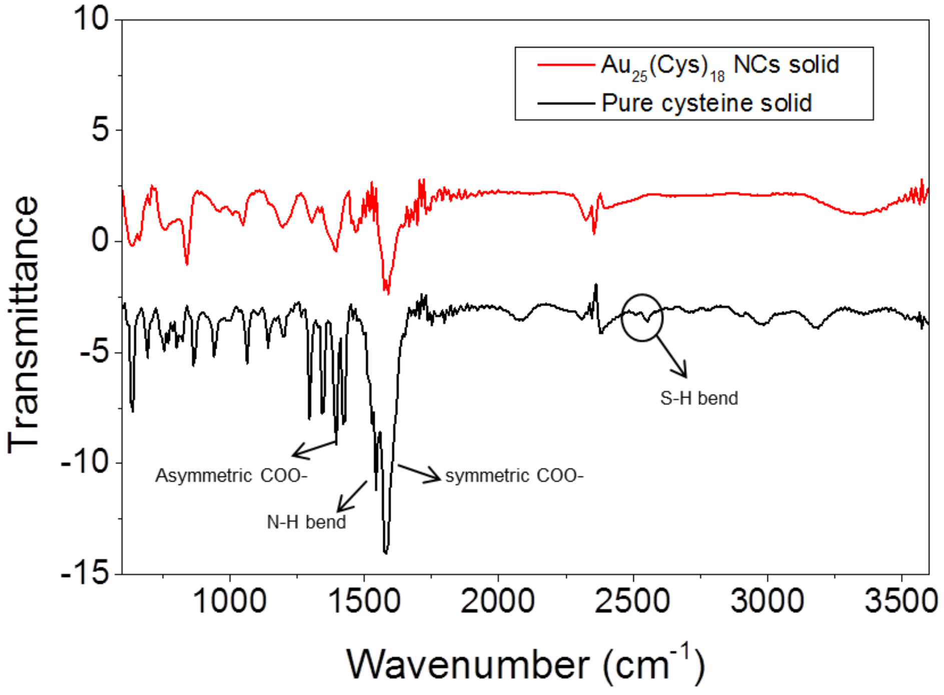

Figure 6-7 IR spectra of pure cysteine solid (black line) and solid $Au_{25}(Cys)_{18}$ (red line) synthesized from 10 mM initial concentration of gold precursor at residence time of 2.9 min, 80 °C, constant organic to aqueous flow ratio of 2 and cysteine to gold concentration ratio of 1.5.

TEM images of synthesized $Au_{25}(Cys)_{18}$ NCs (**Figure 6-8a**) showed an average NC size smaller than 2 nm, which is consistent with previous literature.[287] No large size particles observed from TEM image confirming the high purity of the product in a qualitative respect to monodispersity. The particle size from Small-angle X-ray scattering (SAXS)[*] was calculated by using software 'SAXSGUI' applying Guinier fit, and full fit (**Figure 6-8b**) using a dilute monodispersed sphere model. Both 'Guinier fit' and 'full fit' showed the same particle size of D

---

[*] *SAXS measurement was carried out by Dr. Han Wu, University College London.*

= 1.5 nm, which was in good agreement with TEM result. These results of particle size were larger than previous measured size of Au_{25} NCs in organic solvent (~1 nm),[288] which could be contributed to aggregation of the gold clusters due to ionic strength-dependent aggregation in water solvent under 1 h measuring time.[289] However, neither TEM or SAXS could identify the exact size of the clusters, in other words, the number of gold atoms in the clusters.[65]

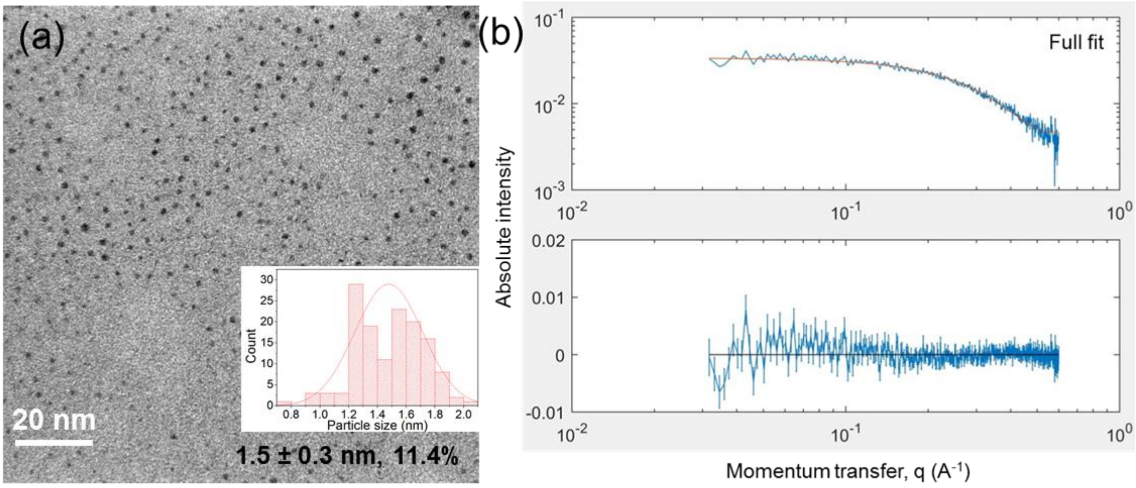

Figure 6-8 (a)TEM image and (b) SAXS full fit image of the as-synthesized $Au_{25}(Cys)_{18}$ NCs with 10 mM initial concentration of gold precursor at residence time of 2.9 min, 80 °C, constant organic to aqueous flow ratio of 2 and cysteine to gold concentration ratio of 1.5.

Thus, ESI-MS* was used to confirm the composition of Au NCs formed. As shown in **Figure 6-9a**, ESI-MS showed the most intense set of peaks at *m/z* ~ 2361.4 in a range of 1500-5200, and an enlarged view of the spectrum in **Figure 6-9b** shows that the base peak at *m/z* 2361.4 (#1) was accompanied by a group

---

* *ESI-MS measurement was carried out by Dr. Kersti Karu, University College London.*

of similar small peaks (#2 to #7) which correspond to H^+ dissociation and Na^+ coordination to $Au_{25}(Cys)_{18}$. Isotope pattern analysis of peak #1 in **Figure 6-9c** showed that the peak spacing between ^{12}C and for ^{13}C was about 0.33. This indicated that $Au_{25}(Cys)_{18}$ carried three negative charges resulting in generation of $[Au_{25}(Cys)_{18}\text{-}3H]^{3-}$, and molecular weight (MW) was about 7083.2 Da. Other identifiable ionised species (#2 to #7) were (#2) $[Au_{25}(Cys)_{18}\text{-}4H+Na]^{3-}$ (MW 7106.1), (#3)$[Au_{25}(Cys)_{18}\text{-}5H+2Na]^{3-}$(MW 7128.1 Da), (#4)$[Au_{25}(Cys)_{18}\text{-}6H+3Na]^{3-}$ (MW 7150.2 Da), (#5)$[Au_{25}(Cys)_{18}\text{-}7H+4Na]^{3-}$, (#6) $[Au_{25}(Cys)_{18}\text{-}8H+5Na]^{3-}$ (MW 7194.1 Da) and (#7) $[Au_{25}(Cys)_{18}\text{-}9H+6Na]^{3-}$ (MW 7216.2 Da) (see **Figure D-5**). Additionally, other sets of cluster peaks were observed at *m/z* ~ 1808.6 and 2411, indicating 3^- and 4^- charged gas phase ions, and all of the peaks corresponded to $Au_{25}(Cys)_{18}$ dissociated with H^+ or coordinated with Na^+, K^+ or Cs^+ which are common contaminant ions in ESI-MS[290] (**Appendix D4**). All the results from UV-Vis, TEM and ESI-MS, show that atomically precise $Au_{25}(Cys)_{18}$ NCs were synthesized with high purity.

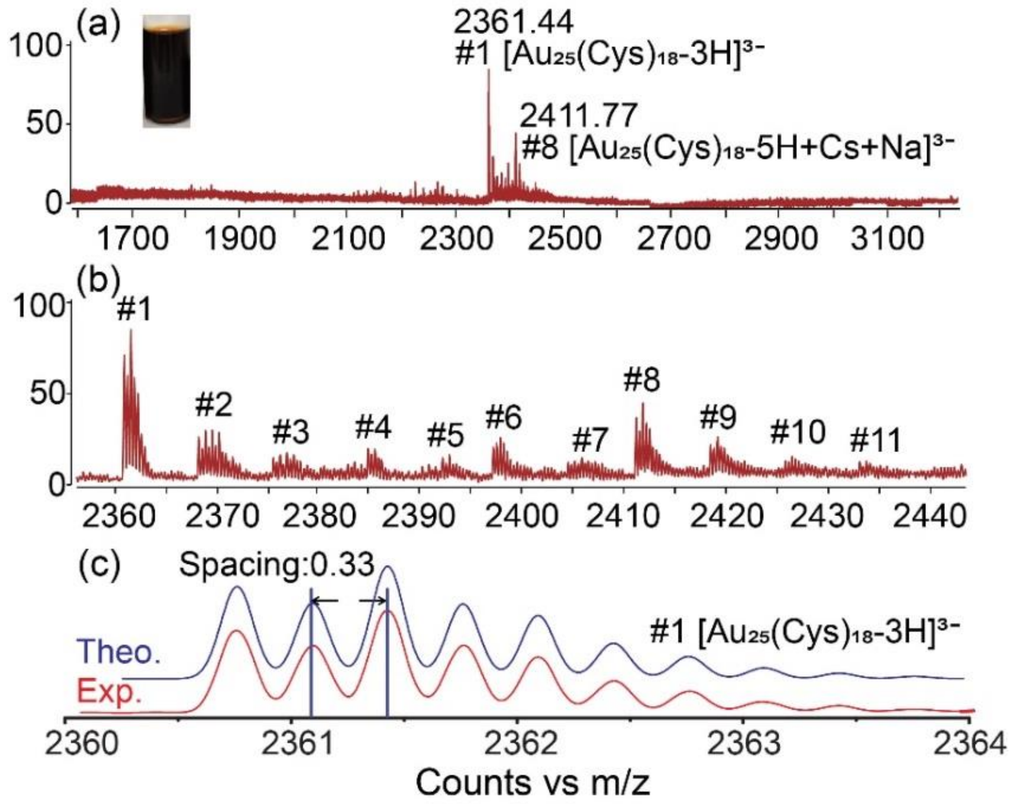

Figure 6-9 ESI mass spectra of synthesized $Au_{25}(Cys)_{18}$ NCs: (a) full-range spectra, (b) zoomed-in spectra in the m/z range of 2360-2440 and (c) comparison between theoretical and experimental isotope pattern of #1 peak of $Au_{25}(Cys)_{18}$ NCs obtained with 10 mM initial concentration of gold ions at residence time of 2.9 min at 80 °C, constant organic to aqueous flow ratio of 2 and cysteine to gold concentration ratio of 1.5. The insert in (a) is the colour of synthesized $Au_{25}(Cys)_{18}$ NCs suspension.

The spectra by MALDI-TOF spectrometry[*] in **Figure 6-10** confirmed the cluster size (Au_{25}), as well as the high purity of the synthesized $Au_{25}(Cys)_{18}$ NCs due to no other peaks found in range of *m/z* up to 15000. Only core mass of the $Au_{25}(Cys)_{18}$ NCs was detected due to the significant fragmentation under the

---

[*] *MALDI-TOF MS measurement was carried out by Dr. Kersti Karu, University College London.*

high laser pulse intensity of MALDI-MS, similar to the observations in literature.[252] The most intense peak indicated the core mass of Au_{25} at m/z~5320. Other small peaks nearby are common residues of $Au_{25}(Cys)_{18}$ NCs like Au_{21} and Au_{24} from dissociation of the gold fragment.[291]

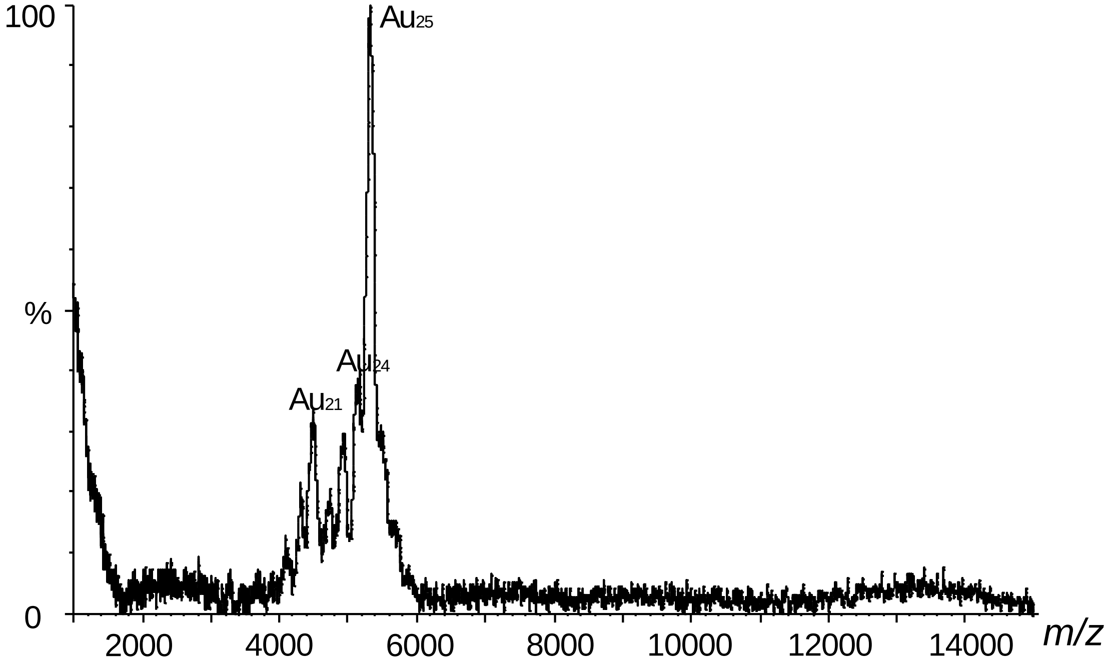

Figure 6-10 The MALDI-mass spectra of synthesized $Au_{25}(Cys)_{18}$ NCs from 10 mM initial concentration of gold precursor at residence time of 2.9 min, 80 °C, constant organic to aqueous flow ratio of 2 and cysteine to gold concentration ratio of 1.5.

In addition, as judged by ESI-MS in **Figure 6-11**, the product remained consistent of high purity and no significant change of the quality was observed, even during continuous operation of 3 days.

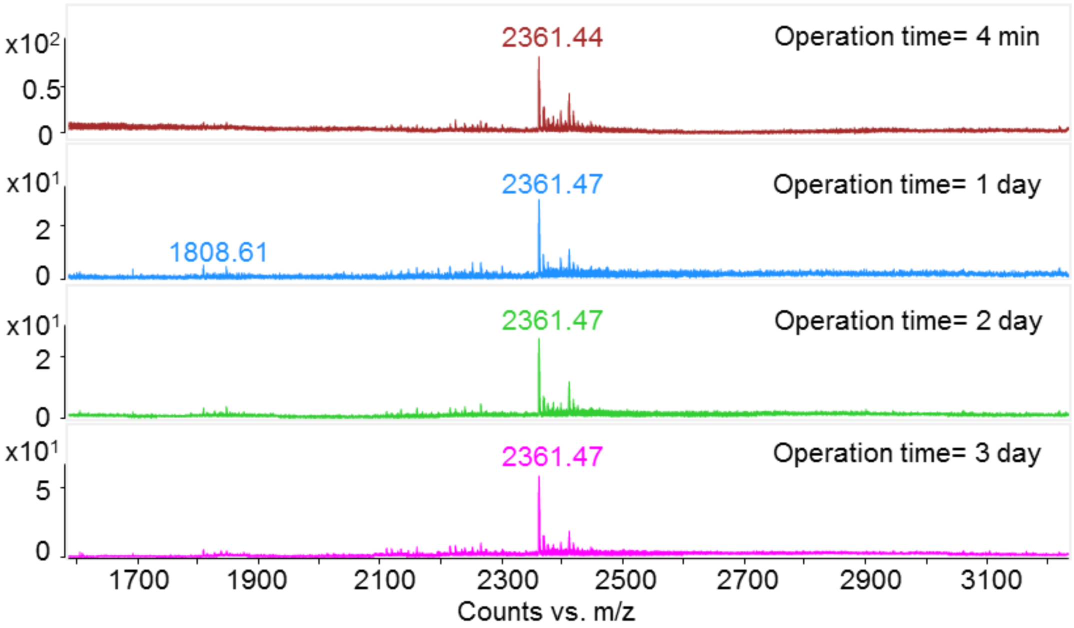

Figure 6-11 The ESI mass spectra of synthesized $Au_{25}(Cys)_{18}$ NCs obtained with 10 mM initial concentration of gold precursor at different operation times (from 4 min to 3 days), residence time of 2.9 min, 80 °C, organic to aqueous flow ratio of 2 and cysteine to gold concentration ratio of 1.5.

6.3.5 Antimicrobial performance test

Based on the sample treatment in swell-encapsulation for antimicrobial test, the aqueous Au NCs needed to be mixed with acetone for 24 h to encapsulate clusters into polyurethane.[292] However, the decreased polarity of the solvent may lead to the precipitation of the cluster. Thus, the ratio of acetone to aqueous sample needed to be determined to make sure that the clusters could be dispersed in the solvent over the course of 24 h encapsulation.

The aqueous Au NCs was mixed with acetone at different volume ratio of acetone to aqueous sample and left for 24 h. After 24 h, there was no visible precipitation for all the samples. A syringe filter with hole size of 0.22 µm was used to test if the clusters were precipitated. **Figure 6-12** showed that the clusters precipitated and could not pass through the filter paper if the ratio of the acetone/water was larger than 3, whereas the solution could maintain the original colour if the ratio was smaller than 2. In the end final ratio of acetone/aqueous cluster sample was set to be 1.

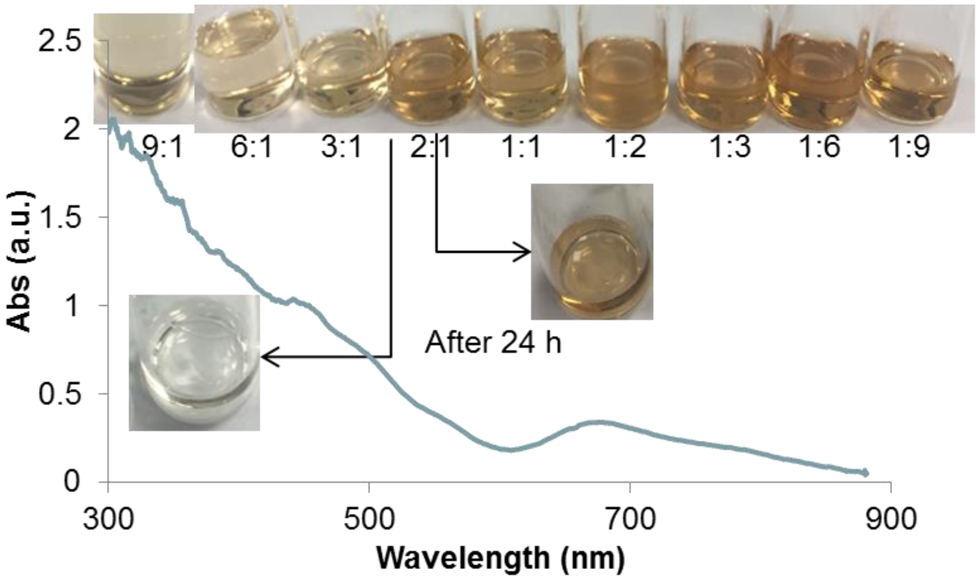

Figure 6-12 UV-Vis spectra and colour of the samples before and after filtration in sample precipitation test at different ratios of acetone/ water at incubation time of 24 h.

Two samples of $Au_{25}(Cys)_{18}$ NCs at continuous operation times of 1-day and 3-day (in **Figure 6-11**) were tested for their antimicrobial activity[*] against *Staphylococcus aureus* which is Gram-positive bacterium. The white light source for photobactericidal test is widely used in U.K. hospital environments, and light intensity of the white lamp was ~ 312 lux in average. **Figure 6-13** shows the antimicrobial activity of the samples against *S. aureus* after 6 h incubation in white light. After 6 h, a reduction in the number of viable bacteria was not observed on 1-day Au nanocluster only, 3-day Au nanocluster only, and CV only

---

[*] *The antimicrobial performance was tested by Dr. Gi-Byoung Hwang, University College London.*

compared to control (P-value >0.1). However, a statistically significant reduction was observed on CV&1-day Au nanocluster, and CV&3-day Au nanocluster (P-value <0.05); compared to control, 1.78 and 1.66 log reductions were observed on CV&1-day Au nanocluster and CV&3-day Au nanocluster, respectively. Additionally, statistically significance difference between on CV&1-day Au nanocluster and CV&3-day Au nanocluster was not observed (P-value >0.1)

Gold nanoclusters were known to have its intrinsic antimicrobial activity.[287] However, the cluster encapsulated silicone did not exhibit antimicrobial activity. This might be because the number of the clusters encapsulated into the polymer was not enough to cause a reduction of bacterial viability. Despite the crystal violet is a light-activated antimicrobial agent,[293] the CV only encapsulated polymer did not show photobactericial activity after 6 h exposure of white light. However, addition of gold nanocluster into CV-treated polymer significantly enhanced photobactericidal activity. It is speculated that an interaction of gold nanocluster and crystal violet reinforces photochemical reactions, resulting in significant increase in the concentration of reactive oxygen species killing bacteria.[293] Through antimicrobial test, it was confirmed that the 3-day synthetic process yielded stable quality of $Au_{25}(Cys)_{18}$ NCs.

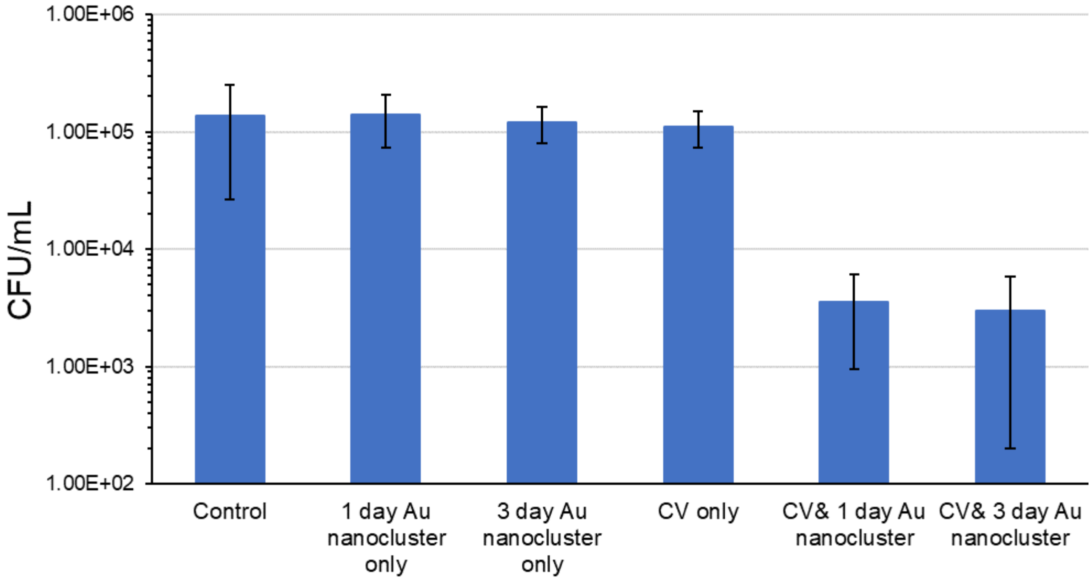

Figure 6-13 Antimicrobial activity of control, and treated silicones after 6 h exposure of white light: Control, 1-day $Au_{25}(Cys)_{18}$ NCs only encapsulated silicone (1-day Au nanocluster only), 3-day $Au_{25}(Cys)_{18}$ NCs only encapsulated silicone (3-day Au NCs only), CV only encapsulated silicone (CV only), CV&1-day $Au_{25}(Cys)_{18}$ NCs encapsulated silicone (CV&1-day $Au_{25}(Cys)_{18}$ NCs), and CV&3-day $Au_{25}(Cys)_{18}$ NCs encapsulated silicone (CV&3-day $Au_{25}(Cys)_{18}$ NCs). All experiment was performed in white light illumination of 312 lux at average temperature of 20°C.

6.4 Conclusion

A rapid synthesis of atomically precise $Au_{25}(Cys)_{18}$ NCs was demonstrated in a microfluidic segmented flow system. The mild reducing agent, CO, gave a gentle reduction environment and better control on the NCs synthesis. The microfluidic segmented flow system at elevated temperature accelerated the thermodynamic processes of size evolution and significantly shortened the total reaction time to as little as 3 min. Our method reduced the synthetic time of atomically precise $Au_{25}(Cys)_{18}$ NCs from a day to a scale of minutes and the throughput could be scaled up to 50 mg/h which shows a big potential for process scale-up. The synthesized clusters proved to have antimicrobial activity which could be applied for a wide of range facilities where sanitisation is required.

7. Conclusions and Future Outlook

7.1 Conclusions

To achieve continuous flow synthesis of monodisperse gold nanoparticles (Au NPs), two reducing agents were investigated to develop facile and robust synthetic processes in a microfluidic system, including the exploration of novel reacting pathways and design of favourable set-up configurations. This doctoral thesis has shown several merits of microfluidics which not only improved the quality of the products, but also reduced the production time and risk of the synthetic process. In addition to this, the challenges rose during the adaptation from batch to microreactors and their solutions presented could provide further guidance for developing other flow syntheses. The as-synthesized products with different sizes and functionalization could be used for a broader sphere of applications, such as catalysis, analytic chemistry, antimicrobial products, etc.

In **Chapter 3**, the feature of high surface-to-volume ratio in microreactor was utilized to enhance the nucleation rate during citrate-only reduction. Sub-3 nm citrate-capped Au NPs, which generally demand stronger reducing agents, were synthesized with faster reduction rate through interaction between reactants and the tubing wall of a circular capillary. It was speculated that the negatively charged tubing-water interface offered heterogeneous nucleation sites for positively charged citrate-gold precursor species, stabilizing the nuclei and inhibiting their growth. The change of the surface charge (from positive to negative) as the gold ions formed citrate-capped Au NPs provided electrostatic repulsion to remove the synthesized gold nanoparticles from the tubing wall. However, this method also revealed one of the common disadvantages of single-phase flow in the microreactor was that fouling occurred. This was reduced to an extent by using fused silica tubing due to its low zeta potential and smooth inner surface.

In **Chapter 4**, carbon monoxide was used as a gas reducing agent to produce monodisperse Au NPs in gas-liquid microfluidic system. The use of gas-liquid flow pattern and coiled flow inverter with special configuration design makes the particles more monodisperse (polydispersity < 5% without any capping agents) with better mixing and the synthesis more flexible to continuously produce various Au NPs with different operational parameters and capping agents, resulting in a big potential for wide applications based on this set-up. However, as the reactants contacted the tubing wall, fouling was still inevitable during the first 5-20 coils of the reactor.

Due to the fouling problem, the set-up was further improved in **Chapter 5** by forming liquid-liquid flow system by dissolving CO into organic phase (octane or heptane) with a Teflon AF-2400 tube-in-tube saturator to isolate the reactants away from the wall. Besides the easier high-pressure operation and fouling prevention, the highly toxic CO was sealed inside the tube-in-tube set-up and only small amount was released at the end of the reactor, which largely reduced the risk. Interfacial absorption was found to be a big problem while using weak capping agent (citrate) in immiscible segmenting fluids in microreactors. The solution was to employ stronger capping agent to prevent irreversible aggregation from self-assembling of synthesized Au NPs at water-organic interface. However, the strong capping agent suppressed the reduction rate which made the total reaction time unfavourably long for continuous flow synthesis at high volumes. Finally, the polar thiol (cysteine) and high temperature (120 °C) was used to enhance the reduction rate to finish the synthesis of 1.5 nm monolayer protected clusters (MPCs) in around 30 min with yield > 95%. However, we did not confirm the actual cluster size at atomic levels due to the limitation of TEM.

As small size gold nanoparticles were known to have intrinsic antimicrobial activity, one of the targets to produce sub-3 nm Au NPs in flow was for antimicrobial application. However, the product in **Chapter 3** (citrate-capped Au NPs, 1.9 ± 0.2 nm, 12.8%) has low yield (< 25%, ~0.067 mM in solution) and is hard to be concentrated due to the weak capping agent used (irreversible aggregation and size change could occur). The product in **Chapter 5** (cysteine-capped Au clusters, 1.4 ± 0.3 nm, 16.5%) has much higher yield (> 95%, ~1 mM in solution). The strong capping agent (thiol) can also avoid irreversible aggregation and size changes during concentrating process (e.g. centrifugation or drying). However, the product in **Chapter 5** was colourless, which was probably due to the smaller cluster size at higher thiol/Au concentration ratio. Before employing them for antimicrobial applications, they should be further characterized to determine the cluster size, which haven't been done during this thesis. In addition, it was hard to monitor in terms of stability with UV-Vis. Thus, in **Chapter 6**, the atomically precise synthesis of $Au_{25}(Cys)_{18}$ nanoclusters (NCs), which proved to be more stable than other cluster size and could be monitored by UV-Vis easily with multiple absorption bands due to quantized energy levels from electronic transitions, was investigated by using the proposed water-heptane microfluidic set-up. The microfluidic segmented flow system at high temperature accelerated the thermodynamic processes of size evolution, which significantly shortened the total reaction time to as little as 3 min compared to few hours/days in batch. The synthesized clusters gave good photobactericidal enhancement. In antimicrobial testing against *S. aureus,* additional encapsulation of Au NCs into crystal impregnated silicone significantly enhanced photobactericidal activity (~1.7 log reduction in viable bacteria) upon 6 h illumination of about 312 lux in average.

7.2 Future outlook

There are some inspiring directions based on presented work for continuous synthesis of NPs in microfluidic systems in both academic and industrial aspects. Specific suggestions are provided below.

7.2.1 One-pot flow system for Au NPs loading and catalysing the reaction

The effect of interaction between tubing wall and reactants on final NPs size was presented based on the experimental results. The reason for no subsequent work in this direction was the low yield (up to 25%) of the products due to fouling which was economically unfavourable. However, from another point of view, this might be a good method to deposit Au NPs onto the surface of tubes as catalysts for further reaction. The particle size of Au NPs was limited up to 3 nm to maintain the high catalyst activity. However, the typical synthetic route for sub-3 nm Au NPs was to use a strong capping agent to passivate the growth, which limits the accessibility of the active sites.[248] The subsequent process of removing capping agent, such as calcination, could lead to increased particle size.[294] The as-synthesized citrate-capped Au NPs deposited on the tubing surface could be used for catalysis immediately and further reaction (e.g. nitrobenzene hydrogenation and styrene oxidation)[294] can be conducted in the same microfluidic system to achieve continuous catalysis deposition and reaction in one step. However, the deposition of gold is random, which highly depends on the surface roughness. The performance needs to be tested and how long the gold could remain must be monitored.

7.2.2 Interfacial absorption for growth process

Chapter 3 showed a unique effect of tubing surface which only occurs at high surface-to-volume ratio. Combining with the interfacial absorption effect observed in **Chapter 5**, new growth method could be developed by amplifying the character of NPs self-assembly at interface in small microchannels. The growth solution (may contain precursor, reducing agent or some additives for special shape synthesis) and the seed particles can be dispersed in two immiscible phases (e.g. water-soluble growth solution and hydrophobic seed particles) to form segmented two-phase flow inside the microchannels. The large surface-to-volume ratio provided by microchannel ensures most of the particles can quickly accumulate at interface to form high concentration spot to enhance the growth. In addition to this, good mixing in segmented microfluidic system gives the continual supply of sufficient reactants at interface. For this design, two things need to be noted. Capping agent should be strong enough to prevent irreversible aggregation during NPs self-assembly. Secondly, capping agent should also be amphiphilic to ensure reduction occur between seed particles and reducing agent as they are in different liquid phases.

7.2.3 Kinetic study of CO reduction during gold nanoparticle synthesis

Even though 5-10 nm Au NPs were synthesized via CO reduction in gas-liquid microfluidic system, there is no quantitative research on the kinetics of CO reduction. The only thing known is the weaker reducing capability of CO than BH_4^-.[295] In order to fully develop the synthesis based on CO reduction, it is necessary to know the kinetics behind CO reduction. To determine the reaction rate, the continuous synthesis in flow has the advantages of capturing the fast reaction based on different reactor positions monitored by in-line UV-Vis spectrophotometry. The kinetic studies will be divided into two parts: kinetic equation of the reduction from Au^{3+} ions to Au^{+} in homogenous system monitored by the disappearance of absorption peak near 313 nm wavelength[31] and kinetics of Au^{0} formation in heterogeneous system monitored by the presence of plasmon absorption bands at 400 nm wavelength.[296] Therefore, both reaction rate constants of Au^{3+} complex ions reduction and Au NP's formation could be determined.

7.2.4 Two-stage growth for larger size Au NPs

As the performance of NPs for most of the applications is affected by their size, shape and functionalization, the proposed set-ups in this thesis could be further updated to produce different kinds of Au NPs. As seen in **Chapter 4**, the weaker reducing agent (TWEEN 80) led to further growth of CO-produced Au NPs in storage container (from 2.7 nm to 4.0 nm with lower polydispersity: 14.6% vs.9.9%), which opens new potential area for the application of CO reduction set-ups. This work could be extended to produce monodisperse Au NPs with larger sizes (>30 nm) in two-stage synthesis using the CO reduction system. When the CO is introduced into the system, large number of nuclei are produced. This fast nucleation process can be quenched when gaseous CO leaves aqueous solution at the outlet of the reactor. The two-stage growth can be obtained easily due to easy removal of the gaseous reducing agent. As a lot of capping agents have weak reducing capability at room temperature (e.g.

citrate[34], TWEEN-80[246] and bovine serum albumin BSA[297]), the secondary reducing agent could play a dual role to stabilize the synthesized Au NPs, too.

7.2.5 Studies of capping agents to synthesize different kinds of Au NPs

In **Chapter 4**, four capping agents were tried to synthesize Au NPs with different sizes. The work was only used to prove the flexibility of the proposed microfluidic system. The study can go further to tune the particle size based on the requirements of different applications. It was found that the good mixing performance of CFI was able to produce turbid aqueous solution containing microdroplets of heptane at high flow rates in **Chapter 6**. The enrichment of micro-size organic droplets significantly increases the surface-to-volume ratio, which can enhance the mass transfer between water and organic phases. In **Chapter 6**, the similar products obtained from different residence times (tuned by flow rate) suggested that the reduction during Au_{25} nanocluster synthesis seems not to be sensitive to mass transfer, whereas in **Chapter 4** the mass transfer affected final particle size. Thus, if more capping agents were studied in CO reduction system, CFI can be a good reactor when mass transfer needs to be enhanced.

7.2.6 Atomically precise synthesis of gold nanoclusters with different cluster sizes

The characterization method of colourless products in **Chapter 5** (mainly based on TEM) has limitation on the accuracy of the size determination. The colourless solution synthesized at high thiol/Au ratio was expected to be smaller cluster size than Au_{25} nanoclusters based on literature.[252] Further characterization is necessary to get more information about cluster sizes. If the cluster size can be confirmed, further research, like parameter optimization with atomically precise control, stability monitoring and new applications dependent on cluster size can be performed.

7.2.7 Green synthesis of Au NPs with solvated electrons

In this thesis, the gaseous capping agent (CO) was used for the purpose of clean products without residues of capping agent. Besides gaseous reducing agents, another clean reduction for Au NPs synthesis is to use electrons immediately as reducing agent. Henglein *et al.* demonstrated that Au NPs could be reduced by creating solvated electrons in a solution of the metal salt by using gamma-radiation from ^{60}cobalt sources.[298] The so-called “solvated electrons” could be also called “hot electrons” but in their lowest energy state. Lately, X-rays are also used to create the solvated electrons.[299] For this kind of reducing agent, a compact and convenient way of introducing solvated electrons needs to be designed and tested for the feasibility to adapt into continuous flow synthesis.

References

1. Jin, R., Quantum sized, thiolate-protected gold nanoclusters. *Nanoscale* **2010,** *2* (3), 343-362.
2. Haruta, M.; Yamada, N.; Kobayashi, T.; Iijima, S., Gold catalysts prepared by coprecipitation for low-temperature oxidation of hydrogen and of carbon monoxide. *J Catal* **1989,** *115* (2), 301-309.
3. Mukherjee, P.; Patra, C. R.; Ghosh, A.; Kumar, R.; Sastry, M., Characterization and catalytic activity of gold nanoparticles synthesized by autoreduction of aqueous chloroaurate ions with fumed silica. *Chemistry of materials* **2002,** *14* (4), 1678-1684.
4. Crooks, R.; Zhao, M.; Sun, L.; Chechik, V.; Yeung, L., Synthesis, characterization, and applications to catalysis. *Acc. Chem. Res* **2001,** *34* (3).
5. De Silva, N.; Ha, J.-M.; Solovyov, A.; Nigra, M. M.; Ogino, I.; Yeh, S. W.; Durkin, K. A.; Katz, A., A bioinspired approach for controlling accessibility in calix [4] arene-bound metal cluster catalysts. *Nature Chemistry* **2010,** *2* (12), 1062-1068.
6. Kim, D.; Park, S.; Lee, J. H.; Jeong, Y. Y.; Jon, S., Antibiofouling polymer-coated gold nanoparticles as a contrast agent for in vivo X-ray computed tomography imaging. *J Am Chem Soc* **2007,** *129* (24), 7661-7665.
7. Chen, H.; Shao, L.; Li, Q.; Wang, J., Gold nanorods and their plasmonic properties. *Chem. Soc. Rev.* **2013,** *42* (7), 2679-2724.
8. Zhao, P.; Astruc, D., Docetaxel nanotechnology in anticancer therapy. *ChemMedChem* **2012,** *7* (6), 952-972.
9. Daniel, M.-C.; Astruc, D., Gold nanoparticles: Assembly, supramolecular chemistry, quantum-size-related properties, and applications toward biology, catalysis, and nanotechnology. *Chemical Reviews* **2004,** *104* (1), 293-346.
10. Gautier, C.; Taras, R.; Gladiali, S.; Bürgi, T., Chiral 1, 1′ ‐ binaphthyl ‐ 2, 2′ ‐ dithiol ‐ stabilized gold clusters: Size separation and optical activity in the UV – vis. *Chirality* **2008,** *20* (3 ‐ 4), 486-493.
11. Shomura, R.; Chung, K. J.; Iwai, H.; Higuchi, M., Gold nanoparticles with cyclic phenylazomethines: one-pot synthesis and metal ion sensing. *Langmuir* **2011,** *27* (13), 7972-7975.
12. Priyadarshini, E.; Pradhan, N., Gold nanoparticles as efficient sensors in colorimetric detection of toxic metal ions: a review. *Sensors and Actuators B: Chemical* **2017,** *238*, 888-902.
13. Li, G.; Li, D.; Zhang, L.; Zhai, J.; Wang, E., One ‐ Step Synthesis of Folic Acid Protected Gold Nanoparticles and Their Receptor ‐ Mediated Intracellular Uptake. *Chem-Eur J* **2009,** *15* (38), 9868-9873.
14. Zhang, D.; Neumann, O.; Wang, H.; Yuwono, V. M.; Barhoumi, A.; Perham, M.; Hartgerink, J. D.; Wittung-Stafshede, P.; Halas, N. J., Gold nanoparticles can induce the formation of protein-based aggregates at physiological pH. *Nano Letters* **2009,** *9* (2), 666-671.
15. Daniel, M.-C.; Grow, M. E.; Pan, H.; Bednarek, M.; Ghann, W. E.; Zabetakis, K.; Cornish, J., Gold nanoparticle-cored poly (propyleneimine) dendrimers as a new platform for multifunctional drug delivery systems. *New Journal of Chemistry* **2011,** *35* (10), 2366-2374.
16. Zheng, M.; Li, Z.; Huang, X., Ethylene glycol monolayer protected nanoparticles: synthesis, characterization, and interactions with biological molecules. *Langmuir* **2004,** *20* (10), 4226-4235.
17. Hao, Y.; Yang, X.; Song, S.; Huang, M.; He, C.; Cui, M.; Chen, J., Exploring the cell uptake mechanism of phospholipid and polyethylene glycol coated gold nanoparticles. *Nanotechnology* **2012,** *23* (4), 045103.

18. Hong, W.; Bai, H.; Xu, Y.; Yao, Z.; Gu, Z.; Shi, G., Preparation of gold nanoparticle/graphene composites with controlled weight contents and their application in biosensors. *The Journal of Physical Chemistry C* **2010,** *114* (4), 1822-1826.

19. Pardo‐Yissar, V.; Gabai, R.; Shipway, A.; Bourenko, T.; Willner, I., Gold Nanoparticle/Hydrogel Composites with Solvent‐Switchable Electronic Properties. *Advanced Materials* **2001,** *13* (17), 1320-1323.

20. Krasteva, N.; Besnard, I.; Guse, B.; Bauer, R. E.; Müllen, K.; Yasuda, A.; Vossmeyer, T., Self-assembled gold nanoparticle/dendrimer composite films for vapor sensing applications. *Nano Letters* **2002,** *2* (5), 551-555.

21. Kinoshita, T.; Seino, S.; Mizukoshi, Y.; Nakagawa, T.; Yamamoto, T. A., Functionalization of magnetic gold/iron-oxide composite nanoparticles with oligonucleotides and magnetic separation of specific target. *Journal of Magnetism and Magnetic Materials* **2007,** *311* (1), 255-258.

22. Haruta, M.; Sano, H.; Kobayashi, T., Method for manufacture of catalyst composite having gold or mixture of gold with catalytic metal oxide deposited on carrier. Google Patents: 1987.

23. Sebastian, V.; Arruebo, M.; Santamaria, J., Reaction engineering strategies for the production of inorganic nanomaterials. *Small* **2014,** *10* (5), 835-853.

24. Marre, S.; Jensen, K. F., Synthesis of micro and nanostructures in microfluidic systems. *Chem. Soc. Rev.* **2010,** *39* (3), 1183-1202.

25. Puigmartí-Luis, J., Microfluidic platforms: A mainstream technology for the preparation of crystals. *Chem. Soc. Rev.* **2014,** *43* (7), 2253-2271.

26. Taifur-Rahman, M.; Rebrov, E., Microreactors for gold nanoparticles synthesis: From faraday to flow. *Processes* **2014,** *2* (2), 466.

27. Saldanha, P. L.; Lesnyak, V.; Manna, L., Large scale syntheses of colloidal nanomaterials. *Nano Today* **2017,** *12*, 46-63.

28. Wagner, J.; Tshikhudo, T. R.; Koehler, J. M., Microfluidic generation of metal nanoparticles by borohydride reduction. *Chem Eng J* **2008,** *135*, S104-S109.

29. Leifert, A.; Pan-Bartnek, Y.; Simon, U.; Jahnen-Dechent, W., Molecularly stabilised ultrasmall gold nanoparticles: Synthesis, characterization and bioactivity. *Nanoscale* **2013,** *5* (14), 6224-6242.

30. Zhao, P.; Li, N.; Astruc, D., State of the art in gold nanoparticle synthesis. *Coordination Chemistry Reviews* **2013,** *257* (3-4), 638-665.

31. Wuithschick, M.; Birnbaum, A.; Witte, S.; Sztucki, M.; Vainio, U.; Pinna, N.; Rademann, K.; Emmerling, F.; Kraehnert, R.; Polte, J., Turkevich in new robes: Key questions answered for the most common gold nanoparticle synthesis. *ACS Nano* **2015,** *9* (7), 7052-7071.

32. Biggs, S.; Chow, M.; Zukoski, C. F.; Grieser, F., The role of colloidal stability in the formation of gold sols. *J. Colloid Interface Sci.* **1993,** *160* (2), 511-513.

33. Zhao, P.; Li, N.; Astruc, D., State of the art in gold nanoparticle synthesis. *Coordination Chemistry Reviews* **2013,** *257* (3), 638-665.

34. Turkevich, J.; Stevenson, P.; Hillier, J., Preparation of 2.5× 10-4 M gold colloids (Sodium citrate reduction method). *Discuss. Faraday Soc* **1951,** *11*, 55-59.

35. Frens, G., Controlled nucleation for the regulation of the particle size in monodisperse gold suspensions. *Nature* **1973,** *241* (105), 20-22.

36. Ji, X.; Song, X.; Li, J.; Bai, Y.; Yang, W.; Peng, X., Size control of gold nanocrystals in citrate reduction: The third role of citrate. *Journal of the American Chemical Society* **2007,** *129* (45), 13939-13948.

37. Kimling, J.; Maier, M.; Okenve, B.; Kotaidis, V.; Ballot, H.; Plech, A., Turkevich method for gold nanoparticle synthesis revisited. *The Journal of Physical Chemistry B* **2006,** *110* (32), 15700-15707.

38. Sivaraman, S. K.; Kumar, S.; Santhanam, V., Monodisperse sub-10nm gold nanoparticles by reversing the order of addition in Turkevich method–The role of chloroauric acid. *J. Colloid Interface Sci.* **2011,** *361* (2), 543-547.

39. Xia, H.; Bai, S.; Hartmann, J. r.; Wang, D., Synthesis of monodisperse quasi-spherical gold nanoparticles in water via silver (I)-assisted citrate reduction. *Langmuir* **2009,** *26* (5), 3585-3589.

40. Piella, J.; Bastús, N. G.; Puntes, V., Size-controlled synthesis of sub-10 nm citrate-stabilized gold nanoparticles and related optical properties. *Chemistry of Materials* **2016,** *28* (4), 1066-1075.

41. Slot, J. W.; Geuze, H. J., A new method of preparing gold probes for multiple-labeling cytochemistry. *European Journal of Cell Biology* **1985,** *38* (1), 87-93.

42. Brown, K. R.; Fox, A. P.; Natan, M. J., Morphology-dependent electrochemistry of cytochrome c at Au colloid-modified SnO_2 electrodes. *J Am Chem Soc* **1996,** *118* (5), 1154-1157.

43. Singh, A.; Shirolkar, M.; Lalla, N. P.; Malek, C. K.; Kulkarni, S., Room temperature, water-based, microreactor synthesis of gold and silver nanoparticles. *International Journal of Nanotechnology* **2009,** *6* (5-6), 541-551.

44. Wu, L.; Zhou, J.; Xu, H., Room temperature ionic liquid assisted synthesis of ultra-stable Au nanoparticles via a modified Brust–Schiffrin method. *RSC Advances* **2016,** *6* (85), 82394-82400.

45. Hostetler, M. J.; Green, S. J.; Stokes, J. J.; Murray, R. W., Monolayers in three dimensions: synthesis and electrochemistry of ω-functionalized alkanethiolate-stabilized gold cluster compounds. *Journal of the American Chemical Society* **1996,** *118* (17), 4212-4213.

46. Templeton, A. C.; Wuelfing, W. P.; Murray, R. W., Monolayer-protected cluster molecules. *Accounts of chemical research* **2000,** *33* (1), 27-36.

47. Brust, M.; Walker, M.; Bethell, D.; Schiffrin, D. J.; Whyman, R., Synthesis of thiol-derivatised gold nanoparticles in a two-phase liquid–liquid system. *J. Chem. Soc., Chem. Commun.* **1994,** (7), 801-802.

48. Polte, J.; Erler, R.; Thunemann, A. F.; Sokolov, S.; Ahner, T. T.; Rademann, K.; Emmerling, F.; Kraehnert, R., Nucleation and growth of gold nanoparticles studied via in situ small angle X-ray scattering at millisecond time resolution. *ACS Nano* **2010,** *4* (2), 1076-1082.

49. Hardt, S.; Doffing, F.; Pennemann, H., Simulation of hydrodynamic dispersion in gas/liquid microreactors. *Nanotech* **2002,** *1*, 54-57.

50. Borovinskaya, E.; Reshetilovskii, V., Microreactors as the new way of intensification of heterogeneous processes. *Russian Journal of Applied Chemistry* **2011,** *84* (6), 1094-1104.

51. Demello, A. J., Control and detection of chemical reactions in microfluidic systems. *Nature* **2006,** *442* (7101), 394-402.

52. Kettemann, F.; Birnbaum, A.; Witte, S.; Wuithschick, M.; Pinna, N.; Kraehnert, R.; Rademann, K.; Polte, J., The missing piece of the mechanism of the Turkevich method: The critical role of citrate protonation. *Chemistry of Materials* **2016**.

53. Sardar, R.; Funston, A. M.; Mulvaney, P.; Murray, R. W., Gold nanoparticles: past, present, and future. *Langmuir* **2009,** *25* (24), 13840-13851.

54. Goulet, P. J.; Lennox, R. B., New insights into Brust− Schiffrin metal nanoparticle synthesis. *Journal of the American Chemical Society* **2010,** *132* (28), 9582-9584.

55. Li, Y.; Zaluzhna, O.; Xu, B.; Gao, Y.; Modest, J. M.; Tong, Y. J., Mechanistic insights into the brust− schiffrin two-phase synthesis of organo-chalcogenate-protected metal nanoparticles. *Journal of the American Chemical Society* **2011,** *133* (7), 2092-2095.

56. Alvarez, M. M.; Khoury, J. T.; Schaaff, T. G.; Shafigullin, M. N.; Vezmar, I.; Whetten, R. L., Optical absorption spectra of nanocrystal gold molecules. *The Journal of Physical Chemistry B* **1997,** *101* (19), 3706-3712.

57. Alvarez, M.; Khoury, J.; Schaaff, T.; Shafigullin, M.; Vezmar, I.; Whetten, R., Critical sizes in the growth of Au clusters. *Chem Phys Lett* **1997,** *266* (1-2), 91-98.

58. Whetten, R. L.; Shafigullin, M. N.; Khoury, J. T.; Schaaff, T. G.; Vezmar, I.; Alvarez, M. M.; Wilkinson, A., Crystal structures of molecular gold nanocrystal arrays. *Accounts of chemical research* **1999,** *32* (5), 397-406.

59. Schaaff, T.; Shafigullin, M.; Khoury, J.; Vezmar, I.; Whetten, R.; Cullen, W.; First, P.; Gutierrez-Wing, C.; Ascensio, J.; Jose-Yacaman, M., Isolation of smaller nanocrystal Au molecules: robust quantum effects in optical spectra. *The Journal of Physical Chemistry B* **1997,** *101* (40), 7885-7891.

60. Chen, S.; Ingram, R. S.; Hostetler, M. J.; Pietron, J. J.; Murray, R. W.; Schaaff, T. G.; Khoury, J. T.; Alvarez, M. M.; Whetten, R. L., Gold nanoelectrodes of varied size: transition to molecule-like charging. *Science* **1998,** *280* (5372), 2098-2101.

61. Negishi, Y.; Takasugi, Y.; Sato, S.; Yao, H.; Kimura, K.; Tsukuda, T., Magic-numbered Au n clusters protected by glutathione monolayers (n= 18, 21, 25, 28, 32, 39): Isolation and spectroscopic characterization. *J Am Chem Soc* **2004,** *126* (21), 6518-6519.

62. Kang, X.; Chong, H.; Zhu, M., $Au_{25}(SR)_{18}$: The captain of the great nanocluster ship. *Nanoscale* **2018**.

63. Luo, Z.; Nachammai, V.; Zhang, B.; Yan, N.; Leong, D. T.; Jiang, D.-e.; Xie, J., Toward understanding the growth mechanism: tracing all stable intermediate species from reduction of Au (I)–thiolate complexes to evolution of Au25 nanoclusters. *Journal of the American Chemical Society* **2014,** *136* (30), 10577-10580.

64. Chen, T.; Yao, Q.; Yuan, X.; Nasaruddin, R. R.; Xie, J., Heating or Cooling: Temperature Effects on the Synthesis of Atomically Precise Gold Nanoclusters. *The Journal of Physical Chemistry C* **2017,** *121* (20), 10743-10751.

65. Jin, R.; Qian, H.; Wu, Z.; Zhu, Y.; Zhu, M.; Mohanty, A.; Garg, N., Size focusing: a methodology for synthesizing atomically precise gold nanoclusters. *The Journal of Physical Chemistry Letters* **2010,** *1* (19), 2903-2910.

66. Qu, X.; Li, Y.; Li, L.; Wang, Y.; Liang, J.; Liang, J., Fluorescent gold nanoclusters: synthesis and recent biological application. *Journal of Nanomaterials* **2015,** *2015*, 4.

67. Wu, Z.; Suhan, J.; Jin, R., One-pot synthesis of atomically monodisperse, thiol-functionalized Au 25 nanoclusters. *Journal of Materials Chemistry* **2009,** *19* (5), 622-626.

68. Yuan, X.; Zhang, B.; Luo, Z.; Yao, Q.; Leong, D. T.; Yan, N.; Xie, J., Balancing the rate of cluster growth and etching for gram - scale synthesis of thiolate - protected Au25 nanoclusters with atomic precision. *Angewandte Chemie* **2014,** *126* (18), 4711-4715.

69. Katla, S. K.; Zhang, J.; Castro, E.; Bernal, R. A.; Li, X. J., Atomically-precise Au25 (SG) 18 nanoclusters: Rapid single-step synthesis and application in photothermal therapy. *ACS applied materials & interfaces* **2017**.

70. Liu, J.; Krishna, K. S.; Losovyj, Y. B.; Chattopadhyay, S.; Lozova, N.; Miller, J. T.; Spivey, J. J.; Kumar, C. S., Ligand - Stabilized and Atomically Precise Gold Nanocluster Catalysis: A Case Study for Correlating Fundamental Electronic Properties with Catalysis. *Chem-Eur J* **2013,** *19* (31), 10201-10208.

71. Nie, X.; Qian, H.; Ge, Q.; Xu, H.; Jin, R., CO oxidation catalyzed by oxide-supported Au25 (SR) 18 nanoclusters and identification of perimeter sites as active centers. *ACS Nano* **2012,** *6* (7), 6014-6022.

72. Lopez-Sanchez, J. A.; Dimitratos, N.; Hammond, C.; Brett, G. L.; Kesavan, L.; White, S.; Miedziak, P.; Tiruvalam, R.; Jenkins, R. L.; Carley, A. F., Facile removal of stabilizer-ligands from supported gold nanoparticles. *Nature Chemistry* **2011,** *3* (7), 551-556.

73. Schulz-Dobrick, M.; Sarathy, K. V.; Jansen, M., Surfactant-free synthesis and functionalization of gold nanoparticles. *J Am Chem Soc* **2005,** *127* (37), 12816-12817.

74. Turkevich, J.; Garton, G.; Stevenson, P., The color of colloidal gold. *Journal of colloid Science* **1954,** *9*, 26-35.

75. Leff, D. V.; Brandt, L.; Heath, J. R., Synthesis and characterization of hydrophobic, organically-soluble gold nanocrystals functionalized with primary amines. *Langmuir* **1996,** *12* (20), 4723-4730.

76. Schmid, G. n.; Pfeil, R.; Boese, R.; Bandermann, F.; Meyer, S.; Calis, G. H.; van der Velden, J. W., Au55 [P (C6H5) 3] 12Cl6? ein Goldcluster ungew hnlicher Gr e. **1981**.

77. Schmid, G. n.; Klein, N.; Korste, L.; Kreibig, U.; Schönauer, D., Large transition metal clusters. VI: Ligand exchange reactions on Au55 (PPh3) 12Cl6—The formation of a water soluble Au55 cluster. *Polyhedron* **1988,** *7* (8), 605-608.

78. Tamura, M.; Fujihara, H., Chiral bisphosphine BINAP-stabilized gold and palladium nanoparticles with small size and their palladium nanoparticle-catalyzed asymmetric reaction. *J Am Chem Soc* **2003,** *125* (51), 15742-15743.

79. Schaaff, T. G.; Knight, G.; Shafigullin, M. N.; Borkman, R. F.; Whetten, R. L., Isolation and selected properties of a 10.4 kDa gold: glutathione cluster compound. *The Journal of Physical Chemistry B* **1998,** *102* (52), 10643-10646.

80. Negishi, Y.; Takasugi, Y.; Sato, S.; Yao, H.; Kimura, K.; Tsukuda, T., Magic-Numbered Aun Clusters Protected by Glutathione Monolayers (n = 18, 21, 25, 28, 32, 39): Isolation and Spectroscopic Characterization. *J Am Chem Soc* **2004,** *126* (21), 6518-6519.

81. Shimmin, R. G.; Schoch, A. B.; Braun, P. V., Polymer size and concentration effects on the size of gold nanoparticles capped by polymeric thiols. *Langmuir* **2004,** *20* (13), 5613-5620.

82. Goodman, C. M.; McCusker, C. D.; Yilmaz, T.; Rotello, V. M., Toxicity of gold nanoparticles functionalized with cationic and anionic side chains. *Bioconjugate chemistry* **2004,** *15* (4), 897-900.

83. Lin, C.-A. J.; Yang, T.-Y.; Lee, C.-H.; Huang, S. H.; Sperling, R. A.; Zanella, M.; Li, J. K.; Shen, J.-L.; Wang, H.-H.; Yeh, H.-I., Synthesis, characterization, and bioconjugation of fluorescent gold nanoclusters toward biological labeling applications. *ACS Nano* **2009,** *3* (2), 395-401.

84. Yu, M.; Zhou, C.; Liu, J.; Hankins, J. D.; Zheng, J., Luminescent gold nanoparticles with pH-dependent membrane adsorption. *J Am Chem Soc* **2011,** *133* (29), 11014-11017.

85. de la Fuente, J. M.; Berry, C. C., Tat peptide as an efficient molecule to translocate gold nanoparticles into the cell nucleus. *Bioconjugate chemistry* **2005,** *16* (5), 1176-1180.

86. Yanagimoto, Y.; Negishi, Y.; Fujihara, H.; Tsukuda, T., Chiroptical activity of BINAP-stabilized undecagold clusters. *The Journal of Physical Chemistry B* **2006,** *110* (24), 11611-11614.

87. Bergeron, D. E.; Coskuner, O.; Hudgens, J. W.; Gonzalez, C. A., Ligand exchange reactions in the formation of diphosphine-protected gold clusters. *The Journal of Physical Chemistry C* **2008,** *112* (33), 12808-12814.

88. Love, J. C.; Estroff, L. A.; Kriebel, J. K.; Nuzzo, R. G.; Whitesides, G. M., Self-assembled monolayers of thiolates on metals as a form of nanotechnology. *Chemical reviews* **2005,** *105* (4), 1103-1170.

89. Porter, L. A.; Ji, D.; Westcott, S. L.; Graupe, M.; Czernuszewicz, R. S.; Halas, N. J.; Lee, T. R., Gold and silver nanoparticles functionalized by the adsorption of dialkyl disulfides. *Langmuir* **1998,** *14* (26), 7378-7386.

90. Li, X.-M.; de Jong, M. R.; Inoue, K.; Shinkai, S.; Huskens, J.; Reinhoudt, D. N., Formation of gold colloids using thioether derivatives as stabilizing ligands. *Journal of Materials Chemistry* **2001,** *11* (7), 1919-1923.

91. Hermes, J. P.; Sander, F.; Peterle, T.; Cioffi, C.; Ringler, P.; Pfohl, T.; Mayor, M., Direct Control of the Spatial Arrangement of Gold Nanoparticles in Organic–Inorganic Hybrid Superstructures. *small* **2011,** *7* (7), 920-929.

92. Hermes, J. P.; Sander, F.; Fluch, U.; Peterle, T.; Thompson, D.; Urbani, R.; Pfohl, T.; Mayor, M., Monofunctionalized Gold Nanoparticles Stabilized by a Single Dendrimer Form Dumbbell Structures upon Homocoupling. *J Am Chem Soc* **2012,** *134* (36), 14674-14677.

93. Peterle, T.; Ringler, P.; Mayor, M., Gold Nanoparticles Stabilized by Acetylene‐Functionalized Multidentate Thioether Ligands: Building Blocks for Nanoparticle Superstructures. *Advanced functional materials* **2009,** *19* (21), 3497-3506.

94. Peterle, T.; Leifert, A.; Timper, J.; Sologubenko, A.; Simon, U.; Mayor, M., Multidentate thioether ligands coating gold nanoparticles. *Chem. Commun.* **2008,** (29), 3438-3440.

95. Thompson, D.; Hermes, J. P.; Quinn, A. J.; Mayor, M., Scanning the potential energy surface for synthesis of dendrimer-wrapped gold clusters: design rules for true single-molecule nanostructures. *ACS Nano* **2012,** *6* (4), 3007-3017.

96. Perumal, S.; Hofmann, A.; Scholz, N.; Rühl, E.; Graf, C., Kinetics study of the binding of multivalent ligands on size-selected gold nanoparticles. *Langmuir* **2011,** *27* (8), 4456-4464.

97. Srisombat, L.-o.; Park, J.-S.; Zhang, S.; Lee, T. R., Preparation, characterization, and chemical stability of gold nanoparticles coated with mono-, bis-, and tris-chelating alkanethiols. *Langmuir* **2008,** *24* (15), 7750-7754.

98. Mie, G., Articles on the optical characteristics of turbid tubes, especially colloidal metal solutions. *Ann. Phys* **1908,** *25* (3), 377-445.

99. Kerker, M., The Scattering of Light and Other Electromagnetic Radiation (New York: Academic) ch 6. **1969**.

100. Hendel, T.; Wuithschick, M.; Kettemann, F.; Birnbaum, A.; Rademann, K.; Polte, J. r., In situ determination of colloidal gold concentrations with UV–Vis spectroscopy: limitations and perspectives. *Analytical chemistry* **2014,** *86* (22), 11115-11124.

101. Haiss, W.; Thanh, N. T. K.; Aveyard, J.; Fernig, D. G., Determination of size and concentration of gold nanoparticles from UV-Vis spectra. *Analytical Chemistry* **2007,** *79*, 4215-4221.

102. Polte, J., Fundamental growth principles of colloidal metal nanoparticles–a new perspective. *CrystEngComm* **2015,** *17* (36), 6809-6830.

103. Datye, A. K.; Smith, D. J., The Study of Heterogeneous Catalysts by High-Resolution Transmission Electron MicroscoDV. *Catalysis Reviews* **1992,** *34* (1-2), 129-178.

104. Villa, A.; Dimitratos, N.; Chan-Thaw, C. E.; Hammond, C.; Veith, G. M.; Wang, D.; Manzoli, M.; Prati, L.; Hutchings, G. J., Characterisation of gold catalysts. *Chem. Soc. Rev.* **2016,** *45* (18), 4953-4994.

105. Laidlaw, I.; Steinmetz, M., Introduction to differential sedimentation. *Analytical ultracentrifugation. The Royal Society of Chemistry, Cambridge* **2005**, 270-290.

106. du Toit, H.; Macdonald, T.; Huang, H.; Parkin, I.; Gavriilidis, A., Continuous flow synthesis of citrate capped gold nanoparticles using UV induced nucleation. *RSC Advances* **2017,** *7* (16), 9632-9638.

107. Ho, C. S.; Lam, C.; Chan, M.; Cheung, R.; Law, L.; Lit, L.; Ng, K.; Suen, M.; Tai, H., Electrospray ionisation mass spectrometry: principles and clinical applications. *The Clinical Biochemist Reviews* **2003,** *24* (1), 3.

108. Trachsel, F. Design of a microreactor for reactions using supercritical fluids as the reaction solvent. ETH Zurich, 2008.

109. Bretherton, F. P., The motion of long bubbles in tubes. *Journal of Fluid Mechanics* **1961,** *10* (2), 166-188.

110. Jun, H.; Fabienne, T.; Florent, M.; Coulon, P.-E.; Nicolas, M.; Olivier, S., Understanding of the size control of biocompatible gold nanoparticles in millifluidic channels. *Langmuir* **2012,** *28* (45), 15966-15974.

111. Shalom, D.; Wootton, R. C.; Winkle, R. F.; Cottam, B. F.; Vilar, R.; Wilde, C. P., Synthesis of thiol functionalized gold nanoparticles using a continuous flow microfluidic reactor. *Materials Letters* **2007,** *61* (4), 1146-1150.

112. Tsunoyama, H.; Ichikuni, N.; Tsukuda, T., Microfluidic synthesis and catalytic application of PVP-stabilized,∼ 1 nm gold clusters. *Langmuir* **2008,** *24* (20), 11327-11330.

113. Luty-Błocho, M.; Fitzner, K.; Hessel, V.; Löb, P.; Maskos, M.; Metzke, D.; Pacławski, K.; Wojnicki, M., Synthesis of gold nanoparticles in an interdigital micromixer using ascorbic acid and sodium borohydride as reducers. *Chem Eng J* **2011,** *171* (1), 279-290.

114. Köhler, J.; Wagner, J.; Albert, J., Formation of isolated and clustered Au nanoparticles in the presence of polyelectrolyte molecules using a flow-through Si chip reactor. *Journal of Materials Chemistry* **2005,** *15* (19), 1924-1930.

115. Wagner, J.; Köhler, J. M., Continuous synthesis of gold nanoparticles in a microreactor. *Nano Letters* **2005,** *5*, 685-691.

116. Wagner, J.; Tshikhudo, T. R.; Köhler, J. M., Microfluidic generation of metal nanoparticles by borohydride reduction. *Chem Eng J* **2007,** *135*, 104-109.

117. Sugano, K.; Uchida, Y.; Ichihashi, O.; Yamada, H.; Tsuchiya, T.; Tabata, O., Mixing speed-controlled gold nanoparticle synthesis with pulsed mixing microfluidic system. *Microfluidics and Nanofluidics* **2010,** *9* (6), 1165-1174.

118. Verma, M.; Kumaran, V., Effect of ultra-fast mixing in a microchannel due to a soft wall on the room temperature synthesis of gold nanoparticles. *Sadhana* **2015,** *40* (3), 973-983.

119. Bandulasena, M. V.; Vladisavljević, G. T.; Odunmbaku, O. G.; Benyahia, B., Continuous synthesis of PVP stabilized biocompatible gold nanoparticles with a controlled size using a 3D glass capillary microfluidic device. *Chem Eng Sci* **2017,** *171*, 233-243.

120. Baber, R.; Mazzei, L.; Thanh, N. T. K.; Gavriilidis, A., An engineering approach to synthesis of gold and silver nanoparticles by controlling hydrodynamics and mixing based on a coaxial flow reactor. *Nanoscale* **2017,** *9* (37), 14149-14161.

121. Yang, S. Y.; Cheng, F. Y.; Yeh, C. S.; Lee, G. B., Size-controlled synthesis of gold nanoparticles using a micro-mixing system. *Microfluid Nanofluid* **2009,** *8*, 303-311.

122. Kitson, P. J.; Rosnes, M. H.; Sans, V.; Dragone, V.; Cronin, L., Configurable 3D-Printed millifluidic and microfluidic 'lab on a chip' reactionware devices. *Lab on a Chip* **2012,** *12* (18), 3267-3271.

123. Ftouni, J.; Penhoat, M.; Addad, A.; Payen, E.; Rolando, C.; Girardon, J.-S., Highly controlled synthesis of nanometric gold particles by citrate reduction using the short mixing, heating and quenching times achievable in a microfluidic device. *Nanoscale* **2012,** *4* (15), 4450-4454.

124. Jamal, F.; Jean-Sébastien, G.; Maël, P.; Edmond, P.; Christian, R., Gold nanoparticle synthesis in microfluidic systems and immobilisation in microreactors designed for the catalysis of fine organic reactions. *Microsystem Technologies* **2012,** *18* (2), 151-158.

125. Gómez-de Pedro, S.; Puyol, M.; Alonso-Chamarro, J., Continuous flow synthesis of nanoparticles using ceramic microfluidic devices. *Nanotechnology* **2010,** *21* (41), 415603.

126. Sugie, A.; Song, H.; Horie, T.; Ohmura, N.; Kanie, K.; Muramatsu, A.; Mori, A., Synthesis of thiol-capped gold nanoparticle with a flow system using organosilane as a reducing agent. *Tetrahedron Letters* **2012,** *53* (33), 4457-4459.

127. Kumar, D. R.; Kulkarni, A.; Prasad, B., Microfluidic platform for continuous flow synthesis of triangular gold nanoplates. *Colloids and Surfaces A: Physicochemical and Engineering Aspects* **2014,** *443*, 149-155.

128. Fu, Q.; Ran, G.; Xu, W., A microfluidic-based controllable synthesis of rolled or rigid ultrathin gold nanoplates. *RSC Advances* **2015,** *5* (47), 37512-37516.

129. Sebastián, V.; Lee, S.; Zhou, C.; Kraus, M. F.; Fujimoto, J. G.; Jensen, K. F., One-step continuous synthesis of biocompatible gold nanorods for optical coherence tomography. *Chem. Commun.* **2012,** *48* (53), 6654-6656.

130. Ishizaka, T.; Ishigaki, A.; Kawanami, H.; Suzuki, A.; Suzuki, T. M., Dynamic control of gold nanoparticle morphology in a microchannel flow reactor by glucose reduction in aqueous sodium hydroxide solution. *J. Colloid Interface Sci.* **2012,** *367* (1), 135-138.

131. Wagner, J.; Kirner, T.; Mayer, G.; Albert, J.; Köhler, J., Generation of metal nanoparticles in a microchannel reactor. *Chemical Engineering Journal* **2004,** *101* (1), 251-260.

132. Song, Y.; Hormes, J.; Kumar, C. S., Microfluidic synthesis of nanomaterials. *Small* **2008,** *4* (6), 698-711.

133. Zhao, C.-X.; He, L.; Qiao, S. Z.; Middelberg, A. P. J., Nanoparticle synthesis in microreactors. *Chemical Engineering Science* **2011,** *66* (7), 1463-1479.

134. Sebastian, V.; Khan, S. A.; Kulkarni, A. A., Perspective Article: Flow Synthesis of Functional Materials. *Journal of Flow Chemistry* **2017,** *7* (3), 96-105.

135. Krishna, K. S.; Li, Y.; Li, S.; Kumar, C. S., Lab-on-a-chip synthesis of inorganic nanomaterials and quantum dots for biomedical applications. *Advanced Drug Delivery Reviews* **2013,** *65* (11-12), 1470-1495.

136. Lohse, S. E.; Eller, J. R.; Sivapalan, S. T.; Plews, M. R.; Murphy, C. J., A simple millifluidic benchtop reactor system for the high-throughput synthesis and functionalization of gold nanoparticles with different sizes and shapes. *ACS Nano* **2013,** *7* (5), 4135-4150.

137. Gomez, L.; Sebastian, V.; Irusta, S.; Ibarra, A.; Arruebo, M.; Santamaria, J., Scaled-up production of plasmonic nanoparticles using microfluidics: from metal precursors to functionalized and sterilized nanoparticles. *Lab on a Chip* **2014,** *14* (2), 325-332.

138. Uson, L.; Sebastian, V.; Arruebo, M.; Santamaria, J., Continuous microfluidic synthesis and functionalization of gold nanorods. *Chemical Engineering Journal* **2016,** *285*, 286-292.

139. Bullen, C.; Latter, M. J.; D'Alonzo, N. J.; Willis, G. J.; Raston, C. L., A seedless approach to continuous flow synthesis of gold nanorods. *Chem. Commun.* **2011,** *47* (14), 4123-4125.

140. Boleininger, J.; Kurz, A.; Reuss, V.; Sönnichsen, C., Microfluidic continuous flow synthesis of rod-shaped gold and silver nanocrystals. *Phys Chem Chem Phys* **2006,** *8* (33), 3824-3827.

141. Sans, V.; Glatzel, S.; Douglas, F. J.; Maclaren, D. A.; Lapkin, A.; Cronin, L., Non-equilibrium dynamic control of gold nanoparticle and hyper-branched nanogold assemblies. *Chemical Science* **2014,** *5* (3), 1153-1157.

142. Bayazit, M. K.; Yue, J.; Cao, E.; Gavriilidis, A.; Tang, J., Controllable synthesis of gold nanoparticles in aqueous solution by microwave assisted flow chemistry. *ACS Sustainable Chemistry & Engineering* **2016,** *4* (12), 6435-6442.

143. Günther, A.; Jensen, K. F., Multiphase microfluidics: from flow characteristics to chemical and materials synthesis. *Lab on a Chip* **2006,** *6* (12), 1487-1503.

144. Nightingale, A. M.; deMello, J. C., Segmented flow reactors for nanocrystal synthesis. *Advanced Materials* **2013,** *25* (13), 1813-1821.

145. Köhler, J. M.; Li, S.; Knauer, A., Why is micro segmented flow particularly promising for the synthesis of nanomaterials? *Chem Eng Technol* **2013,** *36* (6), 887-899.

146. Kim, J. H.; Jeon, T. Y.; Choi, T. M.; Shim, T. S.; Kim, S.-H.; Yang, S.-M., Droplet microfluidics for producing functional microparticles. *Langmuir* **2013,** *30* (6), 1473-1488.

147. Niu, G.; Ruditskiy, A.; Vara, M.; Xia, Y., Toward continuous and scalable production of colloidal nanocrystals by switching from batch to droplet reactors. *Chem. Soc. Rev.* **2015,** *44* (16), 5806-5820.

148. Shang, L.; Cheng, Y.; Zhao, Y., Emerging droplet microfluidics. *Chemical Reviews* **2017,** *117* (12), 7964-8040.

149. Liu, H.; Vandu, C. O.; Krishna, R., Hydrodynamics of taylor flow in vertical capillaries: Flow regimes, bubble rise velocity, liquid slug length, and pressure drop. *Ind. Eng. Chem. Res.* **2005,** *44* (14), 4884-4897.

150. Sebastian Cabeza, V.; Kuhn, S.; Kulkarni, A. A.; Jensen, K. F., Size-controlled flow synthesis of gold nanoparticles using a segmented flow microfluidic platform. *Langmuir* **2012,** *28* (17), 7007-7013.

151. Kulkarni, A. A.; Sebastian Cabeza, V., Insights in the diffusion controlled interfacial flow synthesis of Au nanostructures in a microfluidic system. *Langmuir* **2017,** *33* (50), 14315-14324.

152. Ngai, T.; Bon, S. A., *Particle-stabilized emulsions and colloids*. Royal Society of Chemistry: 2014.

153. Khan, S. A.; Duraiswamy, S., Controlling bubbles using bubbles—microfluidic synthesis of ultra-small gold nanocrystals with gas-evolving reducing agents. *Lab on a Chip* **2012,** *12* (10), 1807-1812.

154. Song, H.; Tice, J. D.; Ismagilov, R. F., A microfluidic system for controlling reaction networks in time. *Angewandte Chemie* **2003,** *115* (7), 792-796.

155. Günther, A.; Jhunjhunwala, M.; Thalmann, M.; Schmidt, M. A.; Jensen, K. F., Micromixing of miscible liquids in segmented gas-liquid flow. *Langmuir* **2005,** *21* (4), 1547-1555.

156. Zhang, L.; Xia, Y., Scaling up the production of colloidal nanocrystals: Should we increase or decrease the reaction volume? *Advanced materials* **2014,** *26* (16), 2600-2606.

157. Christopher, G. F.; Anna, S. L., Microfluidic methods for generating continuous droplet streams. *Journal of Physics D: Applied Physics* **2007,** *40* (19), R319.

158. Garstecki, P.; Fuerstman, M. J.; Stone, H. A.; Whitesides, G. M., Formation of droplets and bubbles in a microfluidic T-junction—scaling and mechanism of break-up. *Lab on a Chip* **2006,** *6* (3), 437-446.

159. Duraiswamy, S.; Khan, S. A., Droplet ‐ based microfluidic synthesis of anisotropic metal nanocrystals. *Small* **2009,** *5* (24), 2828-2834.

160. Duraiswamy, S.; Khan, S. A., Dual ‐ stage continuous ‐ flow seedless microfluidic synthesis of anisotropic gold nanocrystals. *Particle & Particle Systems Characterization* **2014,** *31* (4), 429-432.

161. Duraiswamy, S.; Khan, S. A., Plasmonic nanoshell synthesis in microfluidic composite foams. *Nano letters* **2010,** *10* (9), 3757-3763.

162. Lazarus, L. L.; Yang, A. S.; Chu, S.; Brutchey, R. L.; Malmstadt, N., Flow-focused synthesis of monodisperse gold nanoparticles using ionic liquids on a microfluidic platform. *Lab on a Chip* **2010,** *10* (24), 3377-3379.

163. Lazarus, L. L.; Riche, C. T.; Marin, B. C.; Gupta, M.; Malmstadt, N.; Brutchey, R. L., Two-phase microfluidic droplet flows of ionic liquids for the synthesis of gold and silver nanoparticles. *ACS Applied Materials & Interfaces* **2012,** *4* (6), 3077-3083.

164. Taifur-Rahman, M.; Krishnamurthy, P. G.; Parthiban, P.; Jain, A.; Park, C. P.; Kim, D.-P.; Khan, S. A., Dynamically tunable nanoparticle engineering enabled by short contact-time microfluidic synthesis with a reactive gas. *Rsc Advances* **2013,** *3* (9), 2897-2900.

165. Abalde-Cela, S.; Taladriz-Blanco, P.; de Oliveira, M. G.; Abell, C., Droplet microfluidics for the highly controlled synthesis of branched gold nanoparticles. *Scientific Reports* **2018,** *8* (1), 2440.

166. Hafermann, L.; Köhler, J. M., Small gold nanoparticles formed by rapid photochemical flow-through synthesis using microfluid segment technique. *Journal of Nanoparticle Research* **2015,** *17* (2), 1-8.

167. Lee, K. G.; Hong, J.; Wang, K. W.; Heo, N. S.; Kim, D. H.; Lee, S. Y.; Lee, S. J.; Park, T. J., In vitro biosynthesis of metal nanoparticles in microdroplets. *ACS Nano* **2012,** *6* (8), 6998-7008.

168. Gu, T.; Zheng, C.; He, F.; Zhang, Y.; Khan, S. A.; Hatton, T. A., Electrically controlled mass transport into microfluidic droplets from nanodroplet carriers with application in controlled nanoparticle flow synthesis. *Lab on a Chip* **2018,** *18*, 1330-1340.

169. Zhang, L.; Niu, G.; Lu, N.; Wang, J.; Tong, L.; Wang, L.; Kim, M. J.; Xia, Y., Continuous and scalable production of well-controlled noble-metal nanocrystals in milliliter-sized droplet reactors. *Nano letters* **2014,** *14* (11), 6626-6631.

170. Turkevich, J.; Stevenson, P. C.; Hillier, J., A study of the nucleation and growth processes in the synthesis of colloidal gold. *Discussions of the Faraday Society* **1951,** *11*, 55-75.

171. Kumar, S.; Gandhi, K. S.; Kumar, R., Modeling of formation of gold nanoparticles by citrate method. *Industrial & Engineering Chemistry Research* **2006,** *46* (10), 3128-3136.

172. Agunloye, E.; Gavriilidis, A.; Mazzei, L., A mathematical investigation of the Turkevich organizer theory in the citrate method for the synthesis of gold nanoparticles. *Chem Eng Sci* **2017,** *173*, 275-286.

173. Murphy, C. J.; Gole, A. M.; Stone, J. W.; Sisco, P. N.; Alkilany, A. M.; Goldsmith, E. C.; Baxter, S. C., Gold nanoparticles in biology: Beyond toxicity to cellular imaging. *Accounts of Chemical Research* **2008,** *41* (12), 1721-1730.

174. Xia, H.; Bai, S.; Hartmann, J.; Wang, D., Synthesis of monodisperse quasi-spherical gold nanoparticles in water via silver(I)-assisted citrate reduction. *Langmuir* **2009,** *26* (5), 3585-3589.

175. Su, C.-H.; Wu, P.-L.; Yeh, C.-S., Sonochemical synthesis of well-dispersed gold nanoparticles at the ice temperature. *The Journal of Physical Chemistry B* **2003,** *107* (51), 14240-14243.

176. Shahbazali, E.; Hessel, V.; Noël, T.; Wang, Q., Metallic nanoparticles made in flow and their catalytic applications in organic synthesis. *Nanotechnology Reviews* **2014,** *3* (1), 65-86.

177. Zhang, J.; Wang, K.; Teixeira, A. R.; Jensen, K. F.; Luo, G., Design and scaling up of microchemical systems: a review. *Annual review of chemical and biomolecular engineering* **2017,** *8*, 285-305.

178. Yang, S.; Cheng, F.; Yeh, C.; Lee, G., Size-controlled synthesis of gold nanoparticles using a micro-mixing system. *Microfluidics and Nanofluidics* **2010,** *8* (3), 303-311.

179. Kumar, D. V. R.; Kulkarni, A. A.; Prasad, B. L. V., Microfluidic platform for continuous flow synthesis of triangular gold nanoplates. *Colloids and Surfaces A: Physicochemical and Engineering Aspects* **2014,** *443*, 149-155.

180. Liu, G.; Yang, X.; Li, Y.; Yang, Z.; Hong, W.; Liu, J., Continuous Flow Controlled Synthesis of Gold Nanoparticles Using Pulsed Mixing Microfluidic System. *Advances in Materials Science and Engineering* **2015,** *2015*.

181. Ftouni, J.; Penhoat, M.; Addad, A.; Payen, E.; Rolando, C.; Girardon, J., Highly controlled synthesis of nanometric gold particles by citrate reduction using the short mixing, heating and quenching times achievable in a microfluidic device. *Nanoscale* **2012,** *4* (15), 4450-4454.

182. Singh, A.; Shirolkar, M.; Lalla, N. P.; Malek, C. K.; Kulkarni, S. K., Room temperature, water-based, microreactor synthesis of gold and silver nanoparticles. *International Journal of Nanotechnology* **2009,** *6*, 541-551.

183. Levenspiel, O., The convection model for laminar flow. In *Chemical Reaction Engineering*, 3 ed.; John Wiley and Sons Ltd: United States of America, 1999; pp 339-349.

184. Levenspiel, O., Chemical reaction engineering. *Industrial & engineering chemistry research* **1999,** *38* (11), 4140-4143.

185. Southard, M. Z.; Dias, L. J.; Himmelstein, K. J.; Stella, V. J., Experimental determinations of diffusion coefficients in dilute aqueous solution using the method of hydrodynamic stability. *Pharmaceutical Research* **1991,** *8* (12), 1489-1494.

186. Capretto, L.; Cheng, W.; Hill, M.; Zhang, X., Micromixing within microfluidic devices. In *Microfluidics*, Springer: 2011; pp 27-68.

187. Haiss, W.; Thanh, N. T.; Aveyard, J.; Fernig, D. G., Determination of size and concentration of gold nanoparticles from UV-vis spectra. *Analytical chemistry* **2007,** *79* (11), 4215-4221.

188. Chow, M.; Zukoski, C., Gold sol formation mechanisms: Role of colloidal stability. *Journal Of Colloid and Interface Science* **1994,** *165* (1), 97-109.

189. Pei, L.; Mori, K.; Adachi, M., Formation process of two-dimensional networked gold nanowires by citrate reduction of $AuCl_4^-$ and the shape stabilization. *Langmuir* **2004,** *20* (18), 7837-7843.

190. Rodríguez-González, B.; Mulvaney, P.; Liz-Marzán, L. M., An electrochemical model for gold colloid formation via citrate reduction. *Zeitschrift für Physikalische Chemie* **2007,** *221* (3), 415-426.

191. Pong, B.-K.; Elim, H. I.; Chong, J.-X.; Ji, W.; Trout, B. L.; Lee, J.-Y., New insights on the nanoparticle growth mechanism in the citrate reduction of gold(III) salt: Formation of the Au nanowire intermediate and its nonlinear optical properties. *The Journal of Physical Chemistry C* **2007,** *111* (17), 6281-6287.

192. Turkevich, J.; Stevenson, P. C.; Hillier, J., The formation of colloidal gold. *The Journal of Physical Chemistry* **1953,** *57* (7), 670-673.

193. Caruso, F.; Lichtenfeld, H.; Giersig, M.; Möhwald, H., Electrostatic self-assembly of silica nanoparticle-polyelectrolyte multilayers on polystyrene latex particles. *Journal of the American Chemical Society* **1998,** *120* (33), 8523-8524.

194. Ma, A.; Xie, Y.; Xu, J.; Zeng, H.; Xu, H., The significant impact of polydopamine on the catalytic performance of the carried Au nanoparticles. *Chemical Communications* **2015,** *51* (8), 1469-1471.

195. Yang, S.; Wang, Y.; Wang, Q.; Zhang, R.; Ding, B., UV irradiation induced formation of Au nanoparticles at room temperature: The case of pH values. *Colloids and Surfaces A: Physicochemical and Engineering Aspects* **2007,** *301* (1), 174-183.

196. Polte, J.; Ahner, T. T.; Delissen, F.; Sokolov, S.; Emmerling, F.; Thünemann, A. F.; Kraehnert, R., Mechanism of gold nanoparticle formation in the classical citrate synthesis method derived from coupled in situ XANES and SAXS evaluation. *Journal of the American Chemical Society* **2010,** *132* (4), 1296-1301.

197. Park, J.-W.; Shumaker-Parry, J. S., Structural study of citrate layers on gold nanoparticles: Role of intermolecular interactions in stabilizing nanoparticles. *Journal of the American Chemical Society* **2014,** *136* (5), 1907-1921.

198. Kirby, B. J.; Hasselbrink, E. F., Zeta potential of microfluidic substrates: 1. Theory, experimental techniques, and effects on separations. *Electrophoresis* **2004,** *25* (2), 187-202.

199. Kolská, Z.; Makajová, Z.; Kolářová, K.; Slepičková, N. K.; Trostová, S.; Řezníčková, A.; Siegel, J.; Švorčík, V., Electrokinetic potential and other surface properties of polymer foils and their modifications. In *Polymer Science*, InTech: 2013.

200. Buining, P. A.; Humbel, B. M.; Philipse, A. P.; Verkleij, A. J., Preparation of functional silane-stabilized gold colloids in the (sub) nanometer size range. *Langmuir* **1997,** *13* (15), 3921-3926.

201. Lind, C. J. *Characterization of mineral precipitates by electron microscope photographs and electron diffraction patterns*; United States Geological Survey: United States, 1983.

202. He, S.; Kohira, T.; Uehara, M.; Kitamura, T.; Nakamura, H.; Miyazaki, M.; Maeda, H., Effects of interior wall on continuous fabrication of silver nanoparticles in microcapillary reactor. *Chem Lett* **2005,** *34* (6), 748-749.

203. Liu, H.; Huang, J.; Sun, D.; Lin, L.; Lin, W.; Li, J.; Jiang, X.; Wu, W.; Li, Q., Microfluidic biosynthesis of silver nanoparticles: Effect of process parameters on size distribution. *Chemical Engineering Journal* **2012,** *209*, 568-576.

204. Hecht, K. Microreactors for gas/liquid reactions: The role of surface properties. PhD thesis, KIT-Bibliothek, Western Engineering, Inc., 2014.

205. Evenhuis, C. J.; Guijt, R. M.; Macka, M.; Marriott, P. J.; Haddad, P. R., Variation of zeta ‐ potential with temperature in fused ‐ silica capillaries used for capillary electrophoresis. *Electrophoresis* **2006,** *27* (3), 672-676.

206. Werner, C.; König, U.; Augsburg, A.; Arnhold, C.; Körber, H.; Zimmermann, R.; Jacobasch, H. J., Electrokinetic surface characterization of biomedical polymers - a survey. *Colloids and Surfaces A: Physicochemical and Engineering Aspects* **1999,** *159* (2), 519-529.

207. Bismarck, A.; Kumru, M. E.; Springer, J., Characterization of several polymer surfaces by streaming potential and wetting measurements: Some reflections on acid–base interactions. *Journal of Colloid and Interface Science* **1999,** *217* (2), 377-387.

208. Schwer, C.; Kenndler, E., Electrophoresis in fused-silica capillaries: The influence of organic solvents on the electroosmotic velocity and the zeta potential. *Analytical Chemistry* **1991,** *63* (17), 1801-1807.

209. Ben-Jaber, S.; Peveler, W. J.; Quesada-Cabrera, R.; Cortés, E.; Sotelo-Vazquez, C.; Abdul-Karim, N.; Maier, S. A.; Parkin, I. P., Photo-induced enhanced Raman spectroscopy for

universal ultra-trace detection of explosives, pollutants and biomolecules. *Nature Communications* **2016,** *7*, 12189.

210. Le Ru, E.; Etchegoin, P., *Principles of surface-enhanced Raman spectroscopy: And related plasmonic effects*. Elsevier: 2008.

211. Li, J. F.; Huang, Y. F.; Ding, Y.; Yang, Z. L.; Li, S. B.; Zhou, X. S.; Fan, F. R.; Zhang, W.; Zhou, Z. Y.; Ren, B., Shell-isolated nanoparticle-enhanced Raman spectroscopy. *Nature* **2010,** *464* (7287), 392-395.

212. Le Ru, E. C.; Etchegoin, P. G., Single-molecule surface-enhanced Raman spectroscopy. *Annual Review of Physical Chemistry* **2012,** *63*, 65-87.

213. Osawa, M.; Ikeda, M., Surface-enhanced infrared absorption of p-nitrobenzoic acid deposited on silver island films: Contributions of electromagnetic and chemical mechanisms. *The Journal of Physical Chemistry* **1991,** *95* (24), 9914-9919.

214. Otto, A.; Timper, J.; Billmann, J.; Kovacs, G.; Pockrand, I., Surface roughness induced electronic Raman scattering. *Surface Science Letters* **1980,** *92* (1), L55-L57.

215. Otto, A., The ‘chemical’ (electronic) contribution to surface‐enhanced Raman scattering. *Journal of Raman Spectroscopy* **2005,** *36* (6‐7), 497-509.

216. Tognalli, N. G.; Cortés, E.; Hernández-Nieves, A. D.; Carro, P.; Usaj, G.; Balseiro, C. A.; Vela, M. E.; Salvarezza, R. C.; Fainstein, A., From single to multiple Ag-layer modification of Au nanocavity substrates: A tunable probe of the chemical surface-enhanced Raman scattering mechanism. *ACS Nano* **2011,** *5* (7), 5433-5443.

217. Juvé, V.; Cardinal, M. F.; Lombardi, A.; Crut, A.; Maioli, P.; Pérez-Juste, J.; Liz-Marzán, L. M.; Del Fatti, N.; Vallée, F., Size-dependent surface plasmon resonance broadening in nonspherical nanoparticles: single gold nanorods. *Nano letters* **2013,** *13* (5), 2234-2240.

218. Jana, N. R.; Pal, T., Anisotropic metal nanoparticles for use as surface‐enhanced Raman substrates. *Advanced Materials* **2007,** *19* (13), 1761-1765.

219. Zhang, X.-Y.; Hu, A.; Zhang, T.; Lei, W.; Xue, X.-J.; Zhou, Y.; Duley, W. W., Self-assembly of large-scale and ultrathin silver nanoplate films with tunable plasmon resonance properties. *ACS Nano* **2011,** *5* (11), 9082-9092.

220. Brust, M.; Walker, M.; Bethell, D.; Schiffrin, D. J.; Whyman, R., Synthesis of thiol-derivatised gold nanoparticles in a two-phase liquid–liquid system. *Journal of the Chemical Society, Chemical Communications* **1994,** (7), 801-802.

221. Kimling, J.; Maier, M.; Okenve, B.; Kotaidis, V.; Ballot, H.; Plech, A., Turkevich method for gold nanoparticle synthesis revisited. *Journal of Physical Chemistry B* **2006,** *110*, 15700-15707.

222. Bastús, N. G.; Comenge, J.; Puntes, V., Kinetically controlled seeded growth synthesis of citrate-stabilized gold nanoparticles of up to 200 nm: Size focusing versus Ostwald ripening. *Langmuir* **2011,** *27* (17), 11098-11105.

223. Jana, N. R.; Gearheart, L.; Murphy, C. J., Seeding growth for size control of 5− 40 nm diameter gold nanoparticles. *Langmuir* **2001,** *17* (22), 6782-6786.

224. Ziegler, C.; Eychmüller, A., Seeded growth synthesis of uniform gold nanoparticles with diameters of 15− 300 nm. *The Journal of Physical Chemistry C* **2011,** *115* (11), 4502-4506.

225. Wagner, J.; Kirner, T.; Mayer, G.; Albert, J.; Kohler, J. M., Generation of metal nanoparticles in a microchannel reactor. *Chemical Engineering Journal* **2004,** *101* (1-3), 251-260.

226. Lee, C.-Y.; Chang, C.-L.; Wang, Y.-N.; Fu, L.-M., Microfluidic mixing: a review. *International journal of molecular sciences* **2011,** *12* (5), 3263-3287.

227. Lignos, I.; Maceiczyk, R.; deMello, A. J., Microfluidic technology: Uncovering the mechanisms of nanocrystal nucleation and growth. *Accounts of chemical research* **2017,** *50* (5), 1248-1257.

228. Young, J. K.; Lewinski, N. A.; Langsner, R. J.; Kennedy, L. C.; Satyanarayan, A.; Nammalvar, V.; Lin, A. Y.; Drezek, R. A., Size-controlled synthesis of monodispersed gold nanoparticles via carbon monoxide gas reduction. *Nanoscale Research Letters* **2011,** *6* (1), 428.

229. Krishnamurthy, P. g. Scalable continuous-flow processes for manufacturing plasmonic nanomaterials. National University of Singapore, 2013.

230. CooperáStevenson, P., A study of the nucleation and growth processes in the synthesis of colloidal gold. *Discussions of the Faraday Society* **1951,** *11*, 55-75.

231. Guo, S.; Shi, F.; Gu, Y.; Yang, J.; Deng, Y., Size-controllable synthesis of gold nanoparticles via carbonylation and reduction of hydrochloroauric acid with CO and H_2O in ionic liquids. *Chem Lett* **2005,** *34* (6), 830-831.

232. Karp, G., *Cell and molecular biology: concepts and experiments*. John Wiley & Sons: 2009.

233. Kang, Y.; Ye, X.; Murray, C. B., Size ‐ and shape ‐ selective synthesis of metal nanocrystals and nanowires using CO as a reducing agent. *Angewandte Chemie* **2010,** *122* (35), 6292-6295.

234. Pretzer, L. A.; Nguyen, Q. X.; Wong, M. S., Controlled growth of sub-10 nm gold nanoparticles using carbon monoxide reductant. *The Journal of Physical Chemistry C* **2010,** *114* (49), 21226-21233.

235. Mridha, M.; Nigam, K., Coiled flow inverter as an inline mixer. *Chemical Engineering Science* **2008,** *63* (6), 1724-1732.

236. Kurt, S. K.; Warnebold, F.; Nigam, K. D.; Kockmann, N., Gas-liquid reaction and mass transfer in microstructured coiled flow inverter. *Chem Eng Sci* **2017,** *169*, 164-178.

237. Kang, Y.; Ye, X.; Murray, C. B., Size ‐ and Shape ‐ Selective Synthesis of Metal Nanocrystals and Nanowires Using CO as a Reducing Agent. *Angewandte Chemie International Edition* **2010,** *49* (35), 6156-6159.

238. Gao, Z.-K.; Jin, N.-D.; Wang, W.-X., Definition of Flow Patterns. In *Nonlinear Analysis of Gas-Water/Oil-Water Two-Phase Flow in Complex Networks*, Springer: 2014; pp 7-11.

239. Van Baten, J.; Krishna, R., CFD simulations of mass transfer from Taylor bubbles rising in circular capillaries. *Chem Eng Sci* **2004,** *59* (12), 2535-2545.

240. Onea, A. A., *Numerical simulation of mass transfer with and without first order chemical reaction in two-fluid flows*. Citeseer: 2007.

241. Angeli, P.; Gavriilidis, A., Hydrodynamics of Taylor flow in small channels: a review. *Proceedings of the Institution of Mechanical Engineers, Part C: Journal of Mechanical Engineering Science* **2008,** *222* (5), 737-751.

242. Rossi, D.; Gargiulo, L.; Valitov, G.; Gavriilidis, A.; Mazzei, L., Experimental characterization of axial dispersion in coiled flow inverters. *Chemical Engineering Research and Design* **2017,** *120*, 159-170.

243. Vashisth, S.; Nigam, K., Experimental investigation of void fraction and flow patterns in coiled flow inverter. *Chemical Engineering and Processing: Process Intensification* **2008,** *47* (8), 1281-1291.

244. Kettemann, F.; Birnbaum, A.; Witte, S.; Wuithschick, M.; Pinna, N.; Kraehnert, R.; Rademann, K.; Polte, J. r., Missing piece of the mechanism of the turkevich method: The critical role of citrate protonation. *Chemistry of Materials* **2016,** *28* (11), 4072-4081.

245. Campion, A.; Kambhampati, P., Surface-enhanced Raman scattering. *Chemical society reviews* **1998,** *27* (4), 241-250.

246. Premkumar, T.; Kim, D.; Lee, K.; Geckeler, K. E., Polysorbate 80 as a Tool: Synthesis of Gold Nanoparticles. *Macromolecular Rapid Communications* **2007,** *28* (7), 888-893.

247. Zhao, Y.; Wang, Z.; Zhang, W.; Jiang, X., Adsorbed Tween 80 is unique in its ability to improve the stability of gold nanoparticles in solutions of biomolecules. *Nanoscale* **2010,** *2* (10), 2114-2119.

248. Campisi, S.; Schiavoni, M.; Chan-Thaw, C. E.; Villa, A., Untangling the role of the capping agent in nanocatalysis: recent advances and perspectives. *Catalysts* **2016,** *6* (12), 185.

249. Feng, H.; Yang, Y.; You, Y.; Li, G.; Guo, J.; Yu, T.; Shen, Z.; Wu, T.; Xing, B., Simple and rapid synthesis of ultrathin gold nanowires, their self-assembly and application in surface-enhanced Raman scattering. *Chemical Communications* **2009,** (15), 1984-1986.

250. Bergen, J. M.; Von Recum, H. A.; Goodman, T. T.; Massey, A. P.; Pun, S. H., Gold nanoparticles as a versatile platform for optimizing physicochemical parameters for targeted drug delivery. *Macromolecular Bioscience* **2006,** *6* (7), 506-516.

251. Dixit, V.; Van den Bossche, J.; Sherman, D. M.; Thompson, D. H.; Andres, R. P., Synthesis and grafting of thioctic acid− PEG− folate conjugates onto Au nanoparticles for selective targeting of folate receptor-positive tumor cells. *Bioconjugate Chemistry* **2006,** *17* (3), 603-609.

252. Yu, Y.; Luo, Z.; Yu, Y.; Lee, J. Y.; Xie, J., Observation of cluster size growth in CO-directed synthesis of $Au_{25}(SR)_{18}$ nanoclusters. *ACS nano* **2012,** *6* (9), 7920-7927.

253. Brzozowski, M.; O'Brien, M.; Ley, S. V.; Polyzos, A., Flow Chemistry: Intelligent processing of gas–liquid transformations using a tube-in-tube reactor. *Accounts of chemical research* **2015,** *48* (2), 349-362.

254. Hong, Z.; Weber, S., Teflon AF Materials in Topics in Current Chemistry, Vol. 308. Springer: Berlin, 2012; Vol. 308.

255. Koos, P.; Gross, U.; Polyzos, A.; O'Brien, M.; Baxendale, I.; Ley, S. V., Teflon AF-2400 mediated gas–liquid contact in continuous flow methoxycarbonylations and in-line FTIR measurement of CO concentration. *Organic & biomolecular chemistry* **2011,** *9* (20), 6903-6908.

256. Hansen, S. V.; Wilson, Z. E.; Ulven, T.; Ley, S. V., Controlled generation and use of CO in flow. *Reaction Chemistry & Engineering* **2016,** *1* (3), 280-287.

257. Yang, L.; Jensen, K. F., Mass transport and reactions in the tube-in-tube reactor. *Organic Process Research & Development* **2013,** *17* (6), 927-933.

258. Arif, A. Preparation and Optimization of a Membrane for 3rd Generation Solvent Membrane Contactor. NTNU, 2016.

259. Bernardo, P.; Drioli, E.; Golemme, G., Membrane gas separation: a review/state of the art. *Ind. Eng. Chem. Res.* **2009,** *48* (10), 4638-4663.

260. Matthews, M. A.; Rodden, J. B.; Akgerman, A., High-temperature diffusion of hydrogen, carbon monoxide, and carbon dioxide in liquid n-heptane, n-dodecane, and n-hexadecane. *Journal of Chemical and Engineering Data* **1987,** *32* (3), 319-322.

261. Cohen-Adad R, L. J., "Solubility data series." *Carbon Monoxide. International Union of Pure and Applied Chemistry* **1990,** *43*.

262. Young, J. K.; Lewinski, N. A.; Langsner, R. J.; Kennedy, L. C.; Satyanarayan, A.; Nammalvar, V.; Lin, A. Y.; Drezek, R. A., Size-controlled synthesis of monodispersed gold nanoparticles via carbon monoxide gas reduction. *Nanoscale research letters* **2011,** *6* (1), 1-11.

263. Morrison, I. D.; Ross, S., *Colloidal dispersions: suspensions, emulsions, and foams*. Wiley-Interscience New York: 2002.

264. McGorty, R.; Fung, J.; Kaz, D.; Manoharan, V. N., Colloidal self-assembly at an interface. *Materials Today* **2010,** *13* (6), 34-42.

265. Vella, D.; Mahadevan, L., The "cheerios effect". *American journal of physics* **2005,** *73* (9), 817-825.

266. Hasret, E.; Kırbaşlar, S. a. I. s.; Uslu, H., Extraction of Citric Acid and Maleic Acid from Their Aqueous Solutions Using a Phosphorus-Bonded Extractant, Tri-n-octylphosphineoxide, and a Secondary Amine, Dioctylamine. *Journal of Chemical & Engineering Data* **2017,** *63* (1), 39-48.

267. Reynaert, S.; Moldenaers, P.; Vermant, J., Control over colloidal aggregation in monolayers of latex particles at the oil− water interface. *Langmuir* **2006,** *22* (11), 4936-4945.

268. Wuithschick, M.; Birnbaum, A.; Witte, S.; Sztucki, M.; Vainio, U.; Pinna, N.; Rademann, K.; Emmerling, F.; Kraehnert, R.; Polte, J. r., Turkevich in new robes: key questions answered for the most common gold nanoparticle synthesis. *ACS nano* **2015,** *9* (7), 7052-7071.

269. Ji, X.; Song, X.; Li, J.; Bai, Y.; Yang, W.; Peng, X., Size control of gold nanocrystals in citrate reduction: The third role of citrate. *J Am Chem Soc* **2007,** *129* (45), 13939-13948.

270. Perala, S. R. K.; Kumar, S., On the mechanism of metal nanoparticle synthesis in the Brust–Schiffrin method. *Langmuir* **2013,** *29* (31), 9863-9873.

271. Shon, Y.-S.; Mazzitelli, C.; Murray, R. W., Unsymmetrical disulfides and thiol mixtures produce different mixed monolayer-protected gold clusters. *Langmuir* **2001,** *17* (25), 7735-7741.

272. Templeton, A. C.; Chen, S.; Gross, S. M.; Murray, R. W., Water-soluble, isolable gold clusters protected by tiopronin and coenzyme A monolayers. *Langmuir* **1999,** *15* (1), 66-76.

273. Jadzinsky, P. D.; Calero, G.; Ackerson, C. J.; Bushnell, D. A.; Kornberg, R. D., Structure of a thiol monolayer-protected gold nanoparticle at 1.1 Å resolution. *Science* **2007,** *318* (5849), 430-433.

274. Simpson, C. A.; Farrow, C. L.; Tian, P.; Billinge, S. J.; Huffman, B. J.; Harkness, K. M.; Cliffel, D. E., Tiopronin gold nanoparticle precursor forms aurophilic ring tetramer. *Inorganic chemistry* **2010,** *49* (23), 10858-10866.

275. Chen, T.; Luo, Z.; Yao, Q.; Yeo, A. X. H.; Xie, J., Synthesis of thiolate-protected Au nanoparticles revisited: U-shape trend between the size of nanoparticles and thiol-to-Au ratio. *Chem. Commun.* **2016,** *52* (61), 9522-9525.

276. Jin, R.; Zeng, C.; Zhou, M.; Chen, Y., Atomically precise colloidal metal nanoclusters and nanoparticles: Fundamentals and opportunities. *Chemical reviews* **2016,** *116* (18), 10346-10413.

277. Muhammed, M. H.; Pradeep, T., Luminescent quantum clusters of gold as bio-labels. In *Advanced fluorescence reporters in chemistry and biology II*, Springer: 2010; pp 333-353.

278. Zamborini, F. P.; Hicks, J. F.; Murray, R. W., Quantized double layer charging of nanoparticle films assembled using carboxylate/(Cu2+ or Zn2+)/carboxylate bridges. *J Am Chem Soc* **2000,** *122* (18), 4514-4515.

279. Li, G.; Jin, R., Atomically precise gold nanoclusters as new model catalysts. *Accounts of Chemical Research* **2013,** *46* (8), 1749-1758.

280. Shichibu, Y.; Negishi, Y.; Tsunoyama, H.; Kanehara, M.; Teranishi, T.; Tsukuda, T., Extremely high stability of glutathionate‐protected Au25 Clusters against core etching. *Small* **2007,** *3* (5), 835-839.

281. Murphy, C. J.; Sau, T. K.; Gole, A. M.; Orendorff, C. J.; Gao, J.; Gou, L.; Hunyadi, S. E.; Li, T., Anisotropic Metal Nanoparticles: Synthesis, Assembly, and Optical Applications. *The Journal of Physical Chemistry B* **2005,** *109* (29), 13857-13870.

282. Negishi, Y.; Nobusada, K.; Tsukuda, T., Glutathione-Protected Gold Clusters Revisited: Bridging the Gap between Gold(I)−Thiolate Complexes and Thiolate-Protected Gold Nanocrystals. *J Am Chem Soc* **2005,** *127* (14), 5261-5270.

283. Qian, H.; Jin, R., Controlling Nanoparticles with Atomic Precision: The Case of Au144(SCH2CH2Ph)60. *Nano Letters* **2009,** *9* (12), 4083-4087.

284. Chakraborty, I.; Pradeep, T., Atomically Precise Clusters of Noble Metals: Emerging Link between Atoms and Nanoparticles. *Chemical Reviews* **2017,** *117* (12), 8208-8271.

285. Yu, Y.; Li, J.; Chen, T.; Tan, Y. N.; Xie, J., Decoupling the CO-Reduction Protocol to Generate Luminescent Au22 (SR) 18 Nanocluster. *The Journal of Physical Chemistry C* **2015,** *119* (20), 10910-10918.

286. Aryal, S.; Remant, B.; Dharmaraj, N.; Bhattarai, N.; Kim, C. H.; Kim, H. Y., Spectroscopic identification of SAu interaction in cysteine capped gold nanoparticles. *Spectrochimica Acta Part A: Molecular and Biomolecular Spectroscopy* **2006,** *63* (1), 160-163.

287. Zheng, K.; Setyawati, M. I.; Leong, D. T.; Xie, J., Antimicrobial Gold Nanoclusters. *ACS Nano* **2017,** *11* (7), 6904-6910.

288. Bao, Y. Interaction between Au25 Monolayer Protected Clusters with Lipid Nanodiscs. University of Connecticut Graduate School, 2015.

289. Azubel, M.; Koivisto, J.; Malola, S.; Bushnell, D.; Hura, G. L.; Koh, A. L.; Tsunoyama, H.; Tsukuda, T.; Pettersson, M.; Häkkinen, H., Electron microscopy of gold nanoparticles at atomic resolution. *Science* **2014,** *345* (6199), 909-912.

290. Keller, B. O.; Sui, J.; Young, A. B.; Whittal, R. M., Interferences and contaminants encountered in modern mass spectrometry. *Analytica chimica acta* **2008,** *627* (1), 71-81.

291. Dass, A.; Stevenson, A.; Dubay, G. R.; Tracy, J. B.; Murray, R. W., Nanoparticle MALDI-TOF mass spectrometry without fragmentation: $Au_{25}(SCH_2CH_2Ph)_{18}$ and mixed monolayer Au_{25} $(SCH_2CH_2Ph)_{18-x}(L)_x$. *J Am Chem Soc* **2008,** *130* (18), 5940-5946.

292. Macdonald, T. J.; Wu, K.; Sehmi, S. K.; Noimark, S.; Peveler, W. J.; Du Toit, H.; Voelcker, N. H.; Allan, E.; MacRobert, A. J.; Gavriilidis, A., Thiol-capped gold nanoparticles swell-encapsulated into polyurethane as powerful antibacterial surfaces under dark and light conditions. *Scientific Reports* **2016,** *6*, 39272.

293. Hwang, G. B.; Allan, E.; Parkin, I. P., White light-activated antimicrobial paint using crystal violet. *Acs Appl. Mater. Interfaces* **2016,** *8* (24), 15033-15039.

294. Fang, J.; Li, J.; Zhang, B.; Yuan, X.; Asakura, H.; Tanaka, T.; Teramura, K.; Xie, J.; Yan, N., The support effect on the size and catalytic activity of thiolated Au 25 nanoclusters as precatalysts. *Nanoscale* **2015,** *7* (14), 6325-6333.

295. Chen, T.; Xie, J., Carbon Monoxide: A Mild and Efficient Reducing Agent towards Atomically Precise Gold Nanoclusters. *The Chemical Record* **2016**.

296. Tatarchuk, V. V.; Sergievskaya, A. P.; Druzhinina, I. A.; Zaikovsky, V. I., Kinetics and mechanism of the growth of gold nanoparticles by reduction of tetrachloroauric acid by hydrazine in Triton N-42 reverse micelles. *J Nanopart Res* **2011,** *13* (10), 4997.

297. Xie, J.; Zheng, Y.; Ying, J. Y., Protein-directed synthesis of highly fluorescent gold nanoclusters. *J Am Chem Soc* **2009,** *131* (3), 888-889.

298. Henglein, A., Radiolytic preparation of ultrafine colloidal gold particles in aqueous solution: optical spectrum, controlled growth, and some chemical reactions. *Langmuir* **1999,** *15* (20), 6738-6744.

299. Yamaguchi, A.; Okada, I.; Fukuoka, T.; Sakurai, I.; Utsumi, Y., Synthesis of metallic nanoparticles through X-ray radiolysis using synchrotron radiation. *Japanese Journal of Applied Physics* **2016,** *55* (5), 055502.

Appendix A. Supporting Information _ Continuous Flow Synthesis of Ultrasmall Gold Nanoparticles in a Microreactor using Trisodium Citrate and their SERS Performance

A1. Fouling characterization in PTFE tubing

Figure A-1a shows a picture of the PTFE capillary after use, where the various fouling sections are indicated. The SEM image[*] in **Figure A-1b** shows that the amount of gold attached on the tubing surface in section i) is much less than the pink fouling sections ii) and iii) (**Figure A-1a**). Even though severe fouling was observed in sections ii) and iii) (**Figure A-1c** and **d**) after 47 h operation time, the size of the gold nanoparticles was maintained at < 3 nm. For section iv) near the outlet of the tubing, no fouling was observed, as citrate-capped nanoparticles were stabilized.

---

[*] *The SEM measurements were carried out by Dr. Yaomin Li, University College London.*

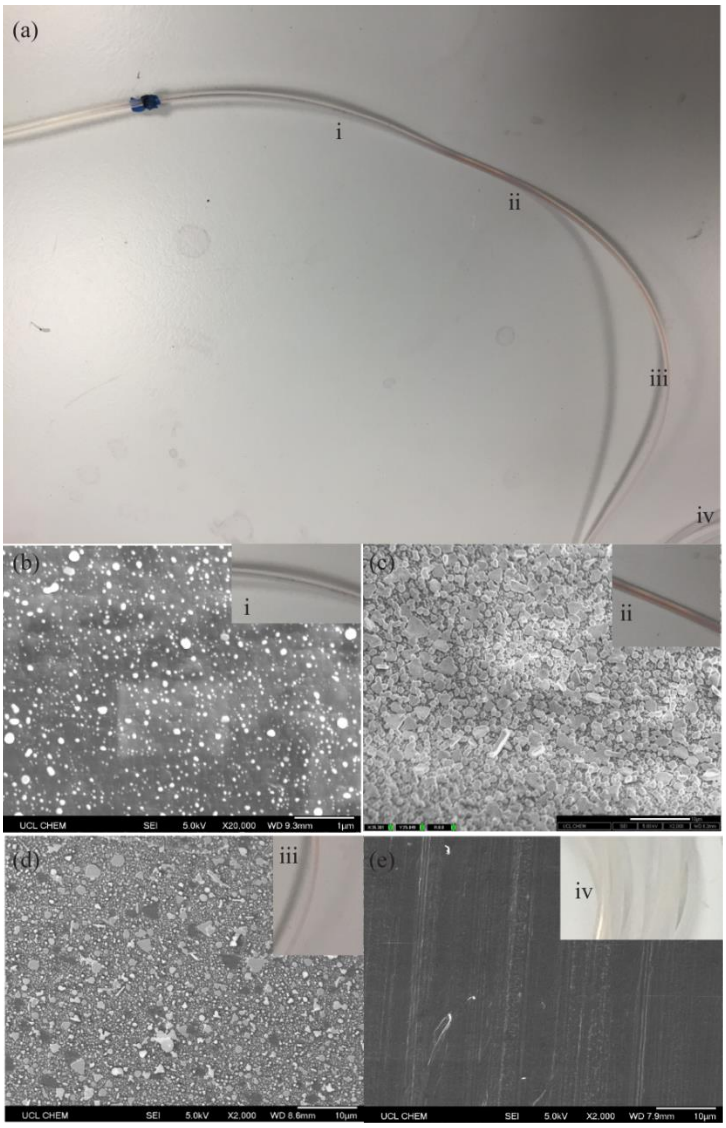

Figure A-1. (a) Photograph of the inlet section of 0.3 mm I.D. PTFE capillary used for gold nanoparticle synthesis with total flow rate 0.006 ml/min (residence time 30 min) at 100 ^{o}C after 47 h operation. The PTFE capillary containing the reaction mixture was taken out of the oil bath immediately for photo shooting with the solution still inside. The SEM images (b) to (e) show the inner surface of the capillary corresponding to the sections indicated in Figure A-1. Section (i) dark fouling near capillary inlet (ii) pink fouling near capillary inlet (iii) light pink fouling downstream of the inlet and (iv) outlet of the capillary. Solutions of 0.54 mM HAuCl4 and 1.7 mM citrate were mixed at 1/1 volumetric flowrate ratio.

A2. Characterization of the internal surfaces of the capillaries and nanoparticles produced with different capillary materials

The SEM images[*] in **Figure A-2** provide qualitative information for the roughness of the various tubing surfaces. The roughness can be observed to be PTFE>PEEK>FEP>fused silica.

---

[*] *The SEM measurements were carried out by Dr. Yaomin Li, University College London.*

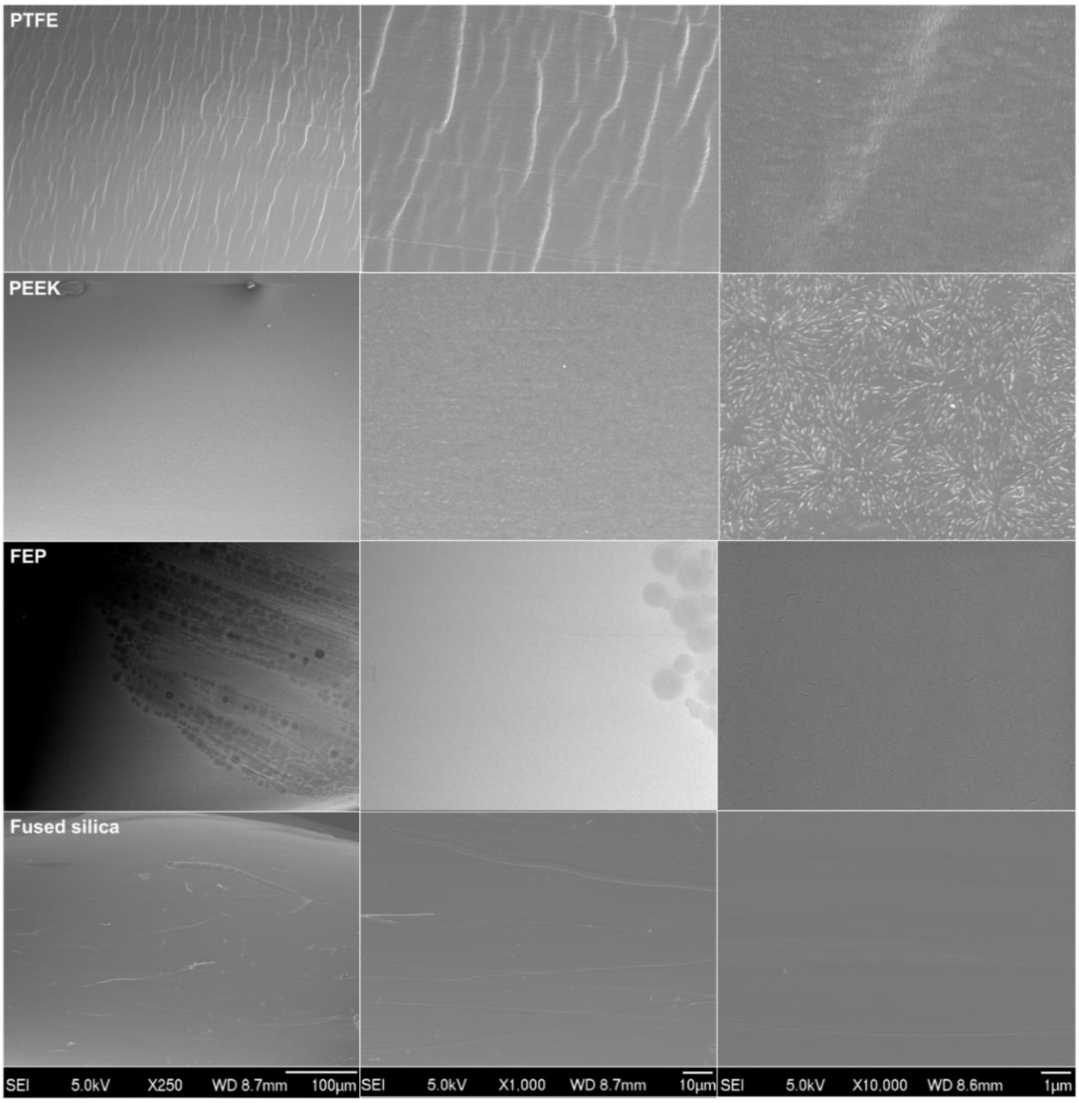

Figure A-2. SEM images of the inner surface of different tubing materials. The scale bars are shown under each of the columns which have the same magnification.

The zeta potential of the internal surface of the various tube materials was measured using an electrokinetic analyzer (SurPASS^{TM} 3, Anton Paar).[*] The streaming potential $U_{streaming}$ of the tubing was determined by measuring the difference in electrical potential at the inlet and outlet of the measuring cells (i.e.

---

[*] *The zeta potential measurement was carried out by Dr. Maximilian Besenhard, University College London, Thomas Luxbacher and Renate Kohl, Anton Paar, Austria*

inlet and outlet of the tubing), while changing the pressure difference ΔP. The obtained slope $dU_{streaming}/d\Delta P$ (**Figure A-3a**), was used to obtain the zeta potential. While the pressure difference was decreasing, the magnitude of the streaming potential decreased proportionally. The zeta potential was calculated *via* the Helmholtz-Smoluchowski equation: $\zeta = dU_{streaming}/d\Delta P \ \mu/(\varepsilon \cdot \varepsilon_0) \cdot \ k$. Here ζ is the (apparent) zeta potential at the tubing wall and, μ is the viscosity, $\varepsilon \cdot \varepsilon_0$ the dielectric coefficient, and k the conductivity of the measured solution.

For all the measurements, the capillaries were mounted to the SurPASS 3 flexible tubing cell (**Figure A-3b**). For ease of sample mounting, measurements for the polymer tubes were performed using tube samples of larger outer and inner diameter from the same manufacturer.

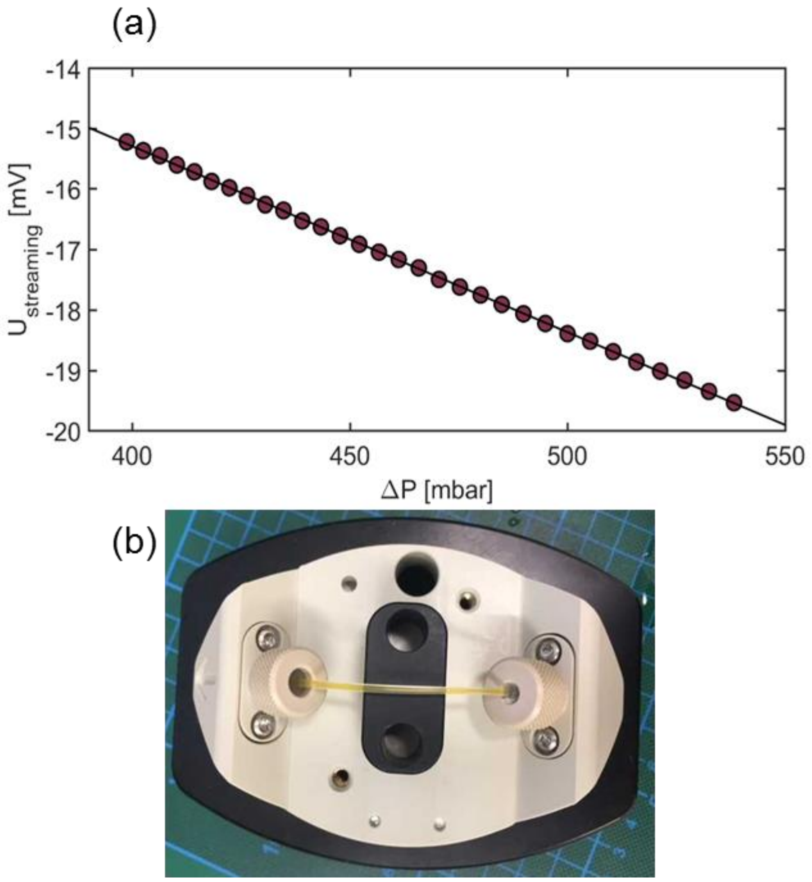

Figure A-3 (a) Example of the change in streaming potential with decreasing pressure difference between the flexible tubing cell's inlet and outlet (PTFE tubing at pH=3.9). (b) Installation example of the fused silica tubing using the SurPASS 3 cell for flexible tubing.

All zeta potential measurements were measured using a 0.001 M KCL solution (initial pH~6). Titrations were performed automatically adding NaOH and HCL solution to set the pH value. Laminar flow conditions were assumed, which was a requirement for the Helmholtz-Smoluchowski equation. The pH dependent zeta potential measurements for all tested tubing materials are shown in **Figure A-4**.

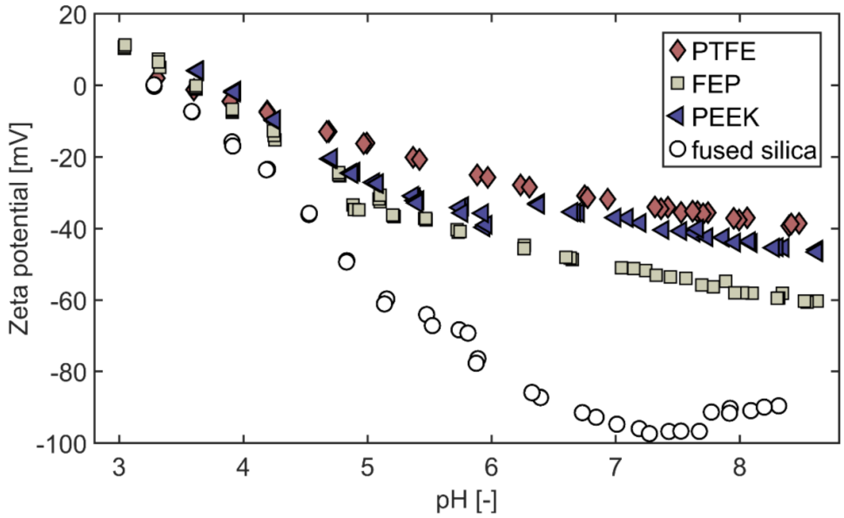

Figure A-4. Zeta potential measured as a function of pH for the four tube materials used in this work. The isoelectric points were determined as: 3.6 for PTFE, 3.7 for PEEK, 3.6 FEP, and 3.2 for fused silica.

Figure A-5 shows TEM images of gold nanoparticles obtained at different operation times with different tubing material. Based on the TEM images, average particle sizes were obtained and are shown in **Figure 3-8**.

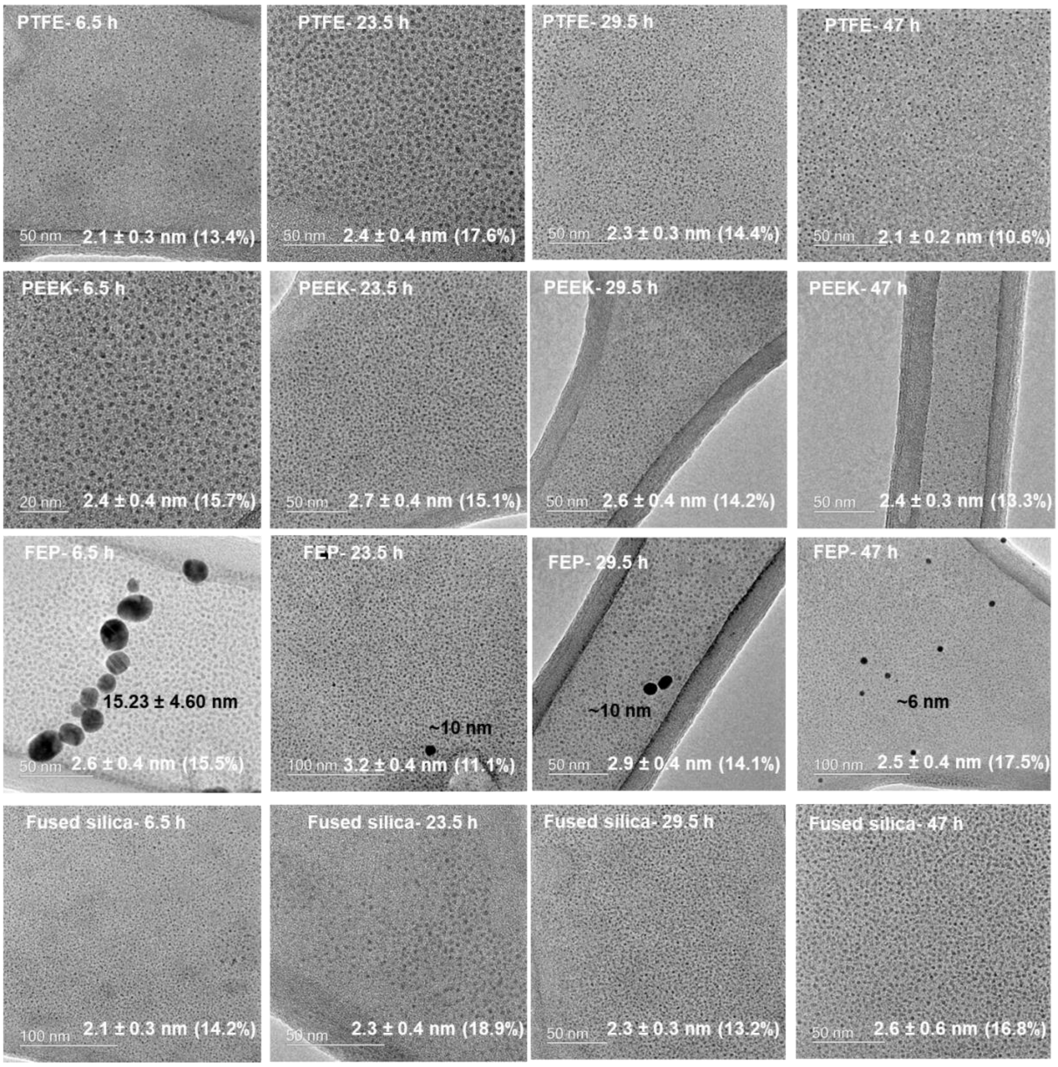

Figure A-5. TEM images of gold nanoparticles obtained at different operation times with different tube materials, with average residence time of 30 min, at 100 ^{o}C. The particle size shown on the TEM images of FEP tubing in black colour was the average size of large particles. The particle size shown on the TEM images of FEP tubing in white colour is the average size of small particles. Solutions of 0.54 mM $HAuCl_4$ and 1.7 mM citrate were mixed at 1/1 volumetric flowrate ratio.

Figure A-6 shows the yield of gold nanoparticles obtained at different operation times with different tube materials as measured by ICP-AES. The highest yields were obtained for the FEP and Fuse silica tubing.

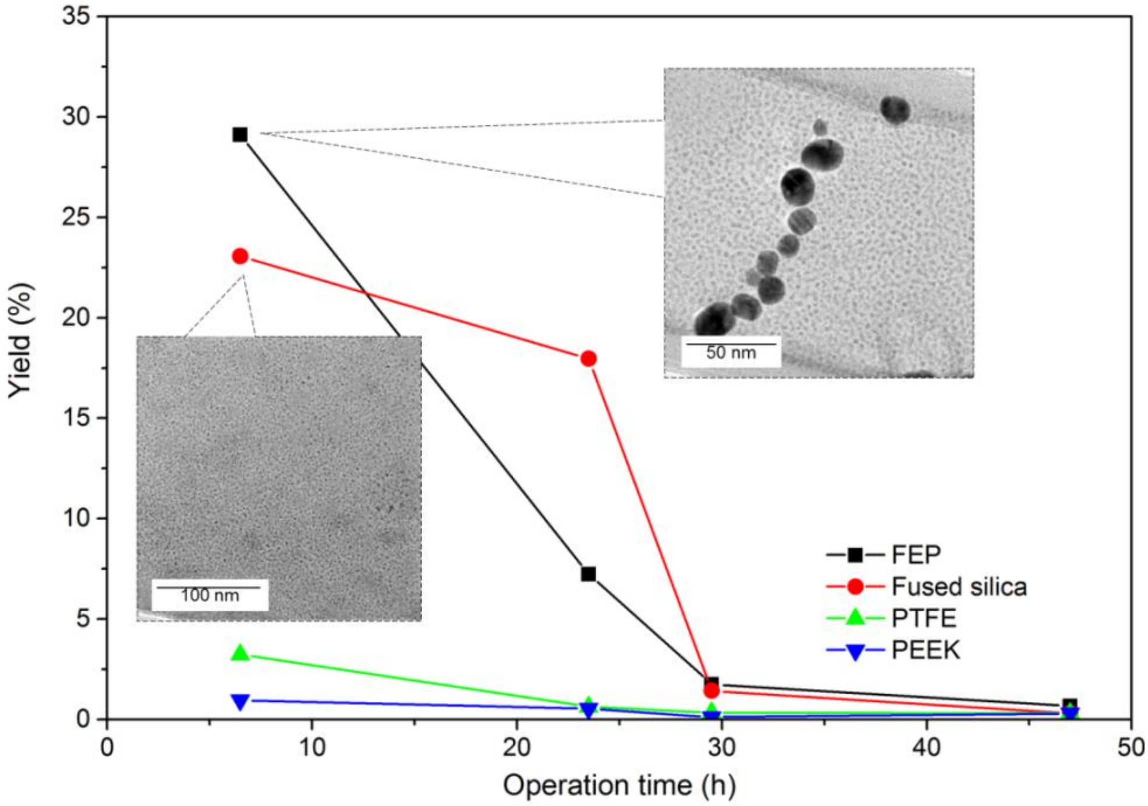

Figure A-6. Yield of gold nanoparticles obtained with different tubing materials measured by ICP-AES from samples collected at different operation times. The experiments were performed with 0.25 mm I.D. FEP, 0.32 mm I.D. fused silica, 0.3 mm I.D. PTFE and 0.25 mm I.D. PEEK tube at average residence time ~30 min and 100 ^{o}C. Solutions of 0.54 mM $HAuCl_4$ and 1.7 mM citrate were mixed at 1/1 volumetric flowrate ratio.

A3. Calculation of SERS enhancement factor (*EF*)

Enhancement factors for the analyte were calculated using Eq (A1) and (A2):

$$EF = I_{SERS} \times N_{bulk}/(I_{RS} \times N_{SERS}) \qquad \text{Eq. (A1)}$$

I_{SERS}: intensity of the band in SERS

I_{RS}: intensity of the band in Raman spectra

N_{bulk}: number of molecules probed in Raman sample

N_{SERS}: number of molecules probed in SERS

For all spectra, baselines were corrected to get peak intensity, while the laser spot size was ≈ 4.4 µm^2.

$$N = cVN_AS_{scan}/S_{sub} \qquad \text{Eq. (A2)}$$

c: molar concentration

c_{SERS}=5×10^{-6} M (10^{-5} M of Rh6G solution mixed with gold colloidal solution at the same volume)

c_{bulk} = powder, whose concentration is 1

V_{SERS}: the volume of the droplet =100µL in SERS

V_{RS} = 100mg in powder

N_A: Avogadro constant= 6.02×10^{23} mol^{-1}

S_{scan}: area of Raman scanning (i.e. Raman spot size) S_{scan}= 4.4 µm$^{2.}$

S_{sub}: area of the substrate; S_{SERS}=8 mm^2, S_{RS} = 4 mm^2.

$N_{SERS} = 5\times10^{-6}\times10^{-4}\times6.02\times10^{23}\times(4.4\times10^{-12})/(6.4\times10^{-5}) = 2.07\times10^{7}$ molecules

$N_{bulk} = 1\times0.01\times6.02\times10^{23}\times(4.4\times10^{-12})/(1.6\times10^{-5}) = 1.66\times10^{15}$ molecules

Three peaks with different band intensities were chosen to calculate the ***EF*** and shown in **Table A-1.**

Table A-1 Enhancement factor of both gold nanoparticles samples

Wavenumber		**Band Intensity**		**Enhancement factor EF**	
	Raman_Rh6G powder	SERS_A	SERS_B	SERS_A	SERS_B
611 cm^{-1}	1137	1923	573	1.35×10^{8}	4.03×10^{7}
1359 cm^{-1}	1097	2449	1305	1.79×10^{8}	9.52×10^{7}
1509 cm^{-1}	1070	1983	1134	1.48×10^{8}	8.47×10^{7}
Average Enhancement Factor				1.54×10^{8}	7.34×10^{7}

SERS_A: citrate-capped 2 nm gold nanoparticles synthesized in this work
SERS_B: commercial phosphate-capped 2 nm gold nanoparticles

Appendix B. Supporting Information _ Facile Synthesis of Monodisperse Gold Nanoparticles with Carbon Monoxide in Microfluidic Segmented Flow system

B1. Characterization of synthesized Au NPs with different initial concentration of gold precursor

The particle size and size distribution of 0.030 mM and 0.54 mM initial concentration of precursor in **Figure 4-5** were obtained from TEM (**Figure B-1**) and DCS (**Figure B-2**) respectively.

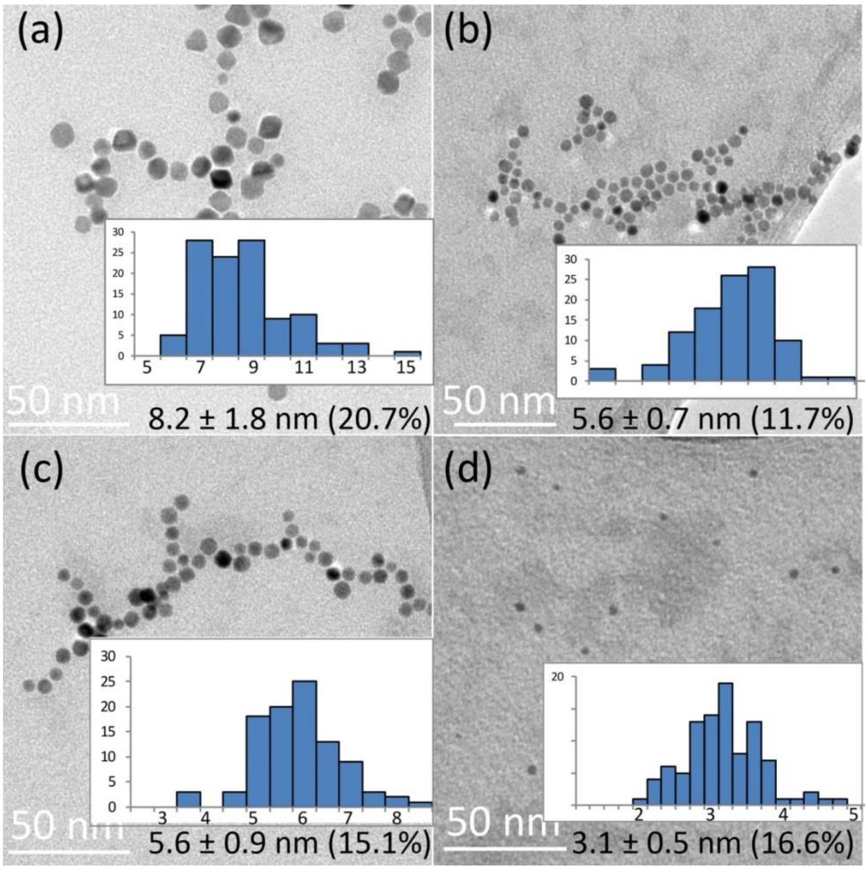

Figure B-1 TEM images of gold nanoparticles at liquid to gas flow ratios of (a) 20, (b) 10, (c) 5 and (d) 2 with 0.030 mM initial concentration of $HAuCl_4$ at room temperature in microfluidic segmented flow system.

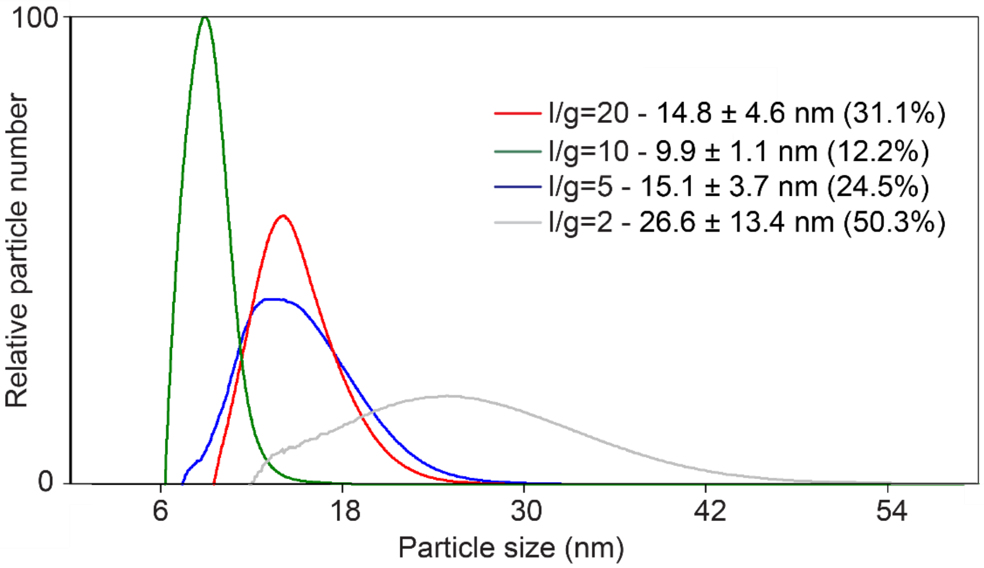

Figure B-2 Particle size and size distribution of gold nanoparticles obtained from DCS at liquid to gas flow ratios of 20 (red line), 10 (green line), 5 (blue line) and 2 (grey line) with 0.54 mM initial concentration of $HAuCl_4$ at room temperature in microfluidic segmented flow system.

Figure B-3 shows the IR spectra of CO-produced Au NPs in aqueous solution. If the CO adsorbed atop the gold surface, there should be a weak band at 2125 cm^{-1}.[1] Its absence in **Figure B-3** indicated that no CO is present on the NPs.

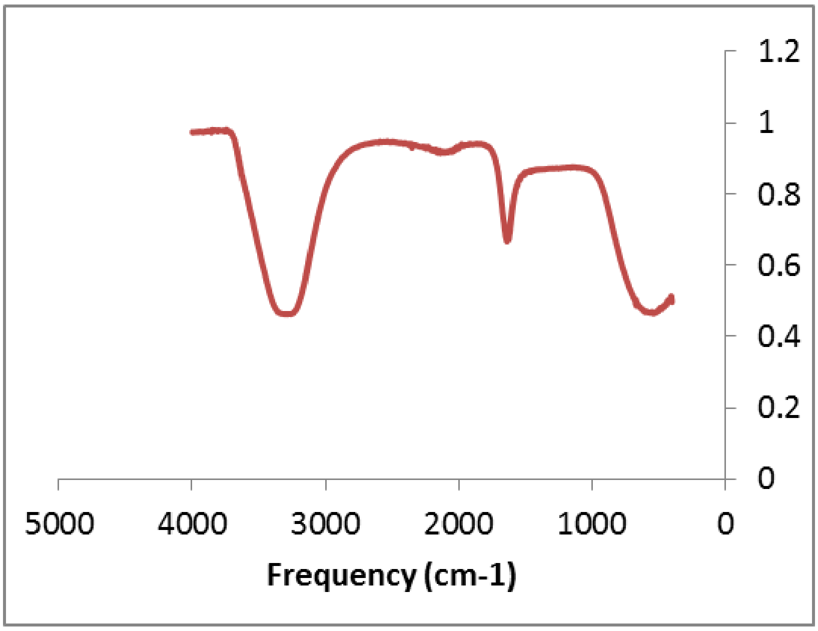

Figure B-3 IR spectra of CO-produced Au NPs in aqueous solution at 0.54 mM initial concentration of $HAuCl_4$, liquid to gas flow ratio of 2, room temperature and residence time of 5 min.

B2. Calculation of enhancement factor EF:

The calculation is similar like section A4. Three peaks were chosen to calculate the EF and shown in **Table B-1**:

Table B-1 Enhancement factor of gold nanoparticles samples

Wavenumber	**Band intensity**					**Enhancement factor EF**			
	Raman_Rh 6G powder	SERS_A	SERS_B	SERS_C	SERS_D	SERS_A	SERS_B	SERS_C	SERS_D
611 cm^{-1}	1137	3752	9291	12516	17997.62	3.30×10^8	8.71×10^8	1.10×10^9	1.58×10^9
1359 cm^{-1}	1097	4509	16084	32196	26588.61	4.11×10^8	1.47×10^9	2.93×10^9	2.42×10^9
1509 cm^{-1}	1070	3956	17672	33952	27540.14	3.69×10^8	1.65×10^9	3.17×10^9	2.57×10^9
Average enhancement factor						3.70×10^8	1.31×10^9	2.40×10^9	2.19×10^9

SERS_A: Commercial citrate-capped 10 nm Au NPs

SERS_B: CO-produced 7.6 nm Au NPs synthesized in this work

SERS_C: CO-produced 26.6 nm Au NPs synthesized in this work

SERS_D: Commercial citrate-capped 30 nm Au NPs

B3. TEM image of Au NPs in oleylamine-only reduction without CO

An experiment was performed where N_2 was used to replace CO at the same experimental conditions to prove that the CO was the dominant reducing agent rather than oleylamine. **Figure B-4** shows that single-crystal nanowires were formed without CO, similar to previous literature[2] that found nanowires for oleylamine reduction.

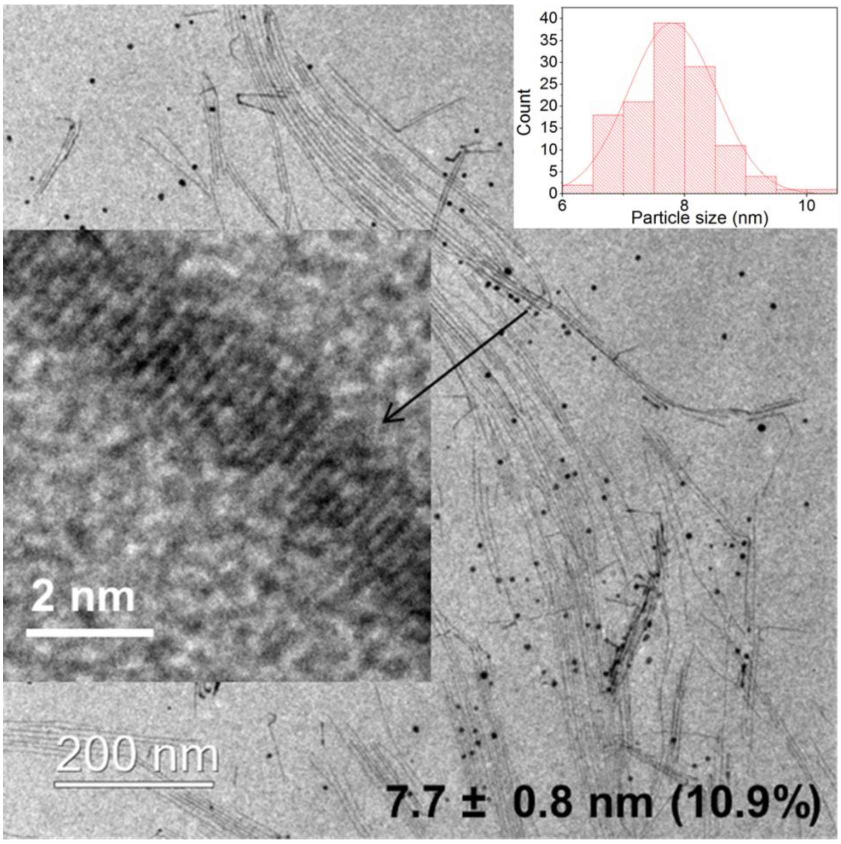

Figure B-4 TEM image of gold nanoparticles in oleylamine-only reduction without CO, the product contains a mixture of spherical gold nanoparticles (7.7 ± 0.8 nm, 10.9%) and Au nanowires (~ 1.7 nm in width and few µm in length). Insert shows a zoomed-in nanowire with lattice.

Appendix C. Supporting Information _ Continuous Synthesis of Gold Nanoparticles with Carbon Monoxide in Liquid-Liquid Microfluidic Segmented Flow system

C1 Flow pattern of three-stream mixing

The cross junction with three inlets was tested to form homogeneous droplet flow patterns. The blue and pink dye was dissolved in water to label different aqueous streams. **Figure C-1** shows the flow pattern after the cross junction by aqueous blue and pink dye solutions and pure heptane. The picture proved that the pink and blue dye mixed perfectly inside one droplet (no individual pink or blue droplet observed). Thus, cross-junction was feasible to form perfect mixing slug flow with three inlets and could be used for mixing water-soluble capping agent and gold precursor with heptane at the same time.

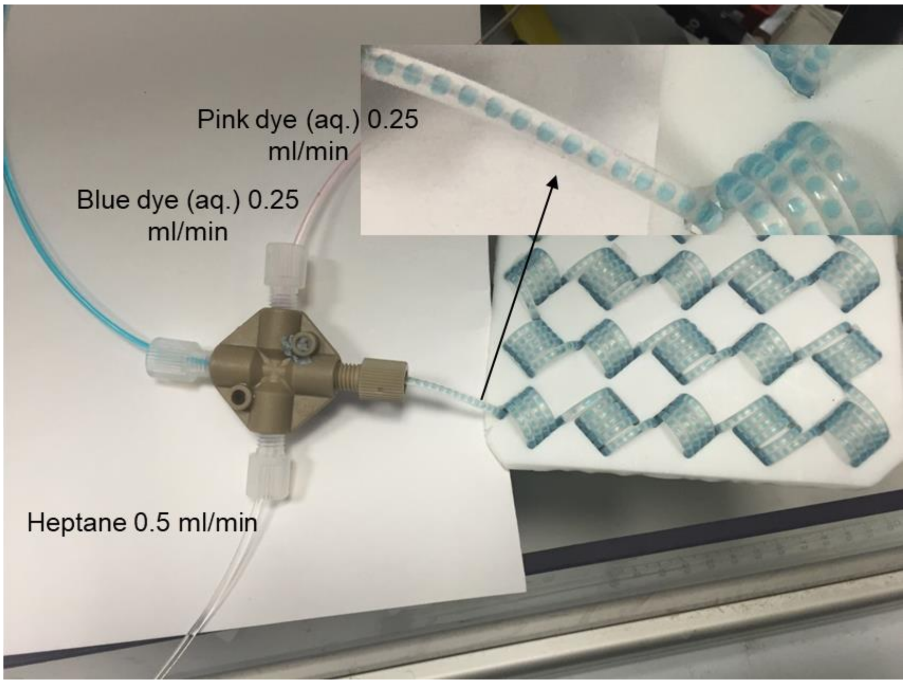

Figure C-1 Homogeneous flow pattern formed from three stream mixing via cross junction at flow rate ratio of heptane/blue dye/pink dye solution of 2:1:1.

C2 Flow pattern with interfacial absorption

Figure C-2 shows the black precipitation at end of the aqueous droplets due to the irreversible aggregation of synthesized particle accumulated on the water-organic interface.

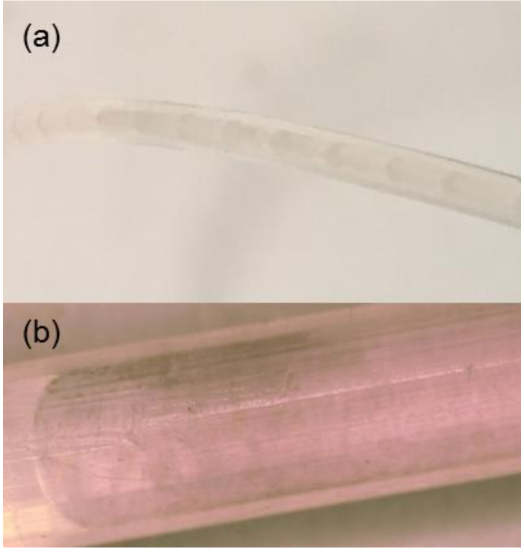

Figure C-2 Flow pattern and black precipitation at end of the aqueous droplets during (a) the synthesis of Au NPs at 0.27 mM $HAuCl_4$ in straight FEP tubing with 1 mm I.D. and 25 cm length at room temperature with initial pH of 4.06 and residence time of 9.8 s; (b) Zoomed-in image of black precipitation inside the tube.

C3 Surface-to-volume ratio calculation

In order to study interfacial absorption, two tubes (1 mm and 0.5 mm I.D.) were used to do the comparison. The flow pattern is shown in **Figure C-3** and surface-to volume-ratio calculation is shown in **Table C-1** and.

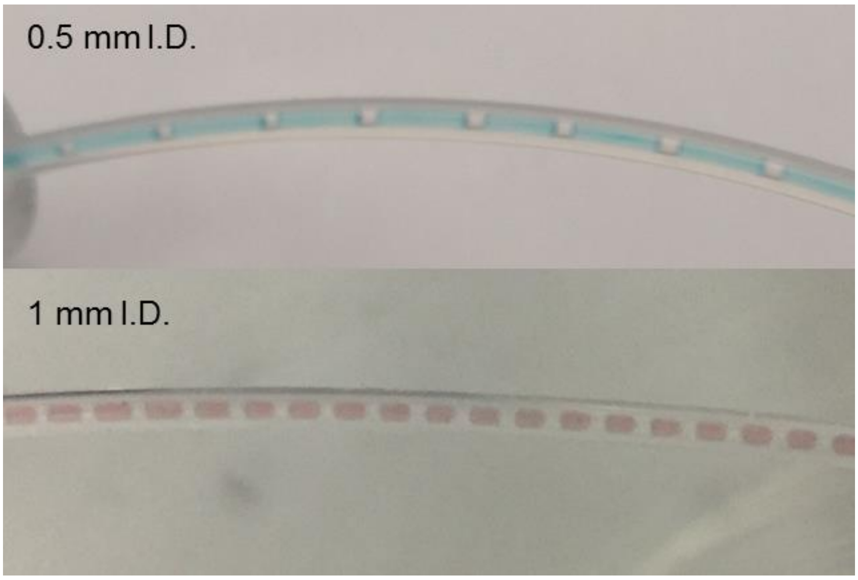

Figure C-3 Flow patterns of different inner diameter tubing (25 cm length) in **Figure 5-8** containing aqueous solution and octane streams at the same total velocity of 0.025 m/s with octane/water flow ratio of 1:2.

Table C-1 Surface-to-volume ratio calculation based on the flow patter in Figure C-3

Inner diamter (mm)	**Water droplet length (mm)**	**Surface (mm^2)**	**Volume (mm^3)**	**Surface-to-volume ratio**
0.50	2.77	4.74	0.54	8.72
1.00	2.11	8.20	1.66	4.95

The flow pattern at different inner diameters used in **Figure 5-15** is shown in **Figure C-4**. Surface-to-volume ratio calculation is shown in **Table C-2**.

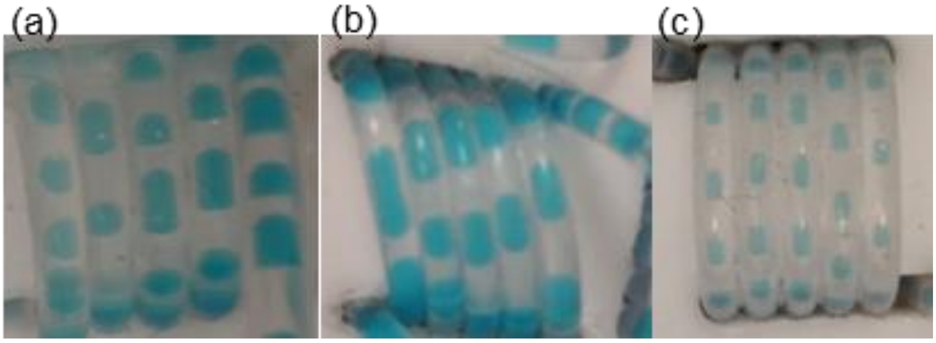

Figure C-4 The flow patterns at different FPA CFI inner diameter (**Figure 5-15**): (a) 1.55 mm I.D. PFA CFI with length of 254 cm, (b) 1 mm I.D. PFA CFI with length of 355 cm and (c) 0.5 mm I.D. PFA CFI with length of 900 cm containing CO-saturated heptane and blue dye labelled aqueous solution at flow ratio of 2, residence time of 32.4 min

Table C-2 Surface-to-volume ratio calculation based on the flow patter in Figure C-4

Inner diameter (mm)	**Water droplet length (mm)**	**Surface (mm^2)**	**Volume (mm^3)**	**Surface-to-volume ratio**
1.55	1.83	12.68	3.45	3.67
1.0	1.95	7.69	1.53	5.03
0.5	1.05	2.04	0.21	9.90

C4. Yield estimation based on DCS

The mass of the particles was given by DCS together with the particle size and size distribution for each sample. Thus, the concentration of the gold could be estimated with known volume. However, the estimation could only be used for qualitative analysis. The error sources could come from the unprecise injection of the sample (here all regarded as 0.1 ml) and the mass of the citrate capped on gold surface was regarded as gold.

Table C-3 The yield estimation based on DCS result of 0.1 ml samples synthesized from 0.27 mM $HAuCl_4$ and CO-saturated octane in straight FEP tubing with 1 mm I.D. and 25 cm length at room temperature and residence time of 9.8 s.

Exp name	**Weigh from DCS (µg)**	**Molar mass (mM)**	**yield %**
0.27 mM-pH~5.6-1 mm I.D.	2.34	0.16	58.16
0.27 mM-pH~4-1 mm I.D.	0.73	0.051	18.79

Table C-4 The yield estimation based on DCS for Figure 5-8. 0.1 ml samples synthesized from aqueous $HAuCl_4$ and CO-saturated octane in straight FEP tubing with different inner diameters (0.5 mm and 1 mm I.D.) and 25 cm length at room temperature, residence time of 9.8 s and citrate/Au concentration ratio=12

Exp name	**Weigh from DCS (µg)**	**Molar mass (mM)**	**yield %**
0.27 mM--1 mm I.D.	2.34	0.16	58.16
0.27 mM-0.5 mm I.D.	0.86	0.06	22.71
1.08 mM-1 mm I.D.	4.09	0.29	26.70
1.08 mM-0.5 mm I.D.	1.05	0.07	6.60

Appendix D. Supporting Information _ Rapid and High-yield Synthesis of $Au_{25}(SR)_{18}$ Nanoclusters via Carbon Monoxide in Microfluidic Segmented Flow system and their antimicrobial performance

D1 Reactants incubation time

For typical protocol of our method, the $HAuCl_4$ solution was pre-mixed with cysteine and NaOH in batch at least 2 h before CO reduction to fully convert Au(III) to Au(I) complexes. **Figure D-1** shows the UV-Vis spectra of synthesized Au NCs if the aqueous reaction solution was used immediately without 2 h incubation. One stream of acidic gold precursor with $[AuCl_4]^-$ ions and another stream of the alkaline cysteine solution tuned by NaOH were mixed in-line through a micromixer chip (residence time inside less than 10 s, Dolomite, Part No. 3000144) before merging with the heptane stream. The reaction time decreased to 14 min as the absorption of the peak at 670 nm at residence time of 14 min and 28 min was nearly identical. However, the peak was not as sharp as **Figure 6-3** which indicates that the product contained NCs with different cluster sizes, rather than pure $[Au_{25}(Cys)_{18}]$. The TEM image in **Figure D-2** also shows the existence of NCs with different sizes. this is because there were several parallel reduction kinetics occurring inside the reactor: the thiol reduction to form thiolate-Au(I) complexes and the CO reduction on Au(III) ions or thiolate-Au(I) complexes. The fast reduction with different rates could form mixed-size Au NCs. Thus, premixing the gold with thiol capping agent to prepare fully-converted thiolate-Au(I) complexes solution is necessary in order to obtain the high purity of $Au_{25}(Cys)_{18}$ clusters under control.

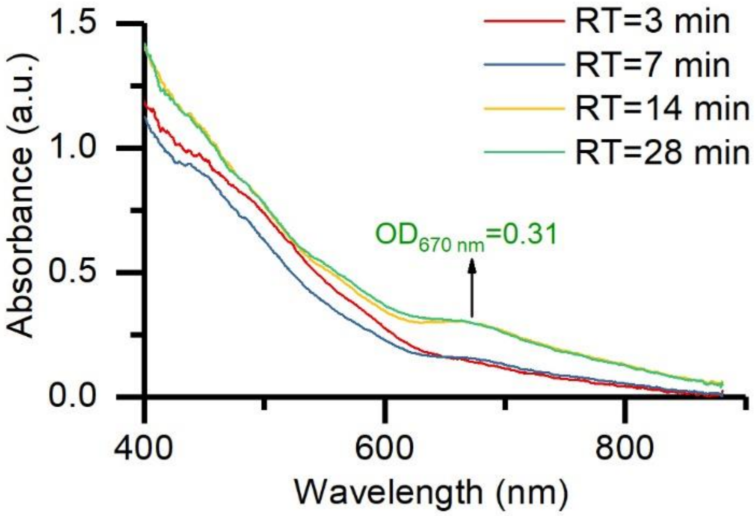

Figure D-1 UV-Vis spectra of the Au NCs from 1 mM initial concentration of $HAuCl_4$ at room temperature with in-line mixing of gold and thiol solution at different residence times (RT) by tuning the flow rate with constant organic to aqueous flow ratio of 2 and cysteine to gold concentration ratio of 1.5.

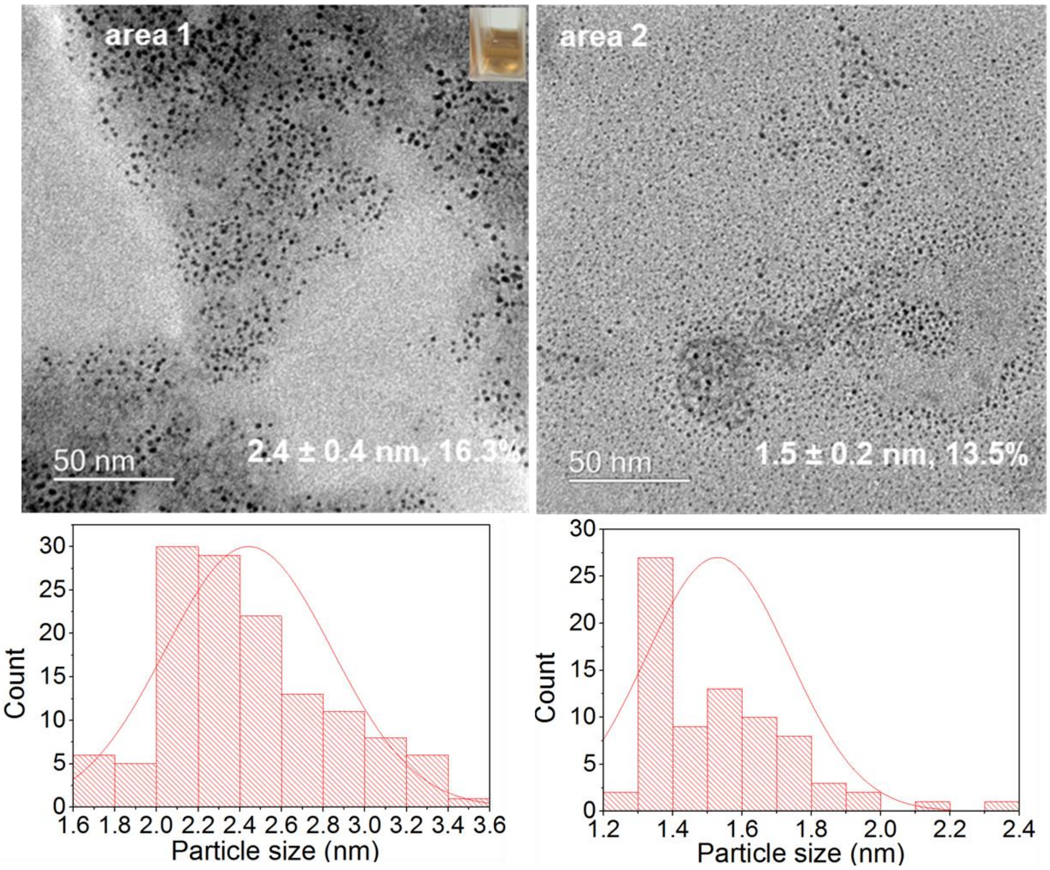

Figure D-2 TEM image of the synthesized Au NCs from 1 mM initial concentration of $HAuCl_4$ at room temperature with in-line mixing of gold and thiol solution at residence time of 14 min with constant organic to aqueous flow ratio of 2 and cysteine to gold concentration ratio of 1.5. The area 1 and 2 was captured from different zones on the same TEM grid.

D2 Stability of as-synthesized Au_{25} NCs in water

It was observed that if the sample was stored in water solution, the characteristic peak would fade away with time evolution. The rate of decay is proportional to the concentration of the clusters. **Figure D-3** indicates that the Au NCs obtaind from 1 mM intial concentration of gold precursor was stable for 2 days in water. After 3 days, the characteristic peak at 670 nm decayed, suggesting the decreased purtiy of the sample. Thus, the sample should be stored as solid form which was stable at least two months.

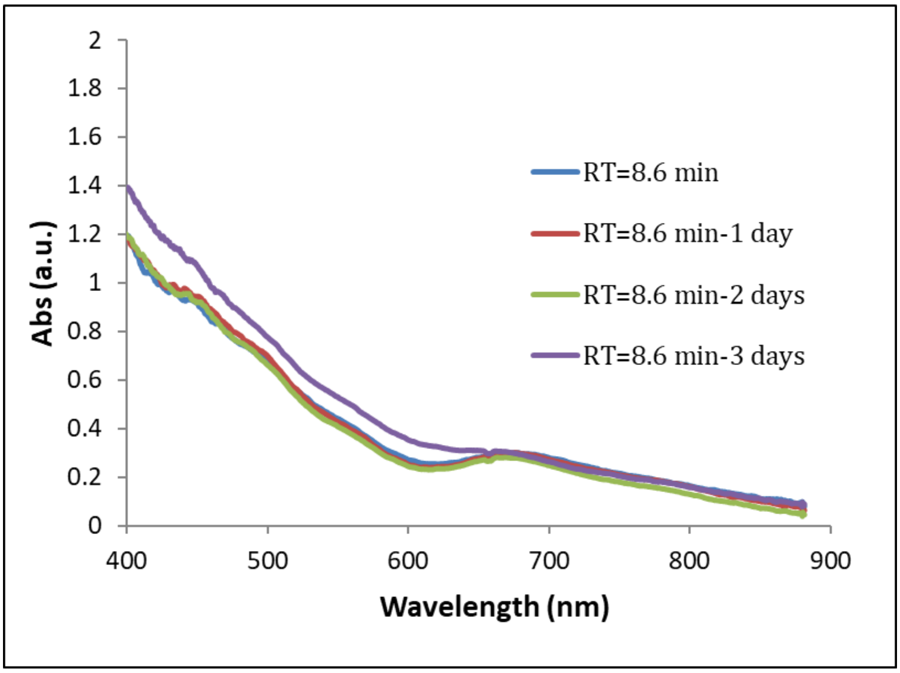

Figure D-3 UV-Vis spectra of the sample stability stored in water at room temperature. The Au NCs were obtained with 1 mM initial concentration of $HAuCl_4$ at 80°C, residence time (RT) of 8.6 min, organic to aqueous flow ratio of 2 and cysteine to gold concentration ratio of 1.5.

D3 Mixing enhancement inside coil flow inverter (CFI)

At the residence time of 2.9 min, output solutions became turbid. To verify if the turbid solution was obtained due to CFI or not, a comparable trial was conducted by using circular FEP capillary (1 mm ID, VICI Jour) instead of CFI with all the other experimental conditions constant. The streams of DI-water and heptane at the flow rate of 0.32 ml/min and 0.64 ml/min, respectively, were pumped into 5 m circular capillary at 80 °C and 500 kPa. **Figure D-4**.shows the output aqueous solution from CFI and circular tubing. The cloudy solution containing homogeneous heptane microdroplets only occurred inside CFI, which proved the significant mixing capability of segmented flow regimes inside CFI.

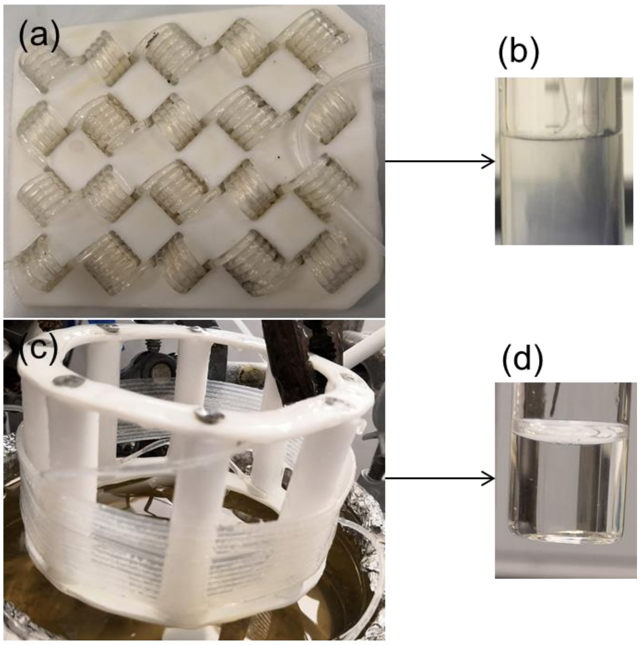

Figure D-4 Comparison of output solution: (b) cloudy solution from (a) CFI; (d) clear solution from (c) circular capillary via water-heptane segmented flow at a residence time of 2.9 min, 80 °C and 500 kPa.

D4 Data analysis for electrospray ionization mass spectrometry (ESI-MS)*

The infusing flow rate was 20 µL/min by using the syringe pump into the Agilent 6510 quadrupole Time-of-Flight (QTOF) mass spectrometer. A capillary dual-nebuliser electrospray ion source was operated in negative-ion mode. Prior to cap-ESI analysis, the QTOF was calibrated with the reference calibration mixture from Agilent. The capillary dual-nebuliser electrospray ion source and ion guide optics settings were experimentally optimised for $Au_{25}(Cys)_{18}$: -Vcapillary voltage 4000 V, fragmentor voltage 175 V, skimmer voltage 65 V, oct RF Vpp 750 V, oct1 DC 45, lens1 43.9 V and lens2 32.7 V, nebuliser 20 psi, drying gas temp 325 °C, drying gas flow 5 L/min. The drying gas was nitrogen. The TOF was tuned using standard tune in the negative ESI mode and operated in total ion mode with peak width narrow, quad DC 37 V, post filter DC 37 V, followed by adjustment of quad amu, pusher, puller, accelerated focus, mirror front and back to achieve symmetrical peak shape and maximum resolution without substantial loss of signal intensity. Following this procedure, resolution values between approximately 14,000 and 22,000 full width at half maximum (FWHM) were routinely achieved (measured at a signal intensity of 2x106). The acquisition parameters were MS mode. The acquisition rate was 1 spectra/sec and acquisition time 1000 ms/spectrum corresponding to 9652 transients/spectrum. All data acquired was at mass range High (10,000 *m/z*).

A typical procedure to determine the cluster formula by ESI-MS was as follows: (a) Determine the charge state (*z*) of the ionised cluster, where *z* equals to

---

* *ESI-MS experiments were performed by Dr. Kersti Karu, University College London.*

$1/\Delta(m/z)$ if the isotopic peak spacing is $\Delta(m/z)$; (b) Calculate the monoisotopic mass (exact mass) of the ionised cluster, which equals to $[Au_{25}(Cys)_{18}\text{-}xH+nM]^{z-}$, where x is number of H^+ dissociated and M is number of Na^+ or Cs^+ or K^+ ions binding; (c) Use the isotope patterns to confirm the monoisotopic mass and charge of ionised species, where a simulated isotope pattern is compared with the experimental one.

The isotope patterns of peaks in **Figure 6-9b** matched perfectly with theoretical isotope patterns in **Figure D-5**. The theoretical isotope patterns of the peak were simulated by Thermo Xcalibur software (2.2.0.48).

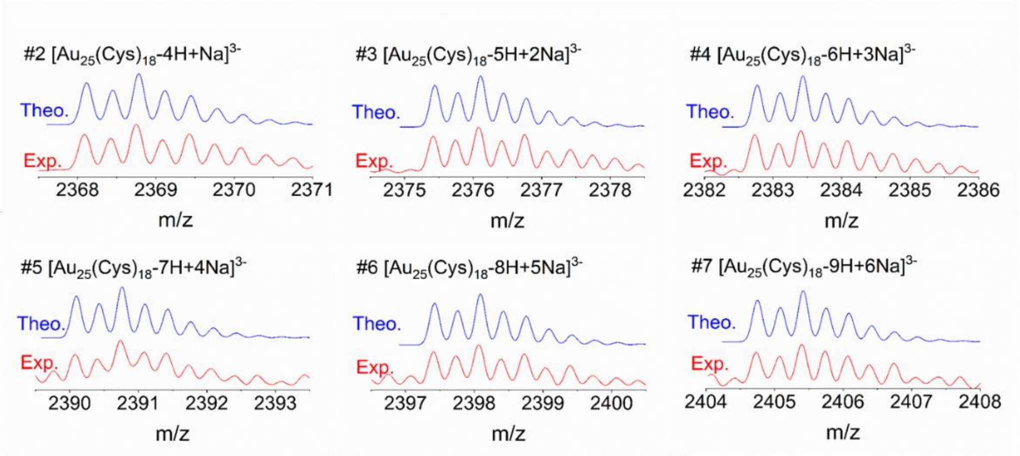

Figure D-5 The theoretical and experimental isotope patterns of #2-#7 peak in Figure 6-9b.

Figure 6-9 also showed the second most intense cluster of #8-#11 peaks were at *m/z* ~ 2411, as well as three consequent peaks until *m/z* range to 2441. The isotopic pattern for the cluster of peaks confirmed that these ions were triply (3-) charged. The #8 peak at *m/z* 2411.09 was assigned as $[Au_{25}(Cys)_{18}\text{-}5H+Cs+Na]^{3-}$ ions (Exact mass 7236.24 Da). The fomula of subsequential ions were $[Au_{25}(Cys)_{18}\text{-}xH+Cs+yNa]^{3-}$, where x and y is dissociation of H^+ and coordination of Na^+. The summary of assigment of these *m/z* peaks is in **Table D-1**.

Table D-1 Summary of *m/z* peaks observed in ESI mass spectrum of the mass range from *m/z* 2411 to 2641 for $Au_{25}(Cys)_{18}$ nanoclusters. These species were triply (3-) charged.

Item	***m/z***	**Elemental composition assigne**	**Gas-phase ions formed under ESI**	**Exact mass, Da**
#8	2411.09	$Au_{25}C_{54}H_{103}N_{18}O_{36}S_{18}CsNa$	$[Au_{25}(Cys)_{18}\text{-}5H+Cs+Na]^{3-}$	7236.24
#9	2418.41	$Au_{25}C_{54}H_{102}N_{18}O_{36}S_{18}CsNa_2$	$[Au_{25}(Cys)_{18}\text{-}6H+Cs+2Na]^{3-}$	7258.22
#10	2425.73	$Au_{25}C_{54}H_{101}N_{18}O_{36}S_{18}CsNa_3$	$[Au_{25}(Cys)_{18}\text{-}7H+Cs+3Na]^{3-}$	7280.21
#11	2433.06	$Au_{25}C_{54}H_{100}N_{18}O_{36}S_{18}CsNa_4$	$[Au_{25}(Cys)_{18}\text{-}8H+Cs+4Na]^{3-}$	7306.19

Additional set of peaks was also observed at lower mass, *m/z* ~1808 (**Figure 6-9**). The analysis of the isotopic pattern determined the isotopic peak spacing as 0.25 (**Figure D-6 insert**). Therefore, these ions were fourtly charged. Zoom-in ESI mass spectrum of this *m/z* region was shown in **Figure D-6**. These gas-$\times10^{1}$ase ions corresponded to dissociation of H^+ and binding of Na^+ and Cs^+ ions. Binding of two Cs^+ ions was also observed. **Table D-2** summarised the assigned *m/z* peaks and their empirical formula and gas-phase ions.

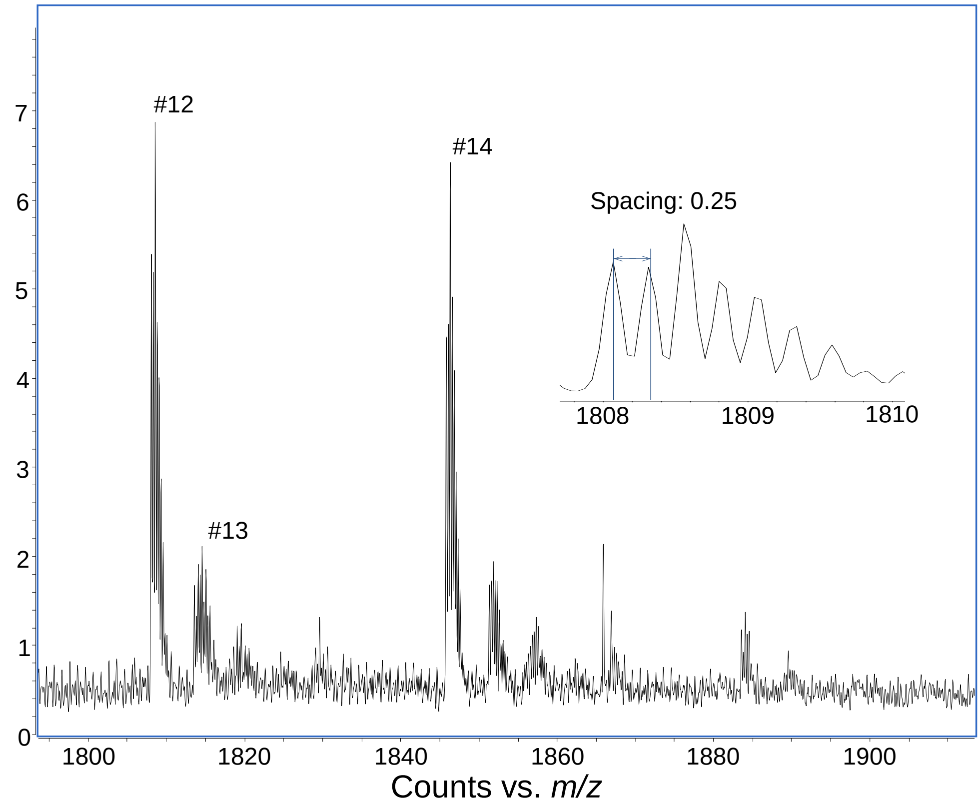

Figure D-6 ESI mass spectrum in the *m/z* range from 1800 to 1910, insert is the isotopic pattern in the *m/z* range from 1808 to 1810.

Table D-2 Summary of *m/z* peaks observed in ESI mass spectrum of the mass range from *m/z* 1800 to 1910 for $Au_{25}(Cys)_{18}$ nanocluster. These ions were fourthly (4-) charged.

Item	***m/z***	**Elemental composition assigne**	**Gas-phase ions formed under ESI**	**Exact mass, Da**
#12	1808.61	$Au_{25}C_{54}H_{100}N_{18}O_{36}S_{18}CsNa$	$[Au_{25}(Cys)_{18}-8H+Cs+Na]^{4-}$	7234.84
#13	1813.55	$Au_{25}C_{54}H_{103}N_{18}O_{36}S_{18}CsNa_2$	$[Au_{25}(Cys)_{18}-6H+Cs+2Na]^{4-}$	7258.22
#14	1845.82	$Au_{25}C_{54}H_{106}N_{18}O_{36}S_{18}Cs_2K$	$[Au_{25}(Cys)_{18}-3H+2Cs+K]^{4-}$	7387.14

References

1. Zhang, T.; Driver, S. M.; Pratt, S. J.; Jenkins, S. J.; King, D. A., Ir-induced activation of Au towards CO adsorption: Ir films deposited on Au {111}. *Surface Science* **2016,** *648*, 10-13.

2. Feng, H.; Yang, Y.; You, Y.; Li, G.; Guo, J.; Yu, T.; Shen, Z.; Wu, T.; Xing, B., Simple and rapid synthesis of ultrathin gold nanowires, their self-assembly and application in surface-enhanced Raman scattering. *Chemical Communications* **2009,** (15), 1984-1986.